STEALTH Modeling of Time-Dependent Flows in Piping

EPRI

EPRI NP-1441
Project 812-1
Final Report
December 1980

Keywords:
STEALTH
Piping
Single Phase
Loads

Prepared by
Science Applications, Incorporated
San Leandro, California

ELECTRIC POWER RESEARCH INSTITUTE

STEALTH Modeling of Time-Dependent Flows in Piping

NP-1441
Research Project 812-1

Final Report, December 1980
Work Completed, May 1980

Prepared by

SCIENCE APPLICATIONS, INCORPORATED
2450 Washington Avenue
San Leandro, California 94577

Principal Investigators
L. M. Cohen
M. B. Gross

Prepared for

Electric Power Research Institute
3412 Hillview Avenue
Palo Alto, California 94304

EPRI Project Manager
J. Carey

Water Reactor System Technology Program
Nuclear Power Division

ORDERING INFORMATION

Requests for copies of this report should be directed to Research Reports Center (RRC), Box 50490, Palo Alto, CA 94303, (415) 965-4081. There is no charge for reports requested by EPRI member utilities and affiliates, contributing nonmembers, U.S. utility associations, U.S. government agencies (federal, state, and local), media, and foreign organizations with which EPRI has an information exchange agreement. On request, RRC will send a catalog of EPRI reports.

NOTICE

Prepared by
Science Applications, Incorporated
San Leandro, California

EPRI PERSPECTIVE

PROJECT DESCRIPTION

STEALTH is a general-purpose explicit finite difference code developed by EPRI for application in the nuclear power industry. The technology is based on methods developed in the defense industry. STEALTH's architecture is designed for easy implementation of special models for specific application with this general-purpose code. The STEALTH code has been applied in fluid-structure interaction, boiling water reactor containment, soil structure interaction, piping loads, welding, and nuclear waste repository analyses.

This project addresses subcooled time-dependent flow phenomena in piping systems using the one-dimensional STEALTH code. Developments include models for piping components, a model for fluid motion losses, and a procedure for force resolution. Example simulations of a feedwater shutdown, pressurizer relief line discharge, pump trip with bypass, Semi-scale 711 experiment, and a pressure pulse experiment are included.

PROJECT OBJECTIVE

The objective of this study is to provide a viable tool for the prediction of fluid loads within piping networks. This study involves the addition of models to STEALTH to simulate the effects of orifices, area changes, tee junctions, valves, turbomachines, and fluid motion losses.

PROJECT RESULTS

STEALTH's capability has been extended to simulate piping systems. The code will locate the regions of intense fluid conditions and resolve the magnitudes of these effects on the piping structure. Additional models will be developed if the users believe it necessary.

This entire project was managed by Dr. John J. Carey.

C. Chan, Program Manager
Water Reactor System Technology Program
Safety and Analysis Department
Nuclear Power Division

ABSTRACT

This report documents technologies that enable the STEALTH 1D numerical code to simulate the time-dependent flow phenomena that can occur in the piping systems of power plants. Fixed-frame control volumes simulate the presence of piping components; these include models for orifices, area changes, valves, tee junctions, and turbo-machines. The hydro version of the STEALTH code, purged of the physics and numerics associated with solid mechanics, can perform efficient flow simulations. The pipe friction and piping component loss model account for irreversible effects associated with flow in piping systems. Instantaneous stream functions account for transient forces that bear on piping components. The plot overlay option can display several nodal histories on one axis system. In demonstration of these technologies, the appendixes describe one-dimensional, numerical simulations of pipe flows that are generic to power plant systems. These include simulations of a feedwater shutdown event, a pressurizer relief line discharge event, a pump trip (with bypass) event, a three-dimensional blowdown event, and the response of a water-filled, straight pipe to a pressure pulse.

Blank Page

ACKNOWLEDGMENT

The Principal Investigators wish to acknowledge several persons who contributed to this work. In the San Leandro office of Science Applications, Inc., Mr. Ronald Hofmann provided guidance on the code architecture, numerics, and physical modeling; Mr. Stewart Silling, Mr. Jack Reaugh, and Dr. Donald Maxwell consulted on physical modeling; Mr. Gaymond Yee assisted with calculations; Ms. Debra Ditzler and Mr. Bence Gerber provided support with the computer system; Ms. Sophie Carman edited and typed the report. From the utility industry: Messrs. Daniel Lehnert and Allen Lim of Detroit Edison Company, and Messrs. Steve Roberts and Paul Baughman of Yankee Atomic Electric Company supplied engineering data for realistic simulations. Others who shared their expertise include: Messrs. David Caraher and George Santee of Intermountain Technologies, Inc., and Drs. Leonard Schwer and Dominic Cagliostro of SRI International.

Blank

CONTENTS

		Page
SECTION 1	INTRODUCTION AND SUMMARY	1
	1.1 Transient Fluid Environments in Piping	1
	1.2 Pressure Waves in Pipe Flows	1
	1.3 Limitations of Existing Techniques	2
	1.4 STEALTH Programs	3
	1.5 Current Developments	4
SECTION 2	PIPING COMPONENT MODELS	7
	2.1 Overview	7
	2.2 Modeling Criteria	8
	2.3 Model Concepts	8
	2.4 Working Models for Subcooled Fluids	13
	2.4.1 Subcooled Area Change	17
	2.4.2 Subcooled Orifice	21
	2.4.3 Subcooled Tee Junction	24
	2.4.4 Subcooled Valve	26
	2.4.5 Subcooled Turbo-machines	28
	2.5 Working Model Simulations	35
	2.6 Additional Models	68
SECTION 3	CONCOMITANT TECHNOLOGIES	69
	3.1 Preliminary Comments	69
	3.2 Hydro Versions	69
	3.3 Fluid Motion Losses	70
	3.4 Force Resolution	72
	3.5 Plot Overlays	76
SECTION 4	CLOSURE	78
REFERENCES		80

CONTENTS (continued)

		Page
APPENDIX A	A RATIONAL PROCEDURE FOR DISTRIBUTING THE LOSS EFFECT OF A PIPING COMPONENT	81
APPENDIX B	SIMULATION OF A FEEDWATER SHUTDOWN EVENT.	88
APPENDIX C	SIMULATION OF A PRESSURIZER RELIEF LINE DISCHARGE EVENT .	111
APPENDIX D	SIMULATION OF A PUMP TRIP WITH BYPASS	155
APPENDIX E	SIMULATION OF THE SEMI-SCALE 711 EXPERIMENT	173
APPENDIX F	SIMULATION OF THE RESPONSE OF A WATER-FILLED, STRAIGHT PIPE TO A PRESSURE PULSE.	188

ILLUSTRATIONS

Figure		Page
1	Examples of Adjacent Regions (I and II) for Typical Piping Component Control Volumes.	9
2	Control Volume with Five Adjoining Grids	11
3	Piping Component Control Volumes with Adjoining Computational Grids.	15
4	Conditions Present in the Subcooled Area Change Control Volume Model.	18
5	Conditions Present in the Subcooled Orifice Control Volume Model .	22
6	Subcooled Tee Junction Control Volume Model.	25
7	Conditions Present in the Subcooled Valve Control Volume Model . .	27
8	Conditions Present in the Subcooled Turbo-Machine Control Volume Model.	30
9	Four-Quadrant Representation of Pump Operation	33
10	20:1 Orifice Pressure Profile at ~ 1 ms.	38
11	20:1 Orifice Pressure Profile at ~ 3 ms.	39
12	20:1 Orifice Pressure Profile at ~ 5 ms.	40
13	Velocity History at 20:1 Orifice	41
14	3:1 Orifice Pressure Profile at ~ 1 ms	42
15	3:1 Orifice Pressure Profile at ~ 3 ms	43
16	3:1 Orifice Pressure Profile at ~ 5 ms	44
17	Velocity History at 3:1 Orifice.	45
18	1:20 Area Change Pressure Profile at ~ 1 ms.	46
19	1:20 Area Change Pressure Profile at ~ 3 ms.	47
20	1:20 Area Change Pressure Profile at ~ 5 ms.	48
21	1:20 Area Change Pressure Profile at ~ 8 ms.	49
22	Velocity History at 1:20 Area Change	50

ILLUSTRATIONS (continued)

Figure		Page
23	20:1 Area Change Pressure Profile at ~ 1 ms	51
24	20:1 Area Change Pressure Profile at ~ 3 ms	52
25	20:1 Area Change Pressure Profile at ~ 5 ms	53
26	20:1 Area Change Pressure Profile at ~ 8 ms	54
27	Velocity History at 20:1 Area Change	55
28	Opening Valve Pressure Profile at ~ 1 ms	57
29	Opening Valve Pressure Profile at ~ 3 ms	58
30	Opening Valve Pressure Profile at ~ 5 ms	59
31	Opening Valve Pressure Profile at ~ 8 ms	60
32	Velocity History at Opening Valve	61
33	Blowdown Pressure Profile at ~ 1 ms	62
34	Blowdown Pressure Profile at ~ 3 ms	63
35	Blowdown Pressure Profile at ~ 4 ms	64
36	Blowdown Pressure Profile at ~ 5 ms	65
37	Blowdown Pressure Profile at ~ 6 ms	66
38	Velocity History at Blowdown Valve	67
39	Free Body Diagram of a Fluid Element Flow Through a Bend	74
40	Demonstration of STEALTH Overlay Capability	77

SECTION 1
INTRODUCTION AND SUMMARY

1.1 TRANSIENT FLUID ENVIRONMENTS IN PIPING

Engineering analysis of power plant systems must include the capability to simulate the transient fluid environments that can develop within pipe networks. These environments produce the maximum loads which the piping must be designed to withstand, safely. Pipe joints and walls, for example, must withstand fluid overpressures without leaking or undergoing permanent deformations; valves and pumps must withstand uncommon differentials in fluid pressure while continuing to provide service; pipe supports must withstand large global forces that are created in network sections when maximum fluid loads bear on pipe bends and junctions. It is important, therefore, to identify the factors that can produce these intense environments in pipe flows, and to account for the ensuing maximum fluid loads.

Typically, transient environments occur within fluid mediums, either static or flowing, as a consequence of pressure waves (or hammers*). Overpressures can develop behind compression hammers, while cavitations or the flashing to vapor of liquid mediums can occur behind rarefaction hammers. Uncommon differentials in pressure can act across either compressions, rarefactions, or wave system combinations of both. Moreover, piping components (such as, e.g., area changes or junctions) or phase changes (such as water flashing to steam) can amplify wave phenomena and exacerbate maximum loads. On the other hand, flow losses (e.g., pipe friction) can attenuate these hammers, thereby reducing maximum loads.

1.2 PRESSURE WAVES IN PIPE FLOWS

Pressure waves develop routinely in the pipe flows of power plants during the normal operation of valves, or whenever pumps and turbines change

*e.g., water hammers.

operating flow rates. These events perturb the flow, which adjusts to the changed conditions through the mechanism of the pressure wave. Non-routine events (pipe breaks, pump or turbine trips, etc.) will also cause flow perturbations that create pressure waves. Both the routine and the non-routine actions that lead to pressure waves are transient events that spawn non-steady wave phenomena. As such, these waves are associated with the time-dependent motion of the fluid medium.

Thus, reasonably accurate numerical predictions of maximum fluid loads within piping systems depend upon pipe flow simulations that account for:

- the time-dependent behavior of fluid motion,
- the geometry (and where appropriate, the dynamics) of piping components,
- the constitutive behavior of fluid materials,
- the flow losses associated with fluid motion in piping.

1.3 LIMITATIONS OF EXISTING TECHNIQUES

Presently, there are techniques which possess the above technologies. But they lack, to some degree, the operational qualities that characterize an off-the-shelf method, which can be easily implemented and cost-effective to use. They fall into one or more of the following categories:

- proprietary techniques, which are either not available or are very costly to acquire;
- complex techniques, which are too cumbersome to tailor to specific applications;
- techniques with complex input, which require an inordinate amount of involvement of senior engineering staff;
- expensive techniques, which incur excessive computer costs, either because of long computing times or large memory storage requirements, or both;
- specialized techniques, which can not simulate the range and types of flow phenomena expected to occur.

1.4 STEALTH PROGRAMS

The STEALTH* programs (Reference 1), however, can incorporate both the technology and the operational qualities that are necessary for realistic, cost-effective pipe flow simulations. The advantages of these codes include the following:

- Availability; the STEALTH codes are in the public domain, sponsored by the Electric Power Research Institute (EPRI).
- Applicability; the STEALTH codes, in general form, are designed to simulate time-dependent continuum phenomena, of which fluid motion in piping systems is a subset; the codes also possess the capability to perform homogeneous equilibrium simulations of two-phase effects.
- Architecture; the top-down, modular design of the STEALTH codes facilitates tailoring to special needs, including the merging of entirely new techniques.
- Documentation; the STEALTH codes are fully documented with user-tested input instructions; this minimizes the user effort needed to assemble input data.
- Economics; the STEALTH codes require only moderate computational times; moreover, because of information overlaying, the codes minimize storage size in memory.
- Accessibility of personnel familiar with the details of the STEALTH codes who are experienced in code usage over a wide range of hydrodynamic applications.

With the addition of models to account for the effects of piping components and flow losses, and a force resolution analysis to calculate force parameters from flow parameters, the 1D STEALTH code becomes a viable technique for the prediction of fluid loads within piping networks. Using combinations of STEALTH grids (for modeling pipe sections) and models of piping components, an engineering analyst can reconstruct (model) pertinent aspects of the networks. These models produce realistic numerical simulations of

*Solids and Thermal hydraulics codes for EPRI Adapted from Lagrange TOODY and HEMP," developed for Electric Power Research Institute by Science Applications, Inc. under Contract RP-307.

critical pipe flow environments, which can then be resolved into the quantitative features and locations of maximum loads.

1.5 CURRENT DEVELOPMENTS

The purpose of the current study is to describe the pipe flow simulation capability for STEALTH 1D. In particular, Science Applications, Inc. (SAI), under contract*, produced the following technologies for the code:

- piping component models;
- STEALTH 1D hydro version;
- fluid motion losses model;
- force resolution analysis;
- history overlay plots.

Moreover, the study also demonstrates these features with simulations of the transient environments which can occur within pipe flows, and which are generic to situations that could be encountered within power plants. This report describes both the development of these features and the construction of the generic simulations.

Section 2 focuses on the development of the models for piping components**; these include:

- orifices
- area changes
- tee junctions
- valves
- turbo-machines

---

*EPRI Contract RP812.

**Except the model for bends; in the 1D sense, a bend is simply a flow loss effect; as such, bends will be discussed in Section 3.

They follow the assumption that the global behavior of a piping component, rather than the detailed local behavior within it, characterizes its influence on a piping system. Each model is a control volume, tailored to the global behavior of a particular piping component. These control volumes communicate through boundary conditions with the computational grids of the STEALTH code. At the beginning of each computational time step, a control volume accepts boundary conditions from the adjoining computational grid (or grids), adjusts itself and simultaneously modifies these conditions in a manner consistent with its tailoring, and then returns the modified boundary conditions to the computational grid(s).

Section 3 discusses the development of the remaining technologies. The STEALTH hydro version contains only that subset of continuum physics which has been purged of non-hydrodynamic phenomena. This increases the efficiency of simulating hydrodynamic environments. Flow losses* are, in effect, external forces which retard fluid motion. Thus, the model for flow losses accounts for this retardation by introducing an increment of deceleration into the equation of motion. The force resolution analysis accounts for the net forces that are required to maintain the global equilibrium of specified regions of pipe networks. These forces must balance the net pressure force acting on the regions, the net momentum flux flowing through the regions, and the rate of momentum growth within the regions. The graphic display package, GRADIS (Reference 1), can produce history overlay plots on one axis system. This increases the usefulness of the force resolution analysis.

The main body of the report closes with Section 4. This section summarizes the previous sections, discusses the implications of these new features in STEALTH 1D, and suggests further developments.

The Appendixes provide additional material that is associated with the main body developments. Although this material complements the previous

*Including the 1D effect of bends.

discussions, each appendix also stands alone as a self-contained presentation. Appendix A presents a rational procedure for distributing the loss effect of a piping component over a specified length. The remaining appendixes describe simulations of pipe flow events which require the construction (modeling) of sections of system networks, using combinations of STEALTH grids and models of piping components. Specifically, these are:

- simulation of a feedwater shutdown event: Appendix B;
- simulation of a pressurizer relief line discharge event: Appendix C;
- simulation of a pump trip with bypass: Appendix D;
- simulation of the Semi-Scale 711 Experiment*: Appendix E;
- simulation of a pipe response experiment**: Appendix F;

---

*Experiment of a three-dimensional blowdown, performed by Idaho Nuclear Engineering Laboratory.

**Experiment of a water-filled, straight pipe response to a pressure pulse, performed by SRI International, Inc.

SECTION 2
PIPING COMPONENT MODELS

2.1 OVERVIEW

Piping components are those elements in a piping system which bound sections of straight pipe. They consist of bends, area changes (reducers), multi-junctions (tees, etc.), orifices, nozzles, valves, turbo-machines (pumps), and reservoirs. They impose forces on the flowing medium, causing it to adjust its motion (such as a direction change, speed change, generation of secondary motions, etc). The fluid reacts by generating pressure waves which impose forces back onto the components. These reaction forces can be substantial, such as with an unsteady flow caused by water hammers.

Since piping components are stationary devices, fixed in position with respect to the piping system, their representations in a predictive calculation occur in the Eulerian (stationary) frame of reference. The STEALTH codes, however, operate in the Lagrangian reference frame of the fluid medium. Hence, the component models must merge the component effects, produced in the stationary frame, with the material frame STEALTH calculations.

The models are control volumes,* that are designed to accomplish this merging. Each control volume is composed of adjacent Eulerian flow regions, one for each flow region present with the represented component. The transfer of information between regions occurs through forms of the conservation equations, which are valid across the interfaces between regions.

The control volumes communicate through boundary conditions with the adjoining Lagrangian grids of the STEALTH codes. This eliminates the need to match the size scale of component models with that of the grids. In effect, the models occupy no length on the size scale of the grids. In practice, this is accomplished by embedding the end nodes of the adjacent grids

*Bends excepted, as footnoted in Section 1.

in the appropriate regions of the control volumes; the velocity of each region and its associated embedded node are kept equal.

Grid rezoning, currently a standard option in STEALTH, maintains the position consistency between the material zones and the stationary control volumes. That is, each node is permitted to move for a prescribed number of time cycles. It is then rezoned to its original position, according to an appropriate constraint [e.g., constant pressure, conservation of mass (and energy), etc].

2.2 MODELING CRITERIA

Each component model must be dynamic, in the sense that it can respond to the states that exist in its adjoining grids. In particular, since these states can change with each computational time step, the model response must be instantaneous. Moreover, the model must be able to account for the time-dependent motion of a variety of fluids; it must respond with the proper acoustic impedance to the pressure waves that act on it from the adjacent grids. Stated succinctly, these considerations define the following modeling criteria:

- The models must respond instantaneously to boundary conditions.
- The models must simulate time-dependent events.
- The models must account for the behavior of any specified fluid material of homogeneous composition, including changes of phase.

2.3 MODEL CONCEPTS

The criteria for modeling provide a basis for developing the fundamental concepts which govern all the models of piping components. Each model is a one-dimensional fixed-frame control volume, which is composed of two, or more, adjacent regions. Each region within a control volume represents one identifiable, instantaneous state that bounds or exists within a particular piping component. Figure 1 displays examples of typical adjacent regions that combine to form a control volume. In Figure 1a, Regions I and

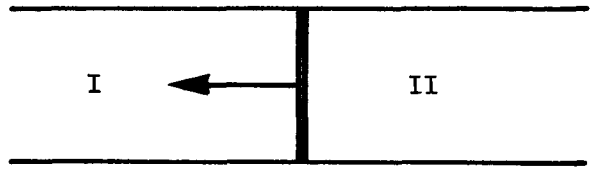

(a) Wave front

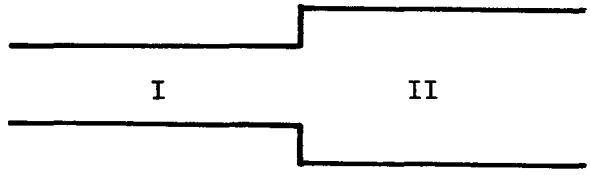

(b) Different flow areas

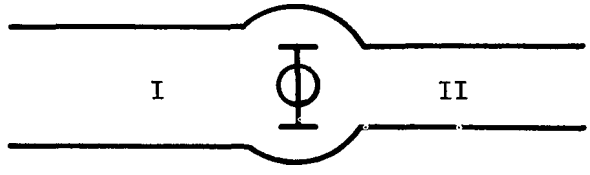

(c) Energy source

Figure 1. Examples of adjacent regions (I and II) for typical piping component control volumes.

II represent the states ahead of and behind, respectively, a wave front; Regions I and II in Figure 1b simulate two consecutive states of different flow areas; Figure 1c illustrates the states, represented by Regions I and II, on either side of an energy source. In effect, each combination of adjacent regions defines a unit flow model. The following discussion explains how this structural concept of a control volume satisfies the modeling criteria of piping components.

In real (actual) flow environments, fluid states interact with one another through the mechanism of waves. Wave fronts are interfaces between two different fluid states, in essence discontinuities which provide the vehicle for the transfer of information within a flow field. Thus, the wave front model (Figure 1a) is the unit flow process by which the piping component control volumes link to the adjoining computational grids. At each location where a control volume and a computational grid meet, a wave front model is embedded within the terminal zone of the latter; see Figure 2. The fronts, in this manner, provide the mechanisms* that match an instantaneous state within a control volume with that in the terminal zone of an adjoining grid. In this respect, all control volumes of piping components are similar; whatever their individual specifics, they all possess wave front models for their boundary structures with the adjoining grids.

The remaining structure of a control volume determines which component of piping it simulates. The control volume of an area change, for example, includes the unit flow process of different flow areas (Figure 1b); on the other hand, the control volume of a turbo-machine includes the unit flow process of an energy source (Figure 1c). The specific details for each control volume are discussed below, in Subsection 2.4.

Because these processes can respond instantaneously to changing flow states, the control volumes can respond instantaneously to boundary conditions and can also simulate time-dependent events. Hence, two of the modeling criteria are satisfied by the structural concepts of the control volumes.

---

*Referred to as jump conditions; see, e.g., Reference 2.

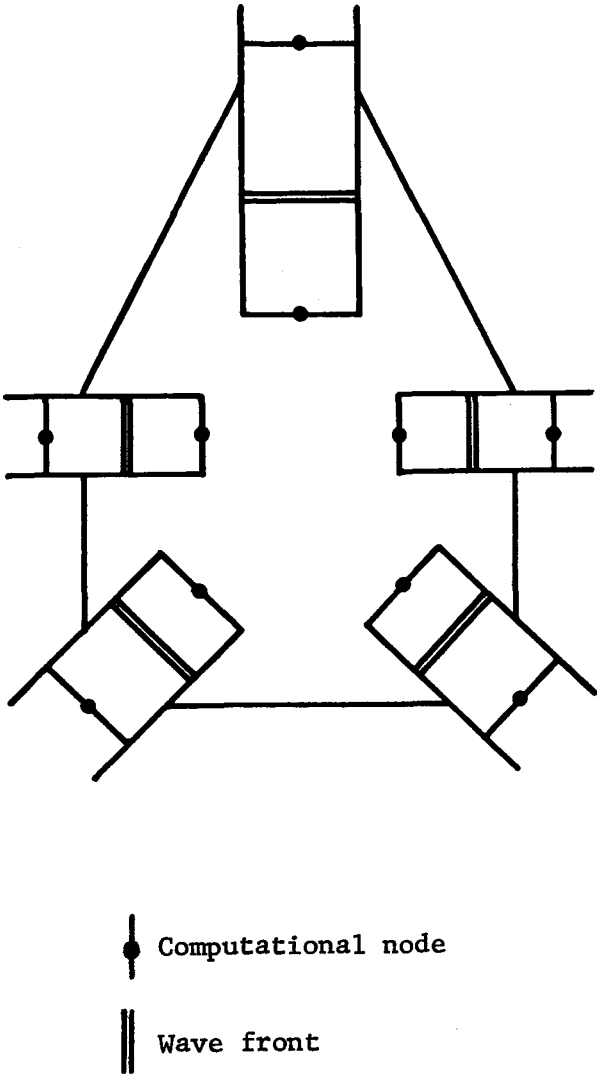

Figure 2. Control volume with five adjoining grids.

The remaining modeling criterion, that of the behavior of the fluid material, enters the model concepts through the mathematical relationships that prescribe the control volume flow dynamics. For the wave fronts, these are the jump conditions (Reference 2) that relate the density (ρ), pressure (p), velocity (U) referenced to the wave coordinate system, and specific internal energy (e) ahead (state I) of the front to those behind (state II):

- $\rho_I U_I = \rho_{II} U_{II}$, continuity
- $\rho_I U_I^2 + p_I = \rho_{II} U_{II}^2 + p_{II}$, momentum
- $\frac{p_I}{\rho_I} + e_I + \frac{U_I^2}{2} = \frac{p_{II}}{\rho_{II}} + e_{II} + \frac{U_{II}^2}{2}$, energy .

For the remaining unit flow processes, the mathematical relationships are the Euler equations for a stream tube, in the following form (Reference 2):

$$\int_I^{II} \frac{dp}{\rho} + \left(\frac{U_{II}^2}{2} - \frac{U_I^2}{2} \right) = \Phi ,$$

where the energy (or loss) source (Φ) can be zero (as, e.g., the idealized process of a change of flow area), and the continuity equation which includes change of flow area (A):

$$\rho_I A_I U_I = \rho_{II} A_{II} U_{II} .$$

A description of the fluid state:

$$e = e(p,\rho)$$

accounts for material behavior of homogeneous composition, and together with

an assumed thermodynamic process, provides the closure conditions necessary to evaluate

$$\int_{I}^{II} \frac{dp}{\rho} \ .$$

The fundamental model concepts apply to virtually any piping component for any fluid of homogeneous composition. These concepts are the starting point for the development of working models that pertain to specific engineering applications. The working models are more restrictive, but provide the necessary detail to perform actual simulations of fluid environments. Gross and Silling (Reference 3) develop working models of piping components which apply primarily to steam/water vapor environments. The remainder of this report concerns the development and application of working models for subcooled fluids.

2.4 WORKING MODELS FOR SUBCOOLED FLUIDS

At a given pressure, a fluid is subcooled when its temperature is below that of vaporization. It is then in a highly compressed state, extremely resistant to further compression. Practically speaking, a subcooled fluid is a liquid.

Barely compressible under the subcooled conditions that can exist within the piping systems of power plants, liquids are capable of only small gradients in density. These gradients give rise to pressure waves which propagate through the fluid at (practically) the local acoustic speed. This situation suggests a set of principles, which form the basis for the subcooled piping component models. These principles are:

- When relationships between two adjacent control volume regions involve both densities, but not the density difference, the densities are set equal.
- Within control volumes, information propagates at acoustic speeds.

- When relationships between two adjacent control volume regions involve a density difference, this difference is evaluated as the pressure difference scaled by the reciprocal of the square of the acoustic speed.

- For adjacent regions of a control volume model, pressures may differ, but acoustic speeds are set equal.

The principles above do not imply complete incompressibility. They are, in fact, a carefully tailored hypothesis which preserves the essential nature of density gradients,* but minimizes the complications that are introduced to the working models. The hypothesis reduces the complexity of the control volume mathematics, as follows:

- The Rankine-Hugoniot jump conditions simplify to:

$$c\bar{\rho}(U_{II} - U_I) = p_I - p_{II}$$

  which is a form of mass conservation across an acoustic (weak**) wave, where c is the acoustic speed and $\bar{\rho}$ is the average of ρ_I and ρ_{II}.

- In the Euler equation of motion, the integral becomes:

$$(p_{II} - p_I)/\bar{\rho} \quad .$$

- The continuity equation takes the form:

$$A_I U_I = A_{II} U_{II} \quad .$$

Henceforth, this discussion turns to the development of subcooled working models for each piping component. These are: orifices, area changes, tee junctions, valves, and turbo-machines. Figure 3 depicts the models, along with their adjoining computational STEALTH grids. Each model spans no length on the scale of grid dimensions.

---

*Density gradients, through the equation of state, drive the physics in the STEALTH code.

**In the limit, acoustic waves support only infinitesimal changes in state properties. In these applications, the waves are almost acoustic; they propagate at nearly acoustic speed, support only small changes in density, but can produce significant changes in pressure.

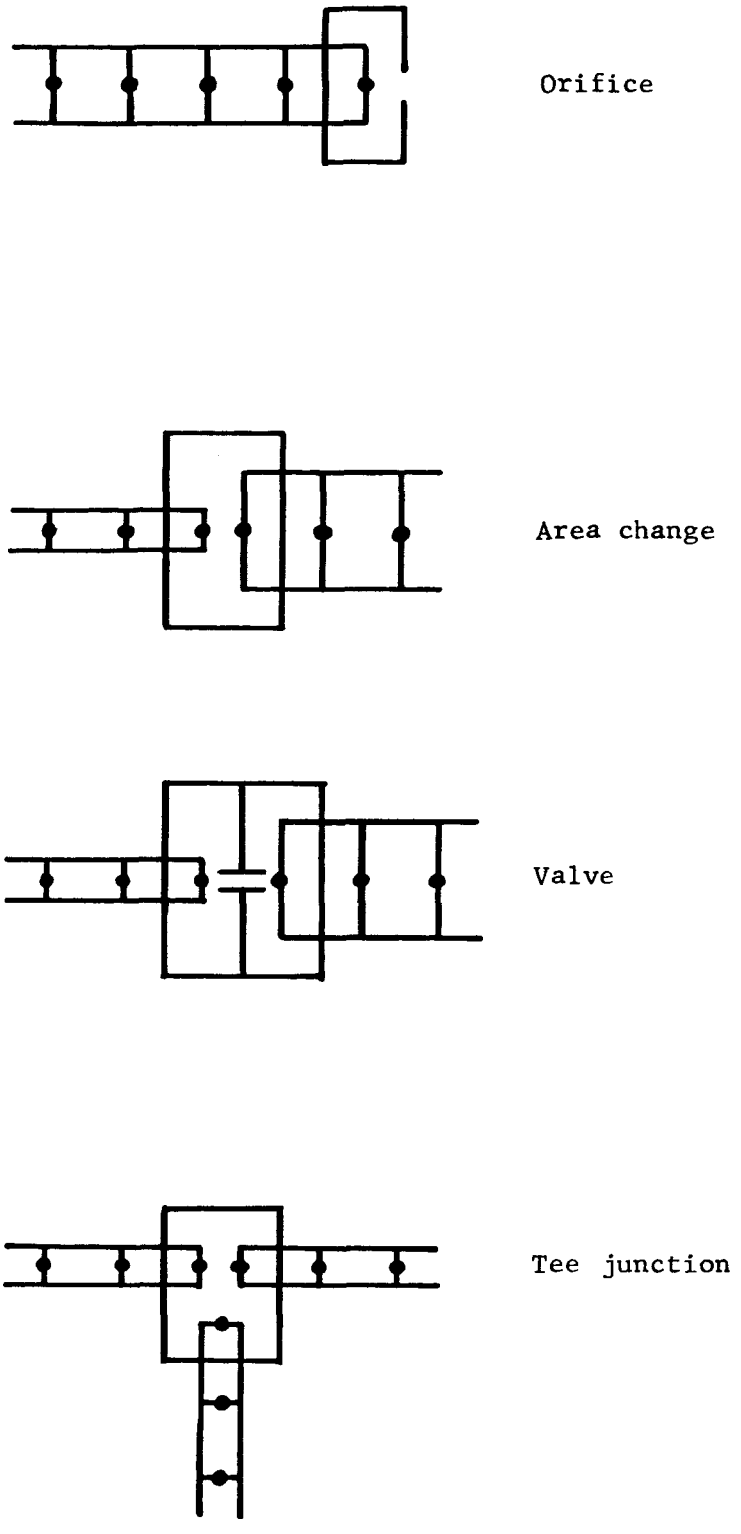

Figure 3. Piping component control volumes with adjoining computational grids.

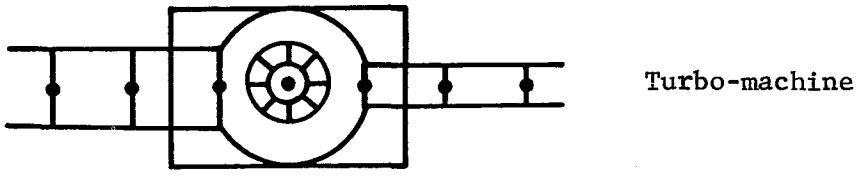

Figure 3 (concluded). Piping component control volumes with adjoining computational grids.

2.4.1 Subcooled Area Change. The area change model is particularly useful in revealing the underlying principles that are common to all control volume models. Thus, its analysis is more detailed than those that follow for the remaining models. However, the discussion for each model will be complete.

Figure 4a illustrates the state of affairs in the control volume at the beginning of a computational time step. Region 1 corresponds to the conditions present in zone N of grid 1; in a similar manner, region 4 is associated with the first zone of grid 2. Figure 4b depicts the working model on which the analysis is based. Velocities u_2 and u_4 are determined and assigned to node N of grid 1 and node 1 of grid 2, respectively. Information generated by the area change is propagated by discrete weak waves, and regions 3 and 4 are the steady states generated behind these waves.

The transformation from the input conditions to the determined conditions follows from:

- conservation of mass across the weak wave between regions 1 and 2,
- conservation of mass across the weak wave between regions 3 and 4,
- conservation of mass between regions 2 and 3,
- conservation of energy between regions 2 and 3 (Euler equation with $\Phi = 0$),
- known states for regions 1 and 4,

from which the velocities in regions 2 and 3 can be determined.

Conservation of mass across the weak wave between regions 1 and 2 is

$$c\rho_1 = (c - u_1 + u_2)\rho_2 ,$$

where

c = acoustic speed

ρ_i = density of region i

u_i = velocity or region i .

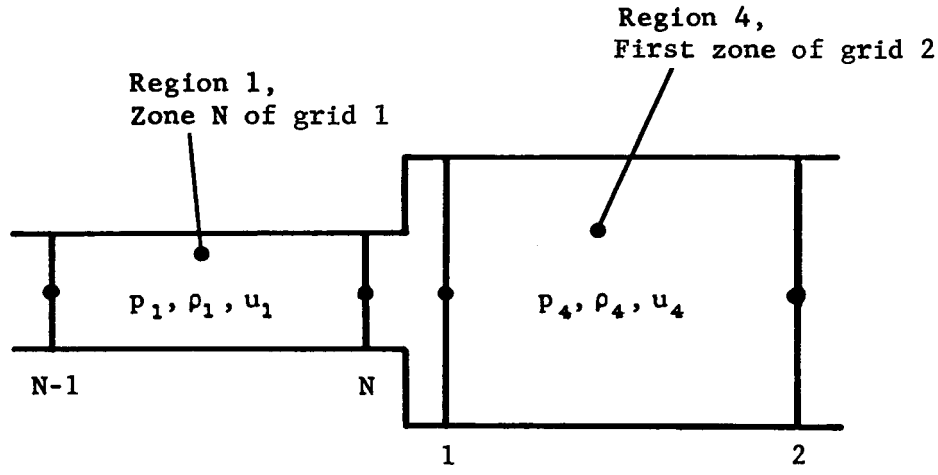

(a) Beginning of computational time step.

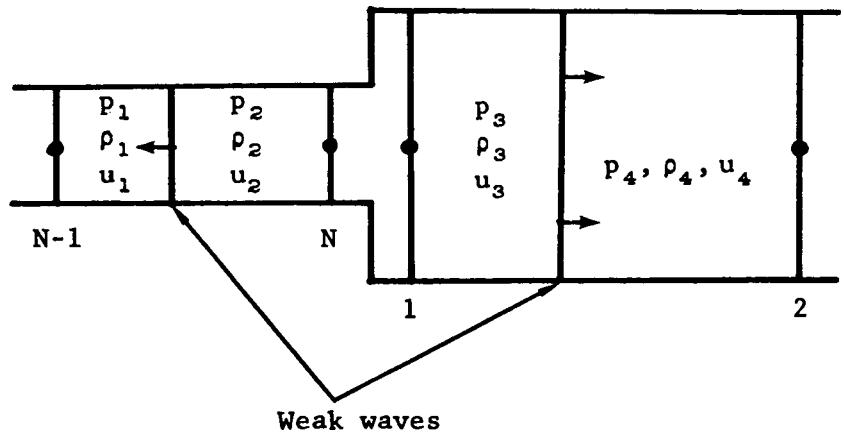

(b) Analysis for area change control volume.

Figure 4. Conditions present in the subcooled area change control volume model.

When combined with the nearly incompressible assumption,

$$\rho_1 - \rho_2 = (p_1 - p_2)/c^2 ,$$

where

$$p_i = \text{pressure of region } i ,$$

mass conservation across the weak wave yields

$$u_2 - u_1 = \frac{(p_1 - p_2)}{c\,\bar{\rho}} \equiv \xi$$

where $\bar{\rho}$ is the average density across the wave.

Similarly, conservation of mass across the weak wave between regions 3 and 4 yields

$$u_3 - u_4 = \frac{(p_3 - p_4)}{c\,\bar{\rho}} \equiv \eta .$$

Conservation of mass between regions 2 and 3 is, simply,

$$u_3 = (A_2 / A_3)u_4$$

where

$$A_i = \text{cross-sectional area of region } i.$$

Conservation of energy between regions 2 and 3 is

$$\frac{p_2 - p_3}{\bar{\rho}} = \frac{1}{2}(u_3^2 - u_2^2)$$

which may be rearranged to

$$\frac{p_2 - p_3}{c\bar{\rho}} = \frac{u_2^2}{2c}\left[(A_2 / A_3)^2 - 1\right] \equiv \psi .$$

The known conditions at regions 1 and 4 yield

$$\frac{p_1 - p_4}{\bar{\rho}\, c} \equiv \varphi .$$

But since

$$p_1 - p_4 = (p_1 - p_2) + (p_2 - p_3) + (p_3 - p_4) ,$$

therefore,

$$\varphi = \xi + \eta + \psi .$$

There are five equations, and the five unknowns: ξ, η, φ, u_2, u_3. The solution becomes

$$u_2 = \frac{-\beta - \sqrt{\beta^2 - 4\alpha\gamma}}{2\alpha}$$

where

$$\alpha \equiv \left[(A_2 / A_3)^2 - 1\right] /2$$

$$\beta \equiv -c\left[1 - (A_2 / A_3)\right]$$

$$\gamma \equiv -\left[c(u_1 + u_4) + \frac{p_1 - p_4}{\bar{\rho}}\right].$$

Finally,

$$u_3 = (A_2 / A_3)u_2 \ .$$

Thus, the control volume analysis determines the velocities in regions 2 and 3; these values are then assigned to node N of grid 1 and node 1 of grid 2, respectively.

2.4.2 Subcooled Orifice. The orifice control volume is essentially a one-sided area change control volume. Figure 5 illustrates this interpretation, depicting the input conditions, Figure 5a, and the working model, Figure 5b. In this case, only u_2 is assigned to the computational grid, at node N. However, the basic assumptions made for the area change apply here, in a similar fashion.

The transformation from the input conditions to determined conditions for this model is based on:

- conservation of mass across the weak wave between regions 1 and 2,
- for outflow, conservation of energy between region 2 and the orifice (Euler equation with $\Phi = 0$),
- for inflow, conservation of energy between the orifice and the outer environment (Euler equation with $\Phi = 0$),
- known states for region 1 and the outer environment,

from which the velocity in region 2 can be determined.

In a manner similar to that for the area change, the transformation principles now lead to the following relationships:

$$u_2 - u_1 = \frac{p_1 - p_2}{\bar{\rho}\, c} \equiv \xi \ .$$

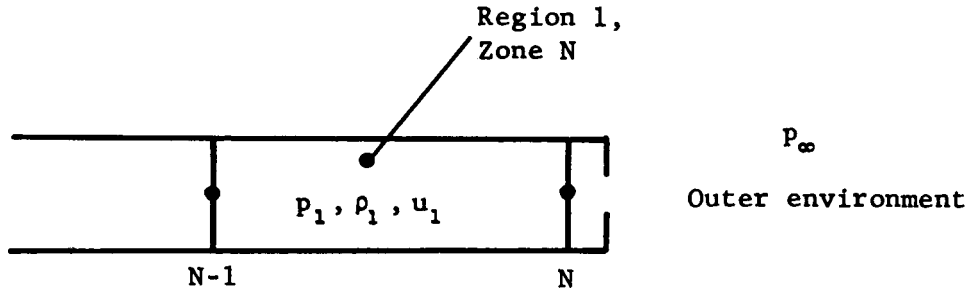

(a) Beginning of computational time step.

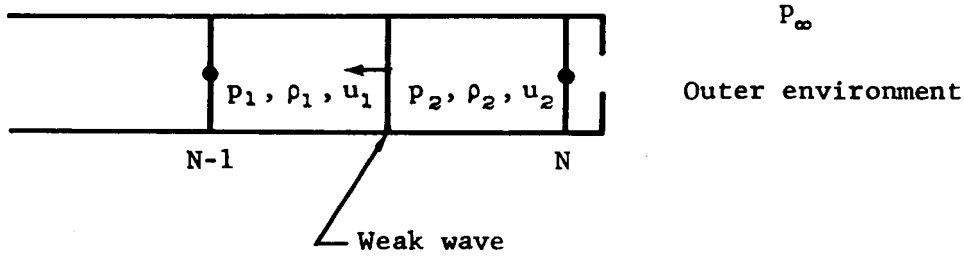

(b) Analysis for orifice control volume.

Figure 5. Conditions present in the subcooled orifice control volume model.

For outflow ($p_{orf} = p_{environment} \equiv p_\infty$):

$$\frac{p_2 - p_\infty}{\bar{\rho}\, c} = \frac{u_2^2}{2c} \left[\left(\frac{A_2}{A_{orf}} \right)^2 - 1 \right] \equiv \psi$$

or, for inflow ($p_{orf} = p_2$, $u_{environment} = 0$):

$$\frac{p_2 - p_\infty}{\bar{\rho}\, c} = - \frac{u_2^2}{2c} \left(\frac{A_2}{A_{orf}} \right)^2 \equiv \psi'$$

and

$$\frac{p_1 - p_\infty}{\bar{\rho}\, c} \equiv \varphi = \xi + \psi \text{ , known .}$$

The three equations determine the three unknowns, ξ, ψ or ψ', and u_2, whence the value of u_2,

$$u_2 = \frac{-c + \sqrt{c^2 + 4\alpha \left(cu_1 + \frac{p_1 - p_\infty}{\rho} \right)}}{2\alpha}$$

is assigned to node N.

The backflowing orifice has no pressure recovery through the area expansion from the orifice station. In effect, this model simulates irreversible flow, with losses. In fact, these losses are comparable with the theoretical loss model for sudden area expansions (see, for example, References 4 and 5).

2.4.3 Subcooled Tee Junction. Conceptually, the tee junction control volume is a generalized area change model with three regions, instead of two. Figure 6 illustrates the model used for control volume analysis. Here, three velocities to be determined are u_2, u_4, and u_6; their values will be assigned to nodes N, 1, and M, respectively.

The applicable transformation principles are:

- Conservation of mass across weak waves

  Region 1 to Region 2
  Region 3 to Region 4
  Region 5 to Region 6 .

- Conservation of energy (Euler Equation with $\Phi = 0$)

  Region 2 to Region 4
  Region 2 to Region 6
  $\sim$ or $\sim$
  Region 2 to Region 4
  Region 4 to Region 6
  $\sim$ or $\sim$
  Region 2 to Region 6
  Region 4 to Region 6 .

- Global mass conservation for the control volume .

Using the definition

$$\delta_i \equiv \frac{p_i}{\bar{\rho} c}$$

the transformation principles become, for example:

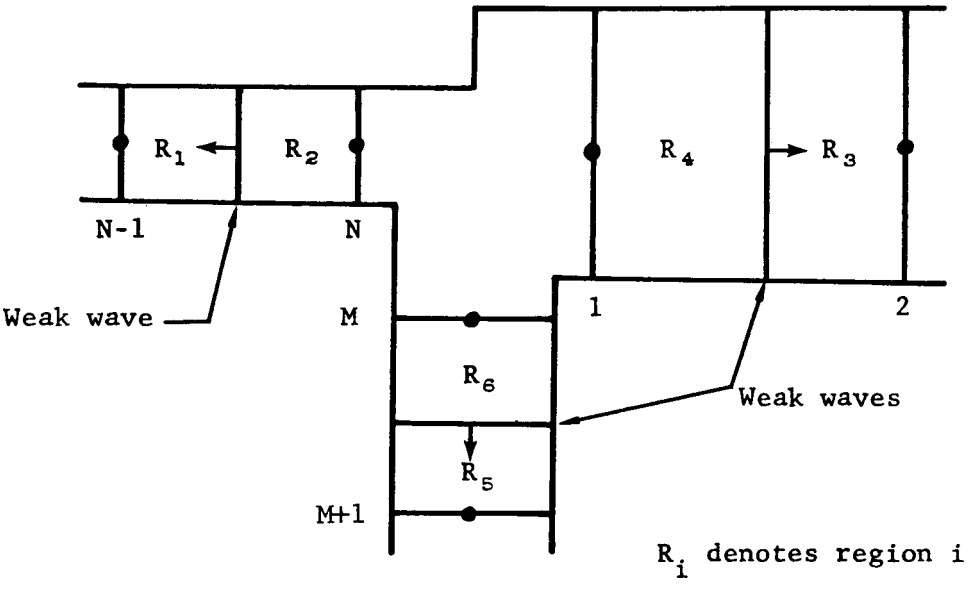

Figure 6. Subcooled tee junction control volume model.

$$\delta_2 - \delta_1 = u_2 - u_1$$

$$\delta_4 - \delta_3 = u_4 - u_3$$

$$\delta_6 - \delta_5 = u_6 - u_5$$

$$\delta_4 - \delta_2 = (u_2^2 - u_4^2)/2$$

$$\delta_6 - \delta_4 = (u_4^2 - u_6^2)/2$$

$$0 = A_2 u_2 + A_4 u_4 + A_6 u_6 .$$

This set of equations contains the known quantities,

$$\delta_i, u_i; \quad i = 1, 3, 5 \quad \text{and} \quad A_i; \quad i = 2, 4, 6$$

and determines the unknown quantities,

$$\delta_j, u_j; \quad j = 2, 4, 6 .$$

The equations are coupled and nonlinear. They are solved in this model by the multi-dimensional Newton-Raphson method.

2.4.4 Subcooled Valve. The control volume model for a valve is similar to an area change, with an orifice-like variable area separating regions 2 and 3. Figure 7 illustrates the model control volume for the valve.

The transformation principles are similar to those for an area change with the following modifications:

- Conservation of energy between regions 2 and 3 is deleted.
- For left-to-right flow, conservation of energy between region 2 and the valve (v) is used (Euler equation with $\Phi = 0$).

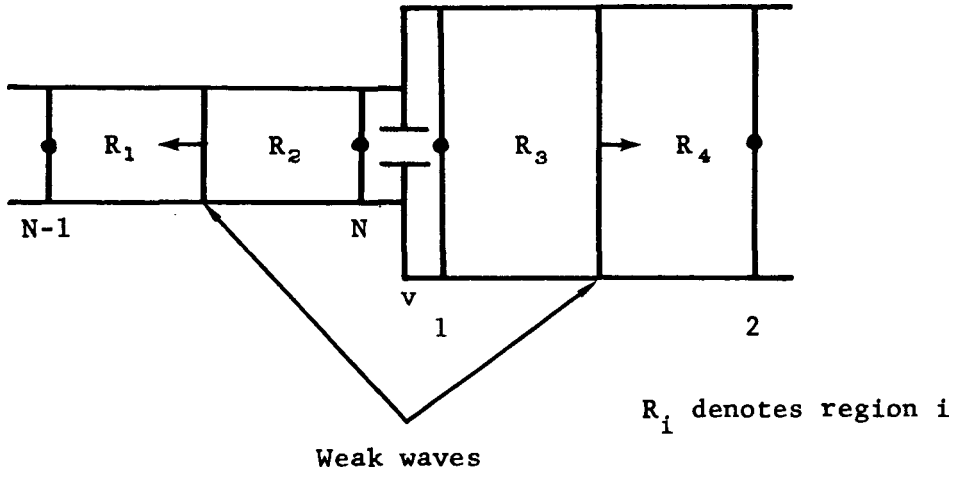

Figure 7. Conditions present in the subcooled valve control volume model.

- For right-to-left flow, conservation of energy between region 3 and the valve (v) is used (Euler equation with $\Phi = 0$).
- A description of the variation of valve area (A_v) is included.

Hence, for left-to-right flow,

$$\psi = \frac{u_2^2}{2}\left[(A_2 / A_v)^2 - 1\right]$$

while for right-to-left flow,

$$\psi = \frac{u_2^2}{2}\left[(A_2 / A_3)^2 - (A_2 / A_v)^2\right].$$

In either case, the description for A_v:

$$A_v = A_v\,(\text{time})$$

or

$$A_v = A_v\,(\text{flowfield, valve dynamics})$$

provides the necessary auxiliary condition to complete the mathematical formulation.

These modifications produce an important difference between the area change and the valve; that is, there is no pressure recovery between the valve orifice and the downstream flow area. This, in turn, causes the valve to be an irreversible device, except when the orifice is fully opened to the smaller flow area and the flow is from the larger area to the smaller. Hence, the valve is a flow device with implicit losses. As with the back-flowing orifice, this is also comparable with theoretical losses.

2.4.5 Subcooled Turbo-machines. Turbo-machines are rotary devices which add or extract energy from a flowing fluid. The dynamic element of such a device is a set of shaft-mounted, rotating blades (rotors) which

remain continuously within the fluid. [There may also be a set of stationary blades (stators), which complement the effect of the rotors.] The local interactions between the blades and fluid can produce a very complex, multi-dimensional flow field. However, on a global scale, the blades are merely a source (or sink) of energy to the flow. In fact, for a steady flow, a turbo-machine produces a time-invariant effect.

The control volume model for these devices is very similar to that for area changes. As is depicted in Figure 8, the turbo-machine control volume is an area change control volume with provision for an energy effect. The discussion of Figure 4 (area change), on Page 17, is equally applicable here. Hence, the transformation principles for the turbo-machine model are nearly identical with those of the area change. In this case, however, the principles include:

- The effect of the turbo-machine on the conservation of energy between regions 2 and 3 (Euler equation with $\Phi \neq 0$).
- A description of the turbo-machine rotor dynamics, insofar as it defines Φ.

The conservation of energy between regions 2 and 3 is

$$\frac{p_3 - p_2}{\rho} + \frac{1}{2}\left(u_3^2 - u_2^2\right) = \Phi \ ,$$

which may be rearranged to

$$\frac{p_2 - p_3}{c\bar{\rho}} = \frac{u_2^2}{2c}\left[\left(A_2/A_3\right)^2 - 1\right] - \frac{\Phi}{c} \equiv \psi \ .$$

This is a generalization of the definition of ψ, as it appears on Page 20.

This completes the general development of the control volume for turbo-machines. To this point, the model is comprehensive, applying to any type of turbo-machine. (In fact, at this stage, the model applies to many forms

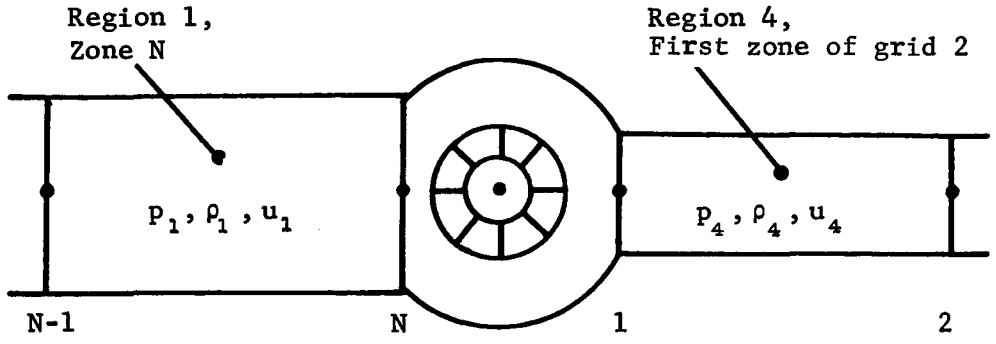

(a) Beginning of computational time step.

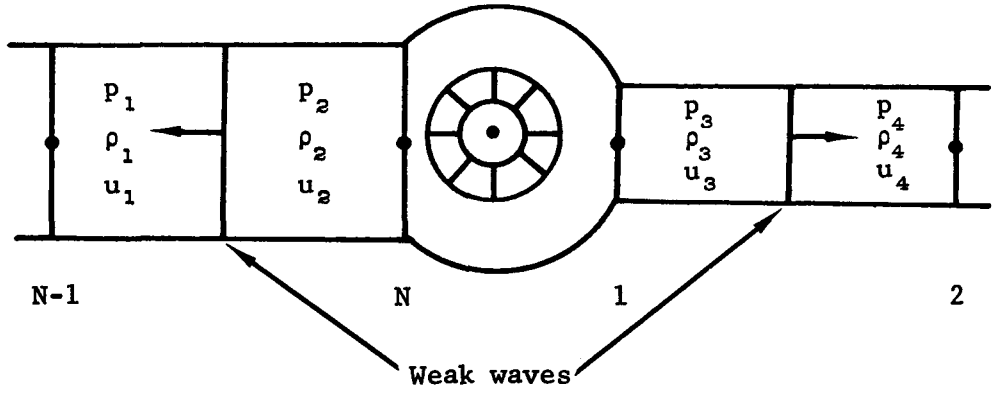

(b) Analysis for turbo-machine control volume.

Figure 8. Conditions present in the subcooled turbo-machine control volume model.

of energy devices, in addition to turbo-machines.) All that remains to be done is the description of the rotor dynamics. This depends, however, on the particular type(s) of turbo-machine(s) under study.

This study is concerned with the simulation of turbopumps. In particular, the operating modes considered are:

- pump failure (or trip)
- pump start-up .

The rotor dynamics of a turbopump couples the energy effect (Φ) and volumetric flow rate (Q) with the rotor torque (TQ) and rotational speed (N). For each pump, there is a set of performance curves which provide two independent relationships among the four parameters. In their standard form (see, e.g., Reference 6), however, these curves are cumbersome to use with the control volume model. Fortunately, Marchal et al. (Reference 7) were able to convert the performance curves to a pair of well-behaved, single-valued relationships (called the four-quadrant curves, for reasons described below). As described by Wylie and Streeter (Reference 8), the basis for the conversions are the pump parameters, non-dimensionalized to the pump rated conditions (subscripted r):

$$\Phi' \equiv \left[\Phi - \frac{1}{2}\,(u_3^2 - u_2^2)\right] \Big/ \left[\Phi - \frac{1}{2}\,(u_3^2 - u_2^2)\right]_r$$

$$Q' \equiv Q/Q_r$$

$$TQ' \equiv TQ/TQ_r$$

$$N' \equiv N/N_r \ .$$

These, in turn, define the converted variables of the four-quadrant curves:

$$\bar{\Phi} \equiv \Phi' / (N'^2 + Q'^2)$$

$$\overline{TQ} \equiv TQ'/(N'^2 + Q'^2)$$

$$\bar{\theta} \equiv \pi + \tan^{-1}(Q'/N') \cdot$$

Figure 9 illustrates the four-quadrant interpretation of pump operation; Figure 9a describes the four-quadrant connection with pump modes, while Figure 9b presents an example of the four-quadrant curves.

The conservation of angular momentum of the rotating mass provides another independent relationship among the pump parameters. The differential (with time, i.e., d/dt) form is

$$TQM - TQ = WR^2 \frac{dN}{dt}$$

where W is the mass and R is the radius of gyration. TQM is the pump motor torque that drives the pump. The motor torque is effectively zero during pump failures; it will be discussed below for pump start-ups.

For the simulation of a pump trip, the control volume model uses the four-quadrant curves and the angular momentum equation in conjunction with the other transformation principles. All together, these provide a complete mathematical description. Unlike the equations for the area change, however, this set of equations cannot decouple into a system which determines the unknowns one by one. These equations reduce to two coupled equations:

- An equivalent Euler equation

$$0 = p_1 - p_4 + c(\rho_4 u_4 - \rho_1 u_1)$$
$$+ c\bar{\rho} Q_r Q' [1 + (A_2/A_3)]/A_2$$
$$+ \bar{\rho} \Phi' [\Phi - \tfrac{1}{2}(u_3^2 - u_2^2)]_r$$

where $\Phi' = \bar{\Phi}(N'^2 + Q'^2)$

with the four-quadrant curve: $\bar{\Phi} = \bar{\Phi}(N', Q')$

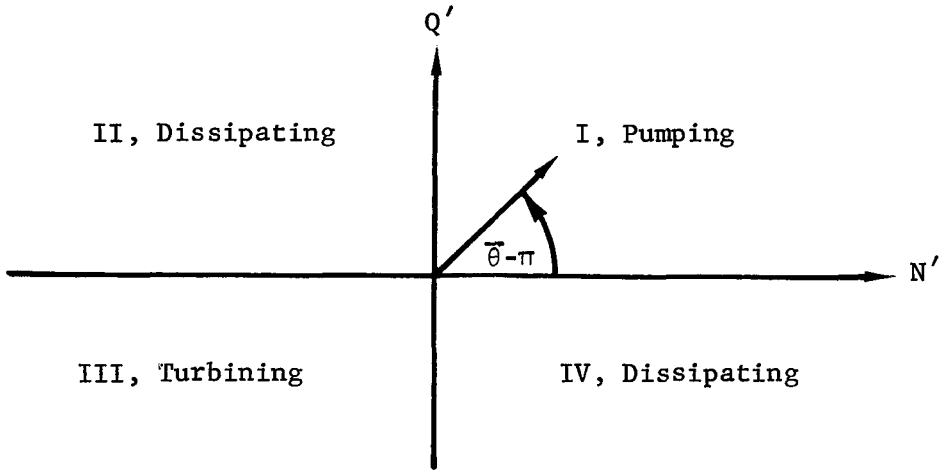

(a) Connection between quadrants and pump models.

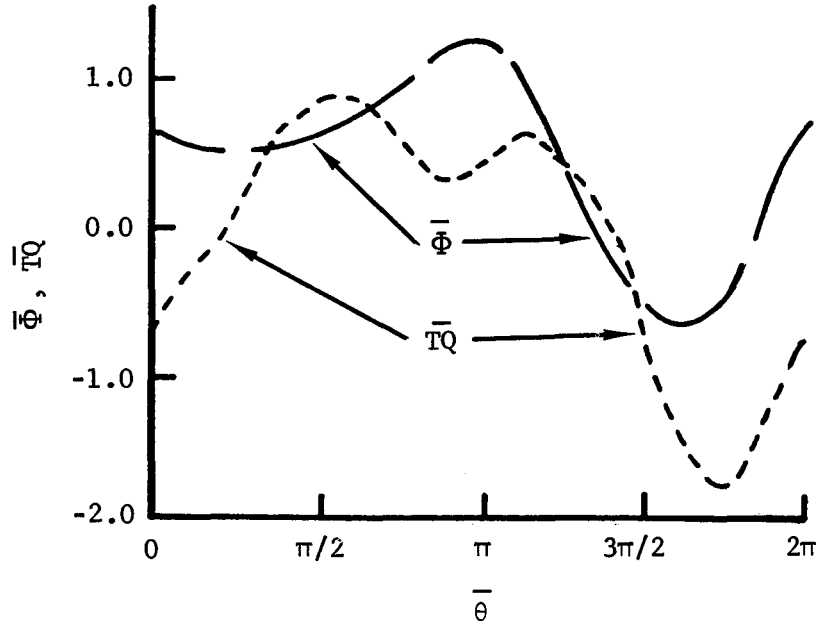

(b) Four-quadrant curves.

Figure 9. Four-quadrant representation of pump operation.

- An equivalent incremental angular momentum equation

$$0 = TQ' + TQ'_o + \frac{2WR^2 (N' - N'_o)}{TQ_r (t - t_o)}$$

where the subscript o denotes conditions at the beginning (t_o) of the time increment, and

$$TQ' = \bar{TQ}(N'^2 + Q'^2)$$

with the four-quadrant curve:

$$\bar{TQ} = \bar{TQ}(N', Q')$$

which determine Q' and N', and a set of decoupled equations which subsequently determines the remaining unknowns. As with the tee junction equations, the multi-dimensional Newton-Raphson technique provides the solution procedure for the coupled equations.

Since pump start-ups are powered by a pump motor, the control volume simulation must account for the motor torque (TQM in the angular momentum equation). One approach would be to supply a torque-speed curve [TQM = TQM(N)] directly, and solve the coupled and decoupled equations as described above for pump trips. The disadvantage to this approach is that torque-speed curves for pump motors are not convenient to obtain. Moreover, it has been found that (e.g., Reference 8), to the degree of accuracy required, the angular momentum equation can be replaced by a simple time history prescription for N'. For a specified rise time (t_s):

$$N' = t/t_s \quad , \quad \text{when } t < t_s$$

$$N' = 1.0 \quad , \quad \text{when } t \geq t_s \, .$$

The control volume model for pump start-ups uses this simplified approach. The immediate consequence is that, with N' specified, the coupled system

reduces to the equivalent Euler equation, implicit in the unknown Q'. In this case, the one-dimensional Newton-Raphson method determines the solution.

2.5 WORKING MODEL SIMULATIONS

Through a series of test simulations, the response of each control volume model provided quantitative information by which model validity could be evaluated. This section describes some of these cases and presents typical results.

In all these simulations, subcooled water properties defined the behavior of the fluid medium. This guaranteed that the flow conditions would remain liquid over a significant range of pressures. Consistent with its subcooled state, the water was modeled as a linear elastic medium with the following pressure-density relationship,

$$p = A + k(\rho/\rho_o - 1) .$$

The constant, A, was 1.51×10^7 N/m^2, which assigns a pressure of 151 bars to the water at a reference density (ρ_o) of 993.16 kg/m^3. The bulk modulus (k) of subcooled water is 1.79×10^9 N/m^2. Under these conditions, the acoustic speed (c_o) of the water at its reference state is:

$$c \equiv \sqrt{k/\rho_o} = 1342.51 \text{ m/s} .$$

Table 1 presents a summary of the test simulations and the associated control volume area ratios. Each control volume formed one portion of a complete physical model which included initial, boundary, and (when applicable) forcing conditions. All models were one-dimensional and set in planar geometry.

The orifice control volumes formed one end of pipes that were 2.9 m long and closed at the opposite ends. These pipes were simulated by calculational grids of 90 nodes. Initially, the pipes were pressurized to 151

TABLE 1. TEST SIMULATIONS

Control Volume Model	Area Ratio
Orifice	20:1
Orifice	3:1
Area Change (explosive valve)	20:1
Area Change (explosive valve)	1/20:1
Opening Valve	1:1
Closing Valve	1:1

bars; subsequently, they exhausted through the orifices to a constant back-pressure of 51 bars. Figures 10 through 13 illustrate typical results for the 20:1 area ratio, while Figures 14 through 17 show similar data for the 3:1 area ratio. For each case, the pressure snapshots show, respectively, the initial left-traveling rarefactions, the reflected right-traveling rarefactions,* and late-time left-traveling compressions. These compressions result from backflow conditions set up by overexpansions in the pipes. The velocity directions at the orifices become negative at late times, thereby signaling the backflow conditions.

The "explosive valve" area change control volumes formed the junctions between two pipes of different flow areas, each 2.9 m long, and closed at their outer ends. Each pipe was simulated by grids of 60 nodes. Initially, the pipes were pressurized to 151 bars and 51 bars, respectively. At time zero, the valves suddenly ("explosively") opened to the full diameter of the smaller pipe. Figures 18 through 22 display predictions for the case where the initial high pressure pipe is the larger of the two; Figures 23 through 27 display similar results for the case where the initial high pressure pipe is the smaller of the two. The pressure snapshots for each case depict early times corresponding to initial left-traveling rarefactions and right-traveling compressions: first, intermediate times after these initial waves reflect off opposite end walls, second, intermediate times after the reflected waves intersect, and late times after the intersected waves again reflect off the opposite end walls. The velocity histories indicate that, again, the flow fields reverse direction at the area change at late times.

Two closed-end pipes with equal cross-sectional areas, each initially pressurized to different pressures, provided the physical model for an opening valve control volume. Each pipe was 2.9 m long and simulated by a grid of 60 nodes. At zero time, one chamber was pressurized at 151 bars, the

*Note that the 3:1 case shows a negative pressure (tension). This is reasonable for the simple linear elastic material model. Since these were only test simulations, no tension limit was provided. Hence, under total expansion to the vacuum state, the tension could approach a value nearly equal in magnitude to the bulk modulus.

Orifice Area 20:1 Pressure 151 to 51 bars Liquid

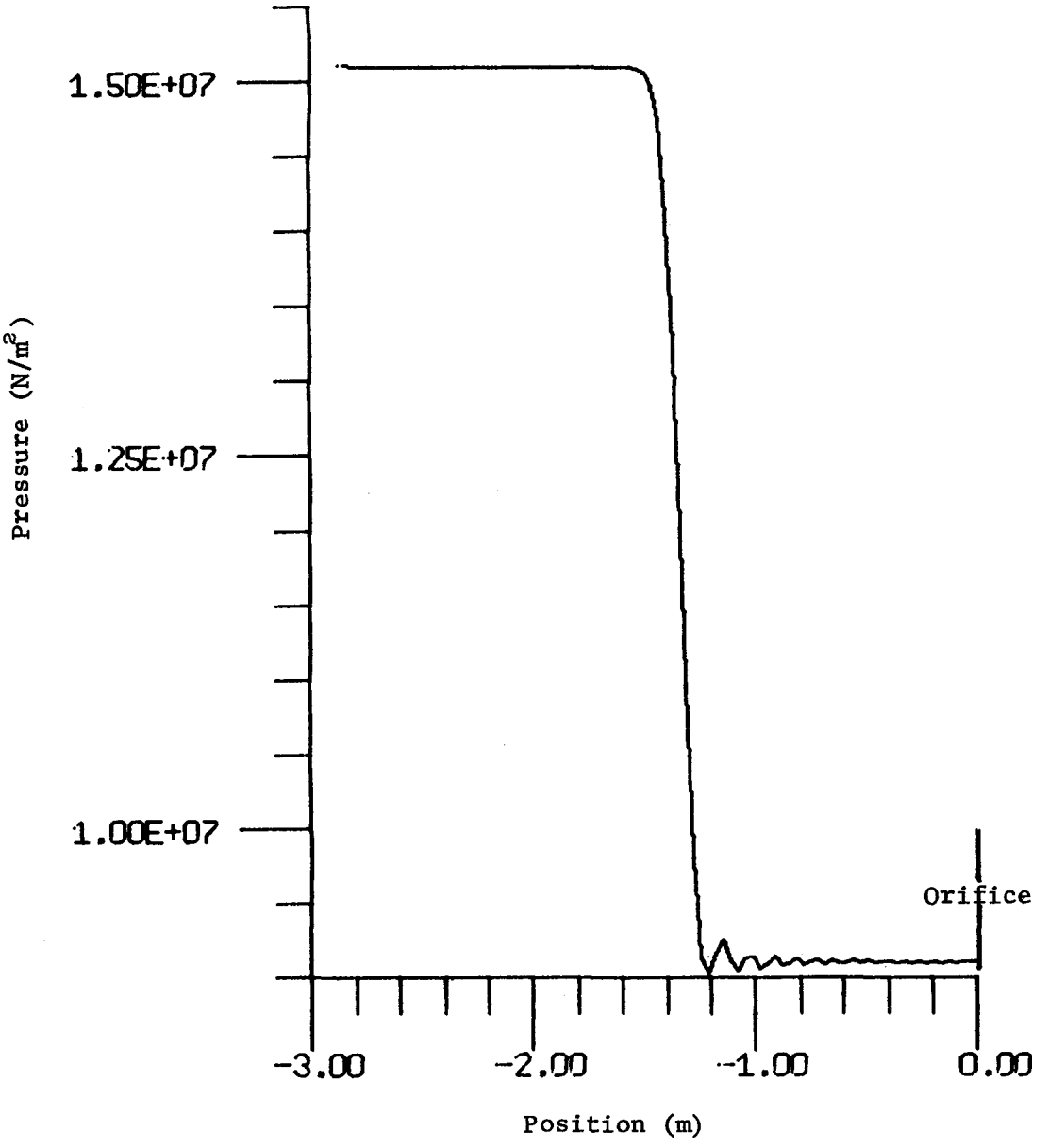

Figure 10. 20:1 Orifice pressure profile at ~ 1 ms.

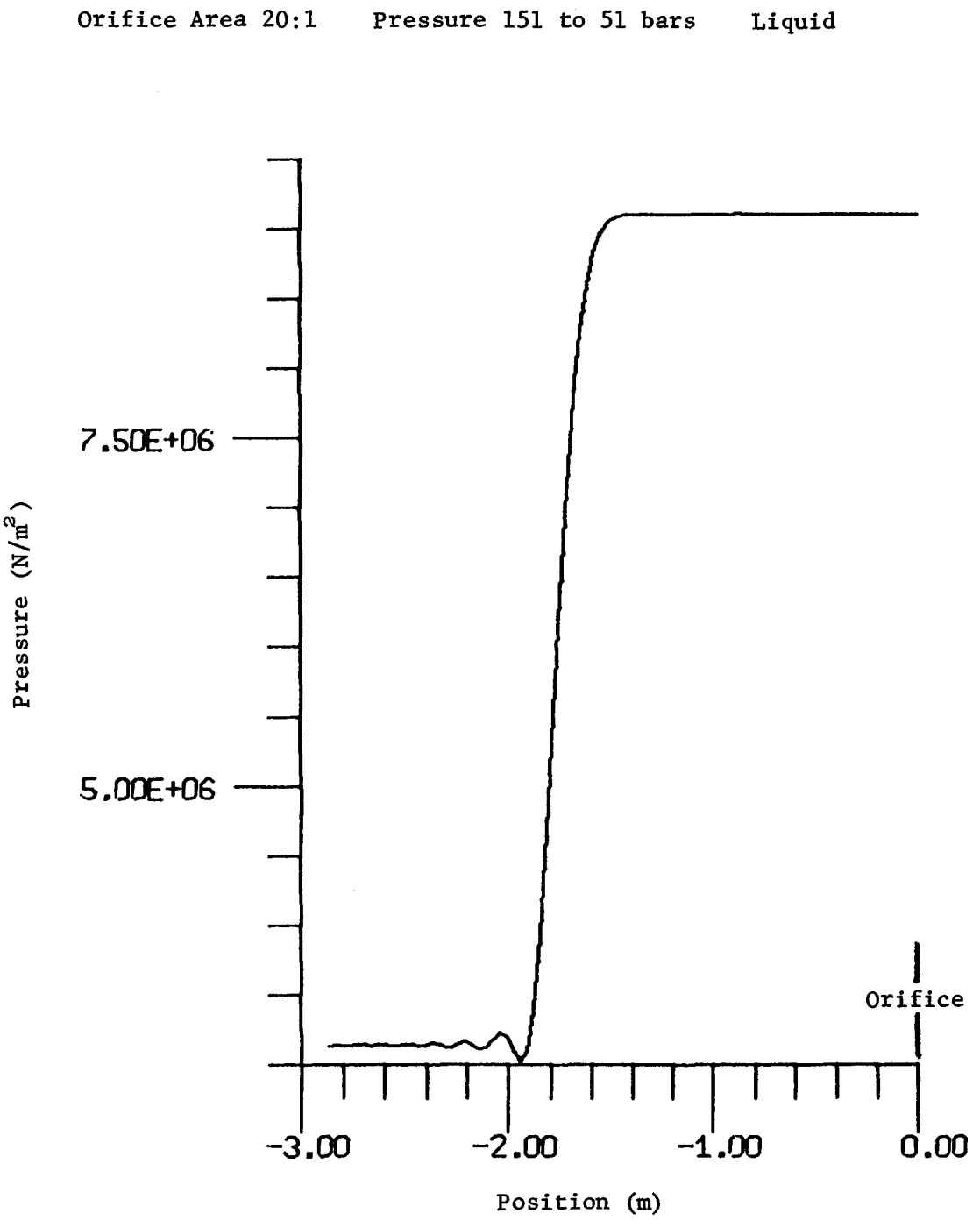

Figure 11. 20:1 Orifice pressure profile at ~ 3 ms.

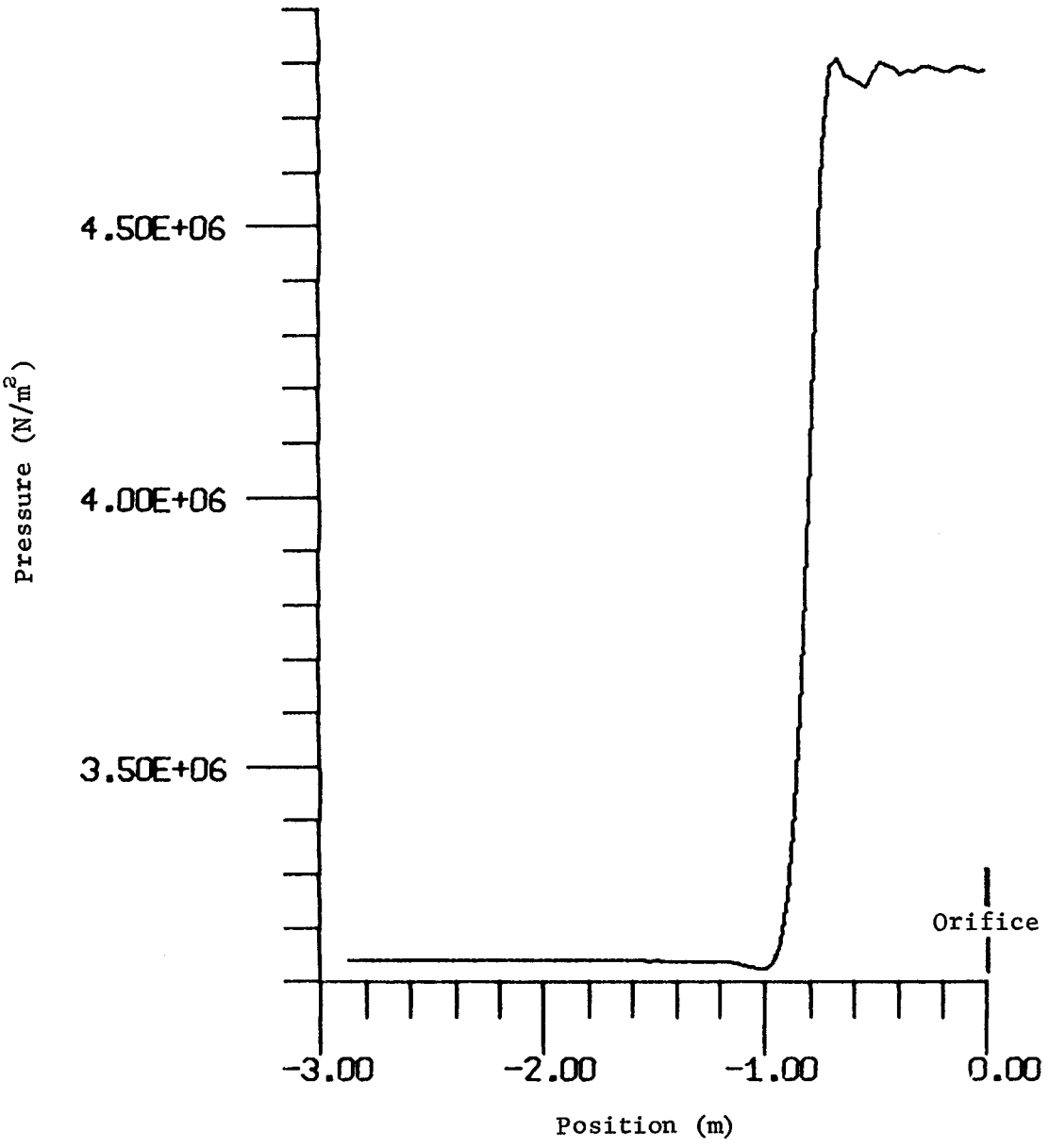

Figure 12. 20:1 Orifice pressure profile at ~ 5 ms.

Orifice Area 20:1 Pressure 151 to 51 bars Liquid

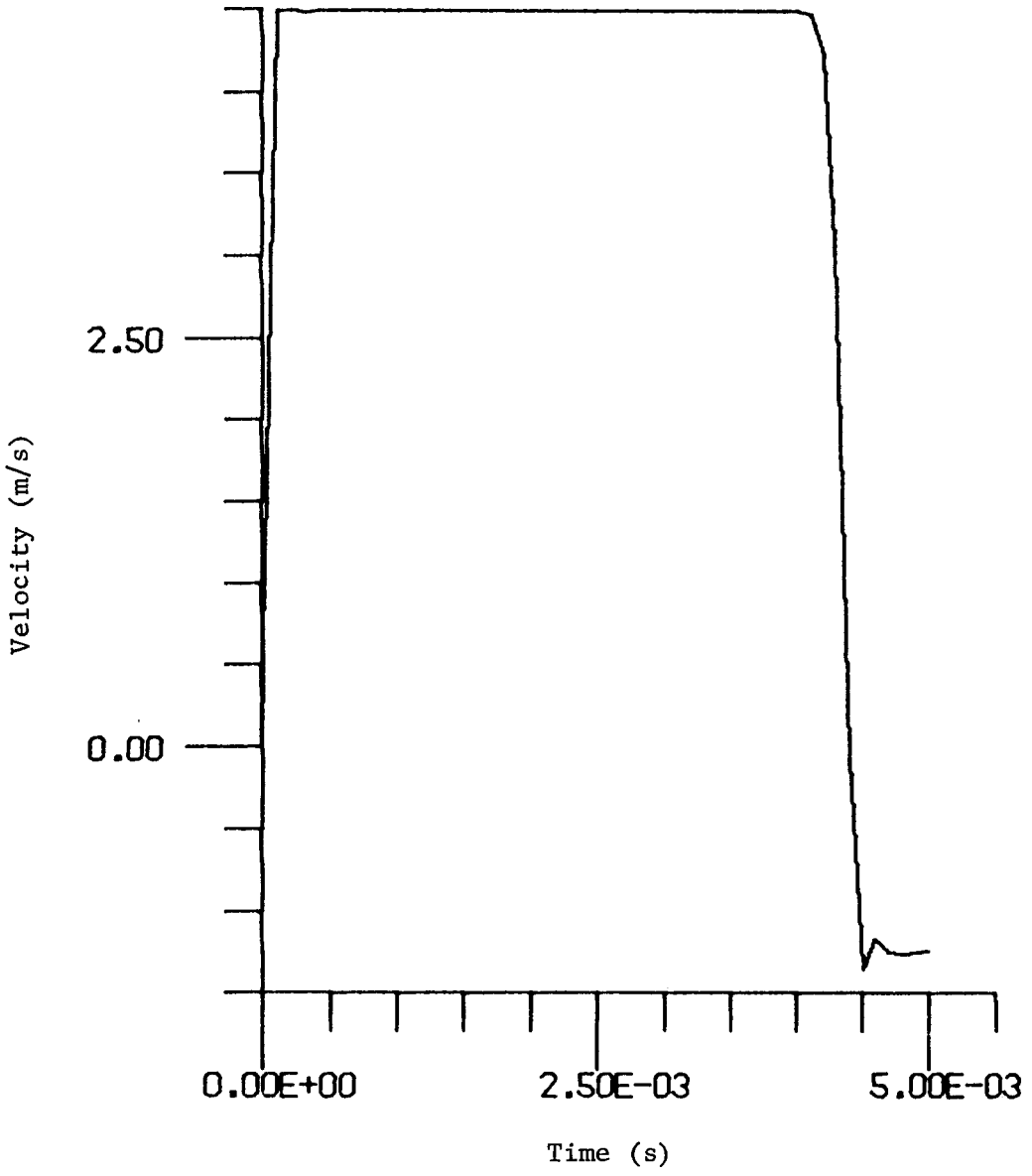

Figure 13. Velocity history at 20:1 orifice.

Orifice Area 3:1 Pressure 151 to 51 bars Liquid

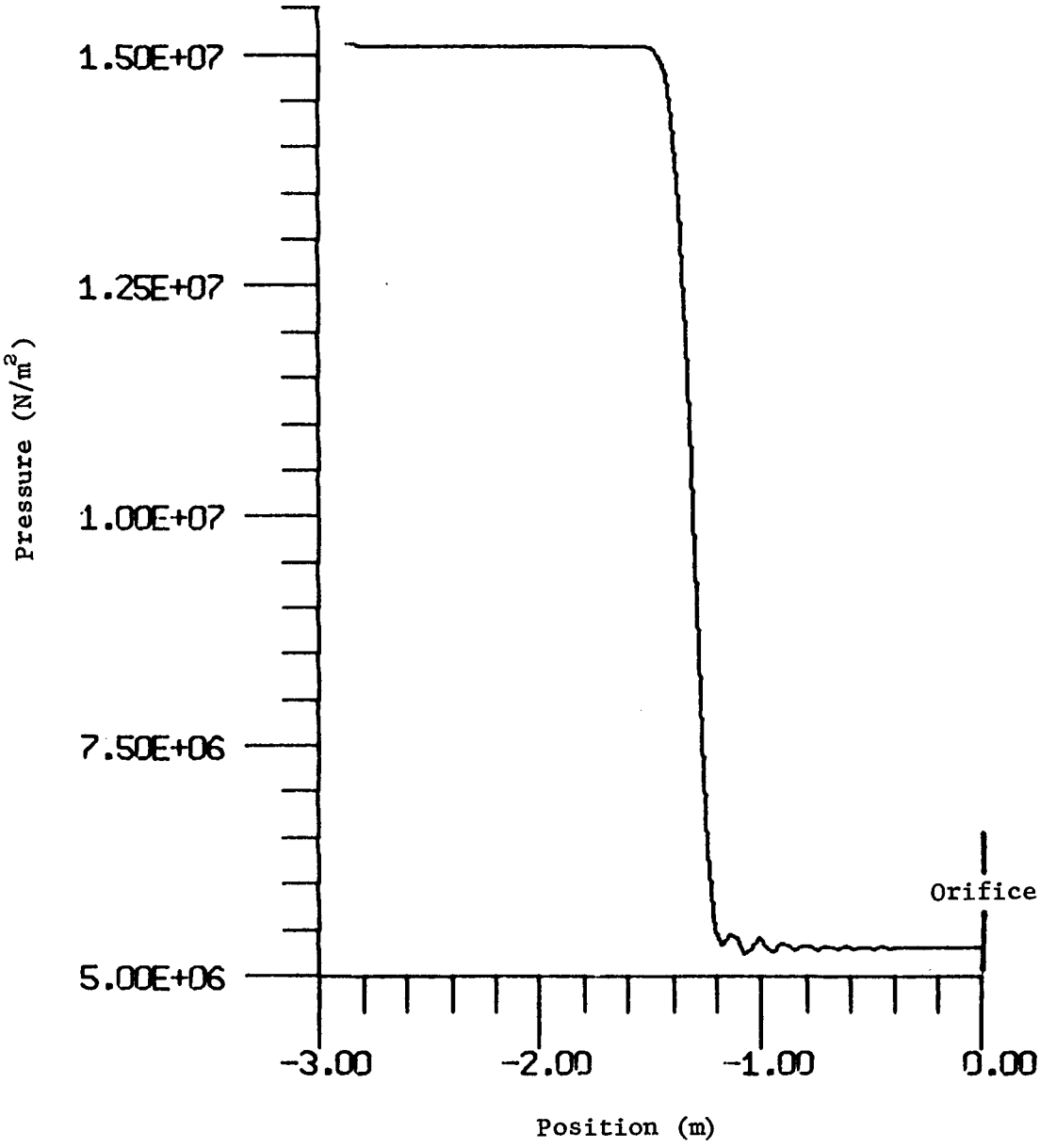

Figure 14. 3:1 Orifice pressure profile at ~ 1 ms.

Orifice Area 3:1 Pressure 151 to 51 bars Liquid

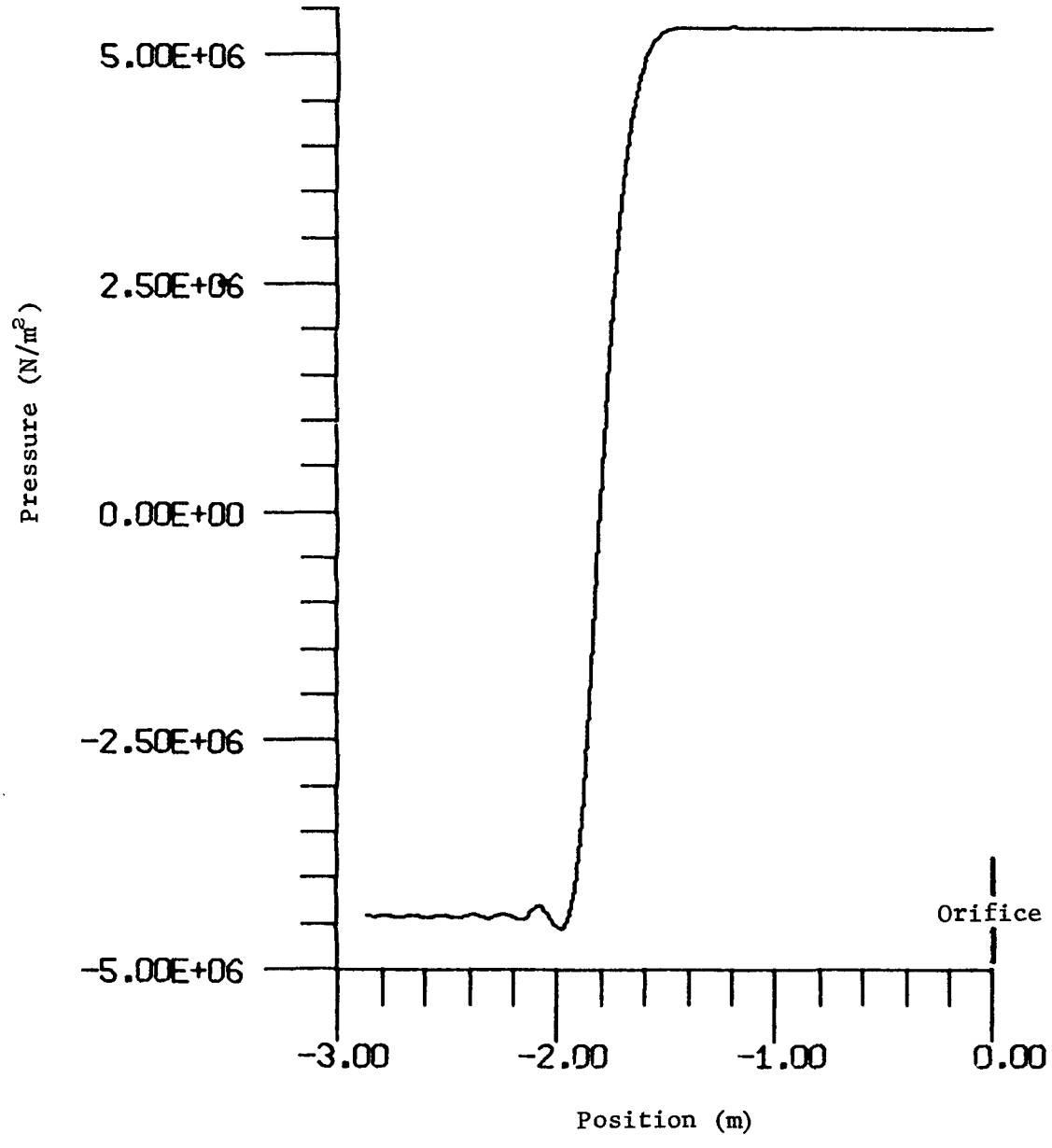

Figure 15. 3:1 Orifice pressure profile at ~ 3 ms.

Orifice Area 3:1 Pressure 151 to 51 bars Liquid

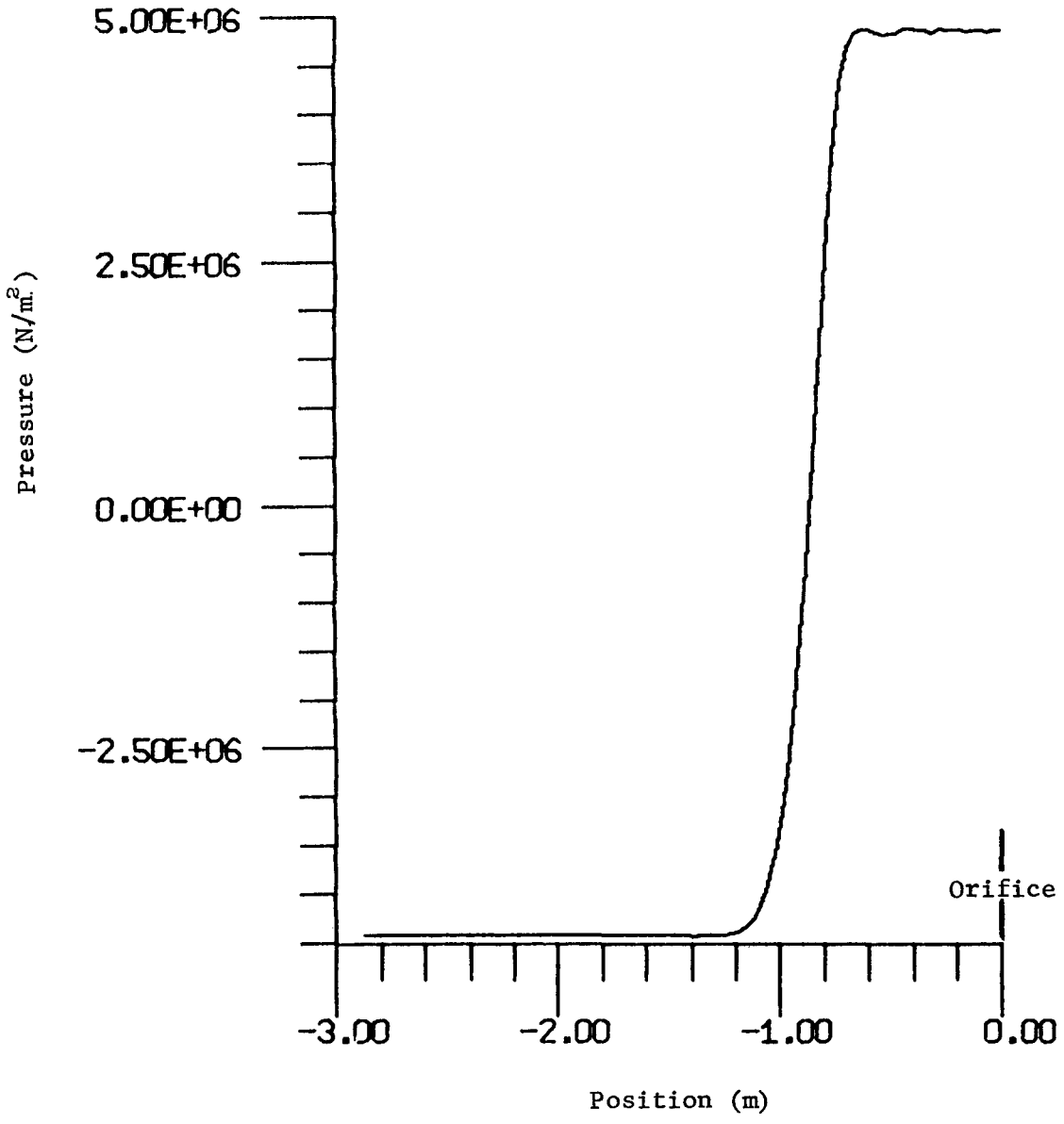

Figure 16. 3:1 Orifice pressure profile at ~ 5 ms.

Orifice Area 3:1 Pressure 151 to 51 bars Liquid

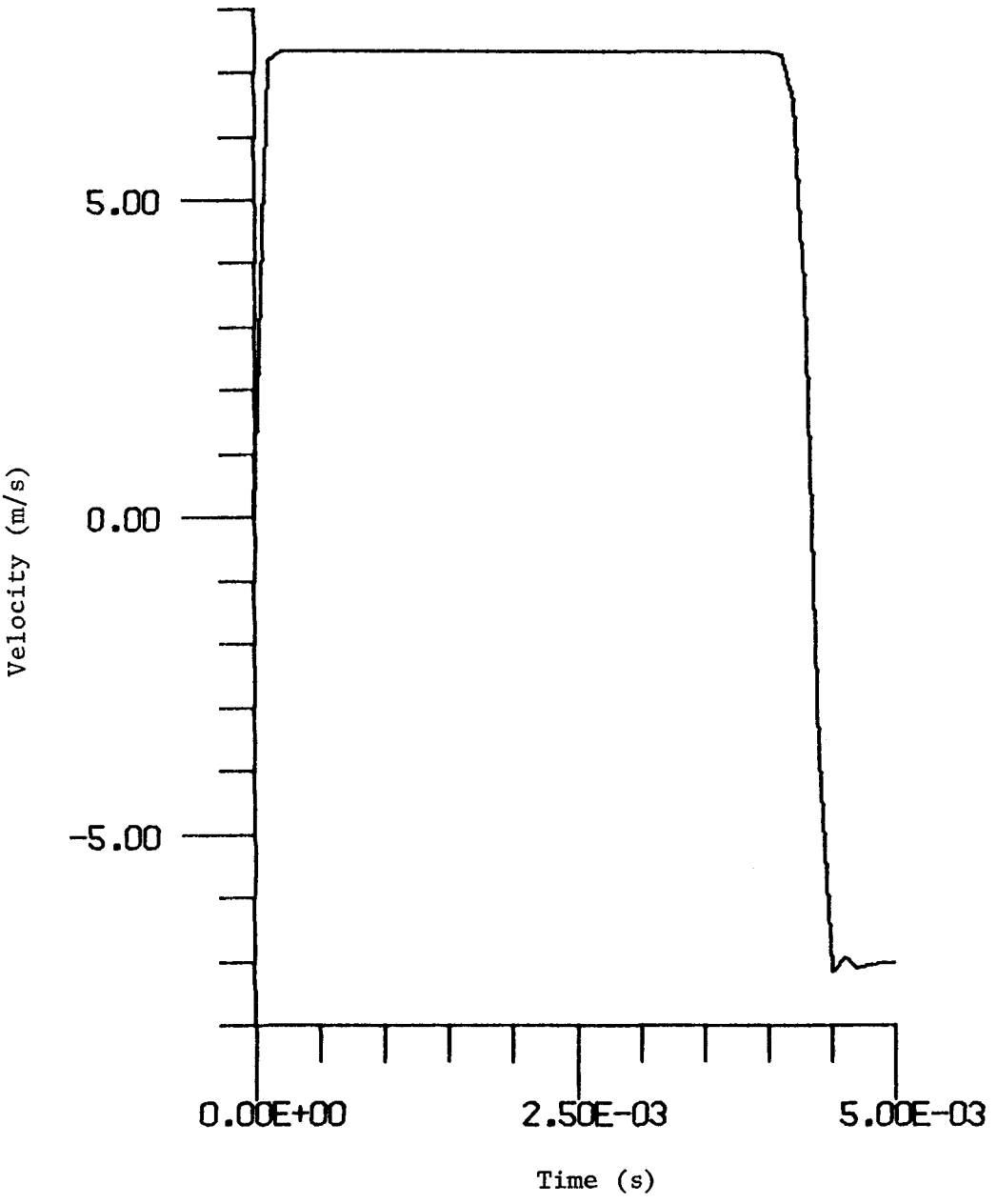

Figure 17. Velocity history at 3:1 orifice.

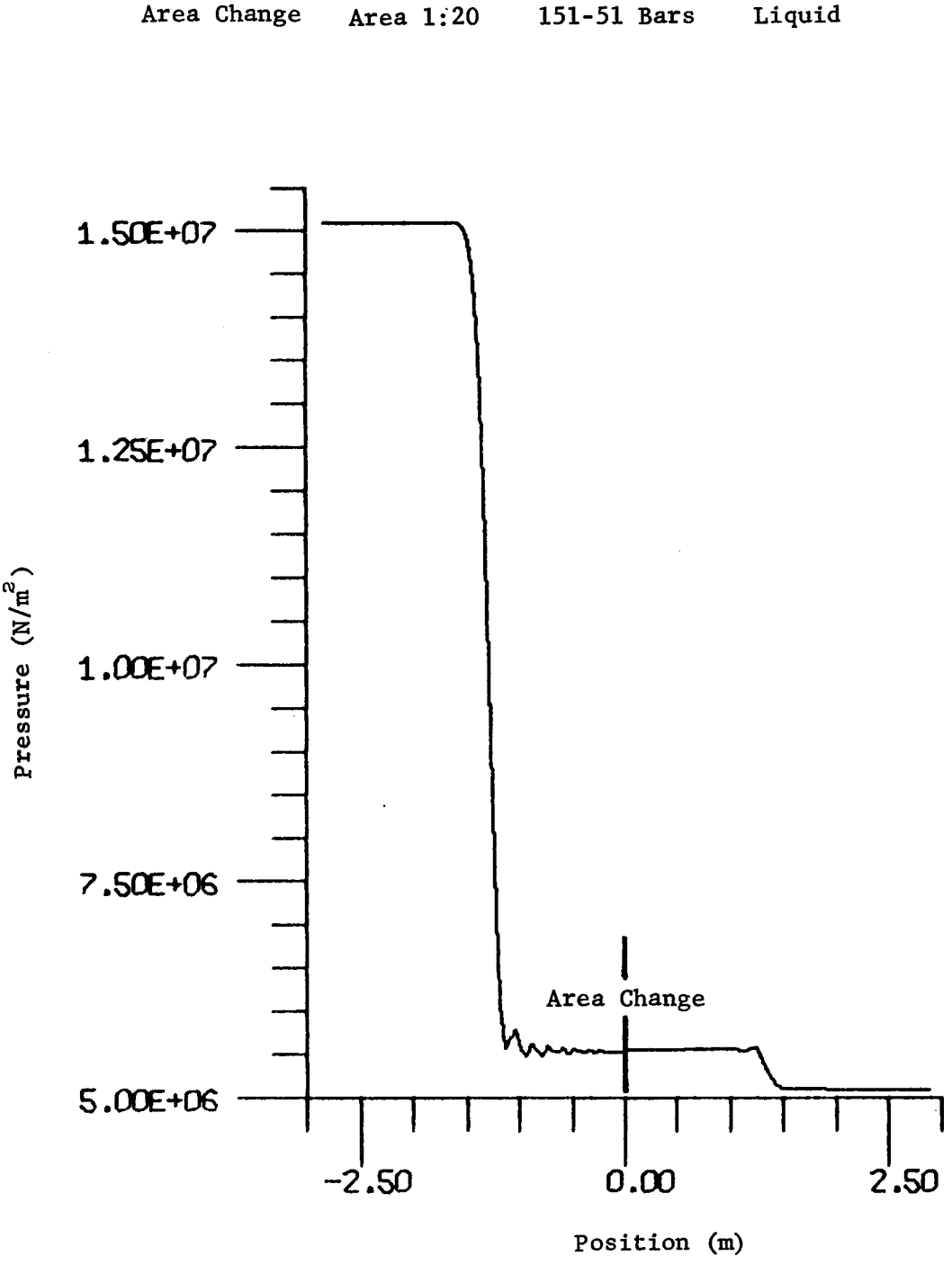

Figure 18. 1:20 Area change pressure profile at ~ 1 ms.

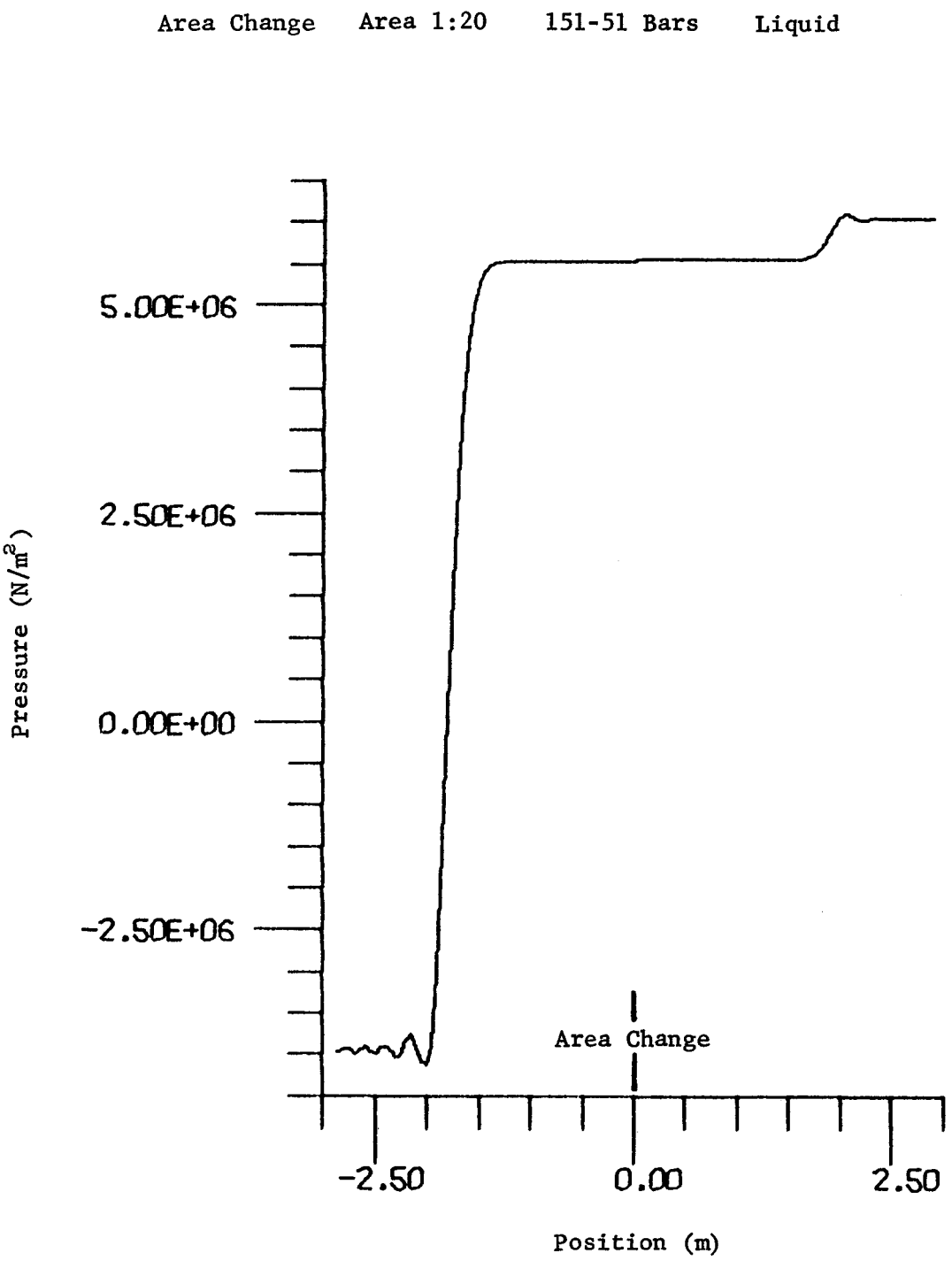

Figure 19. 1:20 Area change pressure profile at ~ 3 ms.

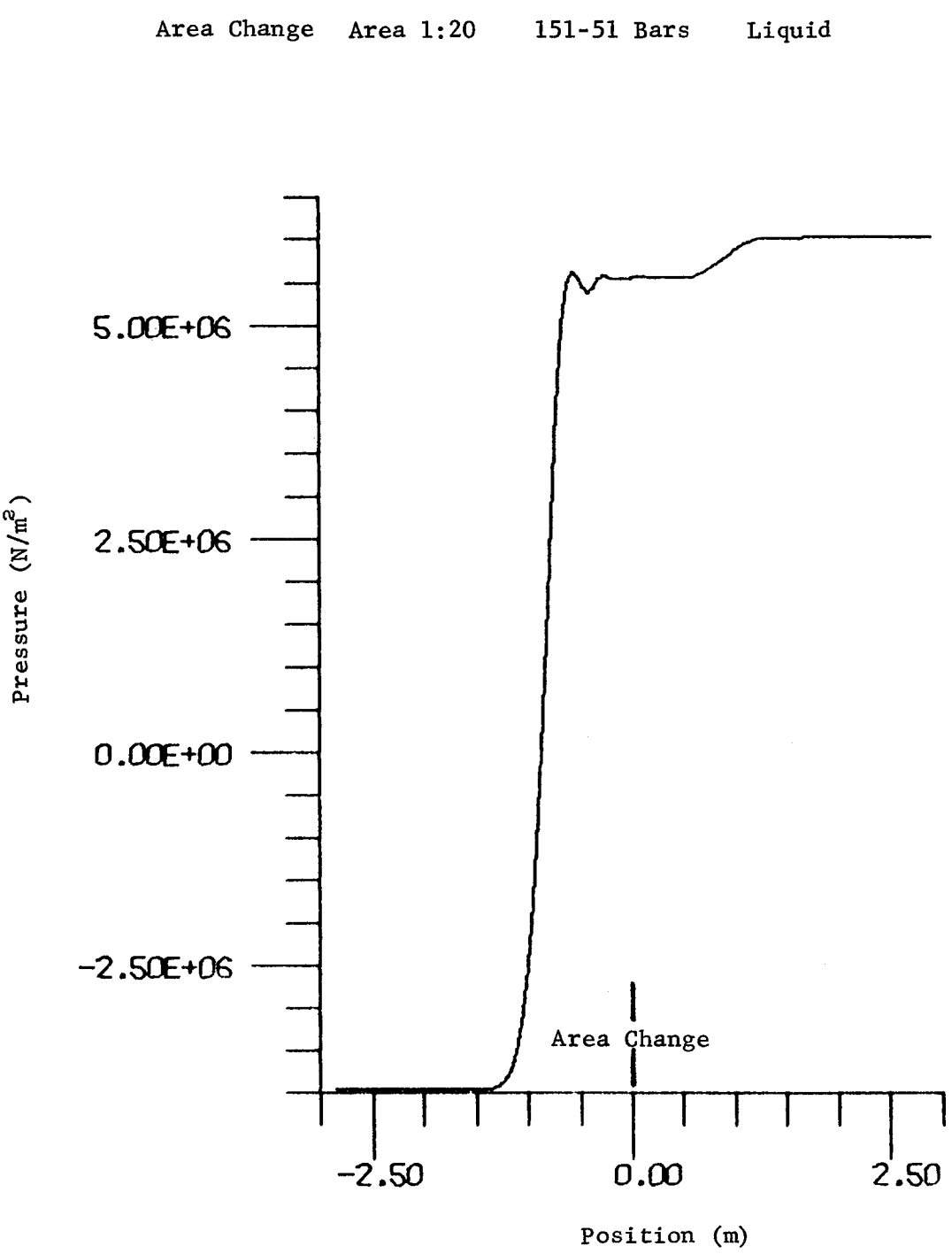

Figure 20. 1:20 Area change pressure profile at ~ 5 ms.

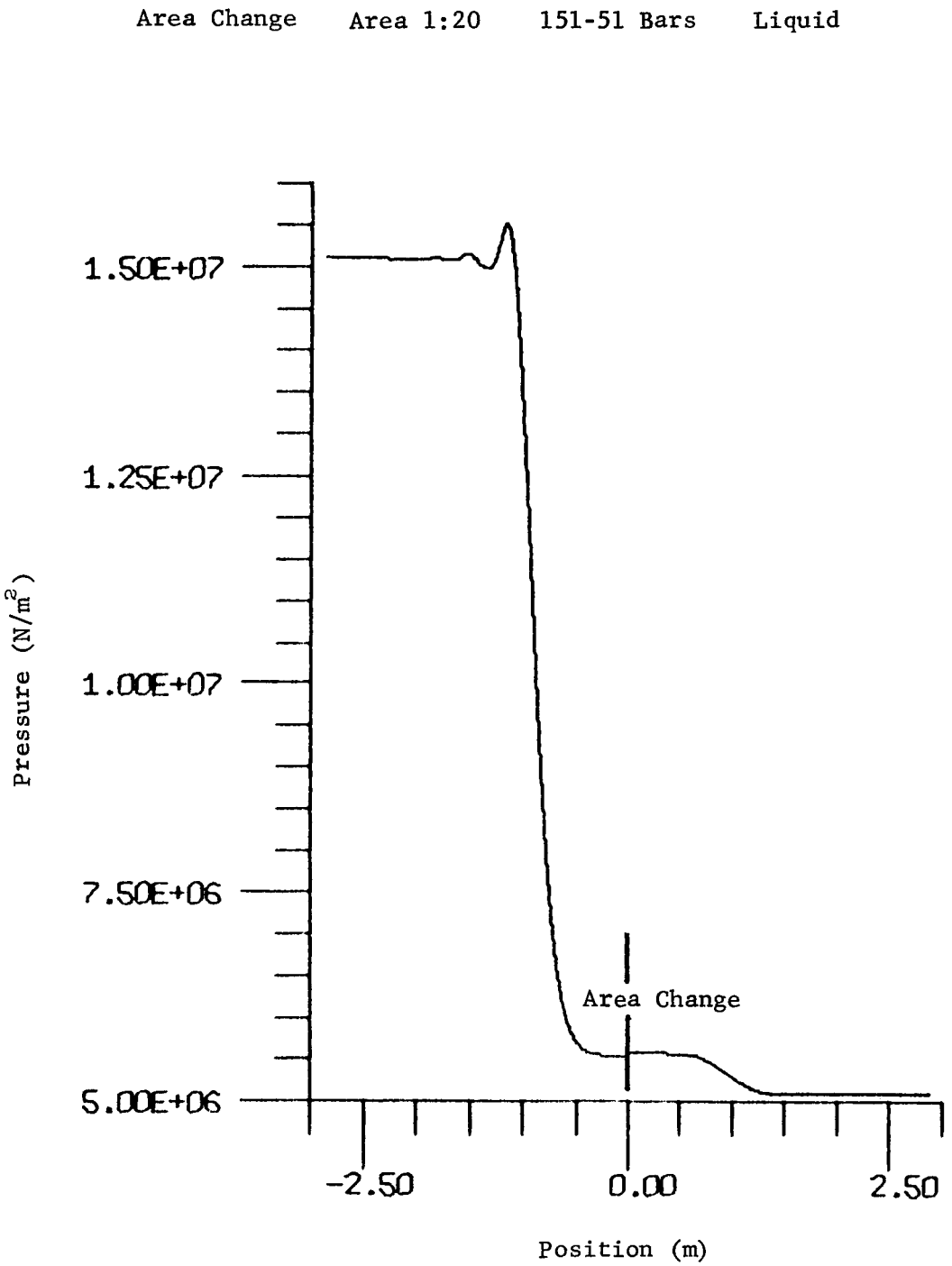

Figure 21. 1:20 Area change pressure profile at ~ 8 ms.

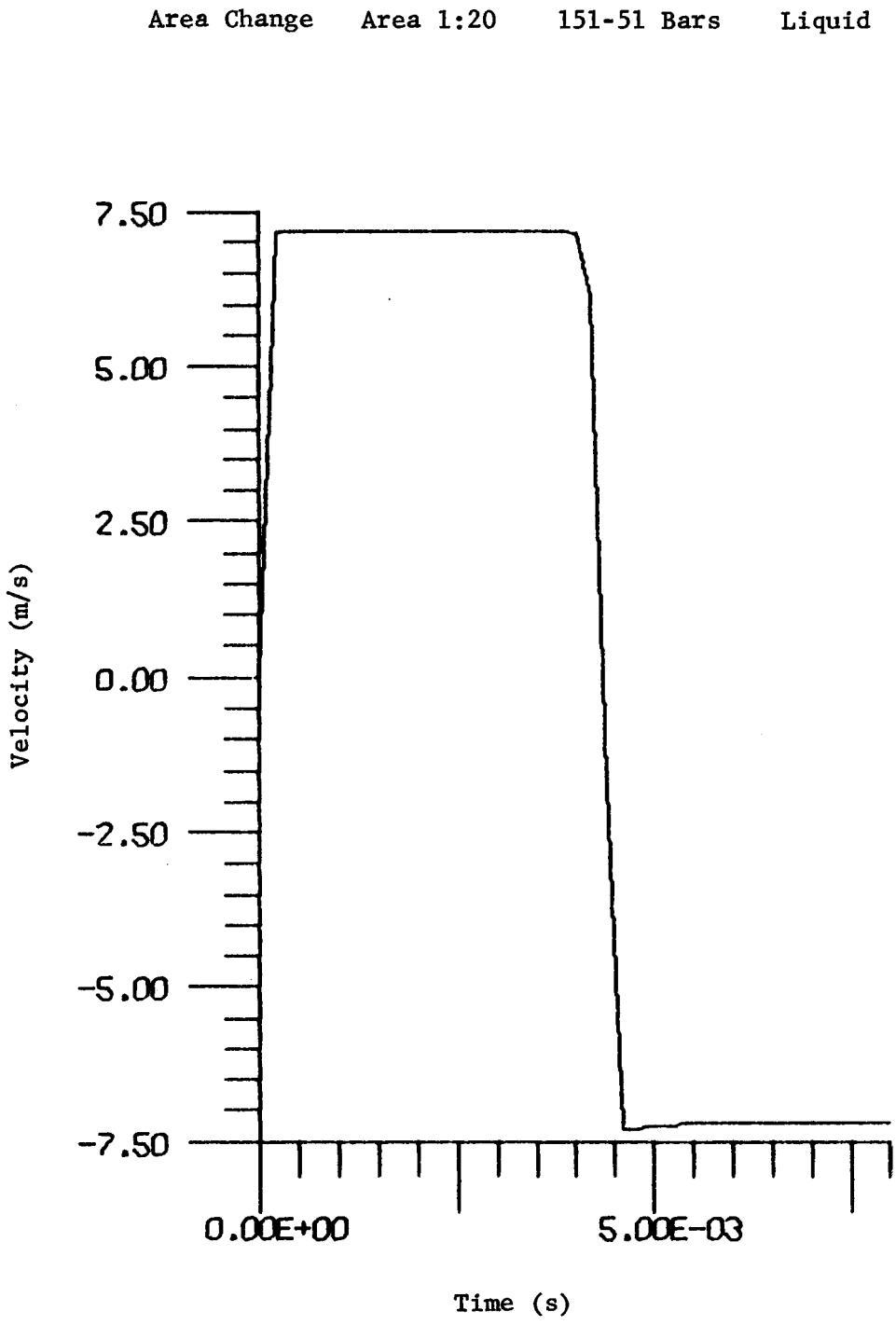

Figure 22. Velocity history at 1:20 area change.

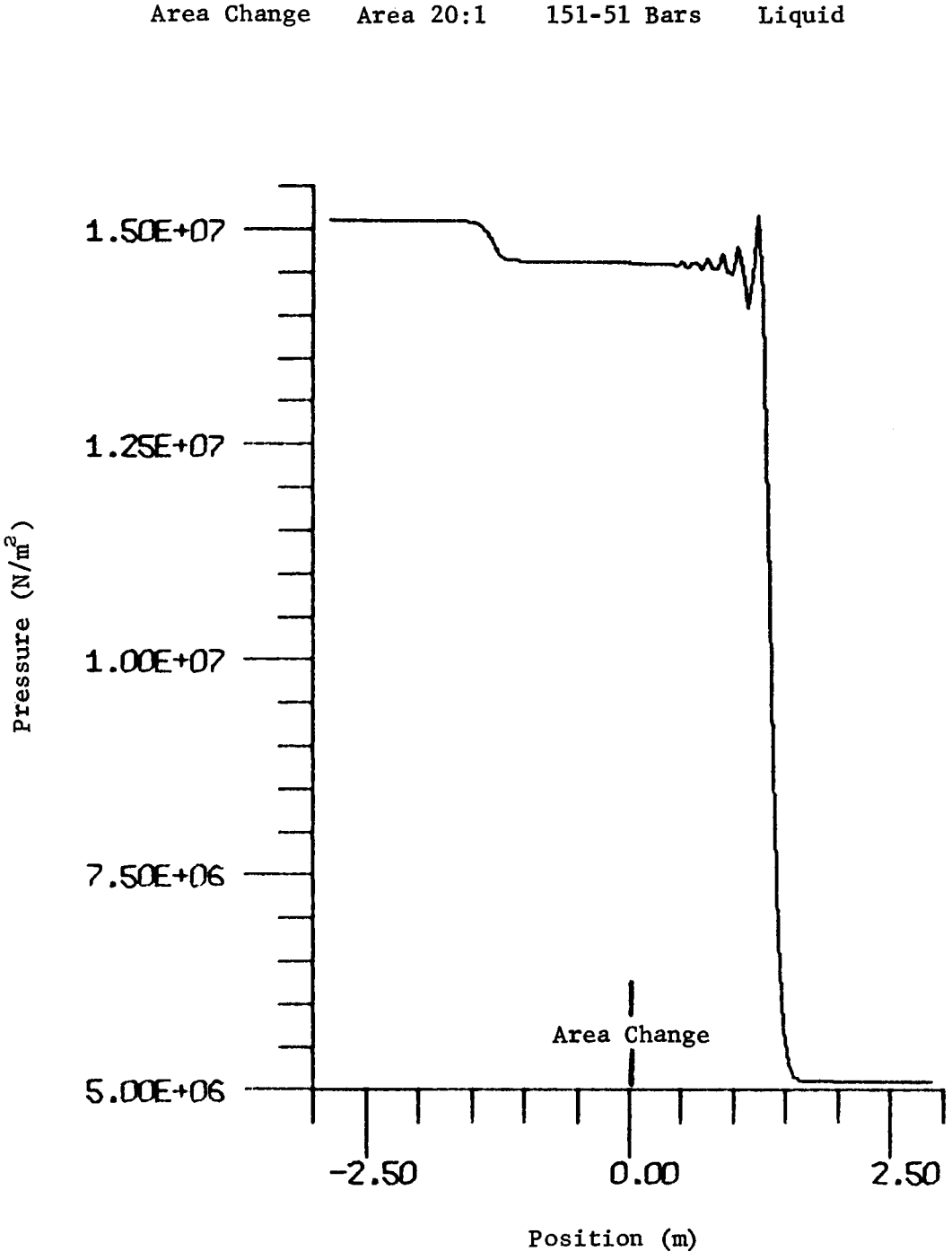

Figure 23. 20:1 Area change pressure profile at ~ 1 ms.

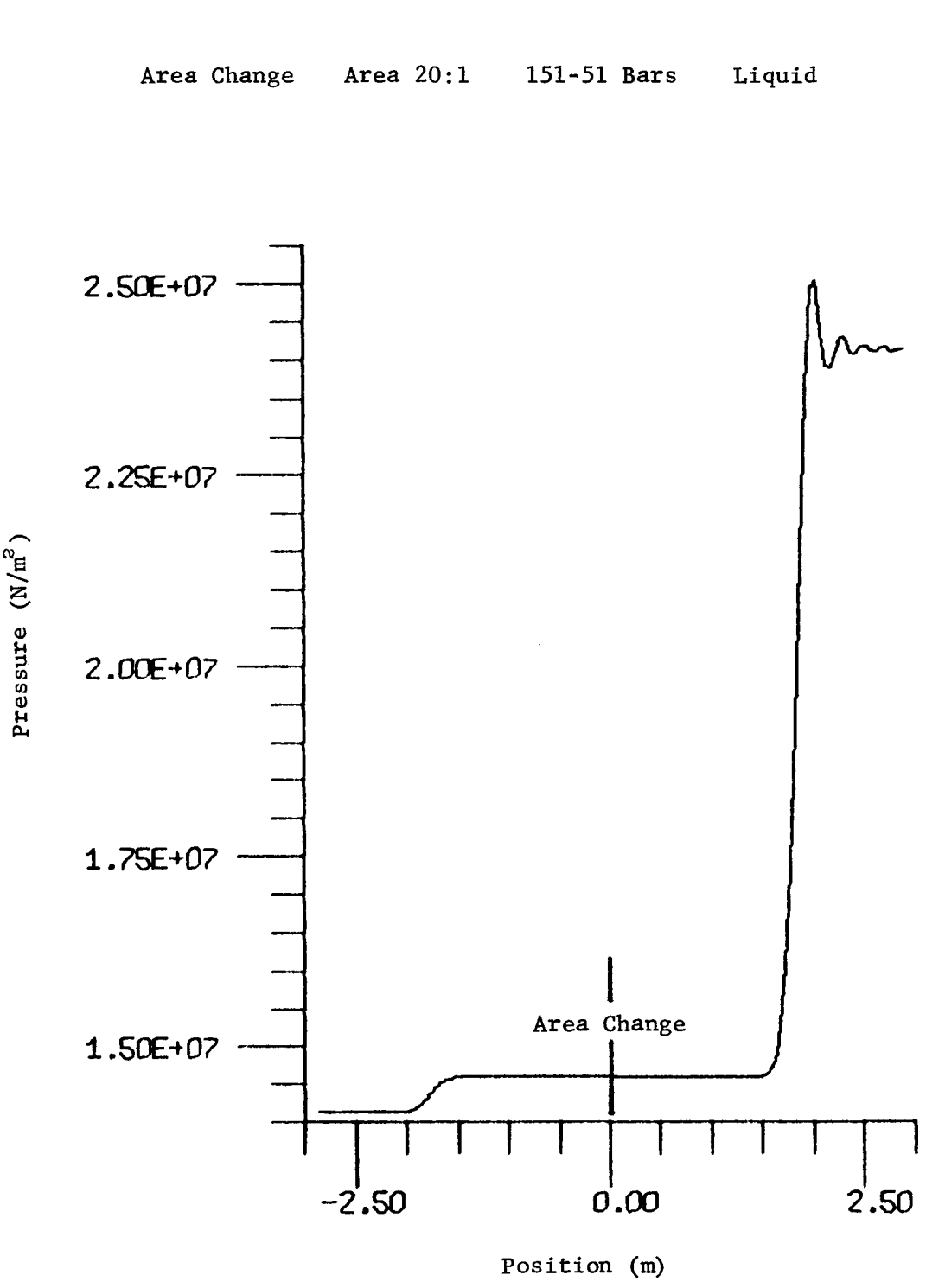

Figure 24. 20:1 Area change pressure profile at ~ 3 ms.

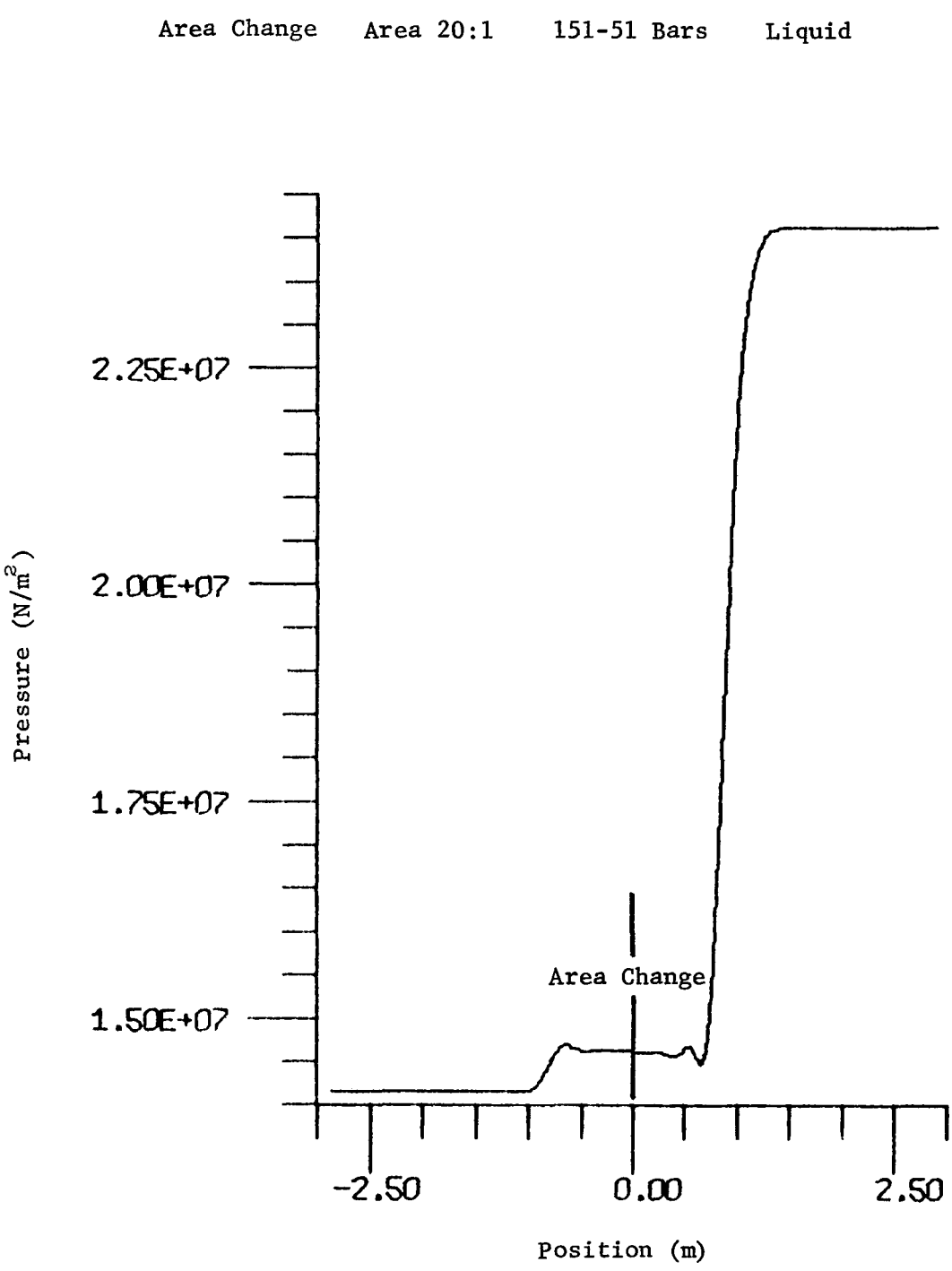

Figure 25. 20:1 Area change pressure profile at ~ 5 ms.

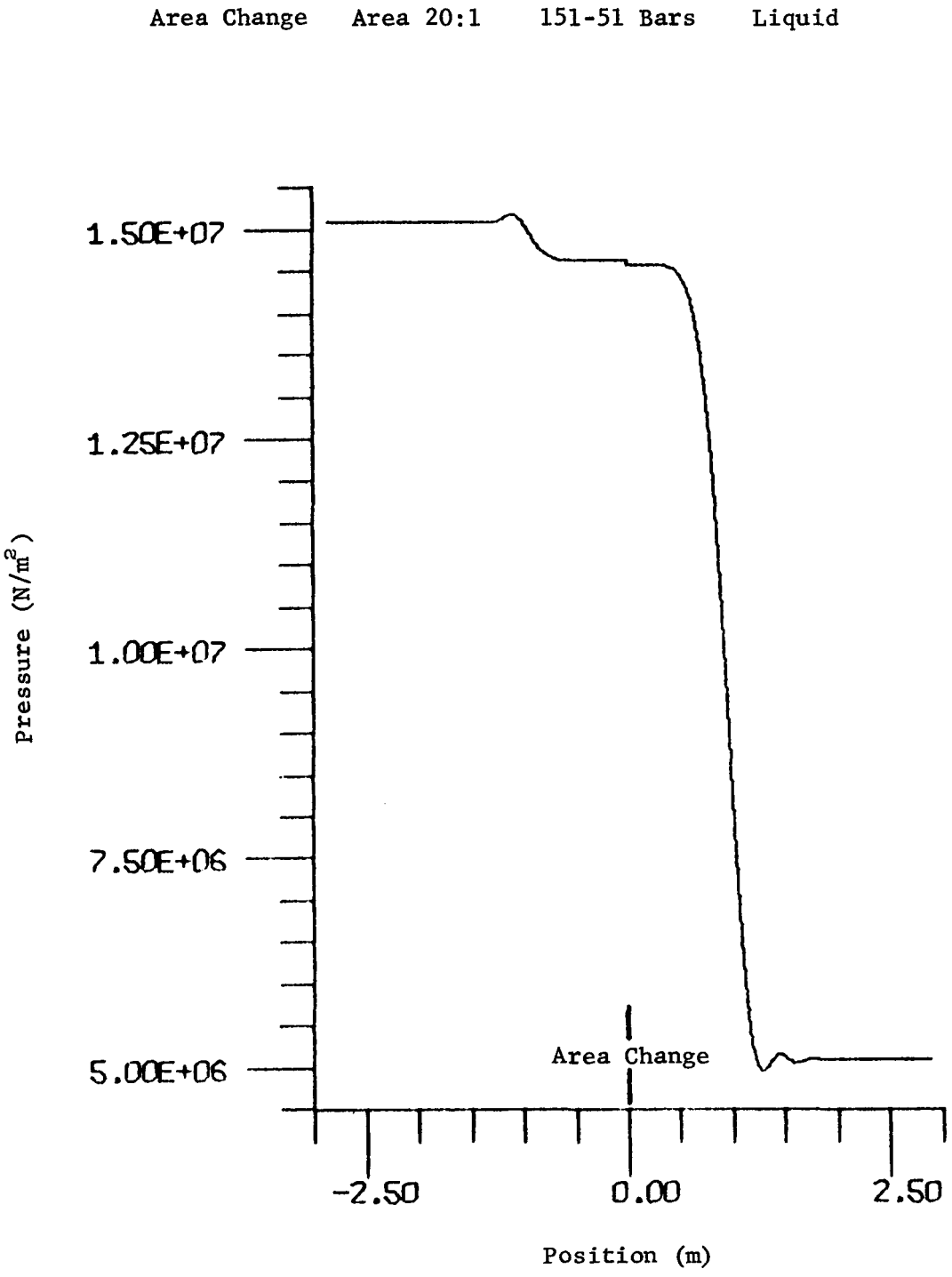

Figure 26. 20:1 Area change pressure profile at ~ 8 ms.

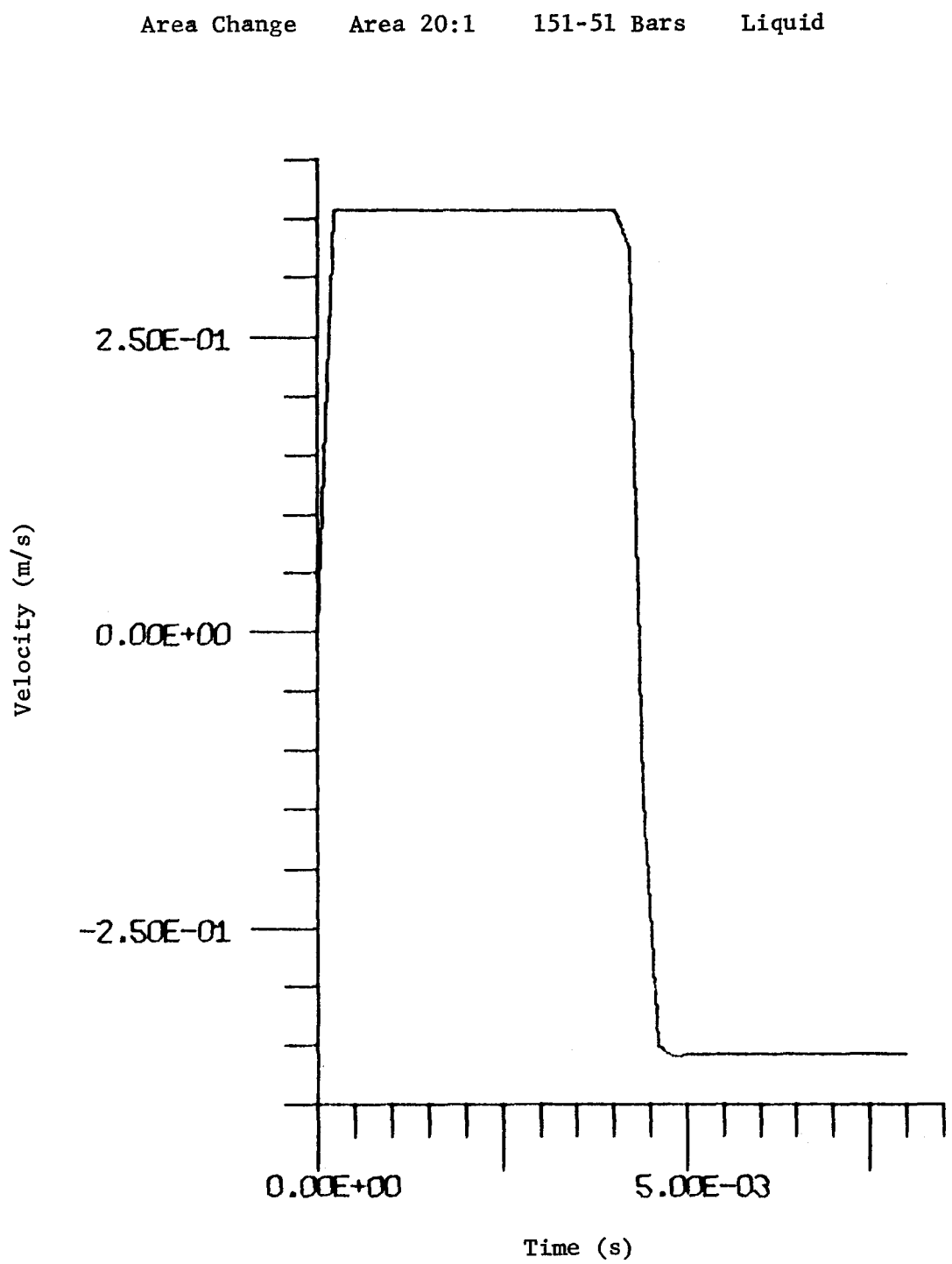

Figure 27. Velocity history at 20:1 area change.

other pipe was pressurized at 51 bars, and the valve was fully closed. The valve area opened linearly with time to reach the full flow area in 5 ms; thereafter, it remained open at the full flow area. Figures 28 through 32 demonstrate snapshot pressure profiles and the velocity history at the valve. The first pressure snapshot shows the initial left-traveling rarefaction and right-traveling compression; the second snapshot shows the wave profile shortly after reflections from the end walls; the third snapshot shows the wave profile after wave intersection, and the fourth profile shows the profile after the second reflections from the end walls. The velocity history at the valve shows that eventually the flow field reverses direction.

The final case described here is that of a model using the control volume of a closing valve. The control volume joins two pipes of equal cross-sectional area, each 2.9 m in length. One pipe is close-ended, the other open-ended, and both are initially pressurized at 151 bars and are in a quiescent state. A constant vacuum exists downstream of the open end. The valve area closes linearly (with time) in 5 ms from the full cross-sectional flow area; thereafter, it remains shut. Figures 33 through 38 describe the flow field behavior. Initially, a rarefaction (Figure 33) travels leftward from the open end as the high pressure fluid exits into the vacuum. Figure 34 depicts the pressure profile after the rarefaction has passed the closing valve; the rarefaction is still traveling leftward. However, owing to the area restriction existing at the valve when the rarefaction passed by, a right-traveling compression wave is generated. It also shows up on Figure 34. At a later time (Figure 35), the continuing closure of the valve, coupled with a flow velocity from left to right, generates a left-traveling compression to the left of the valve, and a right-traveling rarefaction to the right of the valve. Note that the characteristics of the previous profile are also still in evidence. Figure 35 displays the profile at full valve closure. To the right of the valve, a strong rarefaction is following a weak rarefaction out the open end. The latter is the backside of the compression generated earlier. To the left of the valve, the left-traveling compression is about to intersect with the right-traveling reflection of the incident rarefaction. Figure 37 shows one final profile: to the left

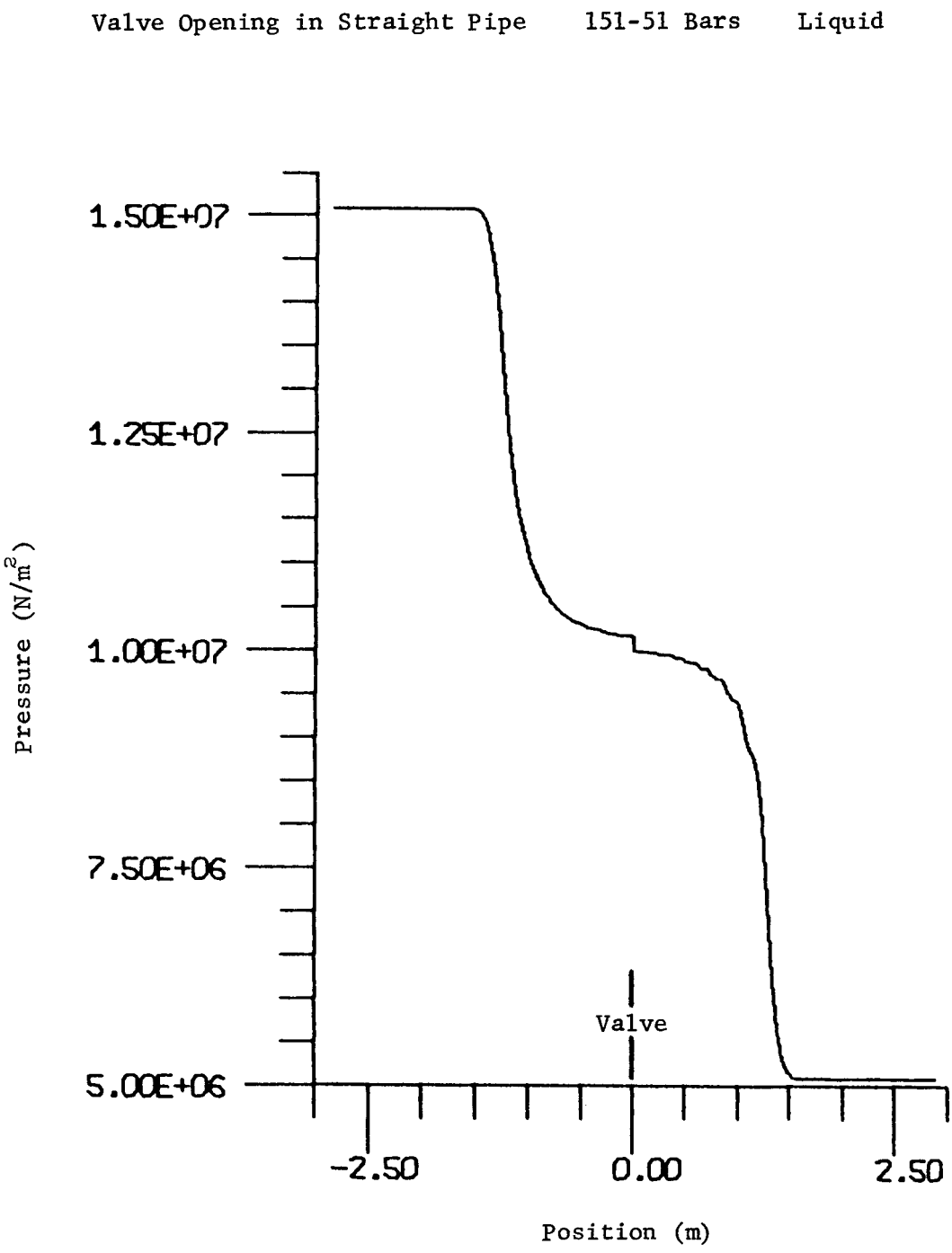

Figure 28. Opening valve pressure profile at ~ 1 ms.

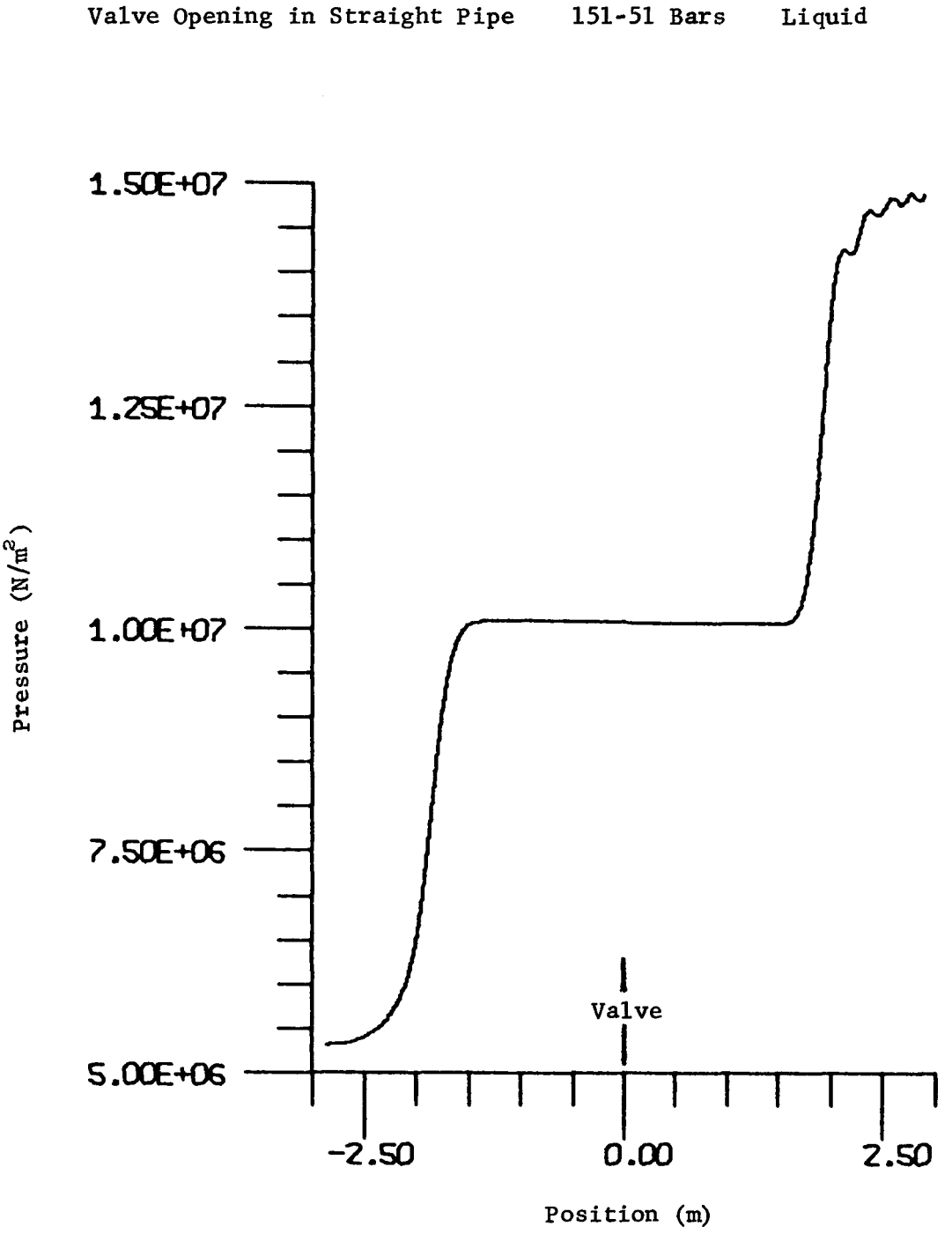

Figure 29. Opening valve pressure profile at ~ 3 ms.

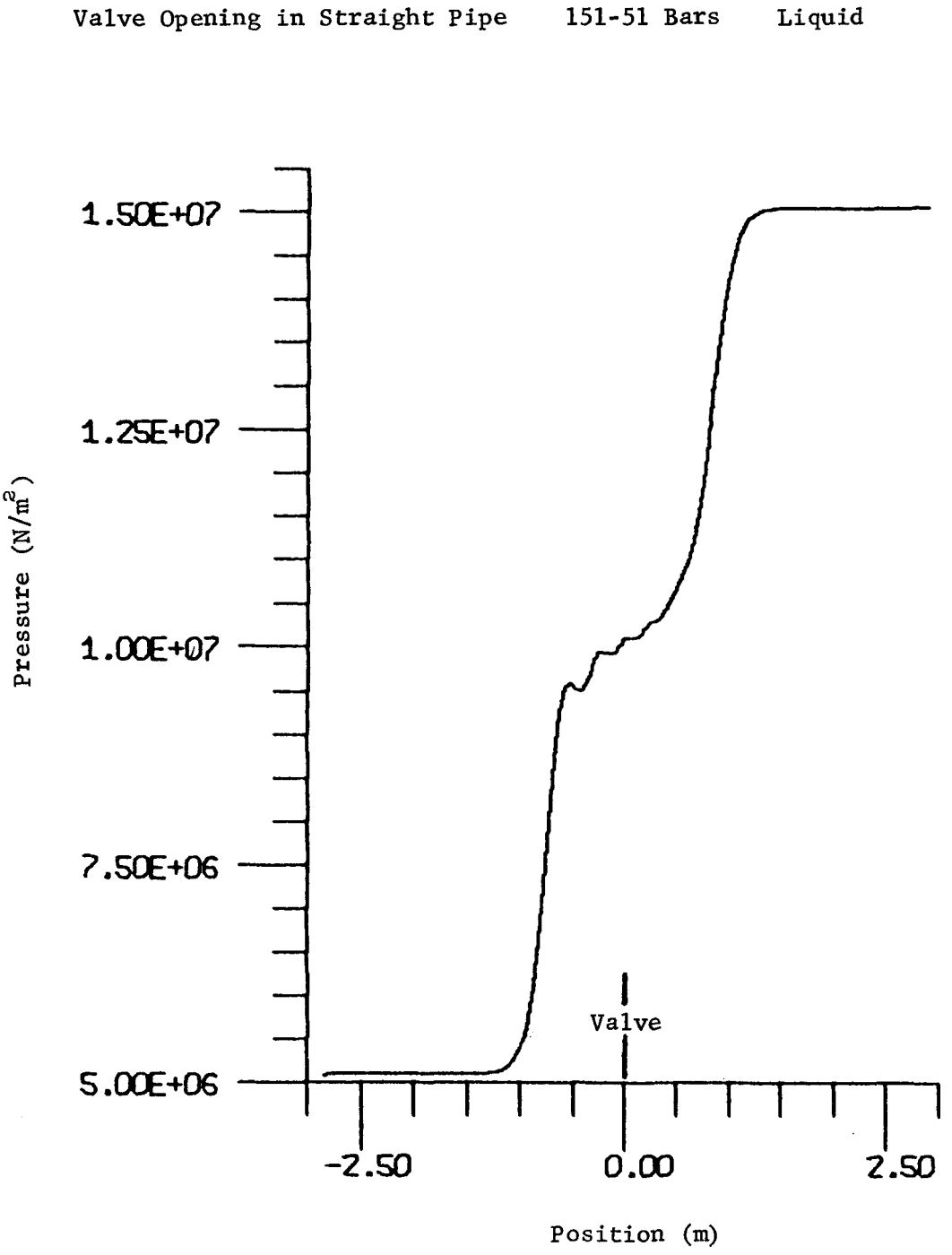

Figure 30. Opening valve pressure profile at ~ 5 ms.

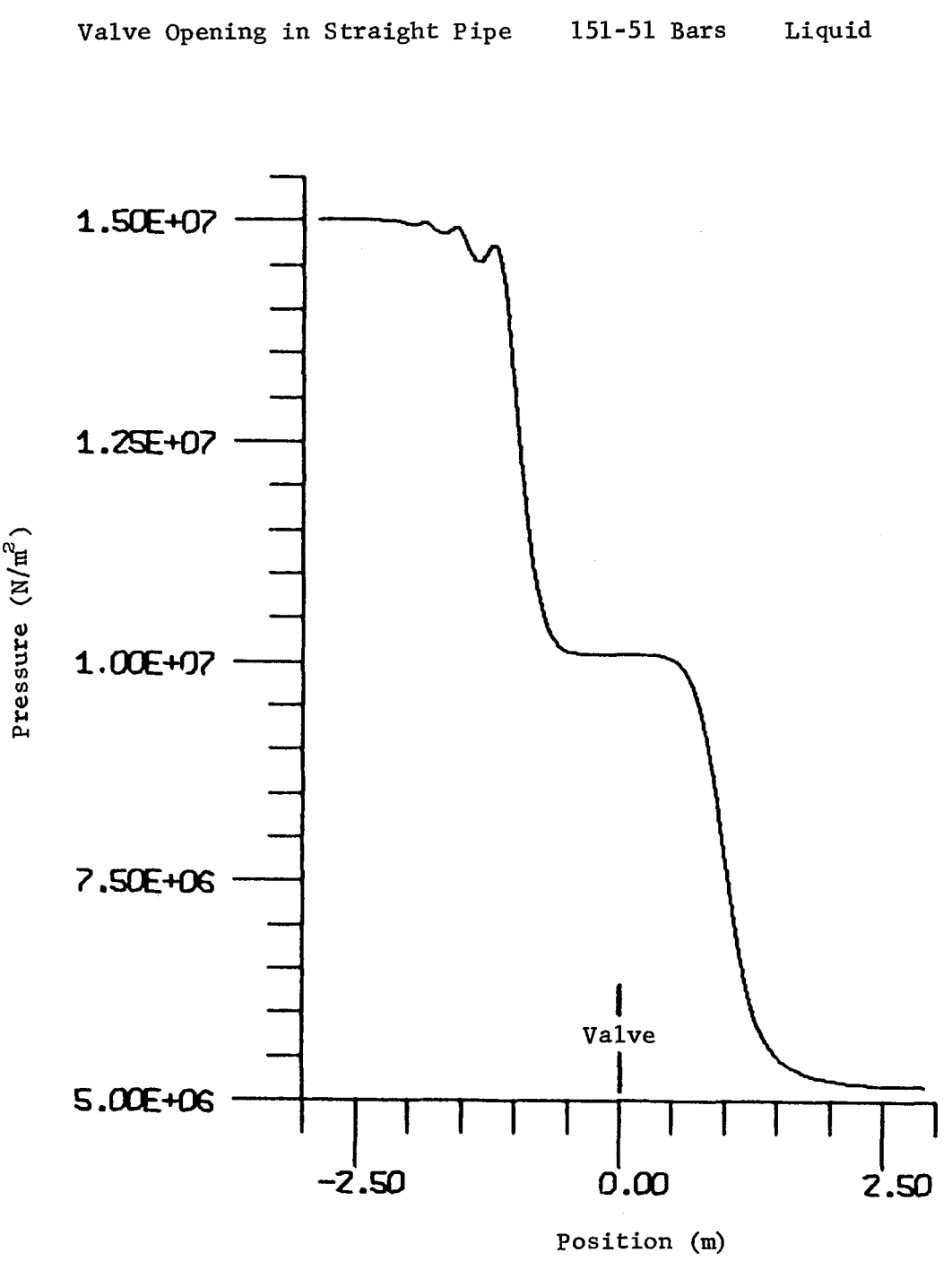

Figure 31. Opening valve pressure profile at ~ 8 ms.

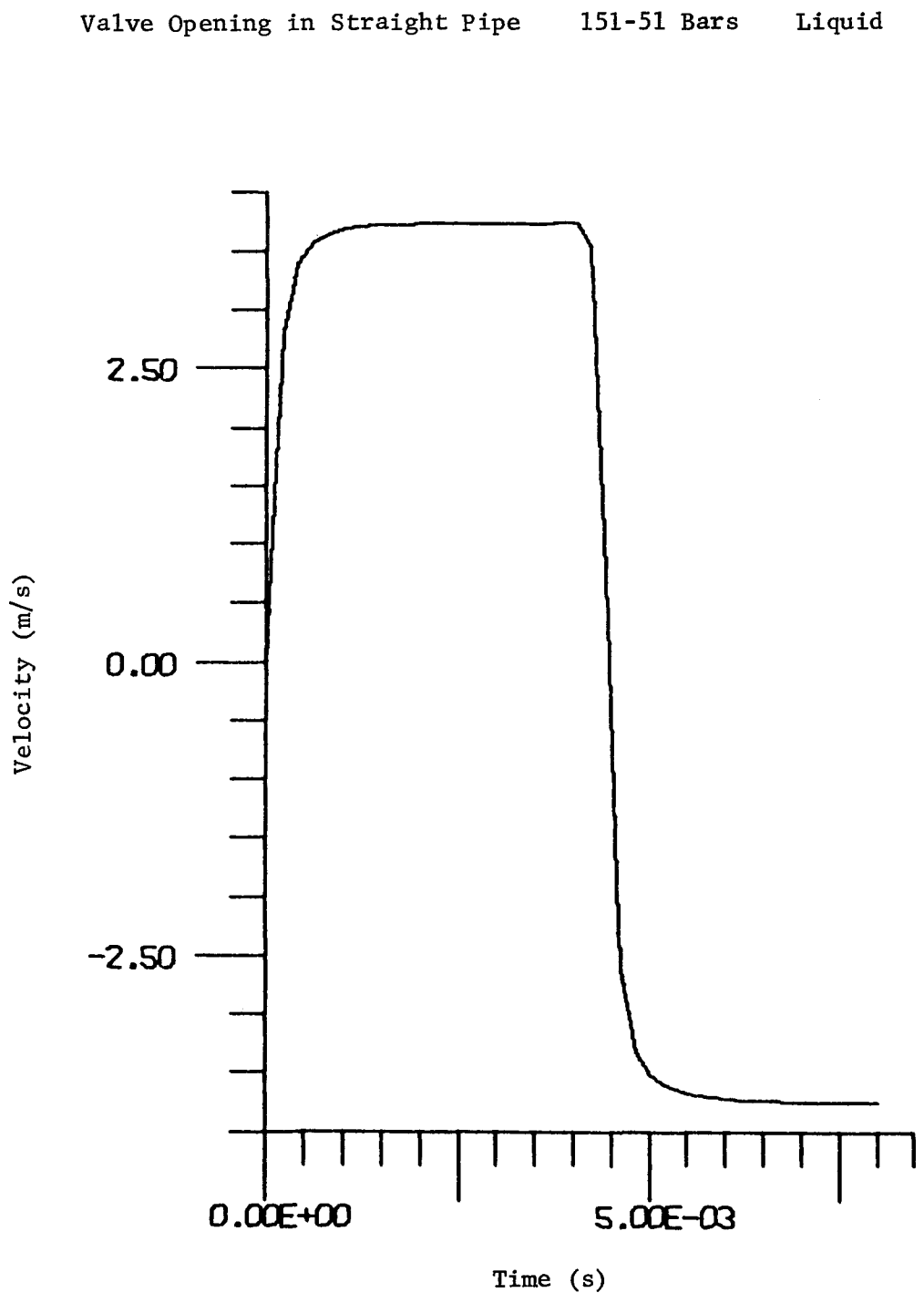

Figure 32. Velocity history at opening valve.

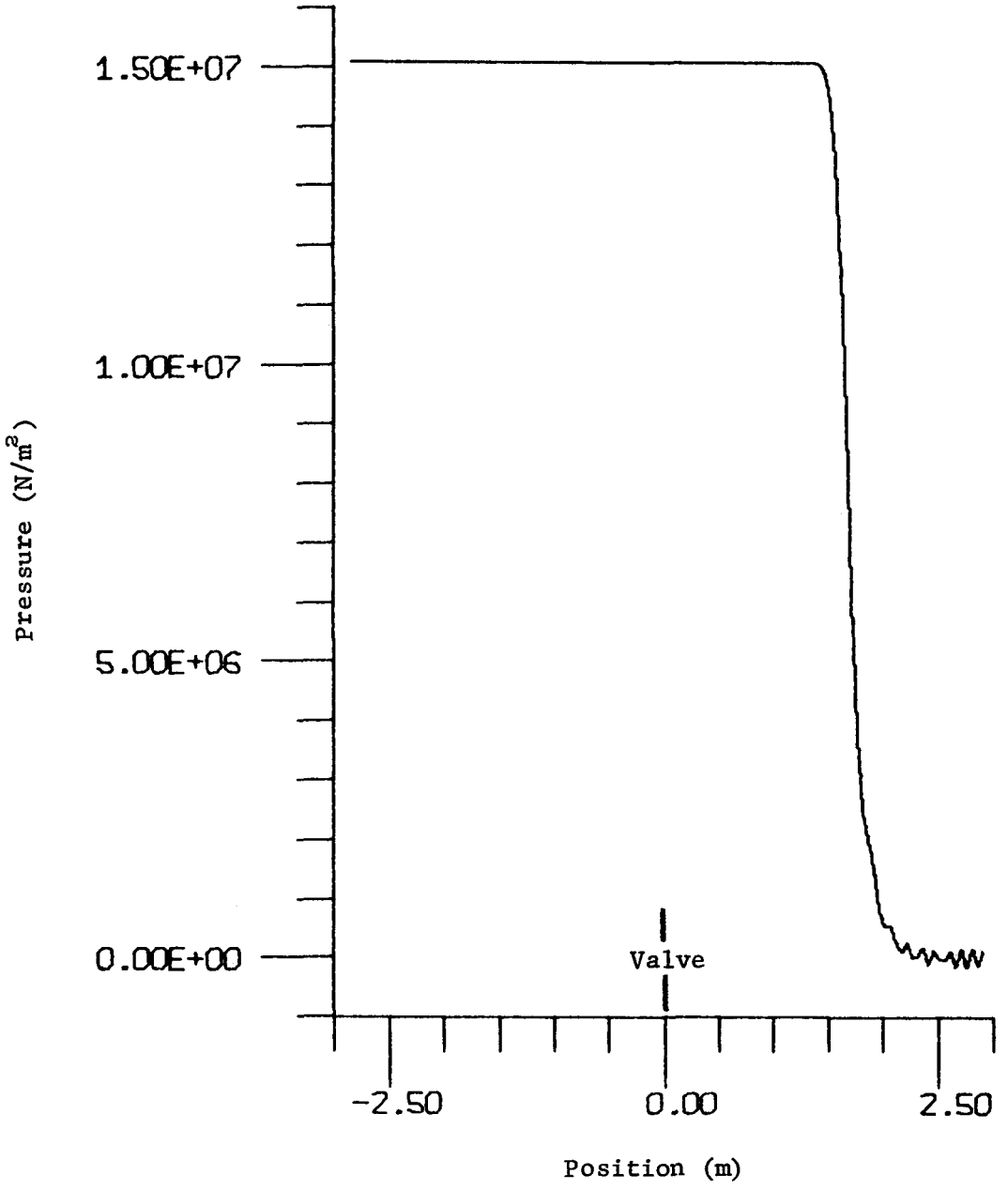

Figure 33. Blowdown pressure profile at ~ 1 ms.

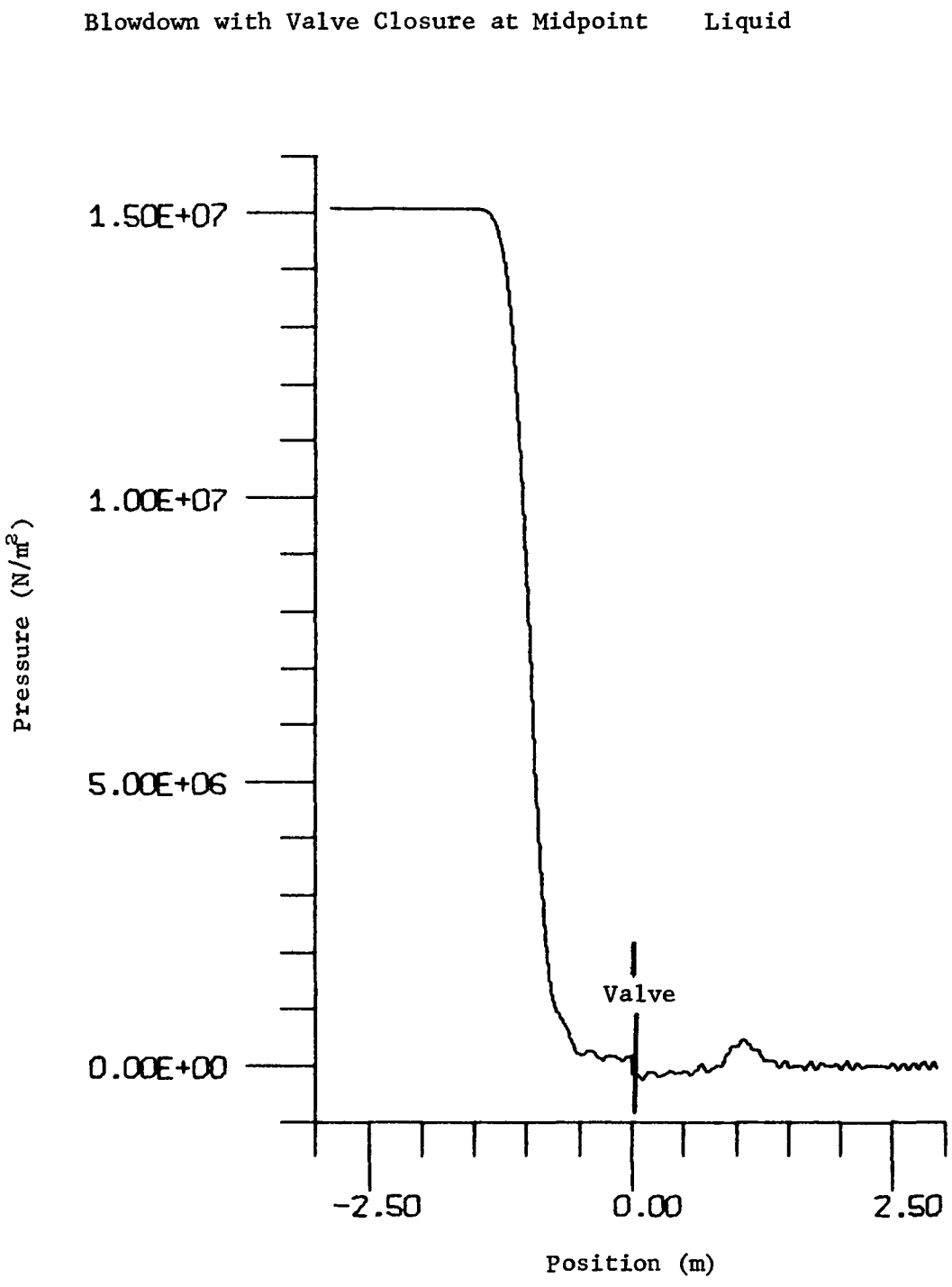

Figure 34. Blowdown pressure profile at ~ 3 ms.

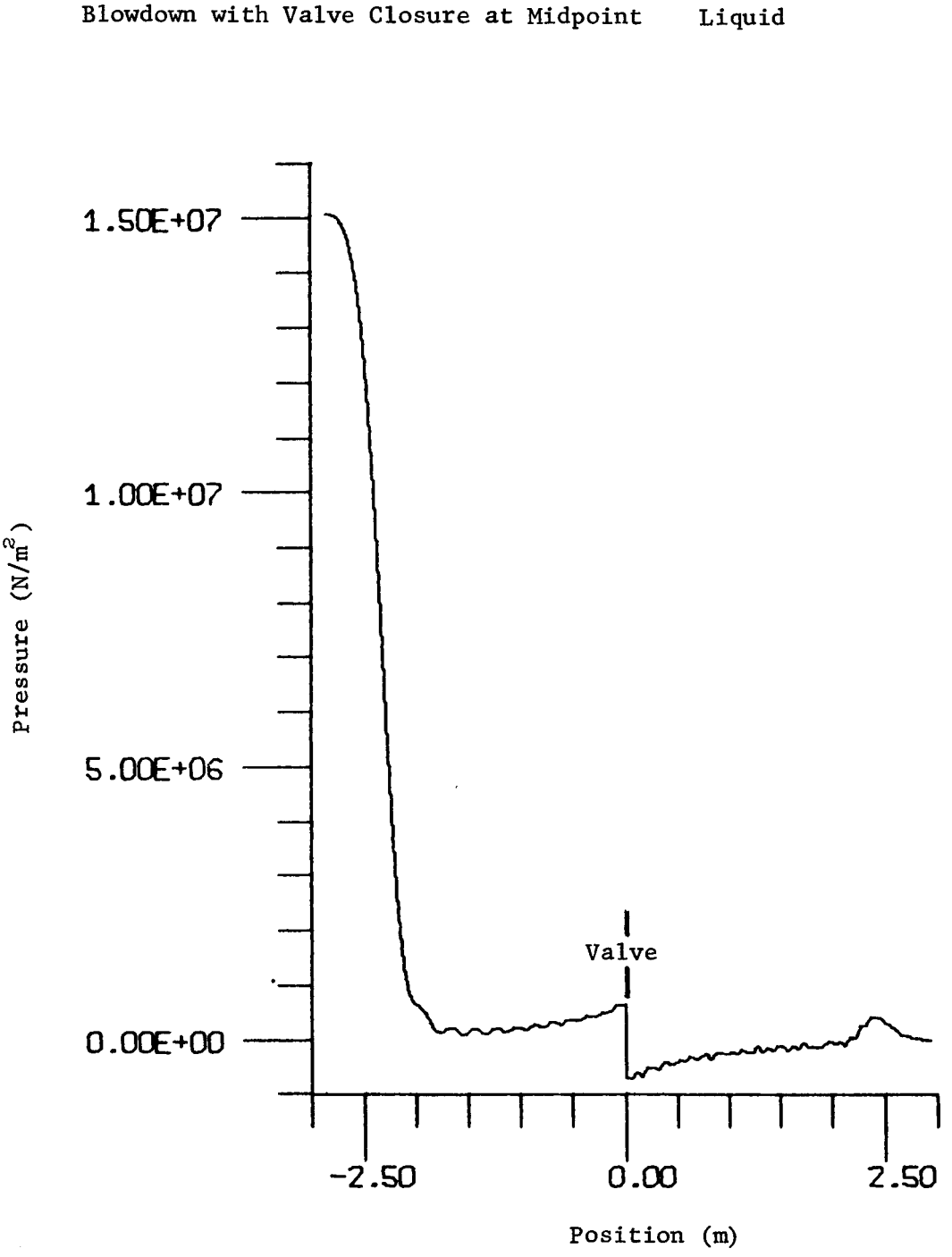

Figure 35. Blowdown pressure profile at ~ 4 ms.

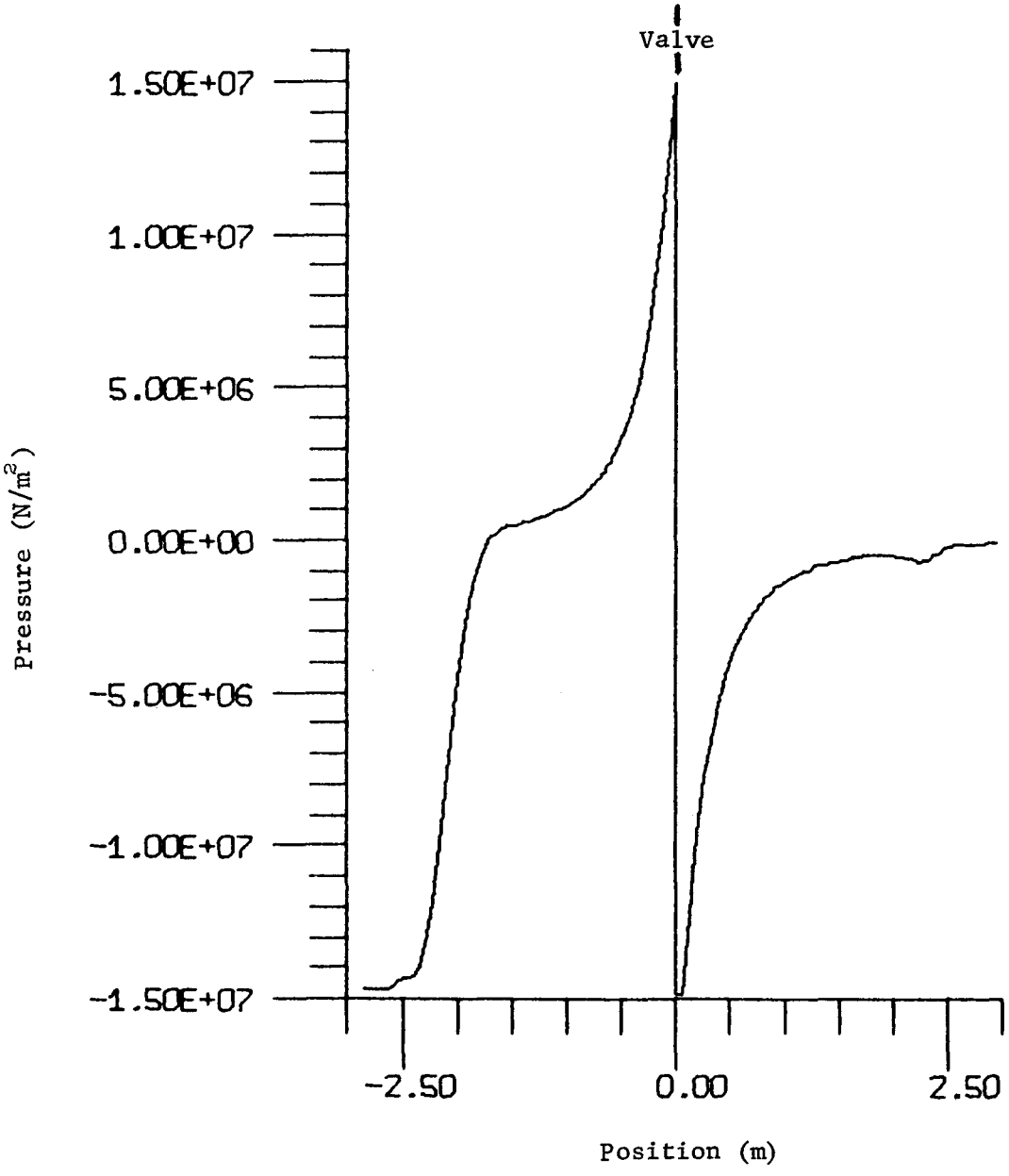

Figure 36. Blowdown pressure profile at ~ 5 ms.

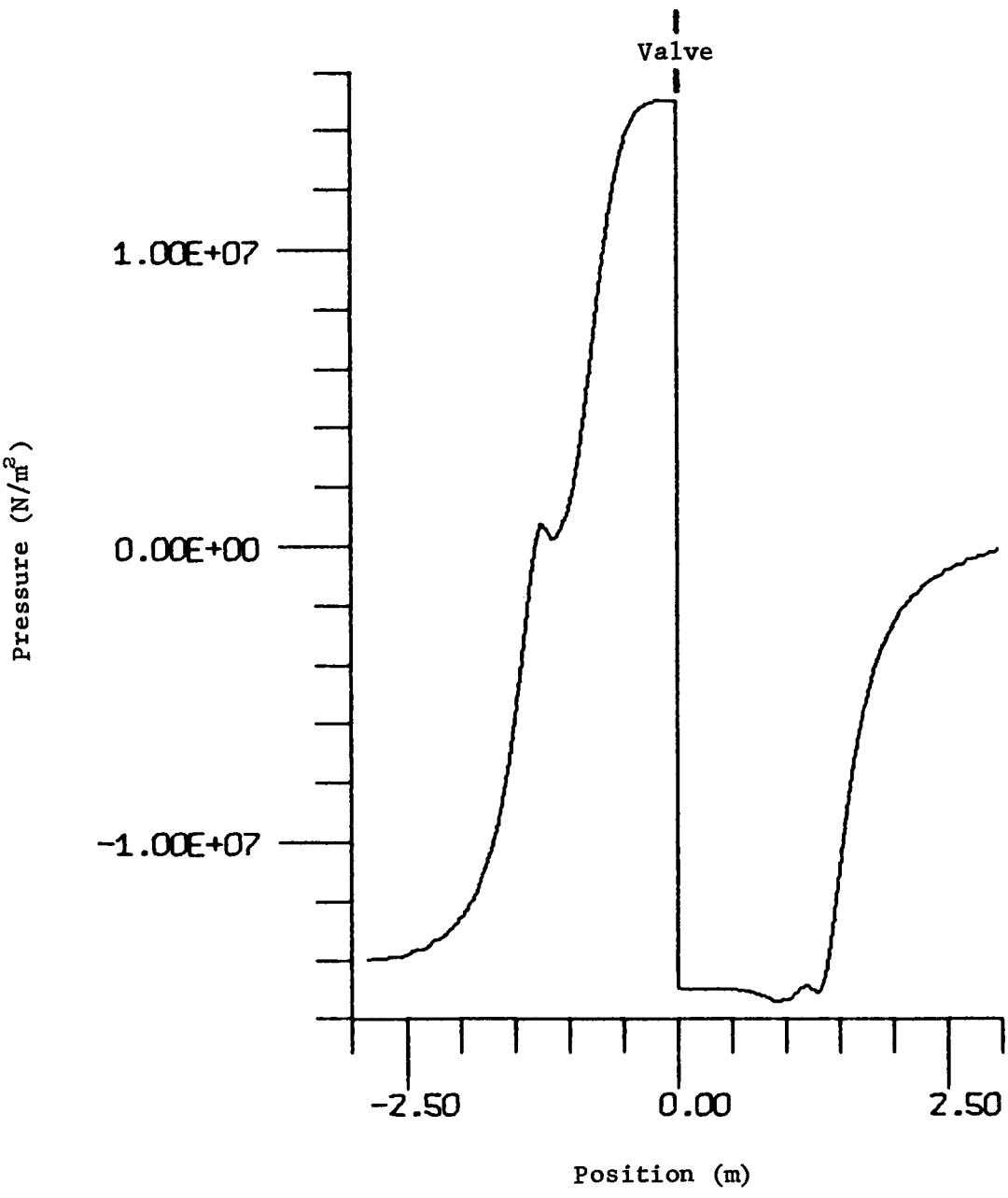

Figure 37. Blowdown pressure profile at ~ 6 ms.

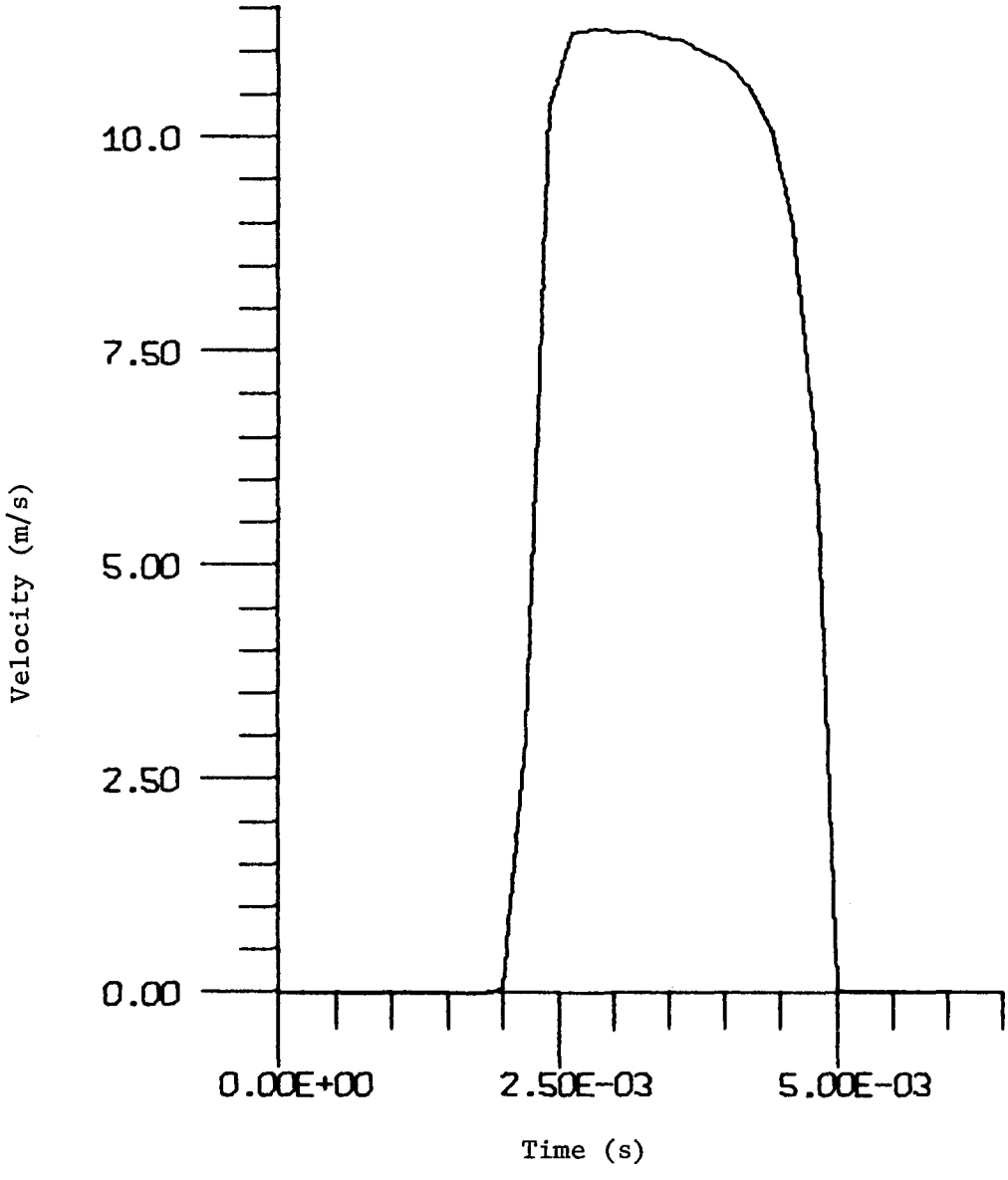

Figure 38. Velocity history at blowdown valve.

of the valve, the compression and rarefaction have just intersected, while to the right of the valve, the rarefaction is about to reflect from the open end. At this point, the model breaks down because the pressure differential demands inflow, but a vacuum has no mass source to sustain inflow. Finally, Figure 38 shows that the material field at the valve is always flowing left until the valve closes.

2.6 ADDITIONAL MODELS

Additional component models under consideration are reservoirs and heat exchangers. Although at present, no control volume models correspond to these components, they can now be simulated in some form. If the need arises to perform more comprehensive simulations, these models could be developed into control volume forms.

Pressure history, velocity history, and temperature history reservoirs are standard options in the present STEALTH codes. Each of these models may be assigned to one or more nodes as forcing functions. In this sense, they represent uncoupled reservoirs with histories independent of grid dynamics. The control volume approach would generalize the reservoirs to coupled regions whose histories would be influenced by, as well as influence, the grid dynamics.

Heat exchangers may currently be modeled as sources (or sinks) of energy. In fact, a subroutine exists in STEALTH which is addressable by input card data. What remains to be done is the development of a control volume model which would generalize the flexibility and response of this heat transfer mechanism.

Further possible developments include the modeling of components with no current representation in STEALTH, including: (1) multi-port junctions, (2) governed turbo-machines, and (3) reciprocating pumps.

SECTION 3
CONCOMITANT TECHNOLOGIES

3.1 PRELIMINARY COMMENTS

With the modeling technology for piping components, STEALTH 1D can simulate a wide range of fluid events that occur within the piping systems of power plants. With the development of a few additional technologies, the efficiency, range, and usefulness of these simulations increase appreciably. In particular, removal of non-hydrodynamic logic from the code increases the computational efficiency of the simulations; modeling to account for flow losses increases the range of the simulations; force resolution modeling and plot overlay capability increase the usefulness of the simulations. This section describes these developments.

3.2 HYDRO VERSIONS

Hydro versions of STEALTH are streamlined continuum codes, from which unnecessary logic has been purged. In particular, they do not contain the physics of solid mechanics and heat transfer. Also removed is the accounting required to add and drop rows (and columns in 2D), as well as the slideline analysis pertinent to relative motion between adjacent grids.

Simulations of hydrodynamic phenomena with the hydro versions are identical with those provided by the standard versions. Moreover, the savings in both computing time and cost by using the hydro versions can approach a factor of 2.

STEALTH hydro is available in both one- and two-dimensional versions. These require the same information as the standard STEALTH codes. The input decks for the standard versions and the hydro versions are practically identical. The user need only specify either standard or hydro versions.

3.3 FLUID MOTION LOSSES

While flowing through piping, a fluid medium is subject to wall friction. Moreover, as it passes through bends and other piping components, the fluid encounters abrupt changes in flow conditions. Both of these effects cause irrecoverable losses to occur in the fluid, leading to a retardation of motion.* Thus, to predict accurately the fluid motion in a piping system, it is necessary to account for these loss mechanisms.

In a one-dimensional, inviscid model of fluid motion, the losses due to pipe friction and piping components are, in effect, external forces which oppose the direction of motion. As such, they contribute an incremental acceleration ($\Delta\ddot{x}$) to each local fluid element, as follows:

$$\Delta\ddot{x} = -F_L \, \delta/m$$

where

F_L ≡ magnitude of the local external force due to pipe friction and/or piping components

$\delta \equiv \dot{x}/|\dot{x}|$, $\dot{x}$ denotes velocity

$m \equiv$ mass of the local fluid element .

Hence, the total local acceleration ($\ddot{x}$) for the fluid element is

$$\ddot{x} = \ddot{x}_o + \Delta\ddot{x}$$

where $\ddot{x}_o$ is the acceleration of the local fluid element if losses due to pipe friction and piping components were absent.

---

*For one-dimensional simulations, this is the total effect of bends on flow conditions.

Since F_L may include losses from both pipe friction and piping components, it is necessary to develop a model for each effect. Therefore, consider that

$$F_L \equiv F_f + F_{pc} \ .$$

F_f is the magnitude of the force due to pipe friction:

$$F_f \equiv (f/4)(\pi d \, \Delta x)(\rho \, \dot{x}^2/2)$$

where

f ≡ Darcy pipe friction coefficient (see, e.g., Reference 9)

Δx ≡ length of local fluid element

d ≡ diameter of local fluid element

ρ ≡ density of local fluid element .

F_{pc} is the magnitude of the force due to the loss associated with a bend, or other piping component:

$$F_{pc} \equiv K_{pc}(\pi d^2/4)(\rho \, \dot{x}^2/2)$$

where K_{pc} is the piping component coefficient (see, e.g., Reference 9).

In practice, $\dot{x}$ is not known in advance of the determination of F_f and F_{pc}. The calculation to determine $\ddot{x}$ must, therefore, converge on $\dot{x}$; it proceeds as follows [$\dot{x}_{old} = \dot{x}(time_{old})$]:

(1) determine $\ddot{x}_o$

(2) determine $\dot{x}_o = \dot{x}_{old} + \ddot{x}$ [time step]

(3) define $\dot{x}_t \equiv ave[\dot{x}_o, \dot{x}_{old}]$

(4) determine F_f and F_{pc} from $\dot{x}_t$

(5) determine $\Delta\ddot{x}$

(6) determine $\ddot{x}$

(7) determine $\dot{x} = \dot{x}_{old} + \ddot{x}[\text{time step}]$

(8) calculate $\epsilon = |\dot{x} - \dot{x}_t|$

(9) if $\epsilon \leq$ specified tolerance, procedure completed; otherwise:

(10) reset $\dot{x}_o = \dot{x}_t$

(11) return to Step 3, above.

This procedure converges rapidly on $\dot{x}$; in typical applications, convergence occurs in two or three iterations.

In the STEALTH model, each node is assigned values of f and K_{pc}, or the means to determine these coefficients from data tables or formulas (see Reference 9). In the case of pipe friction coefficients, it is also necessary to assign (or compute, in the case of flume geometry*) an effective diameter for each node.

It is also useful to be able to distribute the piping coefficient for one component over a number of nodes. This effectively distributes that component's losses over several nodes. For a relatively long component, it is a more realistic accounting of losses than a single node accounting of losses. Appendix A describes one possible distribution procedure.

3.4 FORCE RESOLUTION

Forces on piping components during transient flow conditions can exceed the steady state loadings. In a typical water hammer scenario, the sudden opening or closing of a valve causes intense accelerations to develop in the

*Standard option in STEALTH 1D to account for non-abrupt area effects in 1D flows.

fluid. The flow becomes highly unsteady and propagates strong pressure pulses throughout the system. When these waves reflect off or refract through piping components, they generate sharp impulses which bear directly on the piping. The determination of these dynamic effects is essential to the selection of pipe sizes, the evaluation of component performance, and the design and placement of supporting brackets and hangers.

Consider, as an example, a bend that changes both the direction and magnitude of fluid motion. For this case, Figure 39 illustrates the associated free body diagram. The external forces acting on the fixed control volume* of the local fluid element are the pressure forces at station 1 ($\vec{P}_1$) and at station 2 ($\vec{P}_2$), and the force ($\vec{L}$) exerted on the fluid by the bend. (In fact, $\vec{L}$ is the result of the integrated pressure forces bearing along the control volume surfaces which are in contact with the inner wall of the bend. However, in this analysis, $\vec{L}$ is analyzed simply as a force vector to be determined.) These external forces are balanced by the change in momentum occurring within the control volume, which is due to the flux of momentum across the boundaries at station 1 ($\vec{M}_1$) and at station 2 ($\vec{M}_2$), and the instantaneous rate of momentum ($\vec{M}_t$) within the control volume. $\vec{N}_i$ is the unit vector directed outward from the control volume, perpendicular to the local cross-sectional area (A_i); also listed are the local density (ρ_i) and pressure (p_i), where the latter is understood to include artificial viscous effects, when present.

Conservation of momentum demands that the following relationship be valid (see, for example, Reference 10):

$$\sum \vec{F}_E = \vec{M}_t - \vec{M}_1 + \vec{M}_2$$

*These may include, but are not limited to the control volume models of piping components.

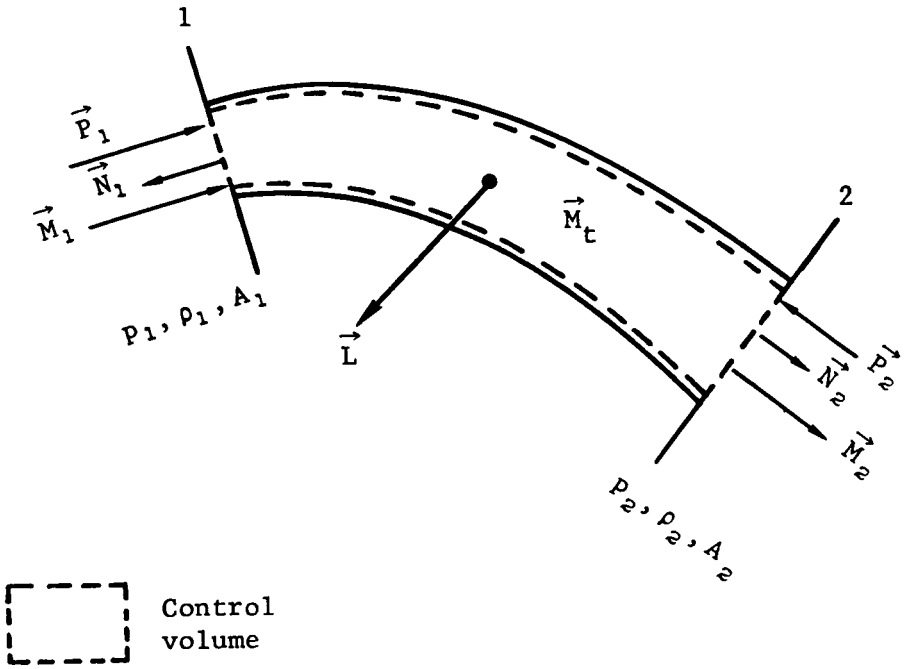

Figure 39. Free body diagram of a fluid element flow through a bend.

where

$$\sum \vec{F}_E = -p_1 A_1 \vec{N}_1 - p_2 A_2 \vec{N}_2 + \vec{L}$$

$$\vec{M}_t = \frac{\partial}{\partial t} \int_{\mathcal{V}} (\rho \vec{u})\, d\mathcal{V}$$

$$\vec{M}_1 = -\rho_1 u_1^2 A_1 \vec{N}_1$$

$$\vec{M}_2 = \rho_2 u_2^2 A_2 \vec{N}_2$$

$\mathcal{V}$ = control volume.

Hence, the reaction force on the bend ($\vec{R} \equiv -\vec{L}$) is resolvable as follows:

$$\vec{R} = -(\vec{N}_1 f_1 + \vec{N}_2 f_2 + \vec{M}_t)$$

where the local stream thrust function (f_i) is defined as $(p + \rho u^2)_i A_i$.

In any given inertial frame of reference, the reaction force is a vector quantity which depends on the orientation of $\vec{N}_i$ and $\partial[\int_{\mathcal{V}} (\rho \vec{u})\, d\mathcal{V}] / \partial t$. These orientations will vary from section to section in a given piping system. Moreover, the reference frame orientation could also vary from one piping system analysis to the next. It is not feasible to provide the flexibility necessary to span all the possibilities, nor all user output format options.

Hence, at present, this model does not compute $\vec{R}$ directly. The code computes and stores on an archive tape the local stream thrust functions, f_1 and f_2, and the instantaneous change of momentum, M_t, for each piping component. The reaction force is then recoverable from this archive

information with a postprocessor which resolves f_i and M_t into the orientation of the chosen frame of reference. The postprocessor can also provide the components of $\vec{R}$ in an output format which is suitable to user needs.

3.5 PLOT OVERLAYS

The capability to overlay a number of nodal force histories from different piping sections is now a standard option of the STEALTH codes. In particular, it is a feature of the GRADIS plotting package of STEALTH. As such, this overlay capability may be used either during the computation run which generates output data, or with STEALTH's postprocessor (ADAPRO), which refines the raw output data stored on an archive file.

Figure 40 displays a typical application of this capability. In this case, histories A, B, and C from three adjacent Lagrangian nodes are overlayed on one time axis. Also overlayed on the same axis is the history (D) of a fixed Eulerian position that is encountered by each Lagrangian node during the time span of the histories.

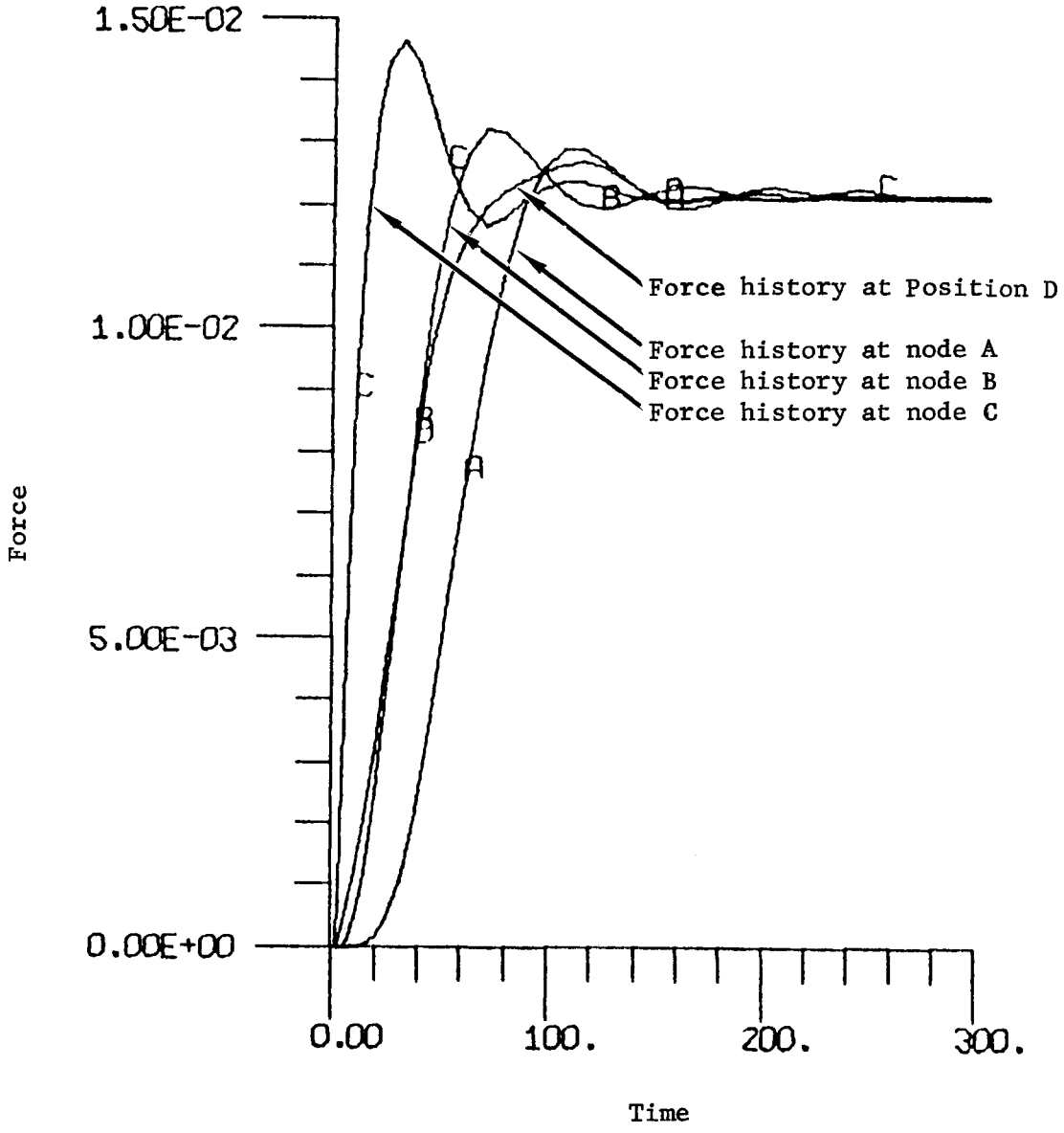

Figure 40. Demonstration of STEALTH overlay capability.

SECTION 4
CLOSURE

The STEALTH 1D code now has the technology to simulate the fluid events that can occur within the piping systems of power plants. This capability is embodied in the features which were described in the previous sections of this report. They are:

- Fixed-frame control volume models, which simulate the global effects of piping components within pipe networks; these models simulate time-dependent behavior, in conjunction with fluid media that behave as materials of homogeneous composition; although not a fundamental limitation of this control volume concept, the scope of the working models developed here is restricted to subcooled fluids.

- A fluid motion loss model, which simulates the irreversible losses associated with pipe wall friction and piping components; based on friction and component loss data, the model determines deceleration increments, which act through the equation of motion to retard fluid motion.

- A force resolution model, which evaluates the instantaneous force parameters which determine the fluid loadings that bear upon the piping structure; the model determines the rate of change of momentum within specified flow regions.

- Plot overlays, which display selected histories of flow parameters on one axis system.

- A hydro version of the code, which produces efficient simulations of fluid phenomena; purged of the physics and numerics associated with solid mechanics, the hydro version fluid simulations are identical with those of the standard version.

The code will determine the locations of intense fluid conditions, resolve the magnitudes of these effects on the enclosing piping structures, and present this information in formats that can be selected for convenience. The hydro version of STEALTH 1D accomplishes these objectives with efficient uses of computer execution time and storage space.

There are a number of developments which, if undertaken, would enhance the STEALTH 1D piping technology. Additional piping components that could be modeled with the control volume approach are:

- reservoirs of finite extent
- heat exchangers
- multi-port junctions
- governed turbo-machines
- reciprocating pumps

The fluid motion loss model could be upgraded to include functional dependence on flow Reynolds number and pipe wall roughness. Finally, the flow loss model could be incorporated directly into the control volume models.

REFERENCES

1. Ronald Hofmann and Bence I Gerber, "STEALTH, A Lagrange Explicit Finite-Difference Code for Solids, Structural, and Thermohydraulic Analysis," EPRI NP-260, Vols. 1-4, Electric Power Research Institute, Palo Alto, California, August 1976. Prepared by Science Applications, Inc., San Leandro, California, under Contract RP307.

2. A. H. Shapiro, The Dynamics and Thermodynamics of Compressible Fluid Flow, Vol. I, The Ronald Press Company, New York, 1953.

3. Michael B. Gross and Stewart A. Silling, "One-Dimensional Piping Component Models for STEALTH," Research Project 1065-2, Electric Power Research Institute, Palo Alto, California, April 1979. Key Phase Report (not intended for publication) prepared by Science Applications, Inc., San Leandro, California.

4. J. E. A. John and W. Haberman, Introduction to Fluid Mechanics, Prentice-Hall, Inc., Englewood Cliffs, New Jersey, 1971.

5. I. H. Shames, Mechanics of Fluids, McGraw-Hill Book Company, New York, 1962.

6. I. J. Karassik, W. C. Krutzsch, W. H. Fraser, and J. P. Messina (editors), Pump Handbook, McGraw-Hill Book Company, New York, 1976.

7. M. Marchal, G. Flesch, and P. Suter, "The Calculation of Waterhammer Problems by Means of the Digital Computer," International Symposium on Waterhammer Pumped Storage Projects, ASME, Chicago, Illinois, 1965.

8. E. B. Wylie and V. L. Streeter, Fluid Transients, McGraw-Hill, Inc., New York, 1978.

9. "Flow of Fluids Through Valves, Fittings, and Pipe," Technical Paper No. 410, Crane Company, Chicago, Illinois, 1978.

10. M. J. Zucrow and J. D. Hoffman, Gas Dynamics, Vol. I, John Wiley and Sons, New York, 1962.

APPENDIX A

A RATIONAL PROCEDURE FOR DISTRIBUTING THE LOSS EFFECT OF A PIPING COMPONENT

For relatively long piping components, the associated flow loss acts over a significant spatial interval. This situation is modeled in Figure A-1; the piping component is equivalent in length to the distance spanned by several consecutive zones of the computational grids. Under these conditions, it is realistic to distribute the loss over a number of computational nodes. This Appendix develops one possible distribution procedure, based on a resistance analysis of the component loss.

Figure A-2 illustrates the resistance concept for a piping component loss. Figure A-2(a) depicts the global flow resistance of the component. This resistance causes a drop in the total pressure of the flow from the upstream value of P_L to the downstream value of P_R, as follows:

$$P_L - P_R = K_{pc}\, \rho_{pc}\, u_{pc}^2/2$$

where

K_{pc} = piping component loss coefficient

ρ_{pc} = effective density within piping component

u_{pc} = effective velocity through piping component .

Figure A-2(b) depicts an equivalent flow resistance, whereby the global resistance is distributed across N discrete resistance units. Each resistance unit contributes to the total pressure drop in the following manner:

$$P_L - P_R = \sum_{i=1}^{N} (P_{i-1} - P_i)$$

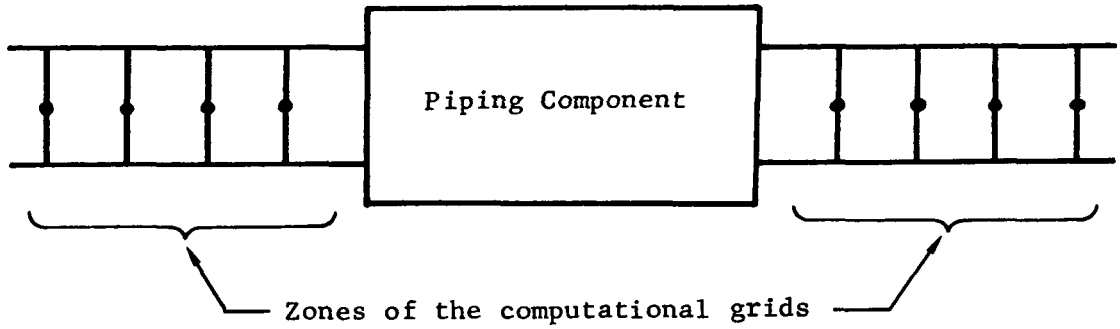

Figure A-1. Relatively long piping component oriented between computational grids.

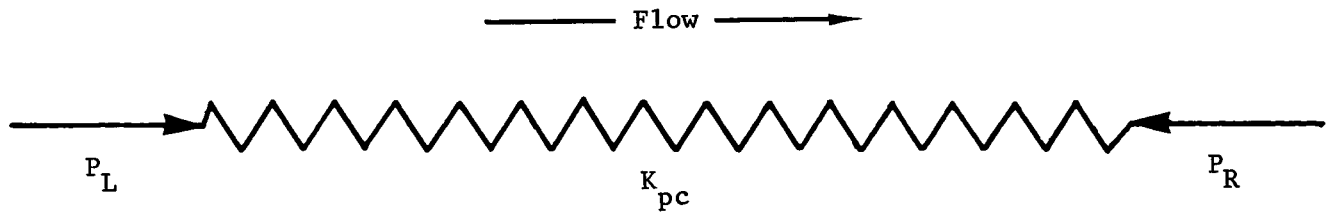

(a) Global resistance schematic of a piping component.

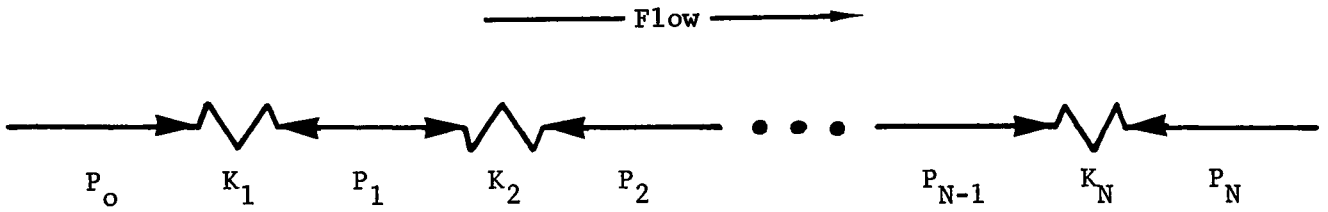

(b) Equivalent resistance schematic of a piping component.

Figure A-2. Resistance concept of a piping component loss.

where

$$P_{i-1} - P_i = K_i \rho_i u_i^2/2$$

with

ρ_i = effective density within unit i

u_i = effective velocity through unit i .

Since

$$\rho_i u_i^2 = \dot{m}^2/\rho_i A_i^2$$

where

$\dot{m}_i$ = mass flow rate through unit i

A_i = flow area of unit i

then the application of mass conservation (assuming steady state),

$$\dot{m}_{pc} = \dot{m}_i, \quad i = 1, 2, \cdots, N$$

with the previous relationships, yields the following:

$$K_{pc}/\rho_{pc} A_{pc}^2 = \sum_{i=1}^{N} (K_i/\rho_i A_i^2) \ .$$

The above expression will determine the K_i's, with the following known parameters:

ρ_i, $i = 1, 2, \cdots, N$

A_i, $i = 1, 2, \cdots, N$

K_{pc},

ρ_{pc}, $(1/N) \sum_{i=1}^{N} \rho_i$

A_{pc}, $(1/N) \sum_{i=1}^{N} A_i$

and the assumption of a desired shape distribution for the K_i's [Figure A-3(a)]. This last condition may be expressed as

$$K_i = \alpha_{ij} K_j, \quad i = 1, 2, \cdots, j, \cdots, N$$

j fixed

where

$\alpha_{ii} = 1$

α_{ij} $(i \neq 1)$ are shape factors, selected to match the desired distribution shape [see Figure A-3(b)].

For convenience, j may be selected such that

$$K_j = \max(K_i)$$

hence,

$$0 \leq \alpha_{ij} \leq 1 .$$

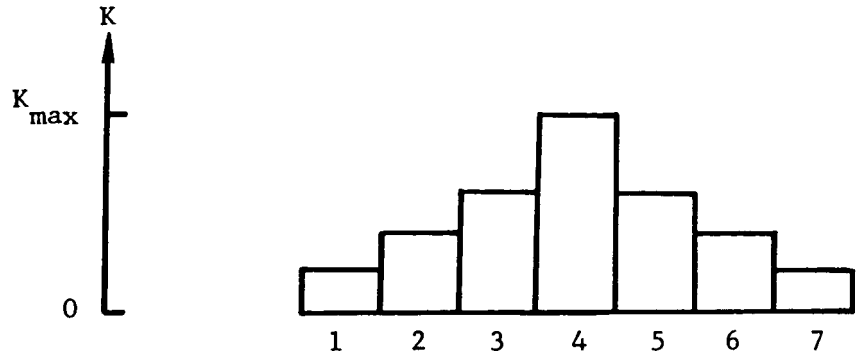

(a) Typical distribution shape of K_i for N = 7.

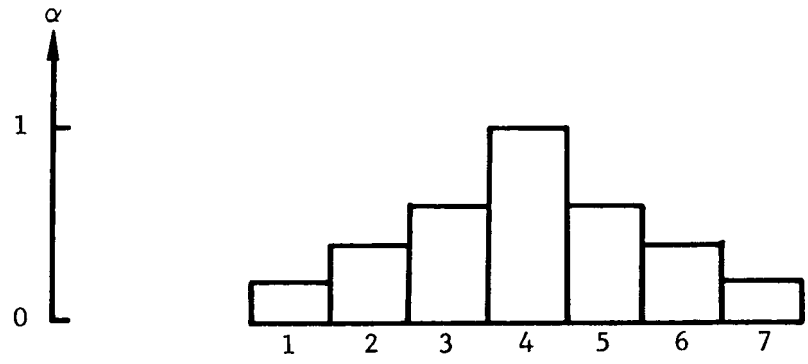

(b) Corresponding distribution of α associated with (a).

Figure A-3. Example of an assumed distribution of K_i.

Under these conditions,

$$K_j = \frac{K_{pc}/\rho_{pc} A_{pc}^2}{\sum_{i=1}^{N} (\alpha_{ij}/\rho_i A_i^2)}$$

or, alternatively,

$$K_j = \frac{N^3 K_{pc}}{\left[\sum_{i=1}^{N} \rho_i\right] \left[\sum_{i=1}^{N} (A_i)^2\right] \left[\sum_{i=1}^{N} (\alpha_{ij}/\rho_i A_i^2)\right]}$$

and

$$K_i = \alpha_{ij} K_j ; \quad i = 1, 2, \cdots, N .$$

APPENDIX B
SIMULATION OF A FEEDWATER SHUTDOWN EVENT

B.1 INTRODUCTION

One typical steam generator configuration in power plant facilities incorporates six feedwater pipes, manifolded into two three-feedpipe branches. Figure B-1 illustrates one of these branches, and its orientation to the steam generator. The branch is a combination of three feedpipes and three intra-branch pipes, linked together by two tee junctions and one reducer; the combination includes a number of bends and a gate valve.*

At the upstream end of the feedwater branch, a fast-acting check valve provides the means of quickly isolating that section from the remainder of the feedwater system. This capability affords protection to the branch in the event of an upstream disturbance (e.g., feedwater pump trip), or protection to the upstream system in the event of a disturbance in the branch or steam generator. However, the necessarily rapid closure of the check valve (60 ms) causes water hammers to propagate, both upstream and downstream, through the previously steady-state feedwater pipe flows. These pressure pulses can produce transient forces in the piping system which are far in excess of the steady-state forces associated with normal feedwater operation. Thus, the design of the feedwater system must take into account the magnitude, direction, and location of water hammer forces associated with a check valve closure.

This Appendix addresses one aspect of providing information related to the water hammers created by the rapid closure of the check valve. In particular, it describes the construction of a numerical simulation of the unsteady flow set up in the pipes of one feedwater branch. The construction

*In this event, the gate valve remains fully open, and thus is only a source of flow loss.

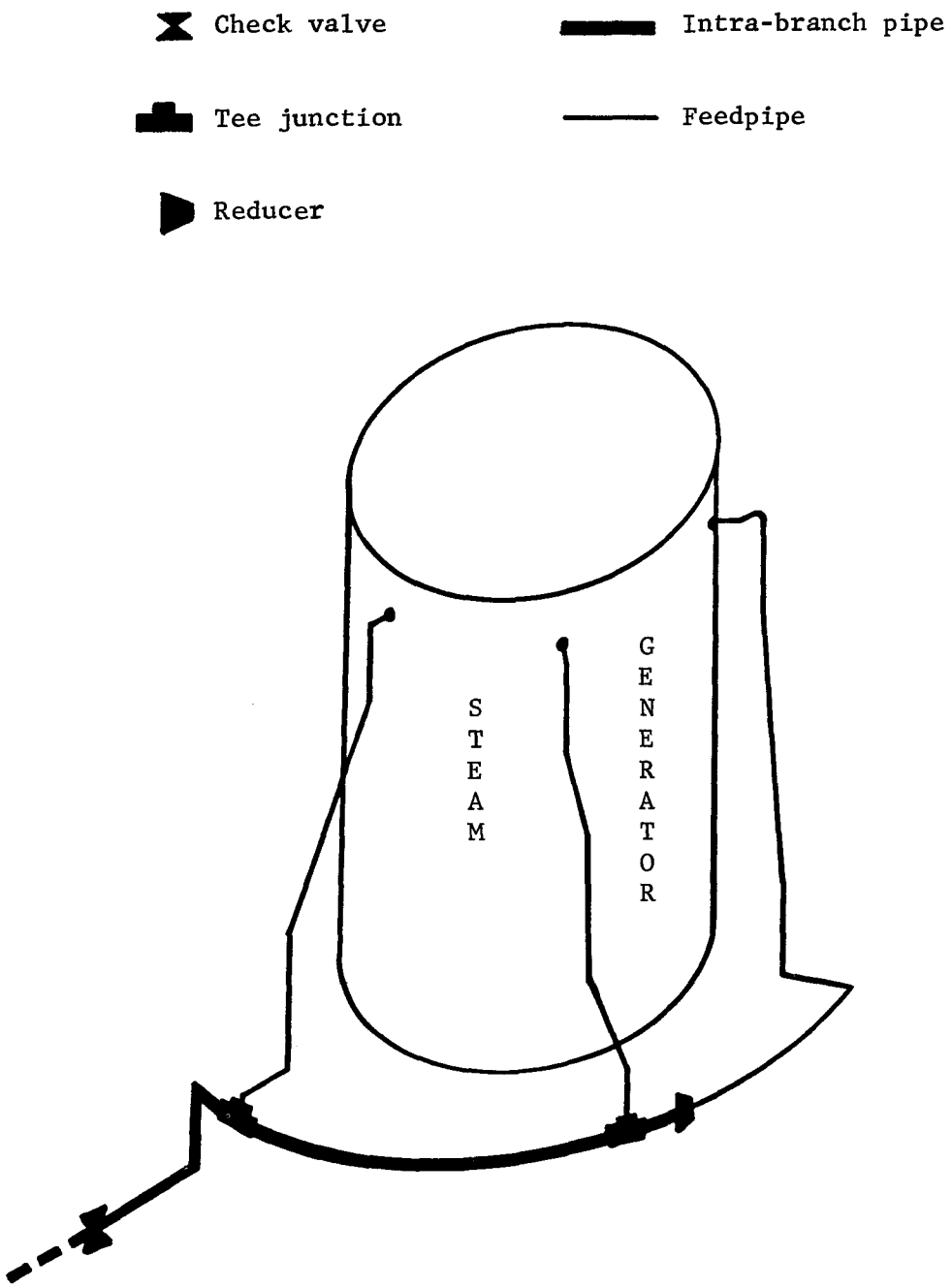

Figure B-1. Feedwater branch configuration for a steam generator.

utilizes the concepts that were discussed in the main body of this report. It illustrates the application of those concepts to produce an analysis that retains the essential features of geometry and flow losses, as well as time-dependent fluid mechanics.

B.2 CONSTRUCTION OF NUMERICAL SIMULATION

The feedwater shutdown simulation incorporates the one-dimensional, hydro version of STEALTH with control volume models for the check valve, the tee junctions, and the reducer. In addition, the simulation includes the effects of flow losses associated with pipe friction and piping components (including elbows). Figure B-2 depicts, schematically, the computational grids, control volumes, and boundary conditions that model one feedwater branch of the steam generator. The control volumes, grid 2 through grid 7, and the downstream pressure boundaries model the actual feedwater branch. This includes the closing check valve, two tee junctions, reducer, six sections of pipe (involving three intra-branch pipes modeled by grids 2, 4, and 6, and three feedpipes modeled by grids 3, 5, and 7), bend losses, gate valve loss, and downstream pressure boundaries. The upstream pressure boundary and grid 1 are designed to eliminate upstream transients from passing through the check valve during the time of its closure; hence, the transient effects generated in the feedwater branch are due only to the action of the valve in conjunction with the initial conditions, branch geometry, and the downstream pressure boundaries.

Figure B-3 illustrates the pertinent details of the control volumes. The maximum flow diameter of the check valve is 1.45 ft. Its flow area decreases linearly with time, attaining full closure in 60 ms. Each tee junction possesses through-run flow diameters of 1.45 ft, and a branch flow diameter of 0.92 ft. The reducer is a junction connecting a flow diameter of 1.45 ft with a flow diameter of 0.92 ft.

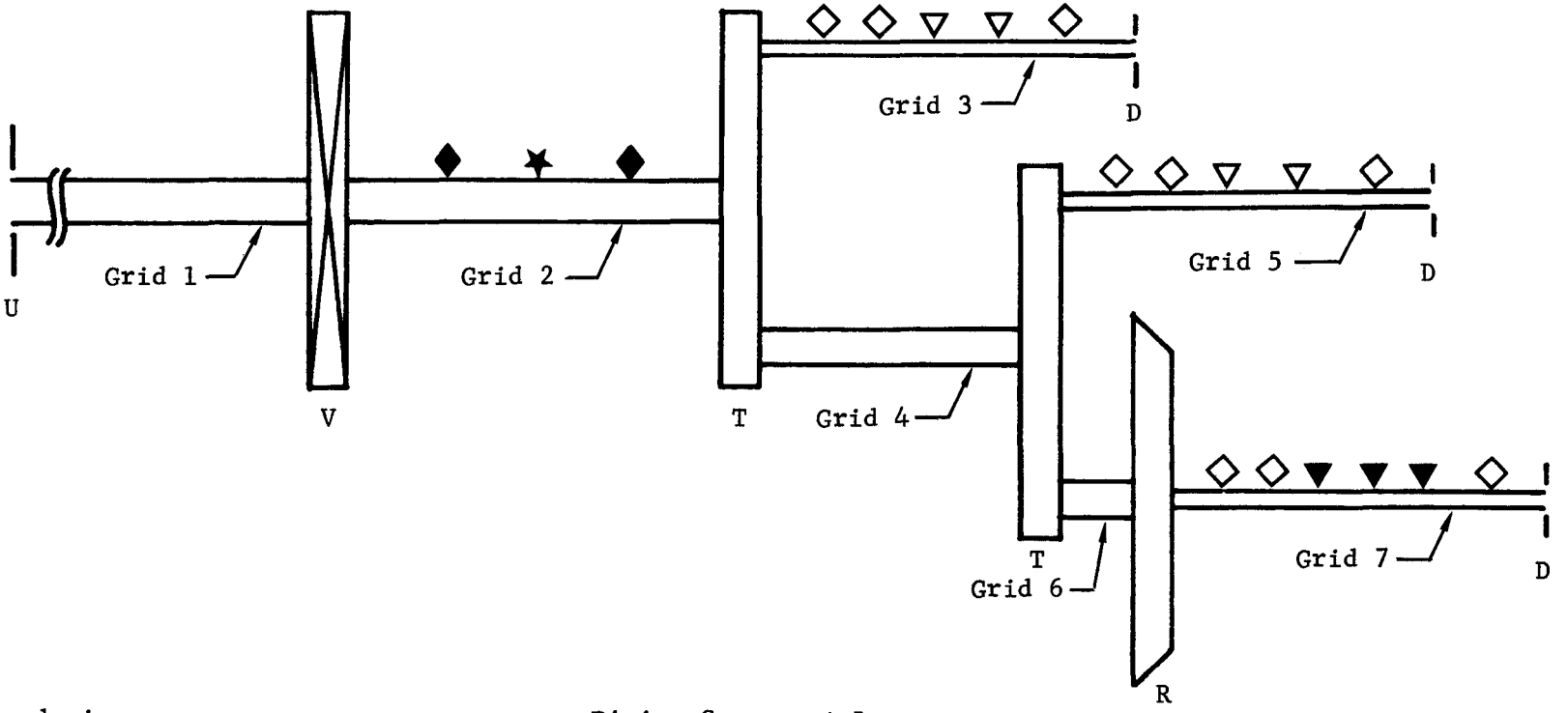

Boundaries

U — upstream pressure boundary

D — downstream pressure boundary

Control Volumes

V — check valve

T — tee junction

R — reducer

Piping Component Losses

◆ — 90° short radii elbows

◇ — 90° long radii elbows

▼ — 45° long radii elbows

▽ — 30° long radii elbows

★ — gate valve

Figure B-2. Simulation schematic of feedwater shutdown configuration.

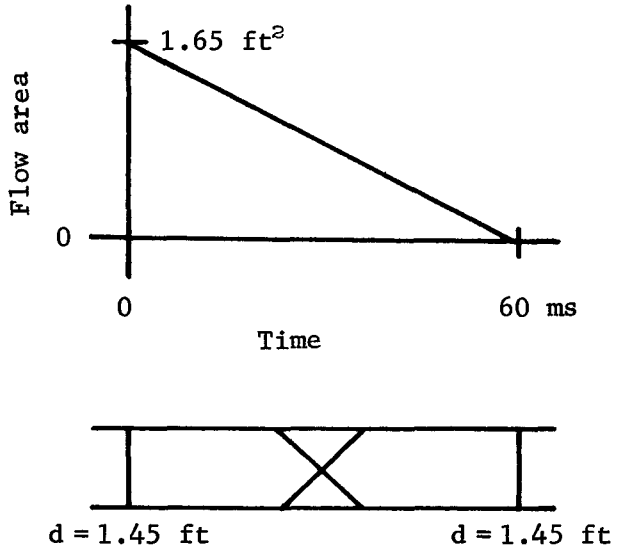

(a) Closing check valve.

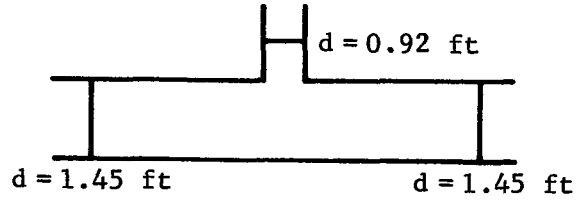

(b) Tee junction

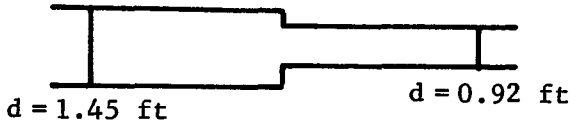

(c) Reducer.

Figure B-3. Control volumes for feedwater shutdown simulation.

The seven computational grids have the following characteristics:

- Grid #1
  - * upstream of the check valve
  - * 48 zones
  - * nodes 1 through 49
  - * 1.45-ft flow diameter
  - * coordinates from -420 ft to 0 ft
  - * length of 420 ft
  - * constant pressure boundary at node 1
  - * check valve at node 49
  - * pipe friction losses, $f = 0.012$

- Grid #2
  - * between the check valve and the first tee junction
  - * 18 zones
  - * nodes 50 through 68
  - * 1.45-ft flow diameter
  - * coordinates from 0 ft to 26.09 ft
  - * length of 26.09 ft
  - * check valve at node 50
  - * first tee at node 68
  - * pipe friction losses, $f = 0.012$
  - * check valve losses, $K_{pc} = 0.93$
  - * two 90^{o} short radii elbow losses, $K_{pc} = 0.24$/elbow
  - * gate valve losses, $K_{pc} = 0.096$

- Grid #3
  - * between the first tee junction and the pressure dome of the steam generator
  - * 28 zones
  - * nodes 69 through 97
  - * 0.92-ft flow diameter

* coordinates from 26.09 ft to 67.20 ft
* length of 41.11 ft
* first tee junction at node 69
* constant pressure dome boundary at node 97
* pipe friction losses, $f = 0.013$
* tee junction losses, $K_{pc})_{fwd} = 2.63$ and $K_{pc})_{rev} = 2.99$
* three 90^{o}-long radii elbow losses, $K_{pc} = 0.182$/elbow
* two 30^{o}-long radii elbow losses, $K_{pc} = 0.111$/elbow

- Grid #4

  * between the first and second tee junctions
  * 21 zones
  * nodes 98 through 119
  * 1.45-ft flow diameter
  * coordinates from 26.09 ft to 57.59 ft
  * length of 31.50 ft
  * first tee run at node 98
  * second tee at node 119
  * pipe friction losses, $f = 0.012$
  * tee run losses, $K_{pc} = 0.26$

- Grid #5

  * between the second tee junction and the pressure dome of the steam generator
  * 31 zones
  * nodes 120 through 151
  * 0.92-ft flow diameter
  * coordinates from 57.59 ft to 103.26 ft
  * length of 45.67 ft
  * second tee junction at node 120
  * constant pressure dome boundary at node 151
  * pipe friction losses, $f = 0.013$
  * tee junction losses, $K_{pc})_{fwd} = 2.63$ and $K_{pc})_{rev} = 2.99$

* three 90^{o}-long radii elbow losses, $K_{pc} = 0.182$/elbow
* two 30^{o}-long radii elbow losses, $K_{pc} = 0.111$/elbow

- Grid #6
  * between the second tee junction and the reducer
  * 3 zones
  * nodes 152 through 155
  * 1.45-ft flow diameter
  * coordinates from 57.59 ft to 61.93 ft
  * length of 4.34 ft
  * second tee run at node 152
  * reducer at node 155
  * pipe friction losses, $f = 0.012$
  * tee run losses, $K_{pc} = 0.26$

- Grid #7
  * between the reducer and the pressure dome of the steam generator
  * 44 zones
  * nodes 156 through 200
  * 0.92-ft flow diameter
  * coordinates from 61.93 ft to 126.85 ft
  * length of 64.92 ft
  * reducer at node 156
  * constant pressure dome boundary at node 200
  * pipe friction losses, $f = 0.013$
  * three 90^{o}-long radii elbow losses, $K_{pc} = 0.182$/elbow
  * three 45^{o}-long radii elbow losses, $K_{pc} = 0.129$/elbow
  * reducer losses, $K_{pc}\big)_{fwd} = 1.85$ and $K_{pc}\big)_{rev} = 2.21$

The locations of the loss coefficients are assigned as follows:

- Pipe Friction Losses
  - * f = 0.012 to all nodes in grids 1, 2, 4, and 6
  - * f = 0.013 to all nodes in grids 3, 5, and 7

- Piping Component Loss Factors
  - * check valve to node 52
  - * gate valve to node 64
  - * reducer to node 156
  - * tee junctions to nodes 69 and 120
  - * tee runs to nodes 98 and 152
  - * 90^{o} short radii elbows to nodes 54 and 66
  - * 90^{o} long radii elbows to nodes 72, 85, 95, 122, 127, 149, 161, 171, and 198
  - * 30^{o} long radii elbows to nodes 81, 87, 130, and 134
  - * 45^{o} long radii elbows to nodes 178, 185, and 195

The node position assignments of component losses in the simulation configuration correspond approximately to the locations of the piping components in the feedwater branch.

The fluid medium is subcooled water. It is characterized as follows:

- 360,000 psi bulk modulus
- 1019 psia reference pressure
- 325 psia saturation pressure
- 56.44 lb_m/ft^3 reference density
- linear elastic material, where the pressure is not permitted to fall below the saturation pressure (to assure a reasonable approximation to the subcooled phase).

There are two types of initial/boundary conditions. The first are independent, and are assigned through input data. These are the:

- downstream dome pressure boundary, assigned a value of 1019 psia
- pipe lengths and piping component locations
- initial flow velocity in the three feedpipes with 0.92-ft diameters, assigned a value of 18.319 ft/sec.

The second type of initial/boundary conditions are dependent, and must satisfy mass and energy conservation in conjunction with the material model, the control volumes, flow losses (when present), and the independent conditions. This second type includes the:

- initial pressure profiles in the grids
- initial density profiles in the grids
- initial velocities in the intra-branch pipe grids and the pipe grid upstream of the check valve
- upstream pressure boundary.

In particular, when flow losses are in effect, the initial pressure and density vary along the pipe grids. The simulation code determines the dependent initial/boundary conditions from the input data of the independent conditions.

During the simulation, rezoning maintains the position consistency between the material frame grid zones and the fixed control volume models. The algorithm periodically returns each grid node* to its original (Eulerian) position. The nodes that are interior to the feedwater branch return under the constraints of mass conservation and energy conservation, while the exterior boundary nodes return according to a constant pressure constraint. Also, the algorithm adjusts the velocities of the rezoned nodes to be consistent with the velocity profiles defined by their neighboring nodes.

*But no two adjacent nodes are rezoned simultaneously.

Figure B-4 displays the input data which define the feedwater shutdown event. It involves the standard input package for the STEALTH code. The loss coefficients are not part of the input package; they are loaded directly into DATA statements, located in the main program routine. Also loaded in this fashion are the pipe diameters associated with each node, and two integer scaling factors which control the magnitude of the effect of the loss coefficients. Figure B-5 illustrates these DATA statements.

B.3 DISCUSSION OF SIMULATION

The simulation begins when the check valve starts to close, and ends after one second of real time. This causes a severe rarefaction water hammer to race downstream, at the acoustic speed of the fluid (> 5400 ft/sec). (There will be no discussion of events created upstream of the check valve; that geometry, as discussed above, is not representative of the actual system and is outside the scope of interest of this simulation.) Since the farthest point in the feedwater branch is less than 130 ft from the check valve, the entire flow field transforms to transient behavior within 24 ms. More specifically, the initial pressure wave reaches and begins interacting with the first tee junction within the first 5 ms. From here, refracted waves reach the second tee and the first pressure dome boundary, within the next 8 ms. The refractions from the second tee junction reach the reducer in less than a millisecond, and the second pressure dome boundary within another 9 ms. The refractions from the reducer reach the third pressure dome boundary within the final 12 ms.

During this initial rarefaction sweep through the feedwater branch, reflected waves are also generated at the sites of piping components. These pulses superimpose on the initial wave patterns, rendering the fluid state extremely unsteady and characterized by many pressure waves at all locations. Figures B-6 through B-11 demonstrate the unsteady nature of the flow at three representative locations in the system. For a simulation with no losses in effect, Figure B-6 shows the pressure history at node 67 in grid #2, Figure B-7 shows the pressure history at node 100 in grid #4, and Figure B-8 shows the pressure history at node 158 in grid #7. Figures B-9 through B-11 show

```
TTL        FEEDWATER SHUTDOWN      SLUGS-FT-SEC
PRB
GRD        1.0                     49.0
GRD        2.0                     19.0
GRD        3.0                     29.0
GRD        4.0                     22.0
GRD        5.0                     32.0
GRD        6.0                     4.0
GRD        7.0                     45.0
END
MAT
I11        1.0
I12        1.0         1.0         1.0         2.0
I21        1.0         1.75
I22        1.0         1.0         146736.0    5.184 E+07
I23        1.0         -1.0        10.0
I36        1.0         46886.40
END
GPT
211        1.0         1.0                     -420.0
211        2.0         50.0                    0.0
211        3.0         69.0                    26.09
211        4.0         98.0                    26.09
211        5.0         120.0                   57.59
211        6.0         152.0                   57.59
211        7.0         156.0                   61.93
221        1.0         1.0         49.0
221        2.0         50.0        68.0
221        3.0         69.0        97.0
221        4.0         98.0        119.0
221        5.0         120.0       151.0
221        6.0         152.0       155.0
221        7.0         156.0       200.0
251        1.0         48.0        -420.0      0.0         0.94
242        2.0         18.0        0.0         26.09
242        3.0         28.0        26.09       41.11
242        4.0         21.0        26.09       31.50
242        5.0         31.0        57.59       45.67
242        6.0         3.0         57.59       4.34
242        7.0         44.0        61.93       64.92
END
```

Figure B-4. Input data for feedwater shutdown simulation.

```
ZON
311         1.0         1.0         49.0
311         2.0         50.0        68.0
311         3.0         69.0        97.0
311         4.0         98.0        119.0
311         5.0         120.0       151.0
311         6.0         152.0       155.0
311         7.0         156.0       200.0
321         1.0         1.0
321         2.0         1.0
321         3.0         1.0
321         4.0         1.0
321         5.0         1.0
321         6.0         1.0
321         7.0         1.0
322         1.0         1.00000260
322         2.0         1.00000260
322         3.0         1.0
322         4.0         0.99999801
322         5.0         1.0
322         6.0         0.99999525
322         7.0         1.0
331         1.0         22.1240074
331         2.0         22.1240074
331         3.0         18.319
331         4.0         14.7492706
331         5.0         18.319
331         6.0         7.37461499
331         7.0         18.319
381         1.0         1.0         1.0
381         2.0         2.0         96.0
381         3.0         97.0        97.0
381         4.0         98.0        150.0
381         5.0         151.0       151.0
381         6.0         152.0       199.0
381         7.0         200.0       200.0
382         1.0         1.0         2.0         2.0         1.0
382         2.0         1.0         2.0         1.0         1.0
382         3.0         1.0         2.0         2.0         1.0
382         4.0         1.0         2.0         1.0         1.0
382         5.0         1.0         2.0         2.0         1.0
382         6.0         1.0         2.0         1.0         1.0
382         7.0         1.0         2.0         2.0         1.0
END
```

Figure B-4. (continued)

```
BDY
421         1.0         2.0         5.0         1.0
421         49.0        7.0         5.0         4011.0
421         50.0        7.0         5.0         4012.0
421         68.0        7.0         5.0         3021.0
421         69.0        7.0         5.0         3022.0
421         97.0        2.0         5.0         2.0
421         98.0        7.0         5.0         3023.0
421         119.0       7.0         5.0         3031.0
421         120.0       7.0         5.0         3032.0
421         151.0       2.0         5.0         3.0
421         152.0       7.0         5.0         3033.0
421         155.0       7.0         5.0         2041.0
421         156.0       7.0         5.0         2042.0
421         200.0       2.0         5.0         4.0
422         1.0         1.0
422         2.0         2.0
422         3.0         3.0
422         4.0         4.0
431         1.0         1.0         0.0         3600.0
431         2.0         1.0         0.0         3600.0
431         3.0         1.0         0.0         3600.0
431         4.0         1.0         0.0         3600.0
432         1.0         146601.350
432         2.0         146736.0
432         3.0         146736.0
432         4.0         146736.0
471         1.0         1.45        1.45        27.5216606
471         2.0         1.45        0.92        1.45
471         3.0         1.45        0.92        1.45
471         4.0         1.45        0.92
END
TIM
511         0.0001
512         0.00001     1.0
513                     0.85
521         1.0         9999.0
END
EDT                                                         1.0
621         1.0         0.0         2.0         0.25
622         1.0         200.0
623         1.0         11.0
623         2.0         12.0
623         3.0         64.0
623         4.0         46.0
623         5.0         93.0
623         6.0         94.0
623         7.0         95.0
623         8.0         96.0
```

Figure B-4. (continued)

```
624         1.0
641         1.0         0.0         1.0         0.20
651         1.0         0.0         1.0         0.001
652         1.0         200.0
653         11.0        12.0        64.0        46.0        93.0        94.0
671         1.0         0.0         2.0         0.001
672         1.0         1.0         64.0        1.0         48.0
672         2.0         1.0         64.0        1.0         52.0
672         3.0         1.0         64.0        1.0         67.0
672         4.0         1.0         64.0        1.0         71.0
672         5.0         1.0         64.0        1.0         100.0
672         6.0         1.0         64.0        1.0         118.0
672         7.0         1.0         64.0        1.0         122.0
672         8.0         1.0         64.0        1.0         154.0
672         9.0         1.0         64.0        1.0         155.0
672         10.0        1.0         64.0        1.0         158.0
672         11.0        1.0         95.0        1.0         48.0
672         12.0        1.0         95.0        1.0         52.0
672         13.0        1.0         95.0        1.0         67.0
672         14.0        1.0         95.0        1.0         71.0
672         15.0        1.0         95.0        1.0         100.0
672         16.0        1.0         95.0        1.0         118.0
672         17.0        1.0         95.0        1.0         122.0
672         18.0        1.0         95.0        1.0         154.0
672         19.0        1.0         95.0        1.0         155.0
672         20.0        1.0         95.0        1.0         158.0
672         21.0        1.0         96.0        1.0         48.0
672         22.0        1.0         96.0        1.0         52.0
672         23.0        1.0         96.0        1.0         67.0
672         24.0        1.0         96.0        1.0         71.0
672         25.0        1.0         96.0        1.0         100.0
672         26.0        1.0         96.0        1.0         118.0
672         27.0        1.0         96.0        1.0         122.0
672         28.0        1.0         96.0        1.0         154.0
672         29.0        1.0         96.0        1.0         155.0
672         30.0        1.0         96.0        1.0         158.0
END
END
```

Figure B-4. (concluded)

```
 DATA DIA /68*1.45,29*0.92,22*1.45,32*0.92,4*1.45,45*0.92/
 DATA FRK /68*.012,29*.013,22*.012,32*.013,4*.012,45*.013/
 DATA XKL /51*0.0,.93,0.0,.24,9*0.0,.096,0.0,.24,2*0.0,2.6,0.0,.182
,.3*0.0,.182,5*0.0,.111,5*0.0,.111,7*0.0,.182,2*0.0,.26,21*0.0,2.6,
.0.0,.182,4*0.0,.182,2*0.0,.111,3*0.0,.111,14*0.0,.182,2*0.0,.26,3*
.0.0,1.85,4*0.0,.182,9*0.0,.182,6*0.0,.129,6*0.0,.129,9*0.0,.129,2*
.0.0,.182,53*0.0,.93,0.0,.24,9*0.0,.096,0.0,.24,2*0.0,3.0,0.0,.182,
.3*0.0,.182,5*0.0,.111,5*0.0,.111,7*0.0,.182,2*0.0,.26,21*0.0,3.0,0
.0,.182,4*0.0,.182,2*0.0,.111,3*0.0,.111,14*0.0,.182,2*0.0,.26,3*0
.0,2.21,4*0.0,.182,9*0.0,.182,6*0.0,.129,6*0.0,.129,9*0.0,.129,2*0
.0,.182,2*0.0/
 DATA LOSSF,LOSSK/0,0/
```

DIA:	pipe diameters
FRK:	pipe friction loss coefficients
XKL:	piping component loss coefficients
LOSSF:	scaling factor for friction coefficients
LOSSK:	scaling factor for component coefficients

Figure B-5. Data statements for feedwater shutdown simulation.

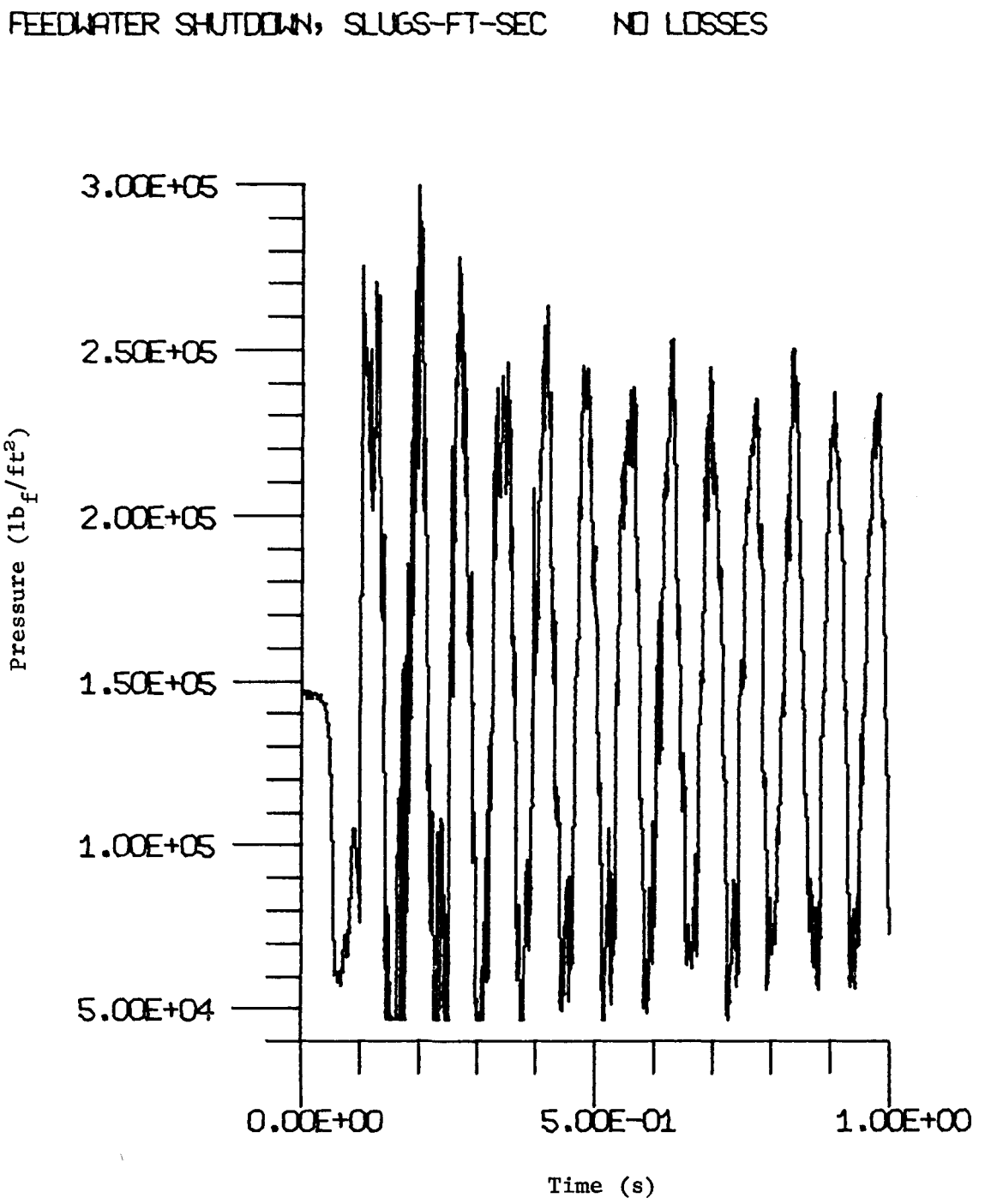

Figure B-6. Pressure time history at zone 67 for simulation with no loses (24.64 ft from check valve).

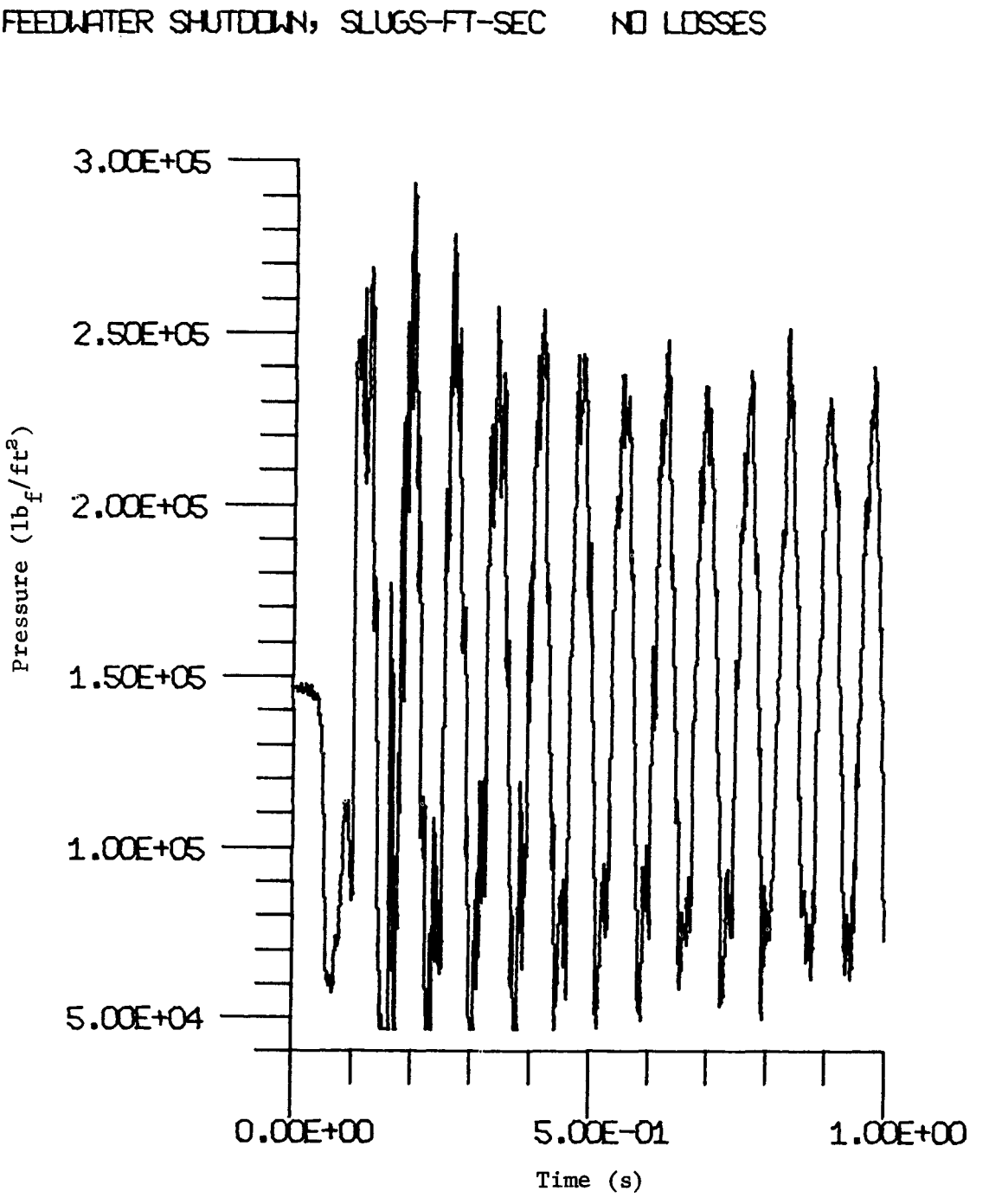

Figure B-7. Pressure time history at zone 100 for simulation with no losses (29.09 ft from check valve).

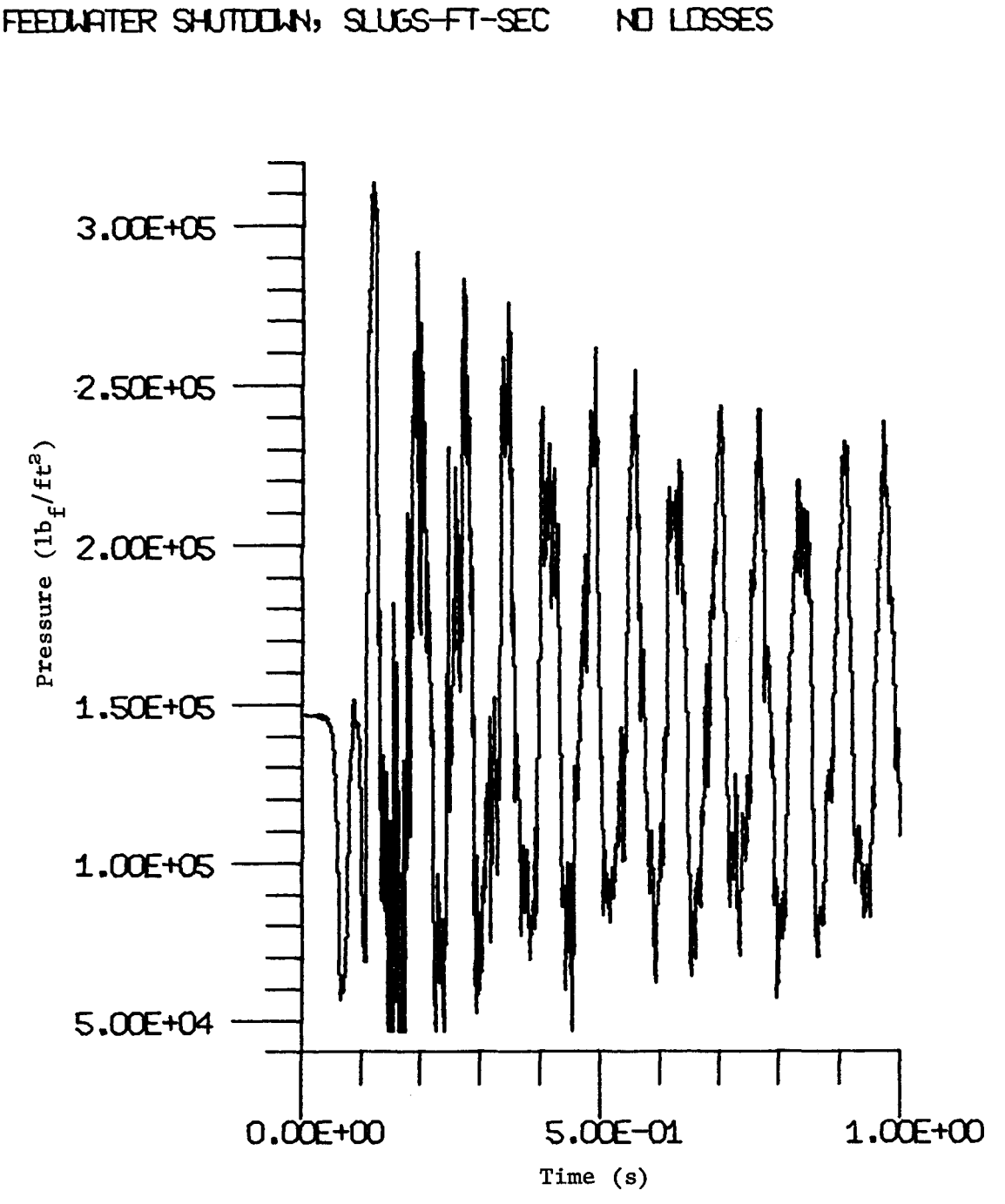

Figure B-8. Pressure time history at zone 158 for simulation with no losses (64.89 ft from check valve).

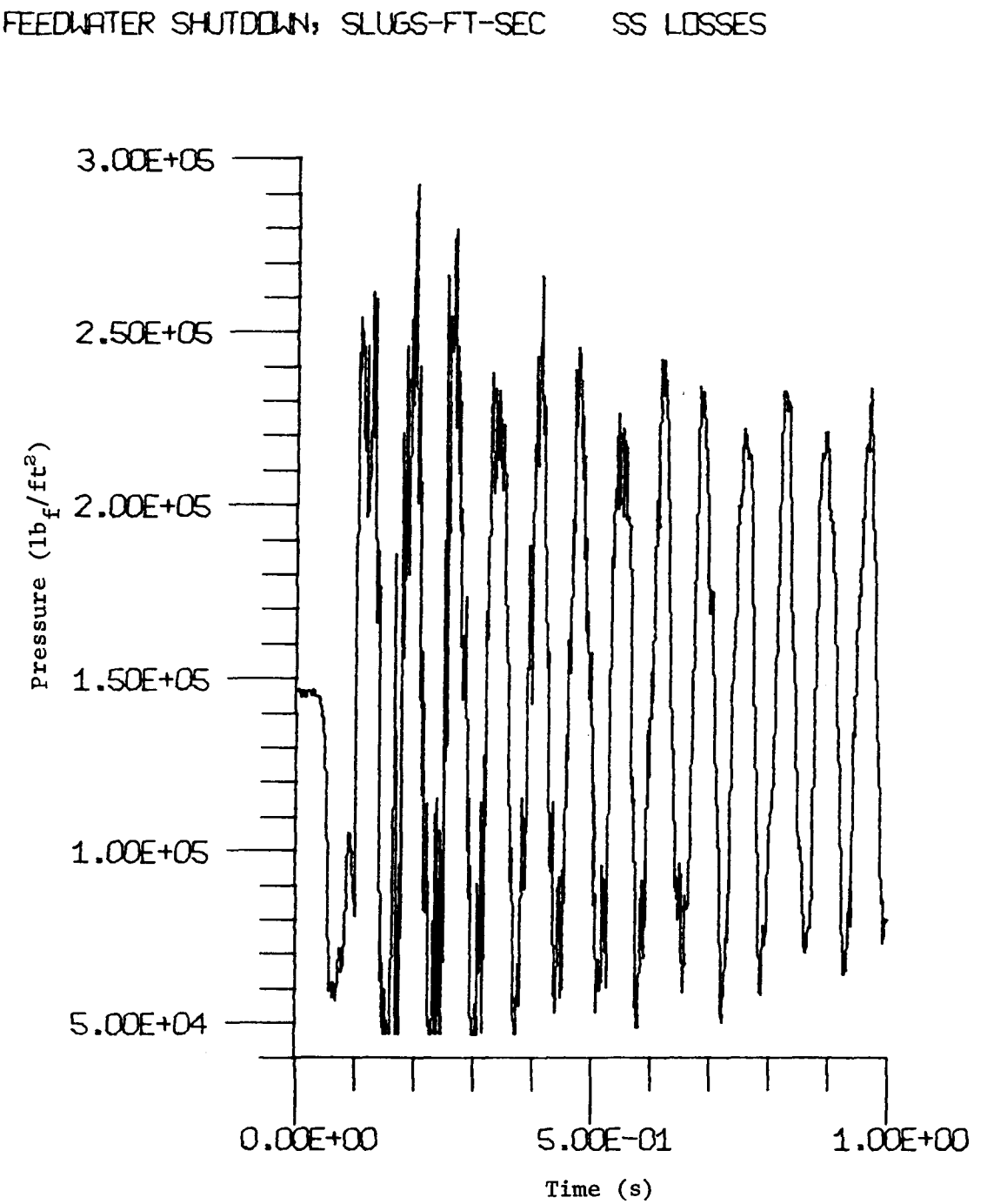

Figure B-9. Pressure time history at zone 67 for simulation with flow losses (25.64 fet from check valve).

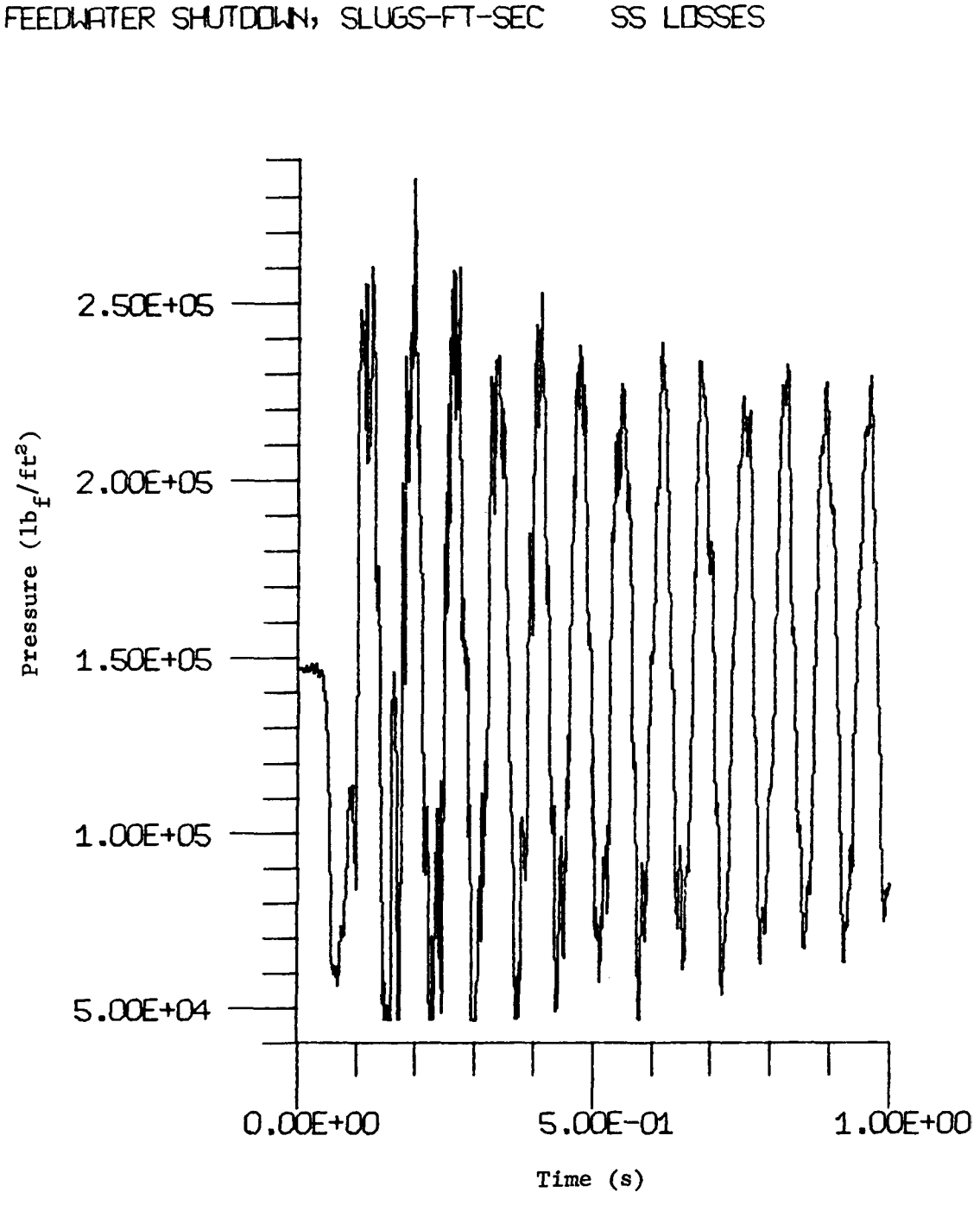

Figure B-10. Pressure time history at zone 100 for simulation with flow losses (29.09 ft from check valve).

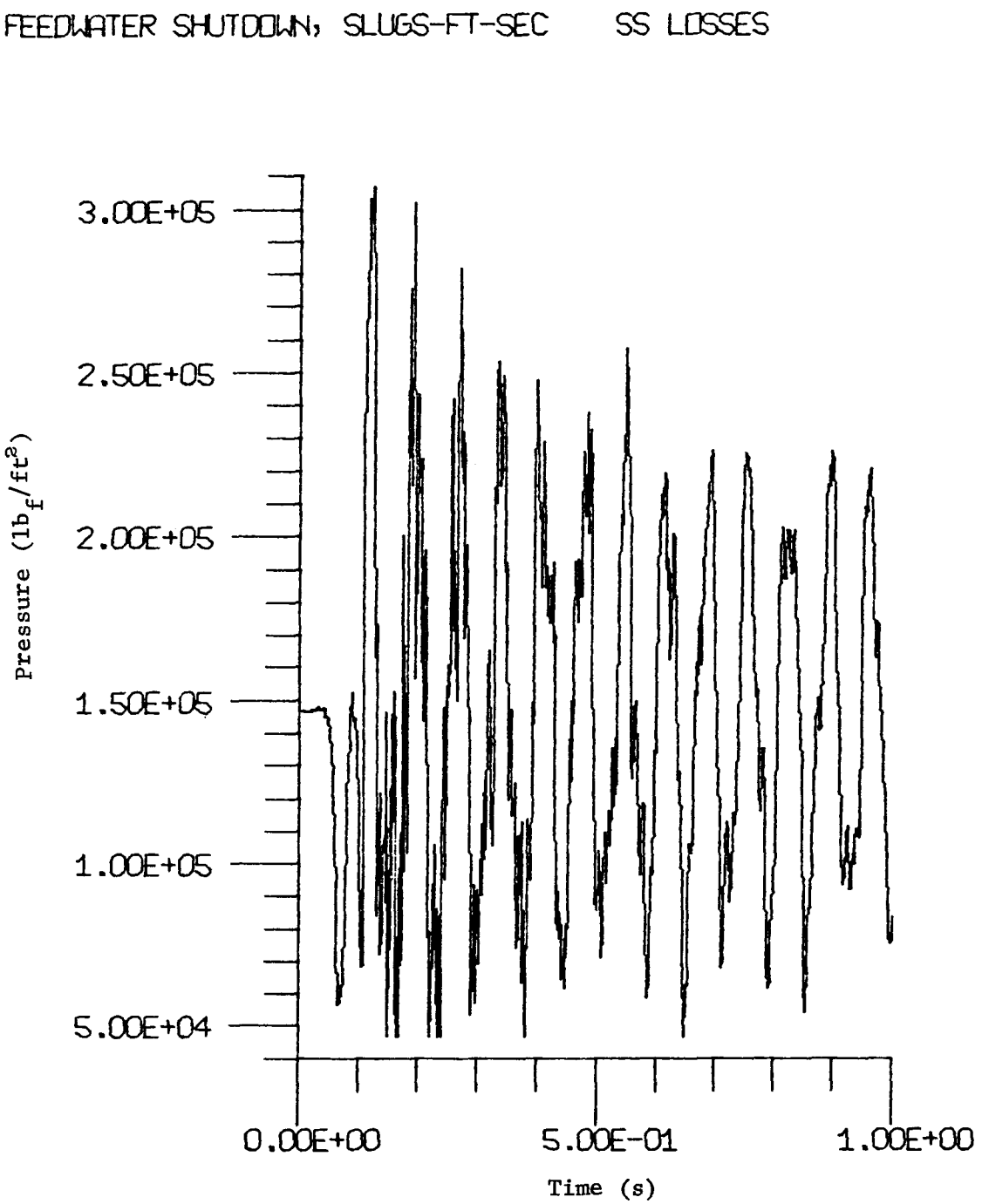

Figure B-11. Pressure time history at zone 158 for simulation with flow losses (64.89 ft from check valve).

the pressure histories at the same nodes for a simulation that included the effects of steady-state loss coefficients. Note that the effect of losses is to attenuate the pulses, somewhat. However, due to relatively small dynamic pressures associated with velocities that never exceed 24 ft/s, the effect of the losses on the pressure pulses is minimal.

B.4 CLOSURE

While these simulations reveal many interesting aspects of water hammer behavior, each a potential candidate for further research, the pragmatic objective of these simulations is to generate a data base from which the transient force histories can be resolved. For this purpose, the stream thrust function at each node and the rate of change of momentum in each zone are computed for each time cycle. These are stored on an archive tape for later processing according to the method described in Subsection 3.4 of the main body of this report.

These simulations require approximately 4400 time cycles to span one second of real time; hence, each simulation involves 880,000 node-cycle calculations. Memory requirements are 133 K (octal). On a CDC 7600 computer, these translate into 5 minutes of machine time and completely core-contained memory storage. Thus, for the feedwater shutdown simulations, STEALTH uses 0.34 CP ms per node-cycle.

APPENDIX C
SIMULATION OF A PRESSURIZER RELIEF LINE DISCHARGE EVENT

C.1 INTRODUCTION

For power plant facilities, it is standard practice to equip the pressurizers with safety relief systems. Figure C-1 depicts a common arrangement for the upstream piping of this system. Here, the relief line consists of a combination of pipes, bends, expanders, and a reducer. The segment connects with the pressurizer through a two-valve link. Normally, the safety valve is closed.

The safety valve can open in 40 ms to relieve excessive pressure within the pressurizer. This initiates a steam discharge from the pressurizer, through the relief line, to a quench tank. The rapid expansion of the steam through the safety valve propagates a steam hammer pulse through the previously quiescent environment within the relief line. Since it can produce intense fluid loads on the piping, this pulse is a design criterion for the structural analysis of the relief system. Moreover, since the hammer can affect the discharge flow rate of the steam, it is also a criterion for the performance analysis of the system.

This Appendix describes a numerical simulation of the pressurizer relief line discharge event through the upstream piping of the safety relief system. Since the event involves steam, which is not a subcooled fluid, and since the simulation was performed before the control volume models for piping components were operational, it is appropriate to mention why this topic appears in this report. Although the report emphasizes models for piping components, subcooled fluids, and piping simulations which incorporate these features, nevertheless an implied objective of this work is to demonstrate that the STEALTH codes can address a broad range of piping applications. Steam modeling demonstrates the ability of the codes to incorporate a homogeneous equilibrium simulation of two-phase effects. The

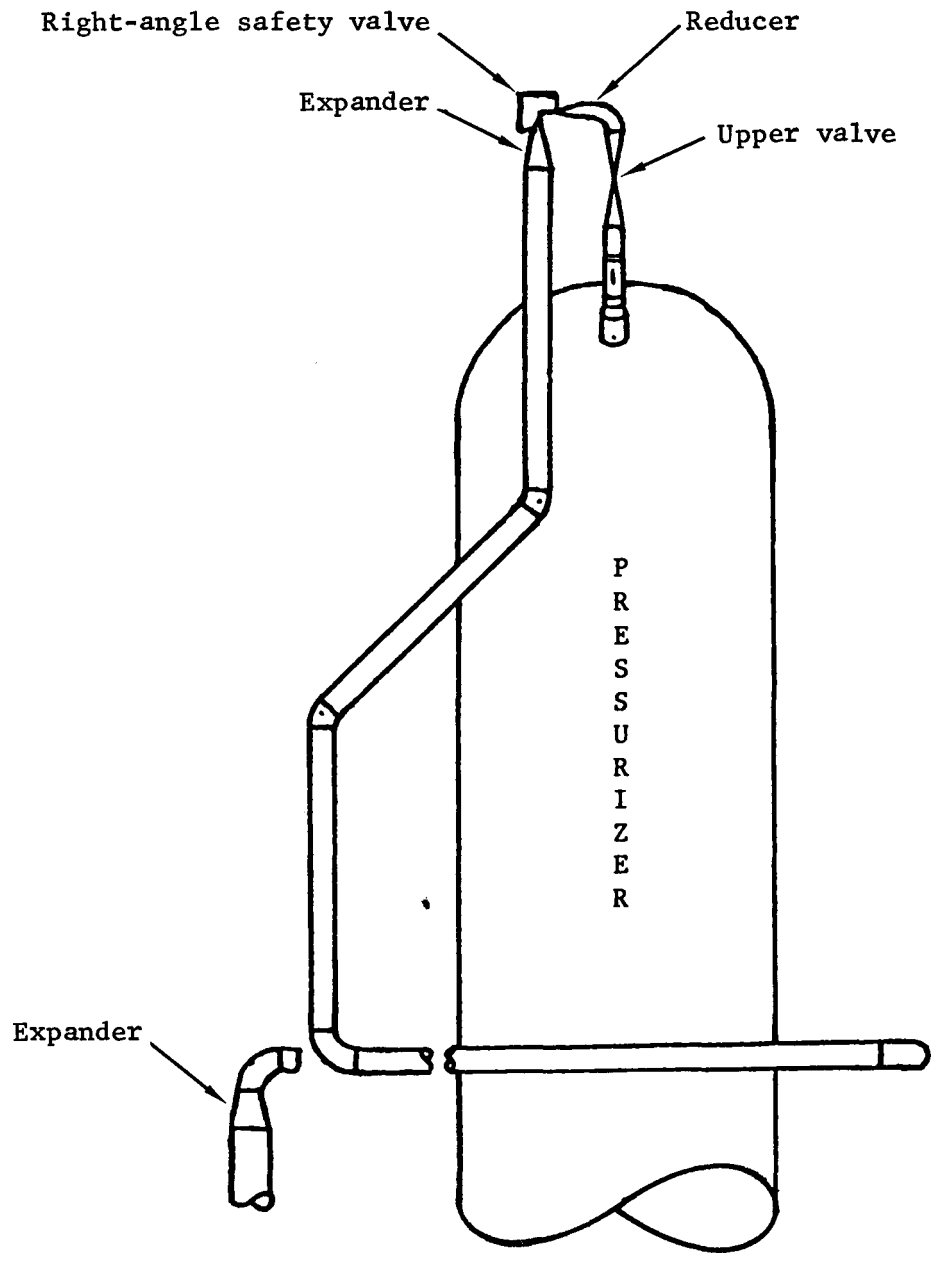

Figure C-1. Upstream segment of a pressurizer safety relief line.

modeling of the safety valve (including kinematics), the expanders, and the reducer, without recourse to control volume models, demonstrates the versatility of the STEALTH flume option: a standard variable flow area feature of the code. Thus, this Appendix provides a timely supplement to those concepts discussed in the main body of this report.

C.2 CONSTRUCTION OF SIMULATION

The simulation of the pressurizer relief line discharge uses the one-dimensional version of STEALTH in conjunction with its standard flume (variable circular flow area) option. This option simulates the time-dependent safety valve area as well as the fixed variable areas of the reducer and the expanders. In addition, the simulation accounts for the flow losses associated with pipe friction and the piping components.

Figure C-2 presents two representations of the computational grid that models the upstream segment of the safety relief line; the grid includes the safety valve and a brief, upstream section of pipe. In the upper representation, the ratio of the Y display scale* to the X display scale is 1.0. This indicates visually the actual geometric relationship between the flow path and the flow diameter. The representation also identifies the positions of the safety valve and the bends. The lower representation of the grid provides a visual indication of both the actual nodal composition of the grid and the geometric relationship between the various flow diameters. [It is a GRADIS (Reference C-1) plot, with a display scale ratio of ~ 277, of the initial data for the simulation.] The lower representation illustrates that the valve links the reducer (5.26-cm diameter to 3.94-cm diameter) to the upstream expander (3.94-cm diameter to 7.78-cm diameter), and that the downstream expander joins the pipe with the 7.78-cm diameter to the one with the 15.4-cm diameter. Also, the lower representation marks the fully open radius (1.97 cm) of the safety valve. The valve diameter varies linearly with time; it is fully open at 40 ms (see Figure C-3).

*The display scale of a coordinate is defined to be the length of the display coordinate per unit length of the simulated coordinate.

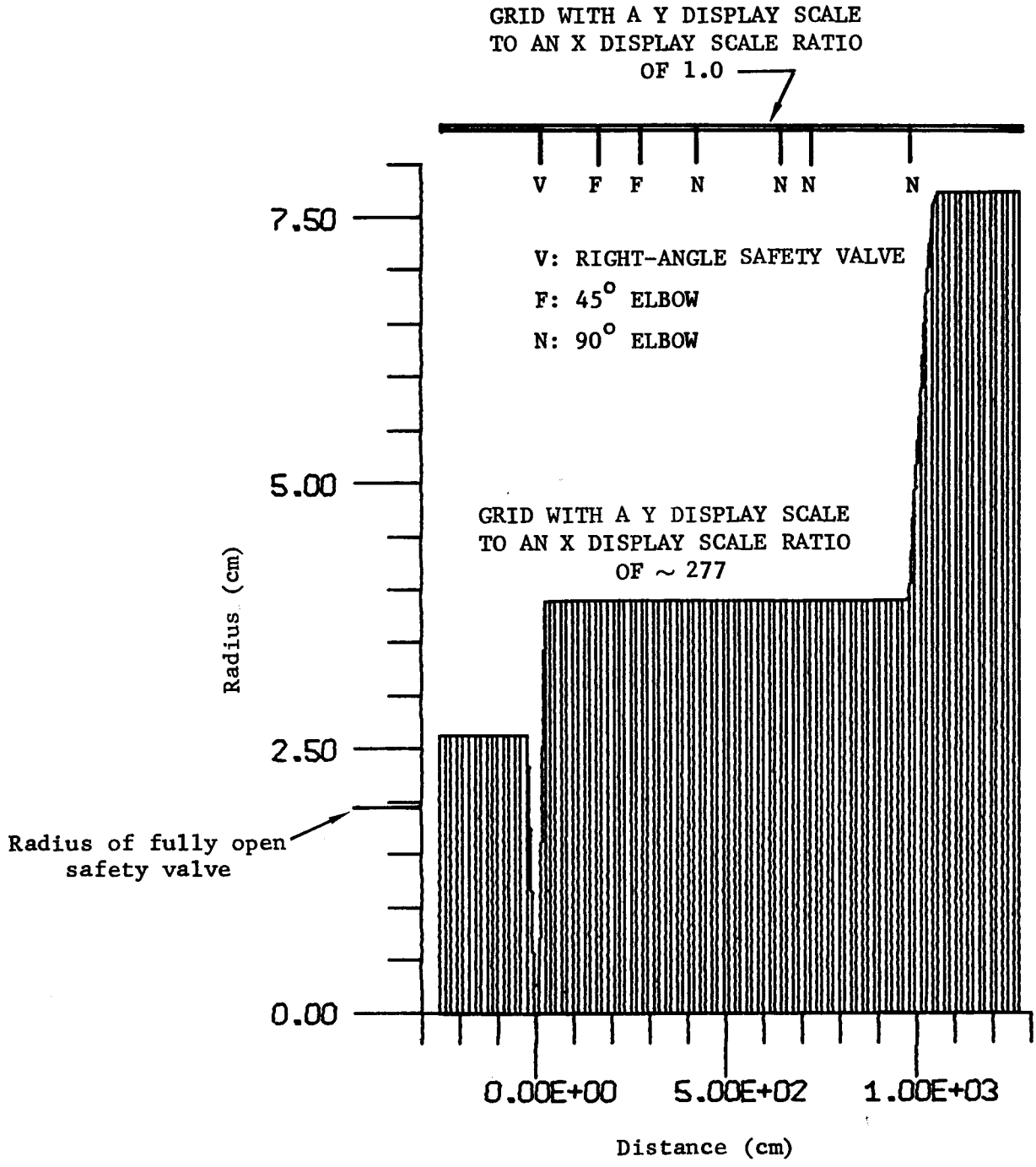

Figure C-2. Grids representing the upstream segment of a pressurizer safety relief line.

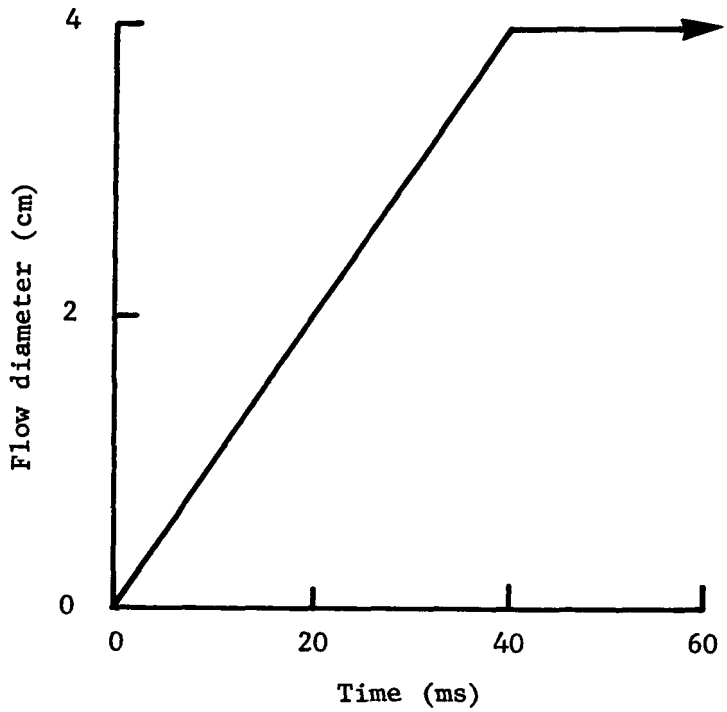

Figure C-3. Safety valve kinematics.

The computational grid is a sequential combination of the following sections:

- Section 1
  - * upstream of reducer
  - * 15 zones
  - * nodes 1 through 16
  - * 5.26-cm flow diameter
  - * coordinates from -252.42 cm to -22.82 cm
  - * length of 229.60 cm
  - * constant pressure boundary at node 1
  - * reducer begins at node 16
  - * pipe friction losses, f = 0.019

- Section 2
  - * reducer
  - * 1 zone
  - * nodes 16 and 17
  - * flow diameter change: 5.26 cm to 3.94 cm
  - * coordinates from -22.82 cm to -7.58 cm
  - * length of 15.24 cm
  - * 5.26-cm diameter pipe ends at node 16
  - * safety valve begins at node 17
  - * friction loss, f = 0.019

- Section 3
  - * safety valve
  - * 1 zone
  - * nodes 17 and 18
  - * full flow diameter of 3.94 cm at 40 ms
  - * coordinates from -7.58 cm to 7.76 cm
  - * length of 15.34 cm
  - * reducer ends at node 17

* first expander begins at node 18
* friction loss, $f = 0.019$
* safety valve loss, $K_{pc} = 2.85$

- Section 4

  * first expander
  * 1 zone
  * nodes 18 and 19
  * flow diameter change: 3.94 cm to 7.78 cm
  * coordinates from 7.76 cm to 22.9 cm
  * length of 15.14 cm
  * safety valve ends at node 18
  * 7.78-cm diameter pipe begins at node 19
  * friction loss, $0.018 \leq f \leq 0.019$

- Section 5

  * between expanders
  * 62 zones
  * nodes 19 through 81
  * 7.78-cm flow diameter
  * coordinates from 22.9 cm to 967.78 cm
  * length of 944.88 cm
  * first expander ends at node 19
  * second expander begins at node 81
  * pipe friction loss, $f = 0.018$
  * two 45^{o} elbow losses, $K_{pc} = 0.139$/elbow
  * four 90^{o} elbow losses, $K_{pc} = 0.252$/elbow

- Section 6

  * second expander
  * 6 zones
  * nodes 81 through 87
  * flow diameter change: 7.78 cm to 15.4 cm

* coordinates from 967.78 cm to 1059.22 cm
* length of 91.44 cm
* 7.78-cm diameter pipe ends at node 81
* 15.4-cm diameter pipe begins at node 87
* friction loss: $0.015 \leq f \leq 0.018$

- Section 7

  * downstream of second expander
  * 14 zones
  * nodes 87 through 101
  * 15.4-cm flow diameter
  * coordinates from 1059.22 cm to 1272.58 cm
  * length of 213.36 cm
  * second expander ends at node 87
  * constant pressure boundary at node 101
  * pipe friction loss, $f = 0.015$

The locations of the loss coefficients are assigned as follows:

- Pipe Friction Losses

  * $f = 0.019$ to nodes 1 through 18
  * $f = 0.018$ to nodes 19 through 82
  * $f = 0.017$ to node 83
  * $f = 0.016$ to nodes 84 and 85
  * $f = 0.015$ to nodes 86 through 101

- Piping Component Loss Factors

  * safety valve to node 18
  * 45^{o} elbows to nodes 28 and 35
  * 90 elbows to nodes 45, 59, 64, and 81

The node position assignments of component losses in the simulation configuration correspond approximately to the locations of the piping components in the relief line.

The fluid medium is a mixture of steam and water. The mixture is homogeneous, with its two phases in thermodynamic equilibrium. Its internal energy density (e) and relative volume (v) determine its pressure (p) and temperature (T), through a reduction of the saturation data (Reference C-2) that is shown on Figure C-4 (in the format of FORTRAN IV DATA STATEMENTS). In particular, there is a saturation point (i) in the data such that

$$E(i-1) \leq e \leq E(i)$$

where

$$E(j) \equiv ESATL(j) + VQ(j)[ESATV(j) - ESATL(j)]$$

and

$$VQ(j) \equiv [v - VSATL(j)]/[VSATV(j) - VSATL(j)]$$

with the remaining symbols as defined on Figure C-4. These conditions determine an energy interpolation ratio (er)

$$er \equiv [e - E(i-1)]/[E(i) - E(i-1)]$$

which reduces the saturation data to a p and v that are consistent with e and v.

$$p = PSAT(i-1) + er[PSAT(i) - PSAT(i-1)]$$

$$T = TSAT(i-1) + er[TSAT(i) - TSAT(i-1)]$$

The interpolation ratio will also reduce the data to evaluate the quality (x)

$$x \equiv (v - v_L)/(v_V - v_L)$$

```
 DATA (TSAT(L),L=1,44)  /0.0,.01,10.,20.,30.,40.,50.,60.,70.,80.,
190.,100.,110.,120.,130.,140.,150.,160.,170.,180.,190.,200.,210.,
2220.,230.,240.,250.,260.,270.,280.,290.,300.,310.,320.,330.,340.,
3350.,360.,370.,371.,372.,373.,374.,374.15/
 DATA (PSAT(L),L=1,44)  /.006108,.006112,1012271,.023368,.042418,
1.07375,.12335,.19919,.31161,.47358,.70109,1.01325,1.4327,1.9854,
22.7011,3.6136,4.7597,6.1804,7.9202,10.027,12.553,15.55,19.08,
323.202,27.979,33.48,39.776,46.941,55.052,64.191,74.449,85.917,
498.694,112.89,128.64,146.08,165.37,186.74,210.53,213.06,215.63,
5218.2,220.9,221.2/
 DATA (VSATL(L),L=1,44) /1.00021,1.0002101,1.0004,1.0018,1.0044,
11.0079,1.0121,1.0171,1.0228,1.029,1.0359,1.0435,1.0515,1.0603,
21.0697,1.0798,1.0906,1.1021,1.1144,1.1275,1.1415,1.1565,1.1726,
31.19,1.2087,1.2291,1.2512,1.2755,1.3023,1.3321,1.3655,1.4036,
41.4475,1.4992,1.562,1.639,1.741,1.894,2.22,2.29,2.38,2.51,2.8,
53.17/
 DATA (VSATV(L),L=1,44) /206288.,206146.,106422.,57836.,32929.,
119546.,12045.,7677.6,5045.3,3408.3,2360.9,1673.,1210.1,891.71,
2668.32,508.66,392.57,306.85,242.62,193.85,156.35,127.19,104.265,
386.062,71.472,59.674,50.056,42.149,35.599,30.133,25.537,21.643,
418.316,15.451,12.967,10.779,8.805,6.943,4.93,4.68,4.4,4.05,3.47,
53.17/
 DATA (ESATL(L),L=1,44) /-.0416,.000611,41.99,83.86,125.66,167.47,
1209.3,251.1,293.,334.9,376.9,419.1,461.3,503.7,546.3,589.1,632.2,
2675.5,719.1,763.1,807.5,852.4,897.7,943.7,990.3,1037.6,1085.8,
31135.,1185.2,1236.8,1290.,1345.,1402.,1462.,1526.,1596.,1672.,
41762.,1892.,1913.,1937.,1969.,2032.,2095./
 DATA (ESATV(L),L=1,44) /2501.,2501.,2519.,2538.,2556.,2574.,2592.,
12609.,2626.,2643.,2660.,2676.,2691.,2706.,2720.,2734.,2747.,2758.,
22769.,2778.,2786.,2793.,2798.,2802.,2803.,2803.,2801.,2796.,2790.,
32780.,2766.,2749.,2727.,2700.,2666.,2623.,2565.,2481.,2331.,2305.,
42273.,2230.,2146.,2095./
```

TSAT:	saturation temperature
PSAT:	saturation pressure
VSATL:	specific volume of saturated liquid
VSATV:	specific volume of saturated vapor
ESATL:	enthalpy of saturated liquid
ESATV:	enthalpy of saturated vapor

Figure C-4. Saturation data for steam/water vapor.

where

$$v_L = VSATL(i - 1) + er[VSATL(i) - VSATL(i - 1)]$$

$$v_V = VSATV(i - 1) + er[VSATV(i) - VSATV(i - 1)]$$

Initially, the conditions upstream of the safety valve are quiescent steam/water vapor at:

- 176.47 bars, pressure
- 7.84 cc/g, specific volume
- 2.3907×10^4 Merg/cc, energy density

while the conditions of the quiescent steam/water vapor downstream are

- 1.00035 bars, pressure
- 169.40 cc/g, specific volume
- 2.50603×10^4 Merg/cc, energy density

The upstream and downstream pressure boundaries remain at 176.47 bars and 1.00035 bars, respectively.

During the simulation, rezoning keeps the material frame grid zones within the relief line geometry. The algorithm periodically* returns each grid node to its original (Eulerian) position. The interior nodes rezone under the constraints of mass and energy conservations, while the two boundary nodes rezone according to a constant pressure constraint. Also, the algorithm adjusts the velocities of the rezoned nodes to be consistent with the velocity profiles defined by their neighboring nodes.

Figure C-5 displays the input data for the pressurizer relief line discharge event. It is the standard input package for the STEALTH code. The

*But no two adjacent nodes are rezoned simultaneously.

```
TTL     PRESSURIZER RELIEF LINE DISCHARGE
PRB                                                    1.0
SYM     4.0
MIN     100.0     1.0       E-3
GRD     1.0       1.0       101.
END
MAT                                                    1.0
111     1.0       6.0
121     1.0       1.0
END
GPT                                                    1.0
211     1.0       1.0       0.0       -251.0
221     1.0       1.0       101.0
243     1.0       100.      -251.42   15.24
212     1.0       -266.7    2.629     2.0
212     2.0       -20.32    2.629     1.0
212     3.0       -10.16    0.254     1.0
212     4.0       10.16     0.254     1.0
212     5.0       20.32     3.899     1.0
212     6.0       982.99    3.899     1.0
212     7.0       1046.0    7.709     1.0
212     8.0       1282.7    7.709     3.0
END
ZON                                                    1.0
311     1.0       1.0       17.0
321     1.0       1.0
322     1.0       7.8395    2.3907 E4
311     2.0       17.0      101.0
321     2.0       1.0
322     2.0       1693.7    25060.3
341     1.0       -176.473  -176.473  -176.473
341     2.0       -1.00035  -1.00035  -1.00035
381     1.0       1.0       1.0
381     2.0       2.0       100.0
381     3.0       101.0     101.0
382     1.0       1.0       2.0       2.0       1.0
382     2.0       1.0       2.0       1.0       1.0
382     3.0       1.0       2.0       2.0       1.0
END
BDY                                                    1.0
421     1.0       2.0       5.0       1.0
421     101.0     2.0       5.0       2.0
422     1.0       1.0
422     2.0       2.0
431     2.0       1.0       0.0       250.0
431     1.0       1.0       0.0       250.0
432     1.0       176.473
432     2.0       1.00035
481     1.0       1.0       2.0
481     2.0       3.0       4.0
481     3.0       5.0       8.0
```

Figure C-5. Input data for pressurizer relief line discharge simulation.

```
482         1.0       1.0       5.0       5.0
482         2.0       1.0       4.0       5.0       3.0
482         3.0       1.0       5.0       5.0
422         3.0       3.0
441 X-VEL   3.0       1.0       0.0       40.0
442 X-VEL   3.0       0.0       0.0       0.0       0.0
443 Y-VEL   3.0       1.0       0.0       40.0
444 Y-VEL   3.0       .04288    0.0       0.0       0.0
END
TIM                                                 1.0
511         .05
512         .004      1000.0
521         160.0     3.0
END
EDT                                                 1.0
621         1.0       0.0       200.0     25.0
621         2.0       0.0       40.0      40.0
622         1.0       101.0
623         1.0       11.0
623         2.0       12.0
623         3.0       64.0
623         4.0       46.0
623         5.0       51.0
623         6.0       13.0
623         7.0       42.0
623         8.0       21.0
623         9.0       71.0
623         10.0      96.0
623         11.0      41.0
623         12.0      24.0
623         13.0      25.0
623         14.0      45.0
623         15.0      66.0
623         16.0      91.0
624         1.0
641         1.0       0.0       200.0     50.0
651         1.0       0.0       200.0     0.5
652         1.0       101.0
653         11.0      12.0      13.0      71.0      64.0      46.0      91.0
653         51.0      66.0      96.0
671         1.0       0.0       200.0     1.0
672         21.0      1.0       71.0      1.0                 157.48
672         31.0      1.0       96.0      1.0                 157.48
672         22.0      1.0       71.0      1.0                 266.7
672         32.0      1.0       96.0      1.0                 266.7
672         23.0      1.0       71.0      1.0                 411.5
672         33.0      1.0       96.0      1.0                 411.5
672         24.0      1.0       71.0      1.0                 635.0
672         34.0      1.0       96.0      1.0                 635.0
672         25.0      1.0       71.0      1.0                 713.7
672         35.0      1.0       96.0      1.0                 713.7
672         26.0      1.0       71.0      1.0                 972.8
```

Figure C-5 (continued).

```
672        36.0       1.0        96.0       1.0              972.8
672        27.0       1.0        71.0       1.0              983.0
672        28.0       1.0        71.0       1.0              998.2
672        29.0       1.0        71.0       1.0              0.0
672        39.0       1.0        96.0       1.0              0.0
672        30.0       1.0        71.0       1.0              15.2
672        40.0       1.0        96.0       1.0              15.2
672        1.0        2.0        71.0       11.0             10.0
672        2.0        2.0        71.0       11.0             20.0
672        3.0        2.0        71.0       11.0             30.0
672        4.0        2.0        71.0       11.0             40.0
672        5.0        2.0        71.0       11.0             50.0
672        6.0        2.0        71.0       11.0             75.0
672        7.0        2.0        71.0       11.0             100.
672        8.0        2.0        71.0       11.0             125.
672        9.0        2.0        71.0       11.0             150.
672        10.0       2.0        71.0       11.0             200.
672        11.0       2.0        12.0       11.0             20.0
672        12.0       2.0        12.0       11.0             40.0
672        13.0       2.0        12.0       11.0             75.0
672        14.0       2.0        12.0       11.0             125.
672        15.0       2.0        12.0       11.0             200.
672        17.0       2.0        12.0       11.0             1.0
672        16.0       2.0        71.0       11.0             1.0
END
END
```

Figure C-5 (concluded).

loss coefficients are not part of the input package; in this simulation, they are calculated directly in the logic for fluid motion losses.*

C.3 DISCUSSION OF SIMULATION

The simulation begins when the safety valve starts to open, and ends after 160 ms of real time. The high pressure vapor, discharging through the opening valve, creates a steam hammer that propagates through the low pressure vapor of the relief line. This wave reaches the downstream boundary in 20 ms, traveling the $\sim$ 1280-cm distance at $\sim$ 62 cm/ms (Mach number of $\sim$ 1.45). During its transit downstream, the wave imparts a 20 cm/ms velocity to the fluid medium; it also spawns secondary waves as it interacts with the elbow losses and expanders. Upon reaching the downstream boundary, the steam hammer reflects as a rarefaction hammer. Traveling through the medium at the local acoustic speed of 42 cm/ms, against the 20 cm/ms fluid current, the rarefaction reaches the safety valve approximately 40 ms after the valve reaches its full open position. This wave also spawns additional waves, interacting with elbows, expanders, and the secondary waves created by the initial steam hammer. At this point, the flow field is a complex structure of unsteady wave motions.**

The velocity profiles of the flow field illustrate the effects of the geometry on fluid motion. Figure C-6 shows the flow conditions near the valve after 1 ms. The valve is the smallest (throat) area in the line; it restricts the flow velocity to the local acoustic speed (42 cm/ms). The peak velocity on Figure C-6 is 46 cm/ms, corresponding to supersonic conditions in the expander just downstream of the valve. Figure C-7 shows that at $\sim$ 20 ms, the entire relief line has an active flow field. The effects of the elbows are strikingly prominent as local velocity minima (virtual cusps), and the velocity increase through the second expander peaks at the initial

---

*Subsequent to this simulation, the loss coefficients are loaded directly into DATA statements that assign values to each node.

**The physics upstream of the safety valve will not be discussed.

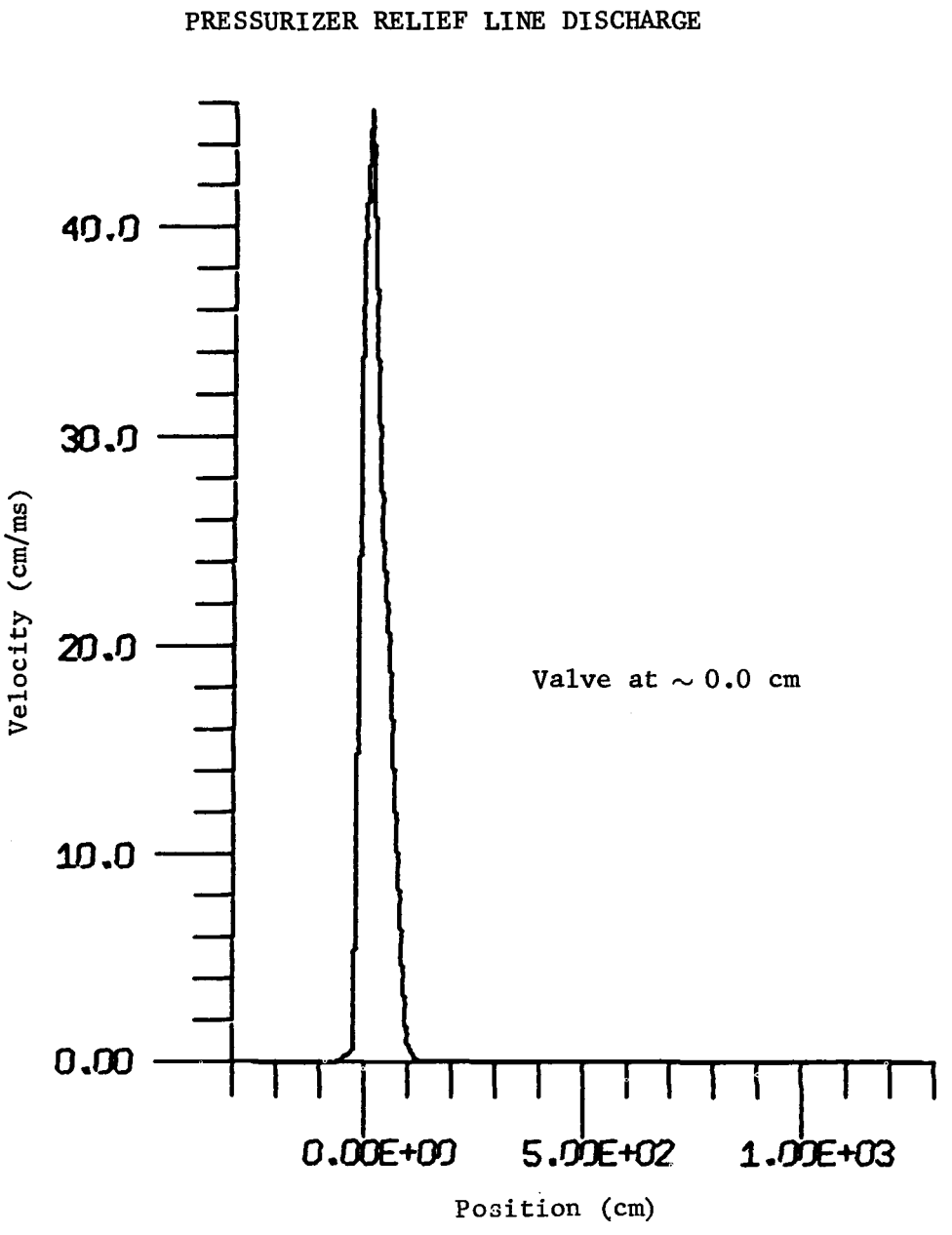

Figure C-6. Velocity profile at 1.0 ms.

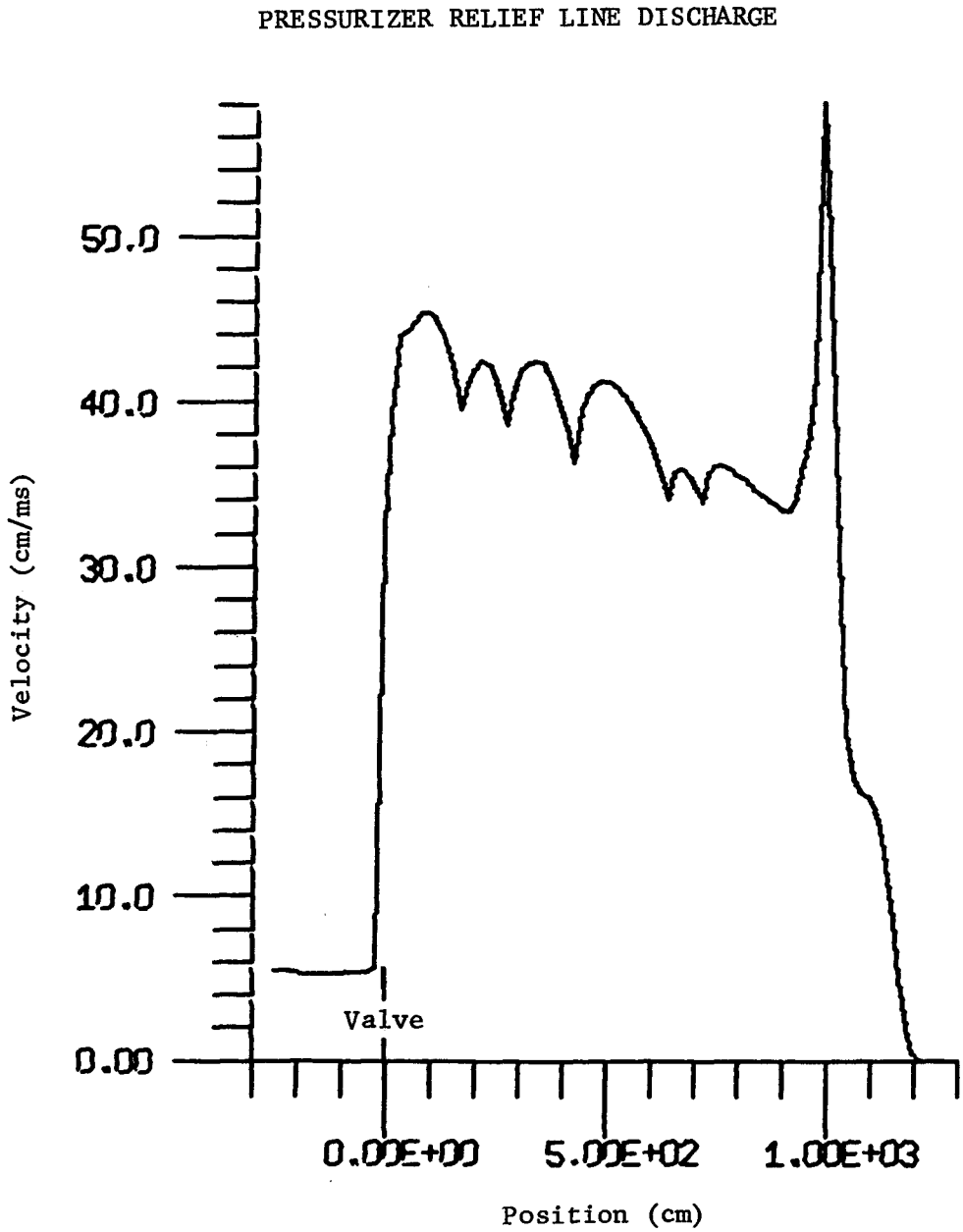

Figure C-7. Velocity profile at 20.0 ms.

steam hammer velocity ($\sim$ 62 cm/ms). Figures C-8 through C-10 display later velocity profiles. Figure C-8 shows that the effect of the rarefaction hammer at 40 ms has accelerated the flow to $\sim$ 85 cm/ms, and that the effects of the secondary waves have unchoked the valve; Figures C-9 and C-10 depict the sharp rise in velocity needed, at late times, to match the downstream pressure boundary.

Figures C-11 through C-15 show the fluid stress* profiles that correspond to the previously discussed velocity profiles. These show the progressive effects of the wave motions as they pressurize the relief line. In particular, they show the pressure cusps that are formed where elbow losses retard fluid motion, as well as the increase in fluid stress through the second expander.

Figures C-16 through C-23 display time histories of fluid stress at the various piping components in the relief line. The high frequency oscillations at the two expanders are not physical, but noisy numerics. This noise signals that, on the local time step scale, the code numerics cannot adjust fully to the relative suddenness of the expander area changes. However, on the global time scale, the oscillations are bounded, and do not destroy the simulation. This phenomenon is, in fact, one reason for modeling abrupt area changes with a control volume model which can respond instantaneously to flow conditions.

Figures C-24 through C-31 show the corresponding time histories of fluid loads at the piping components. They also display the same bounded high frequency oscillations. Again, however, the global histories are preserved.

*Fluid stress is defined as the negative of hydrostatic pressure.

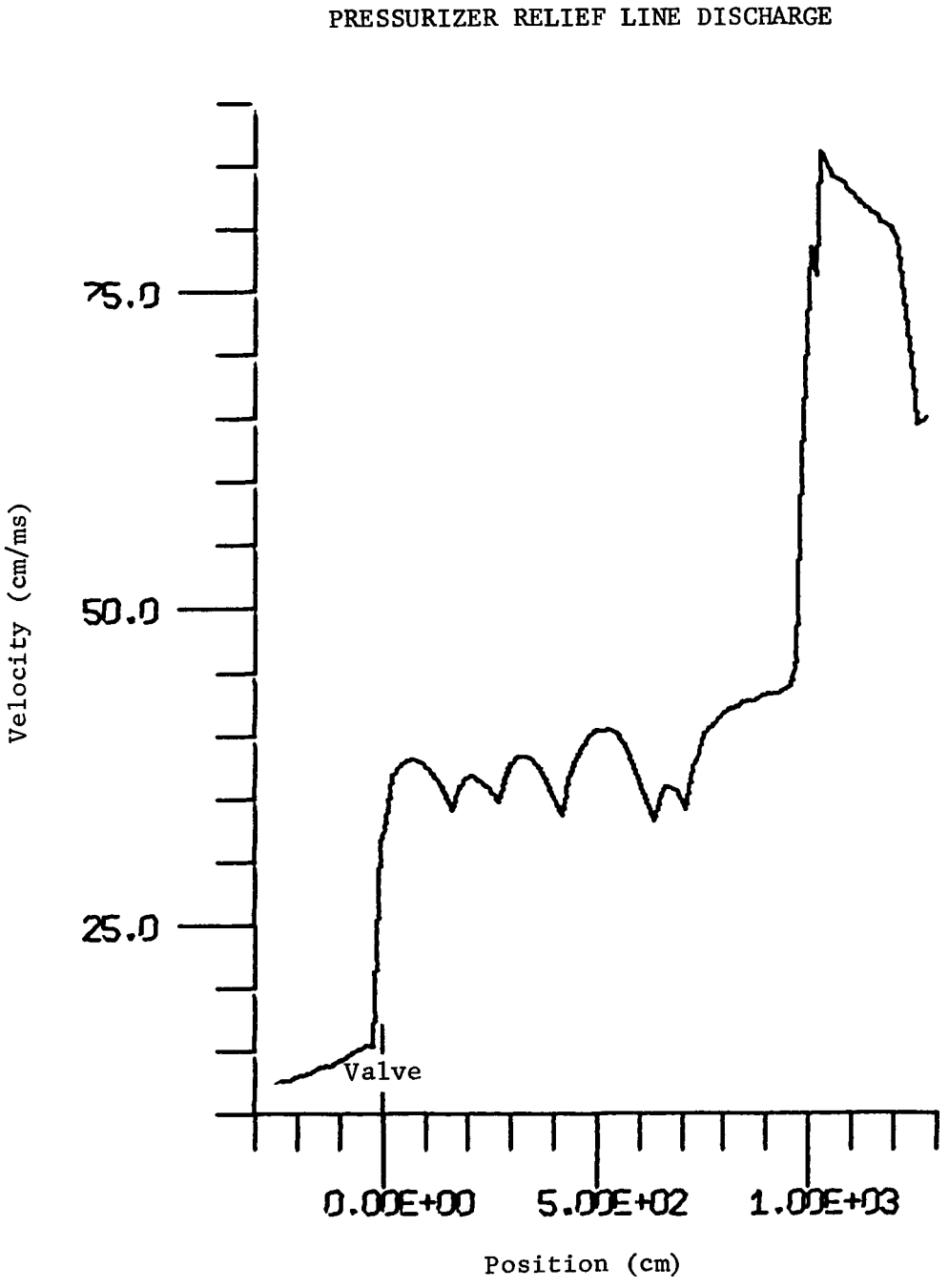

Figure C-8. Velocity profile at 40.0 ms.

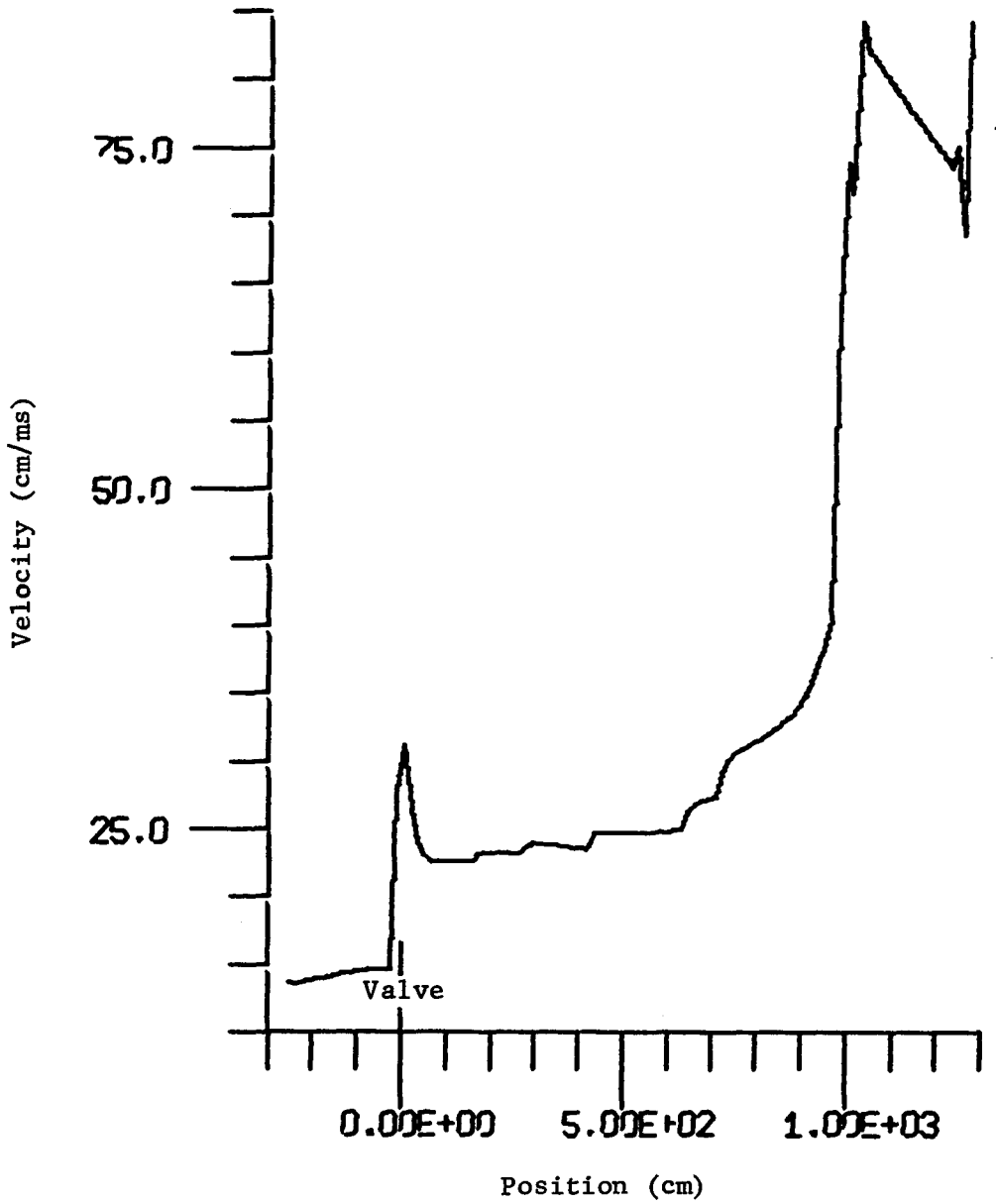

Figure C-9. Velocity profile at 75.0 ms.

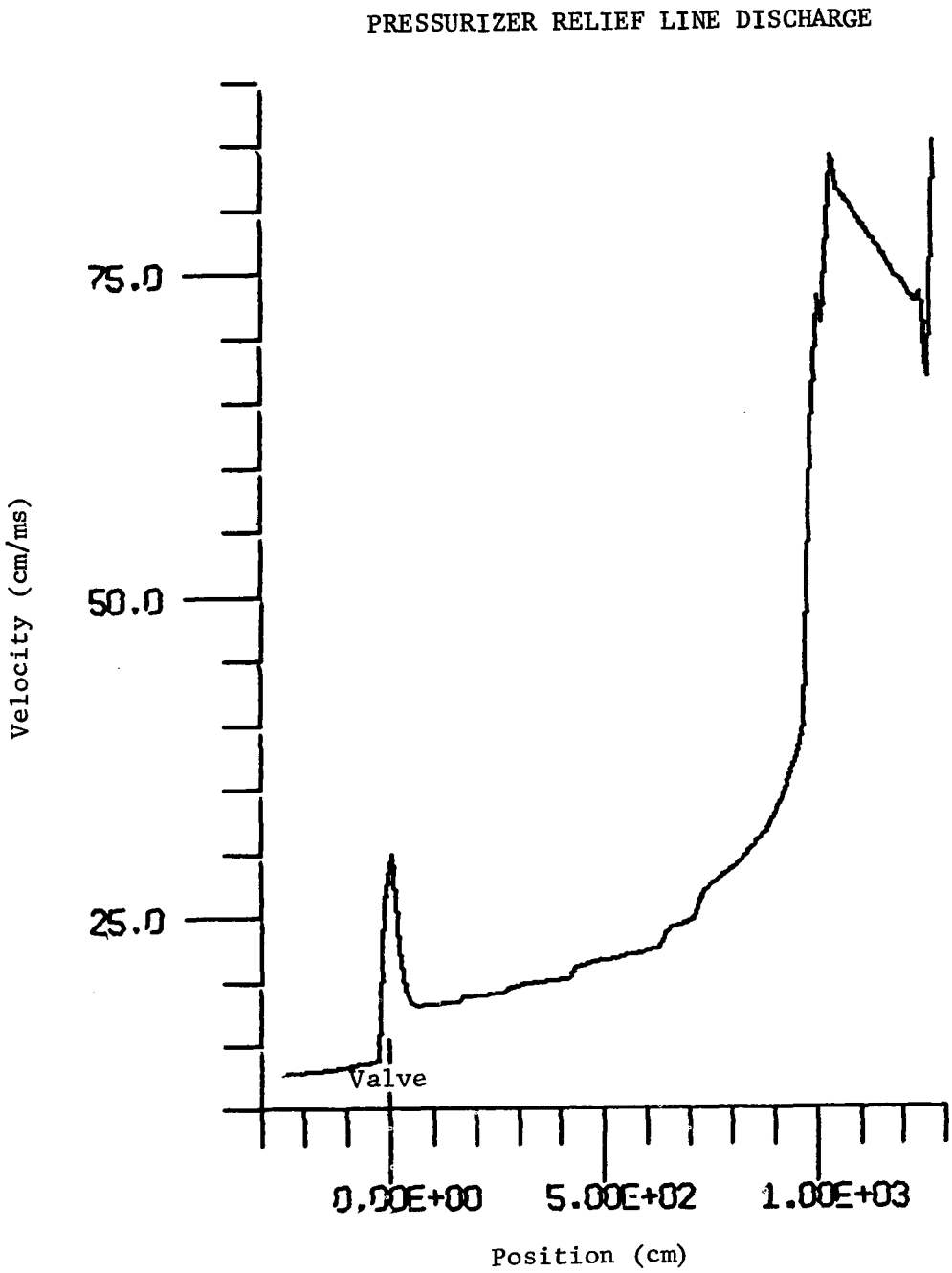

Figure C-10. Velocity profile at 125.0 ms.

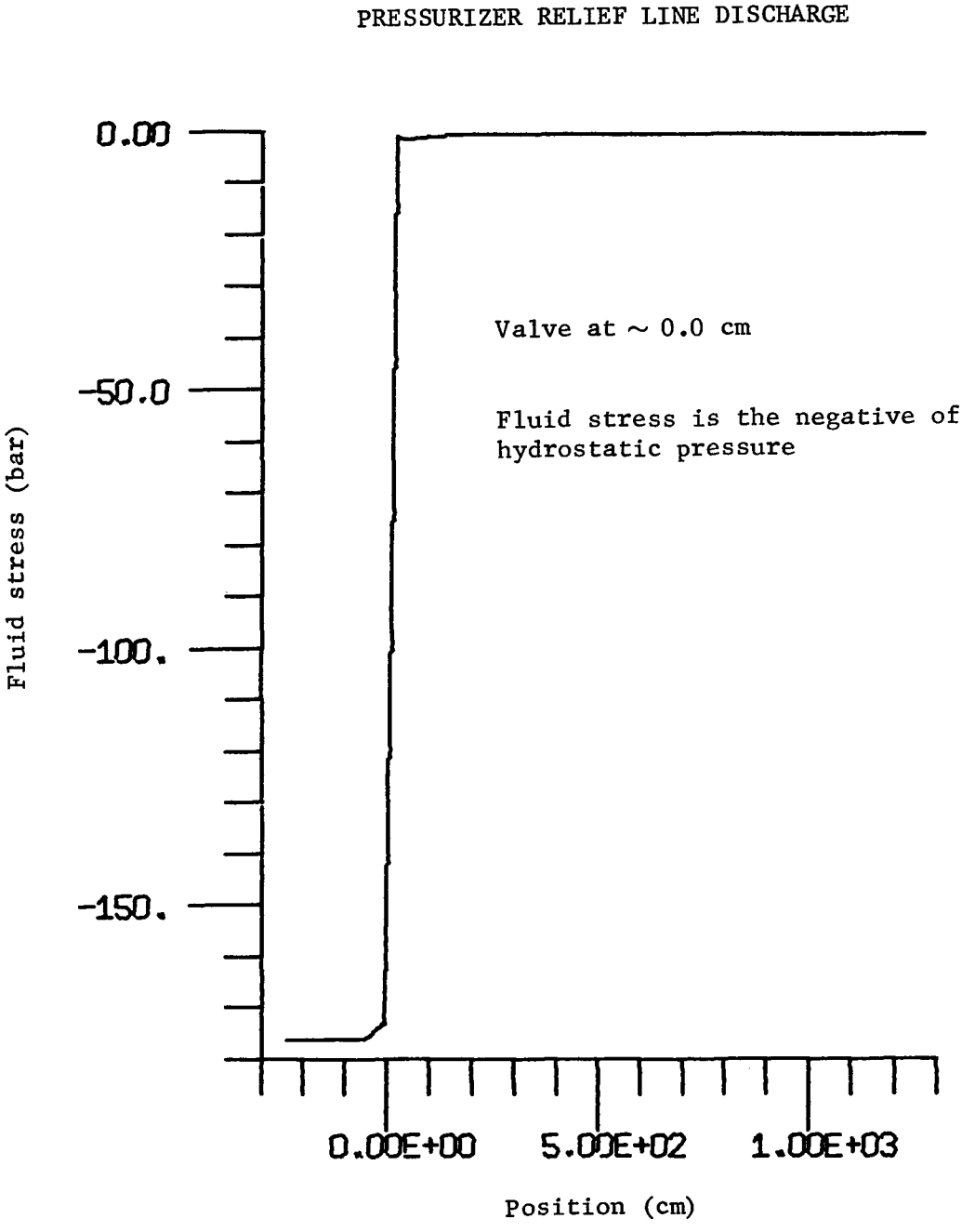

Figure C-11. Fluid stress profile at 1.0 ms.

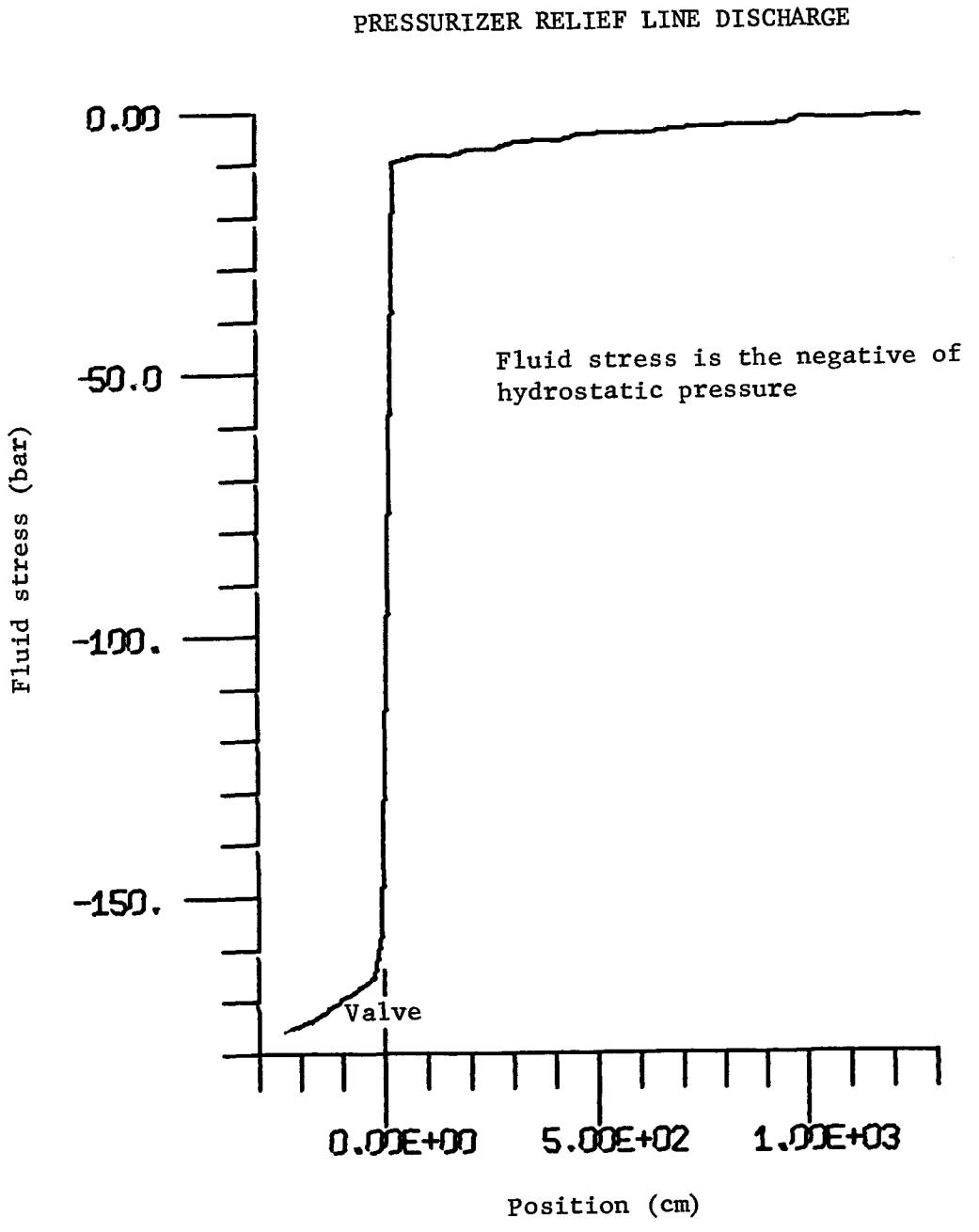

Figure C-12. Fluid stress profile at 20.0 ms.

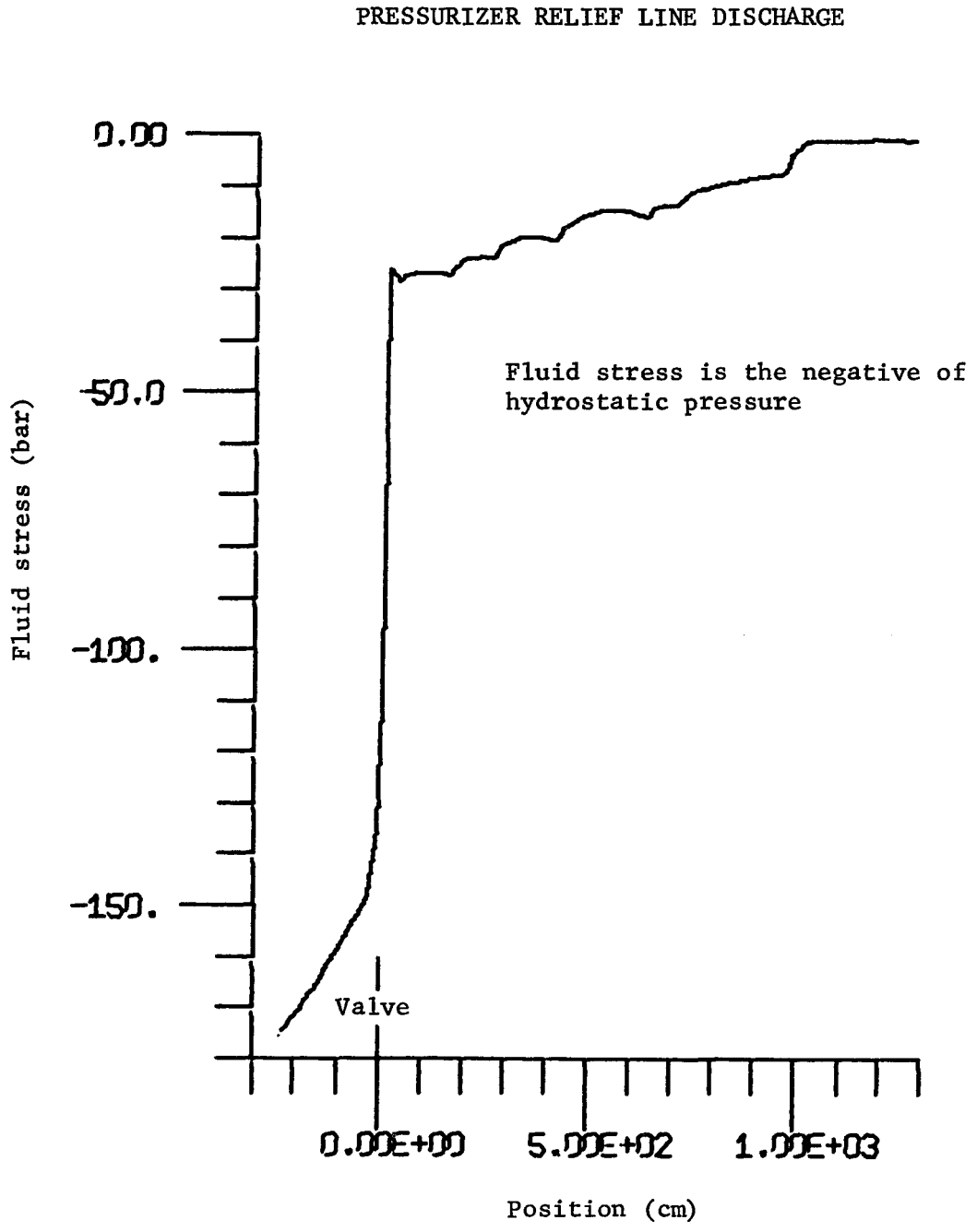

Figure C-13. Fluid stress profile at 40.0 ms.

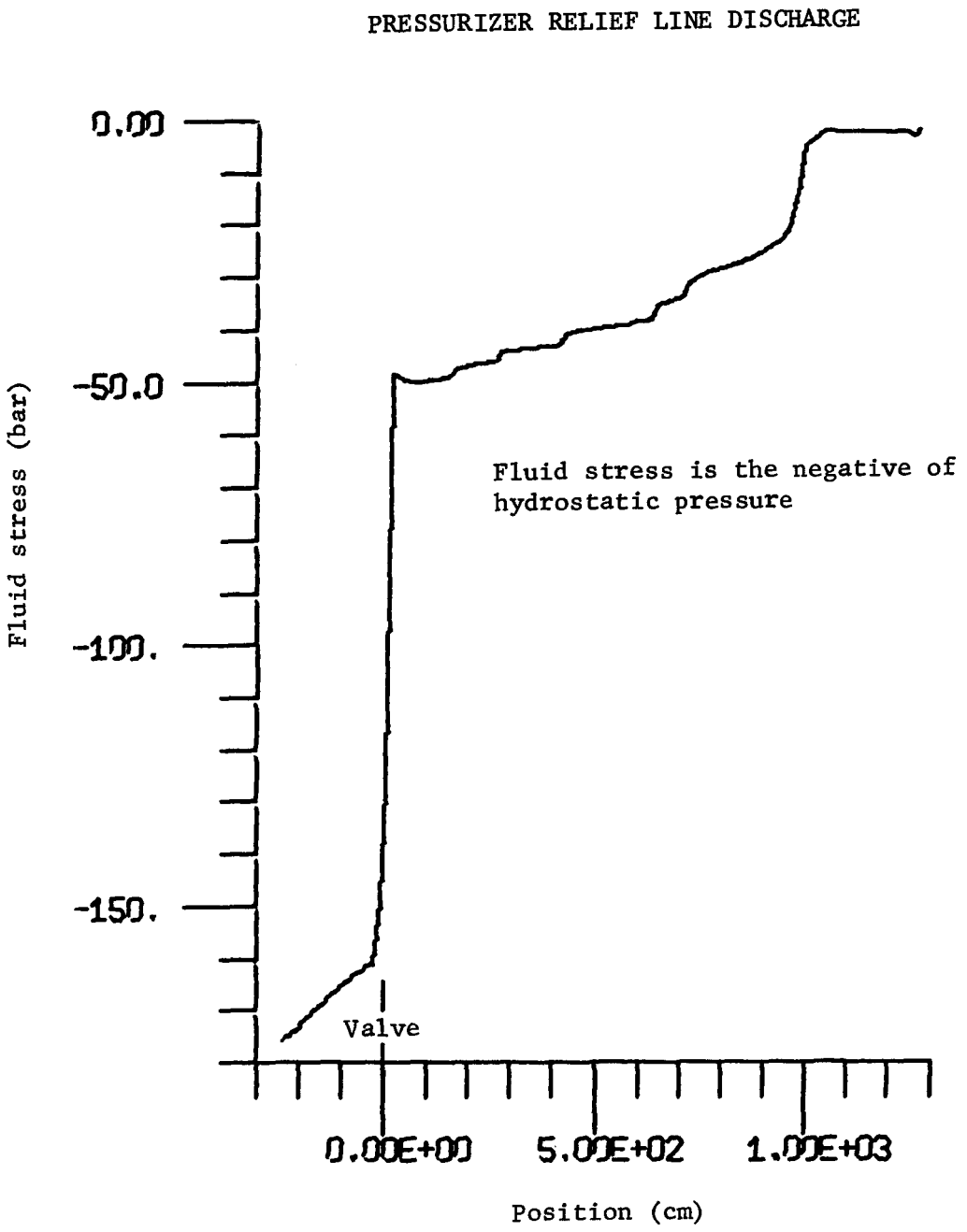

Figure C-14. Fluid stress profile at 75.0 ms.

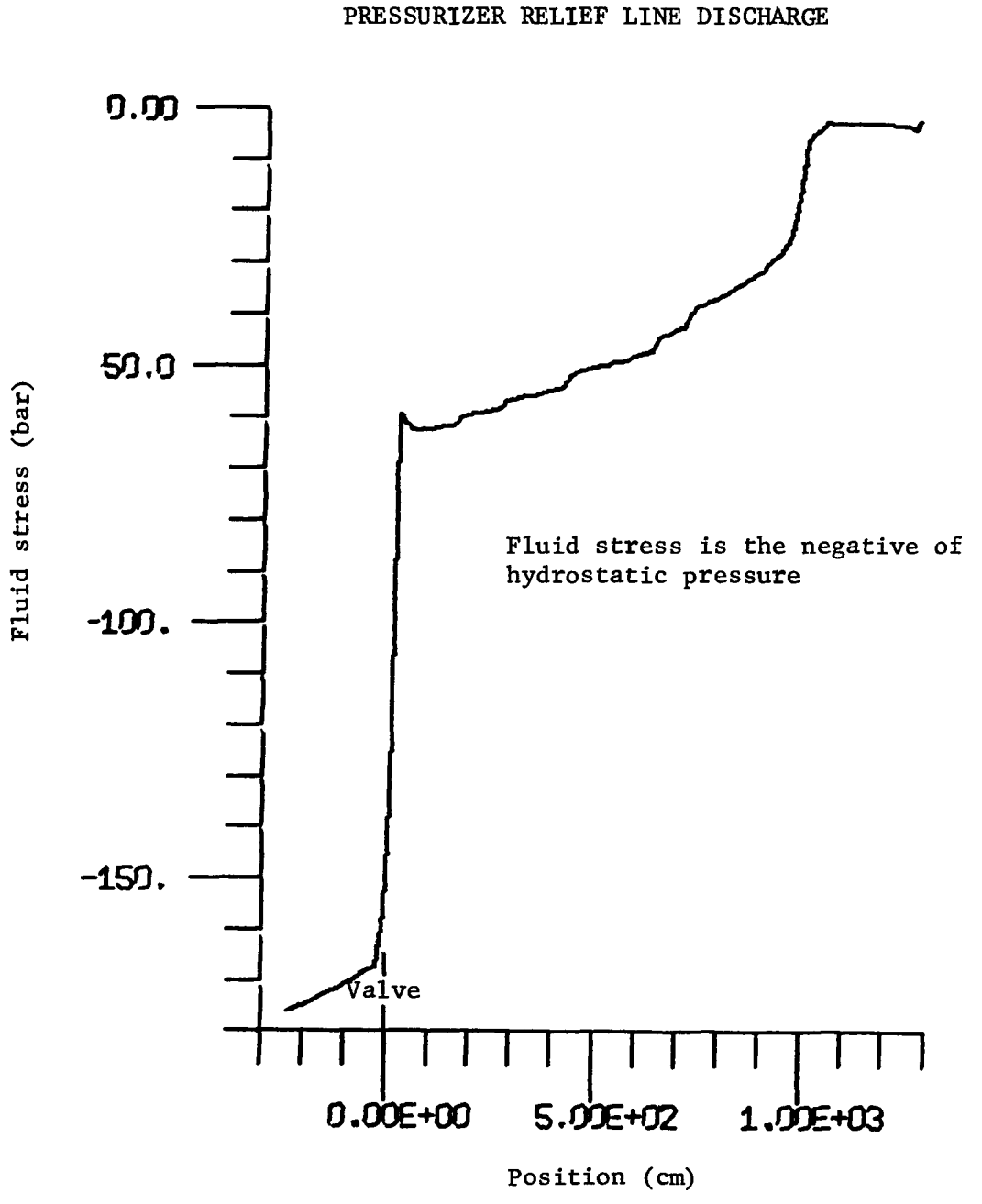

Figure C-15. Fluid stress profile at 125.0 ms.

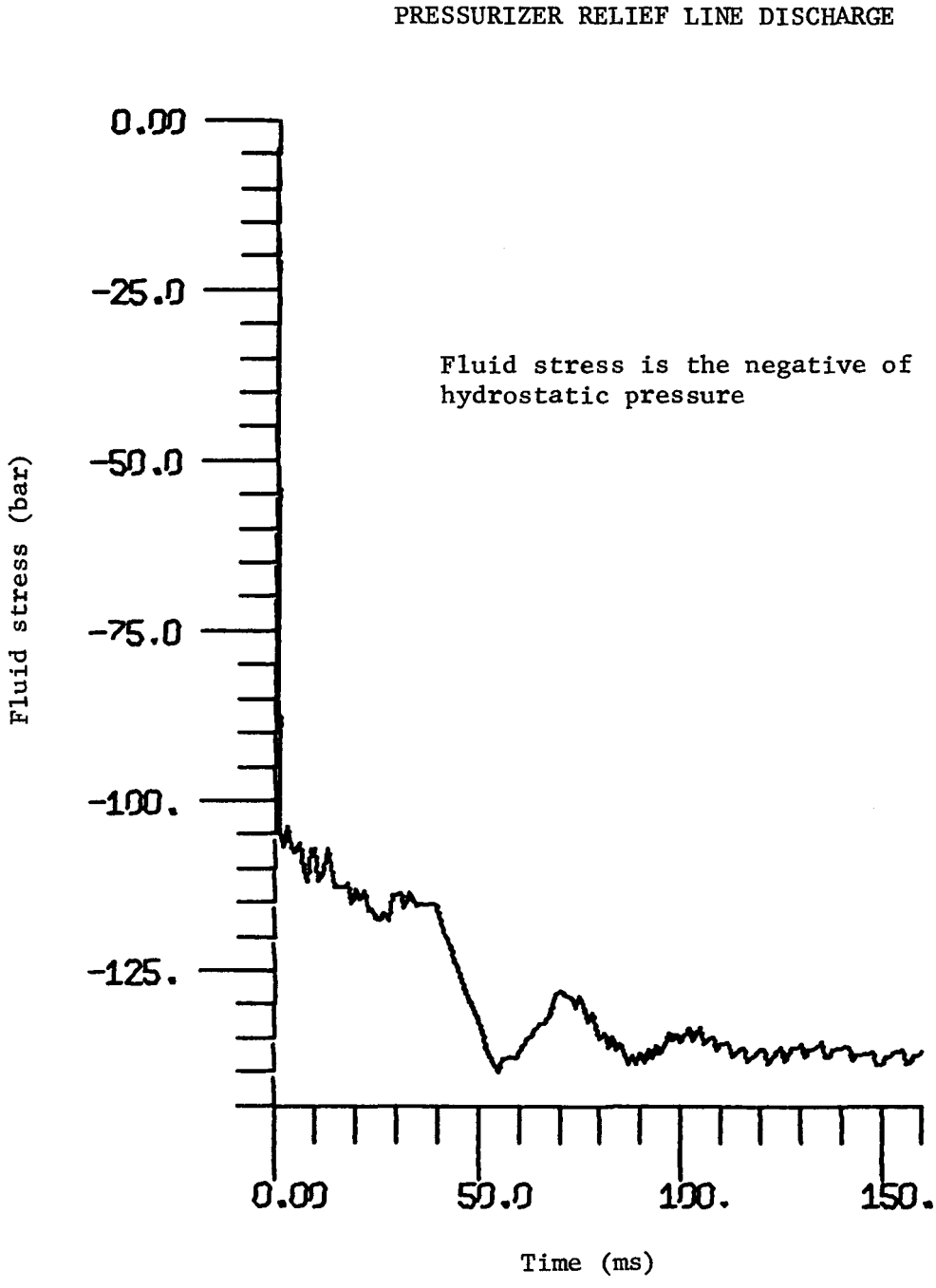

Figure C-16. Fluid stress time history at the safety valve.

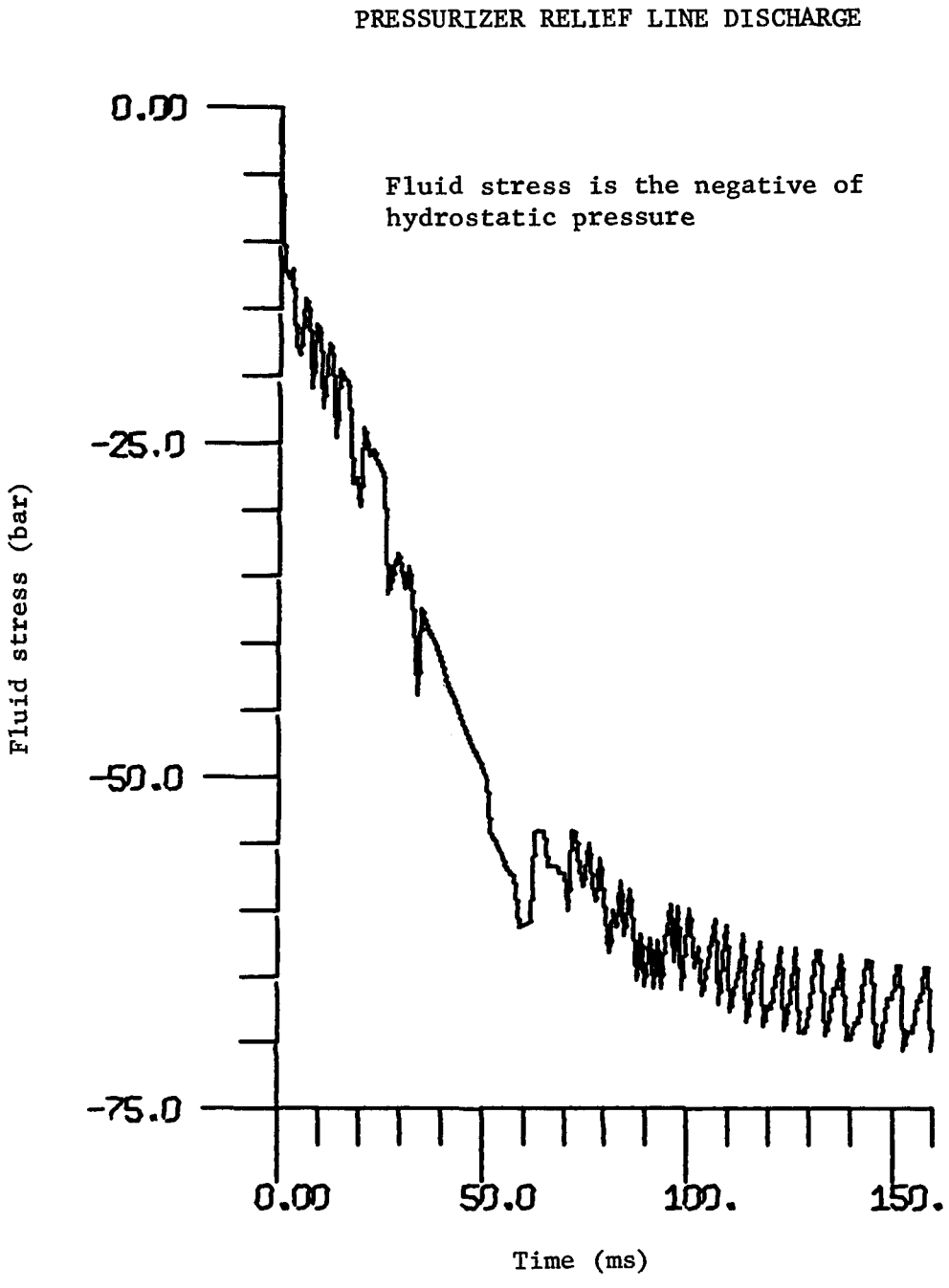

Figure C-17. Fluid stress history at the first expander.

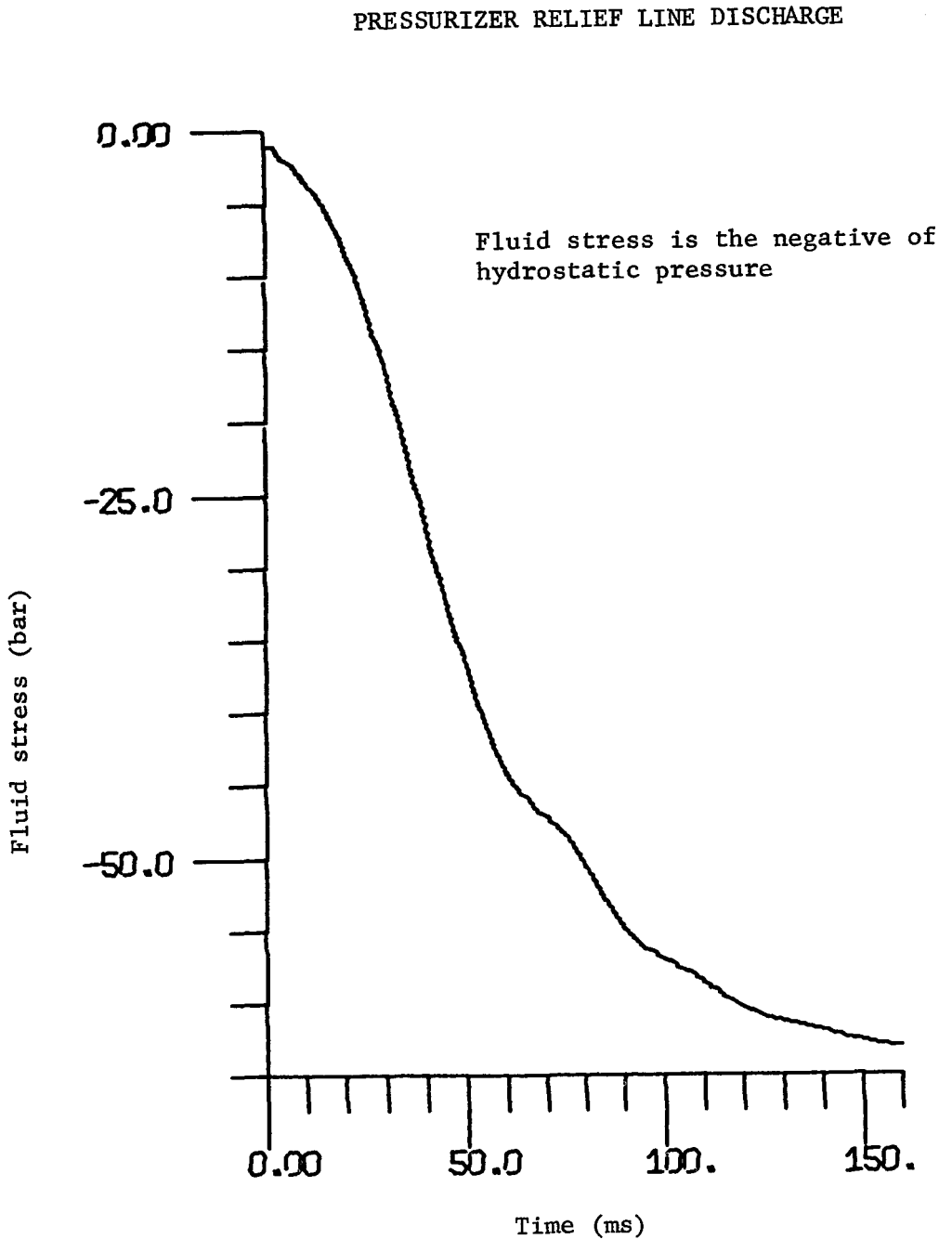

Figure C-18. Fluid stress history at the first 45° elbow.

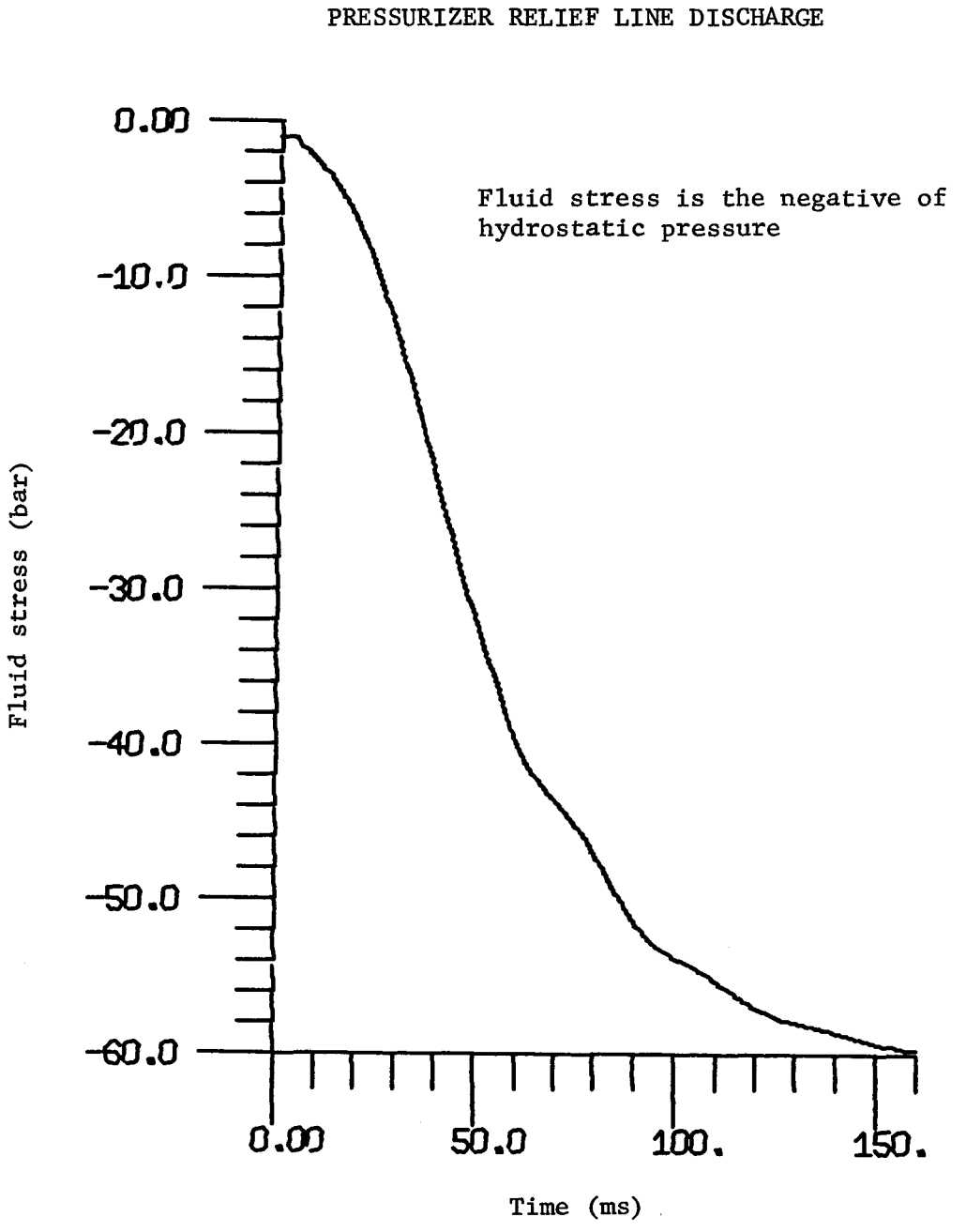

Figure C-19. Fluid stress history at the second 45° elbow.

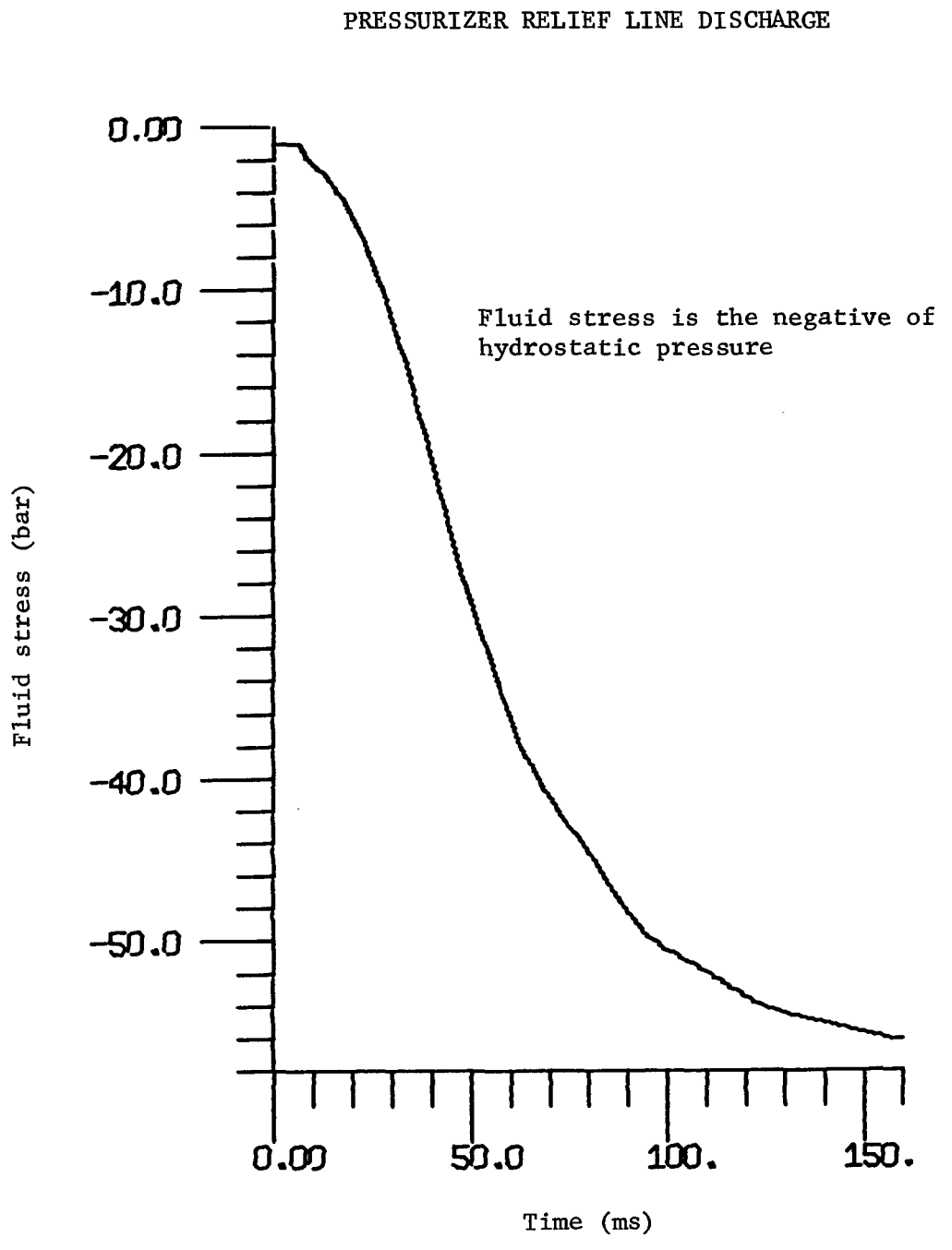

Figure C-20. Fluid stress history at the first 90° elbow.

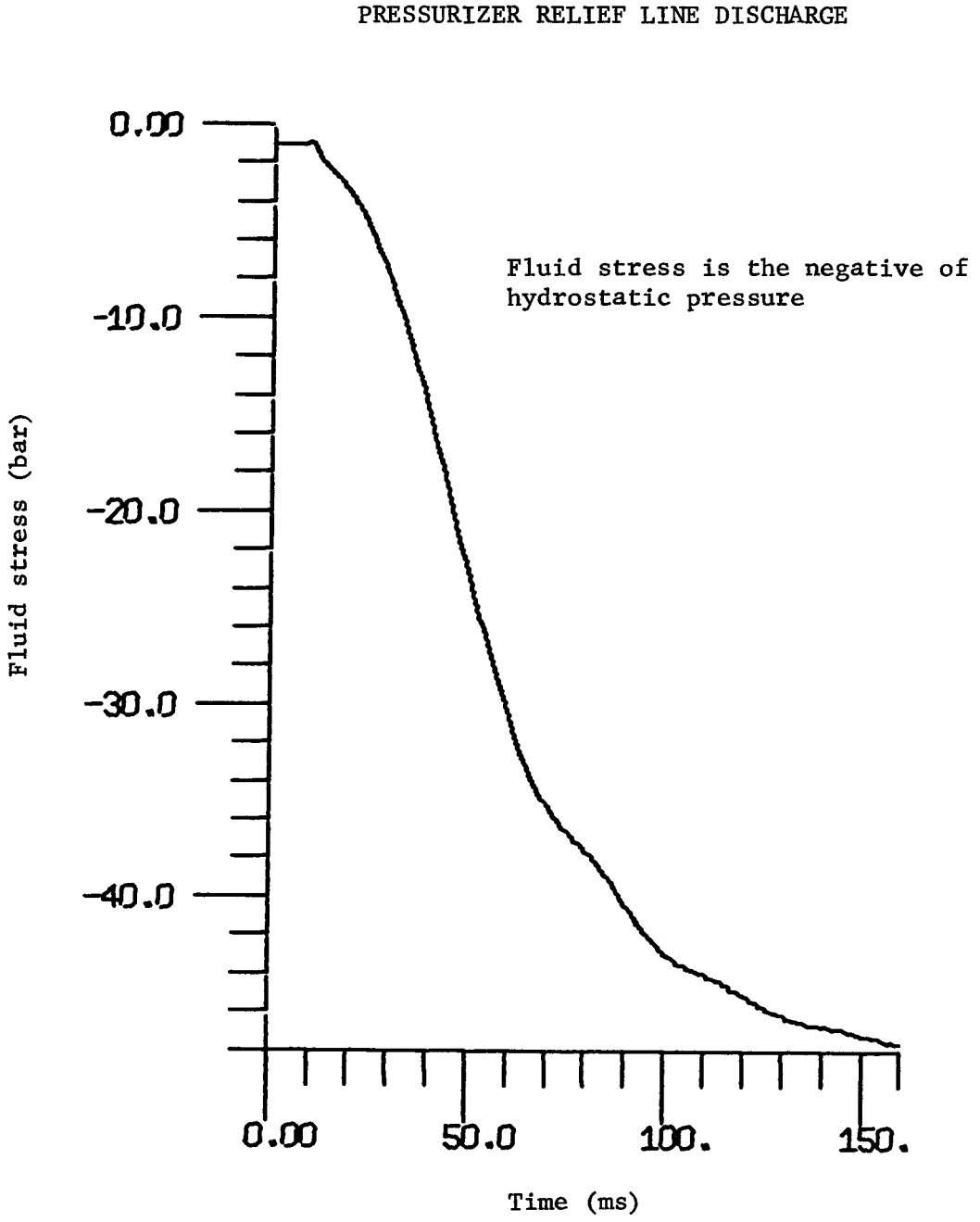

Figure C-21. Fluid stress history at the second 90° elbow.

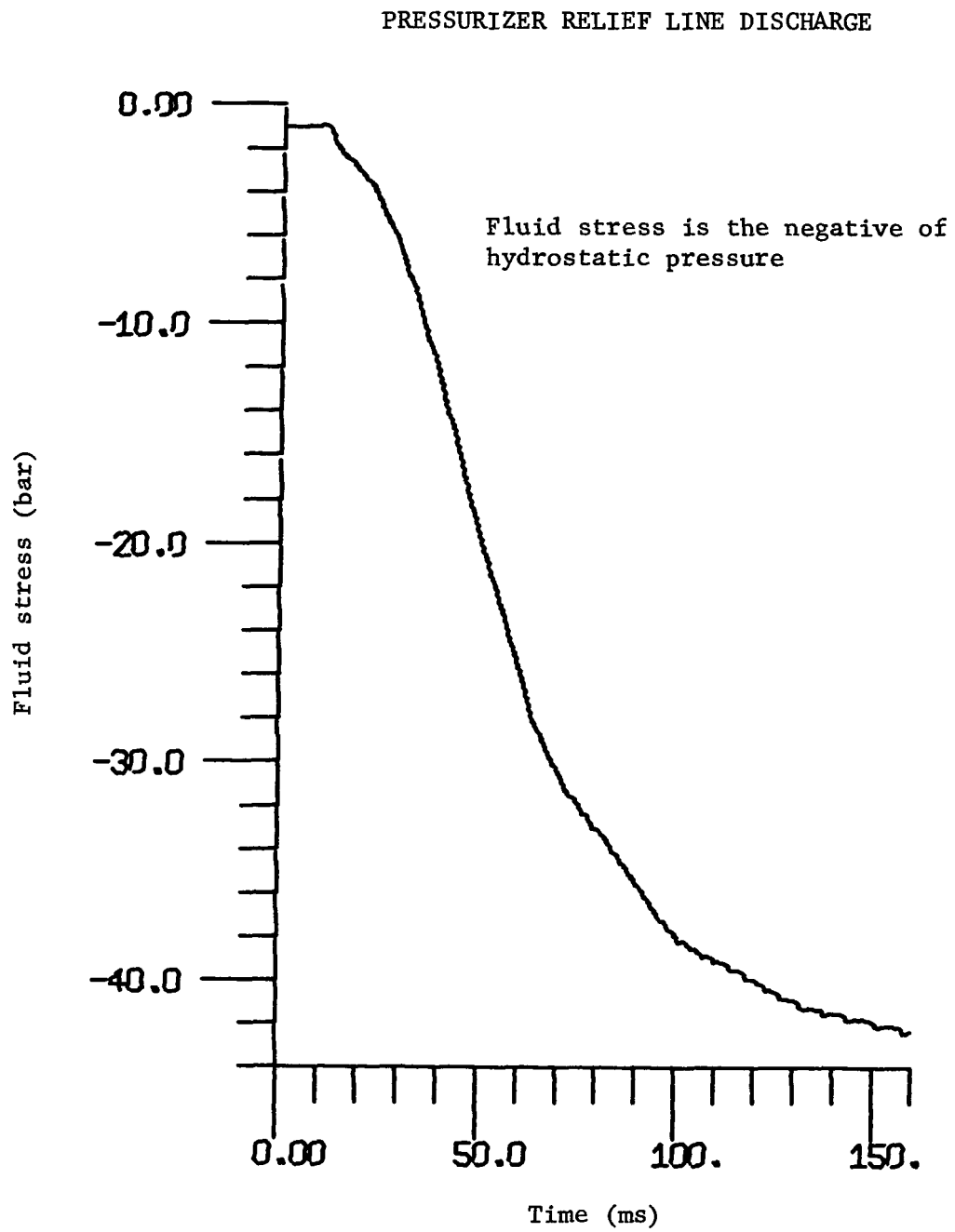

Figure C-22. Fluid stress history at the third 90° elbow.

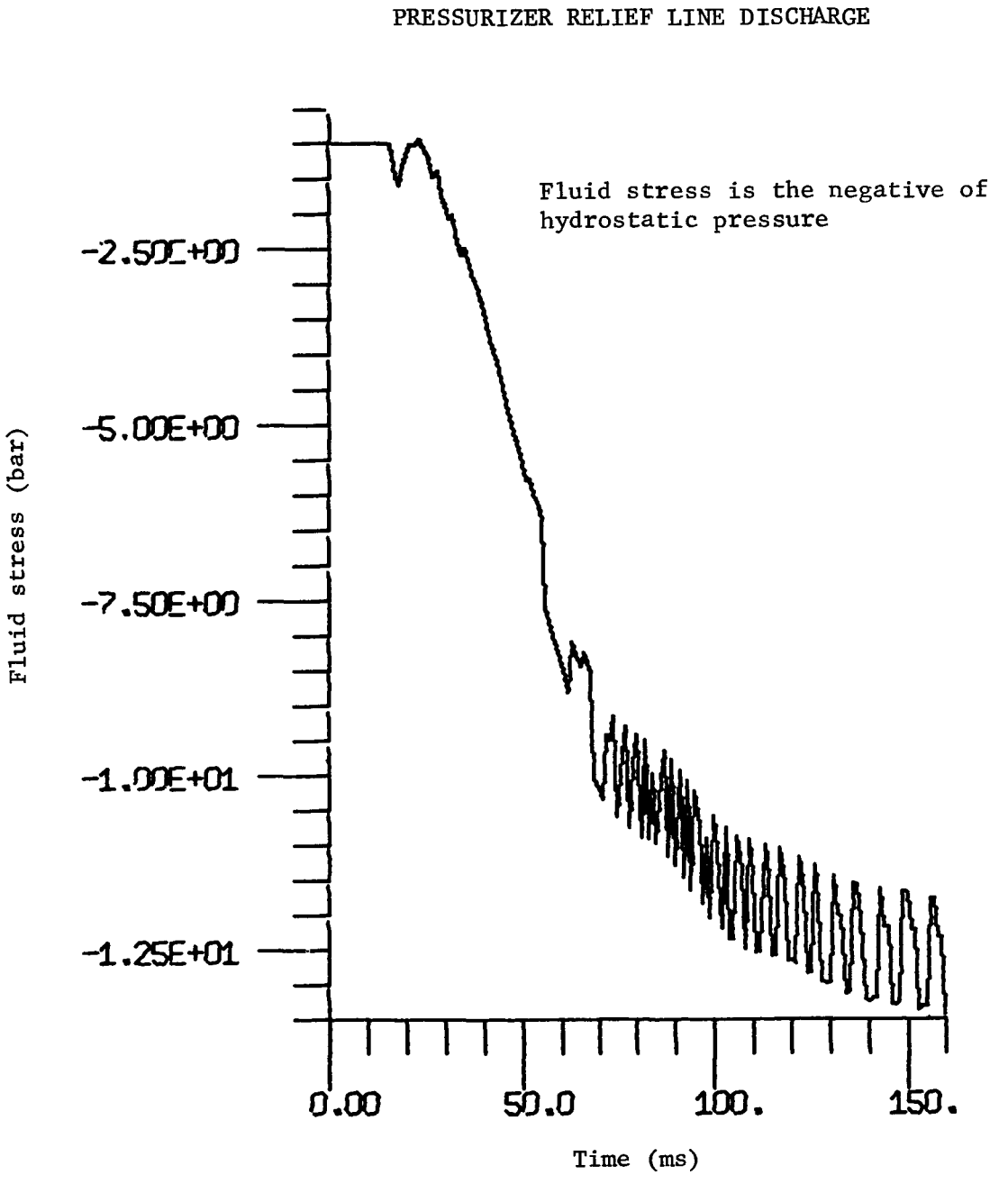

Figure C-23. Fluid stress history at the second expander.

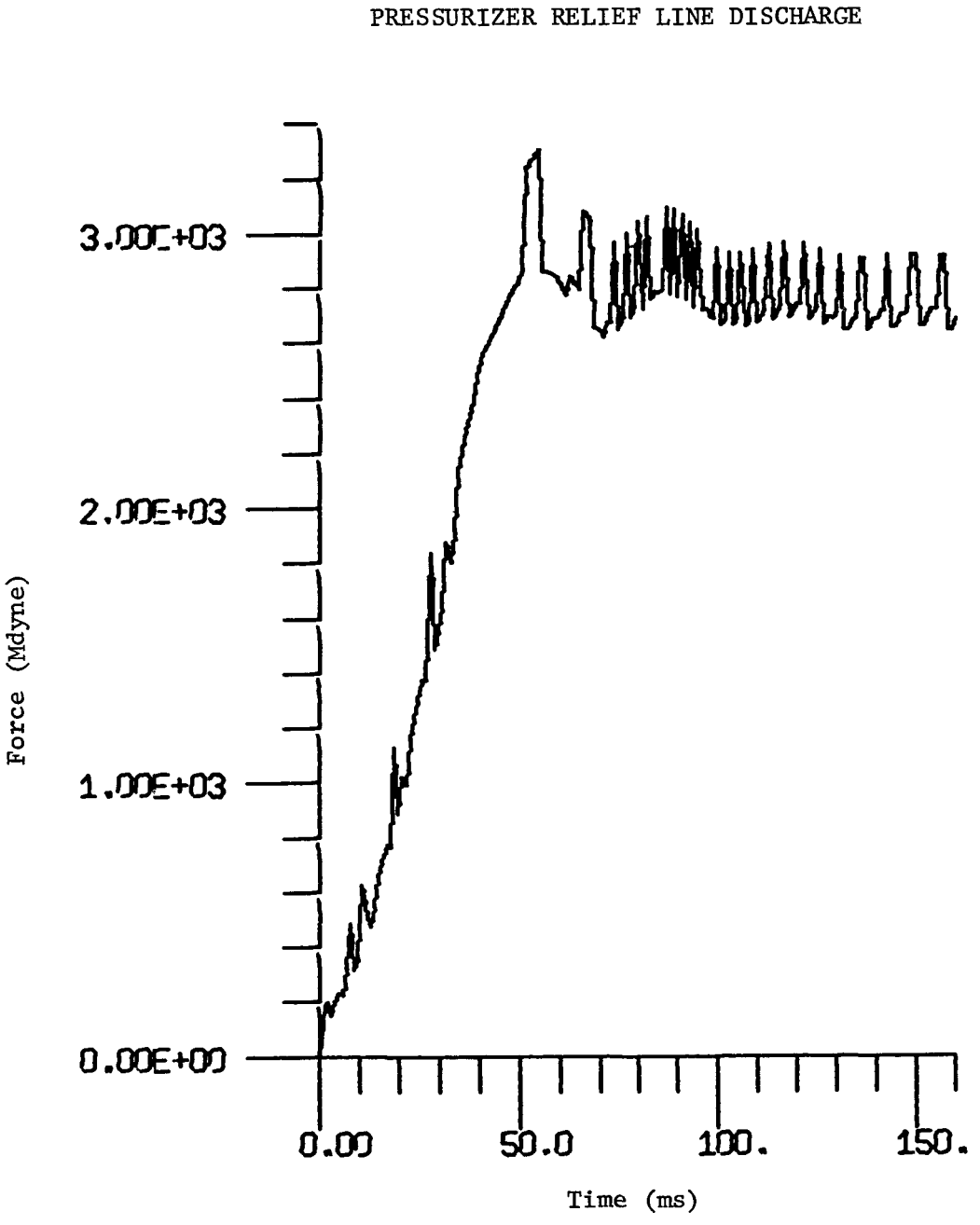

Figure C-24. Force history at the safety valve.

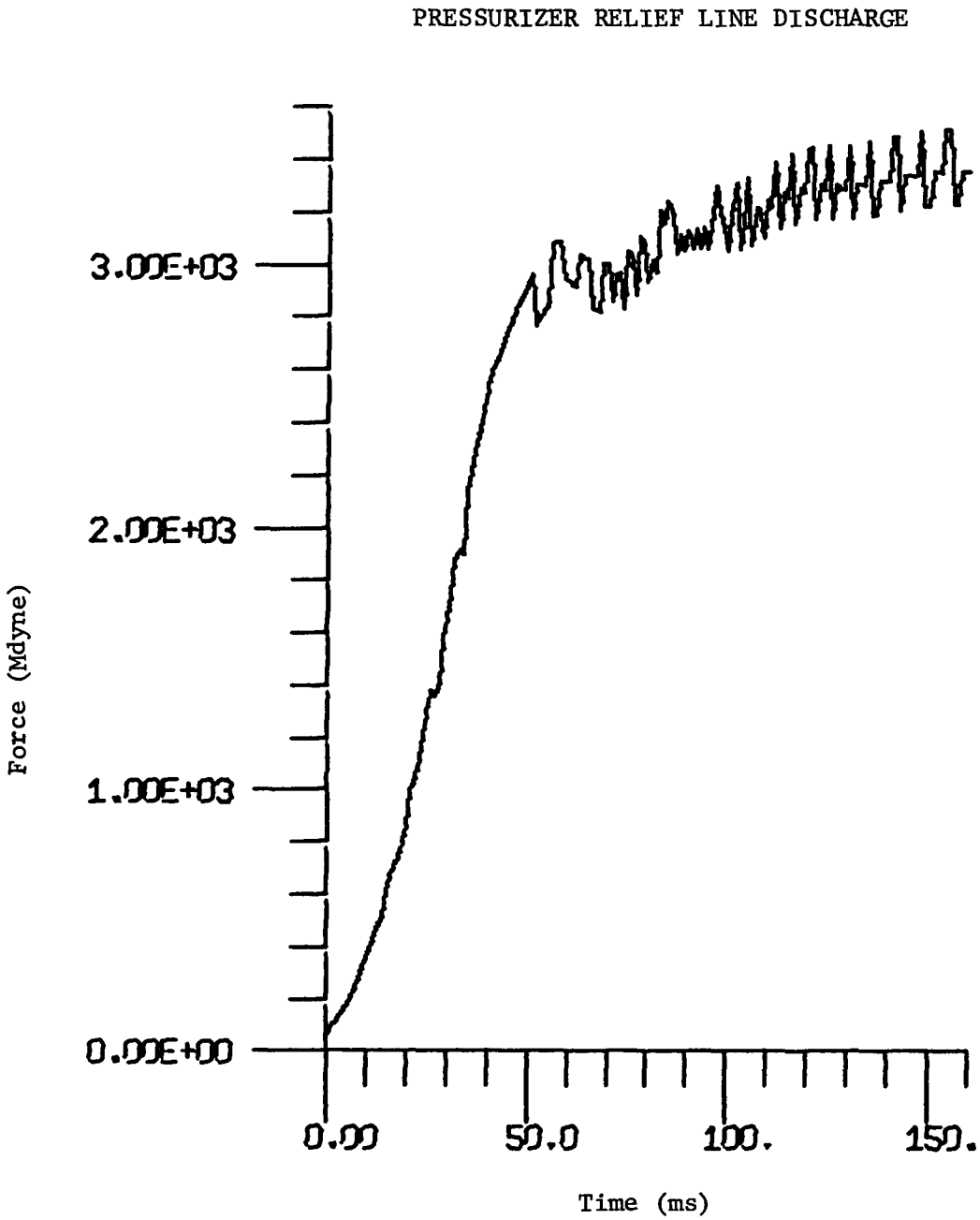

Figure C-25. Force history at the first expander.

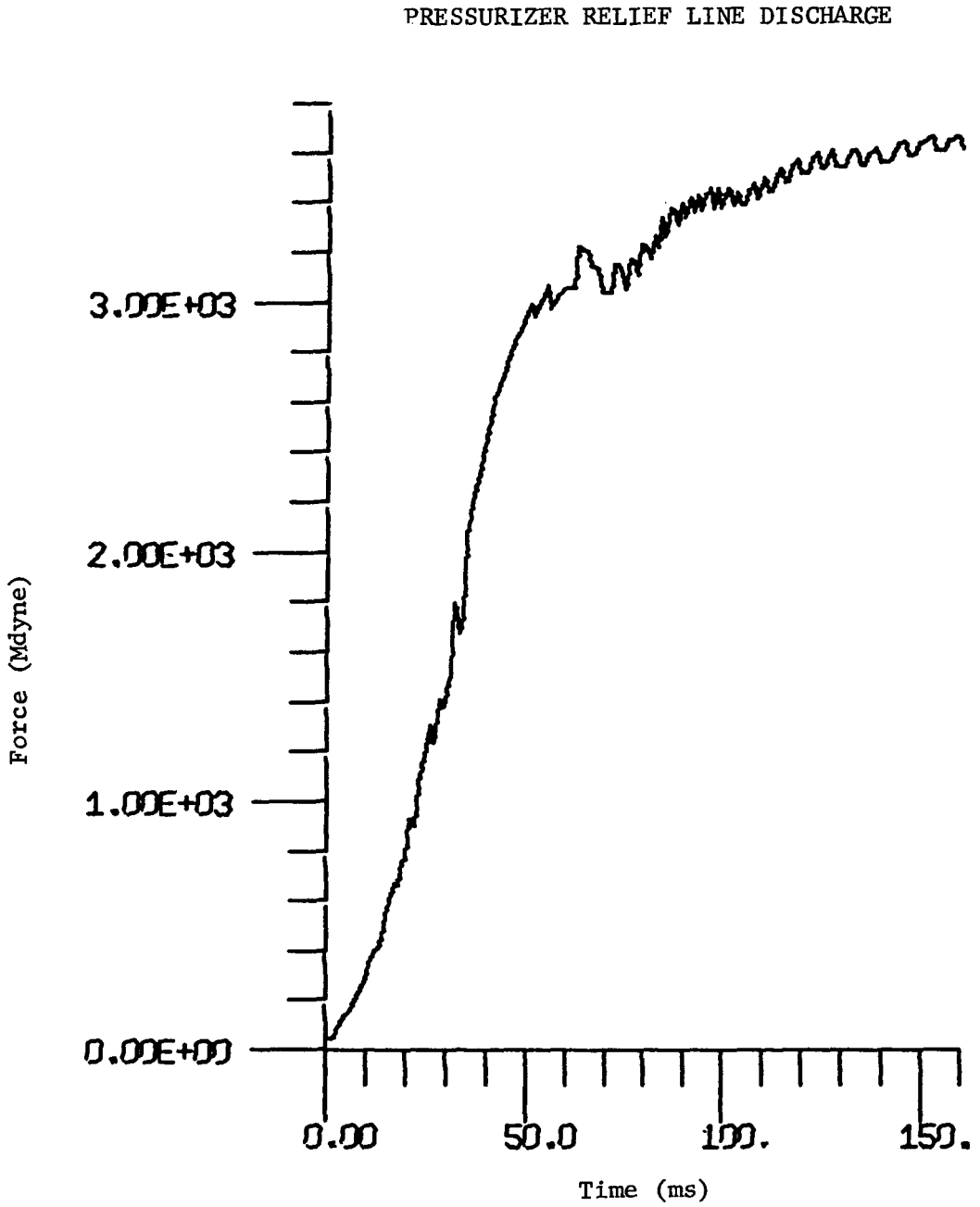

Figure C-26. Force history at the first 45^{o} elbow.

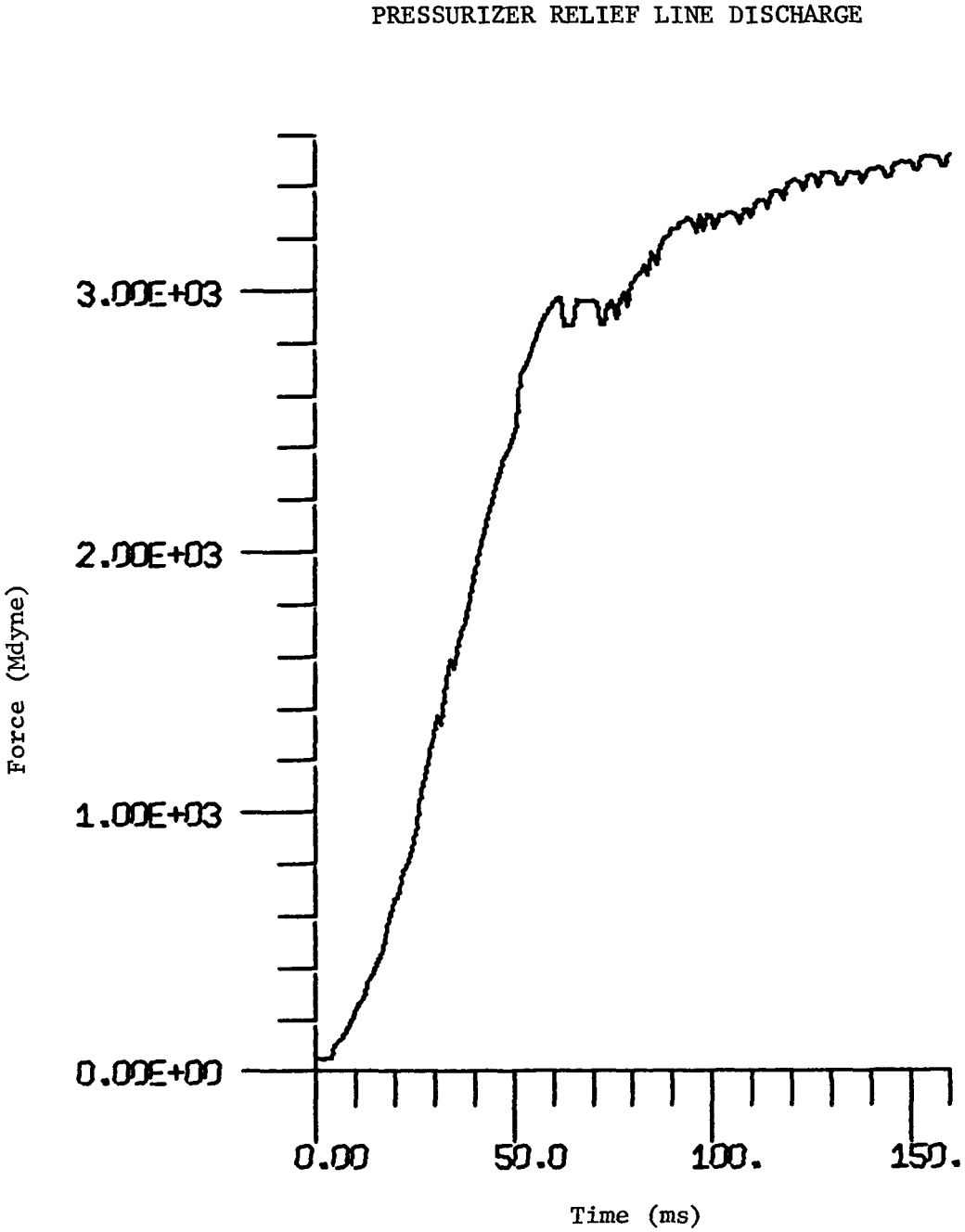

Figure C-27. Force history at the second 45° elbow.

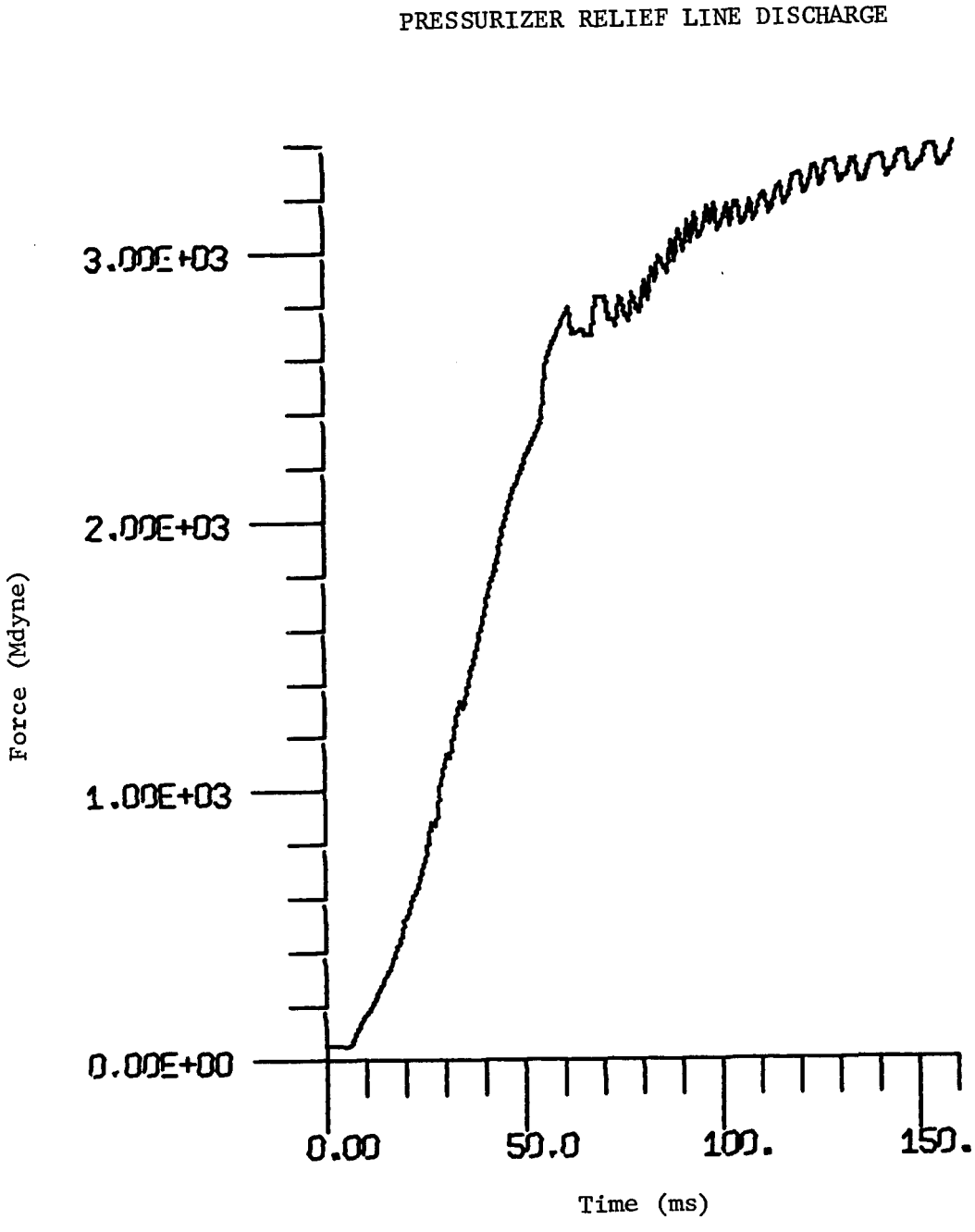

Figure C-28. Force history at the first 90° elbow.

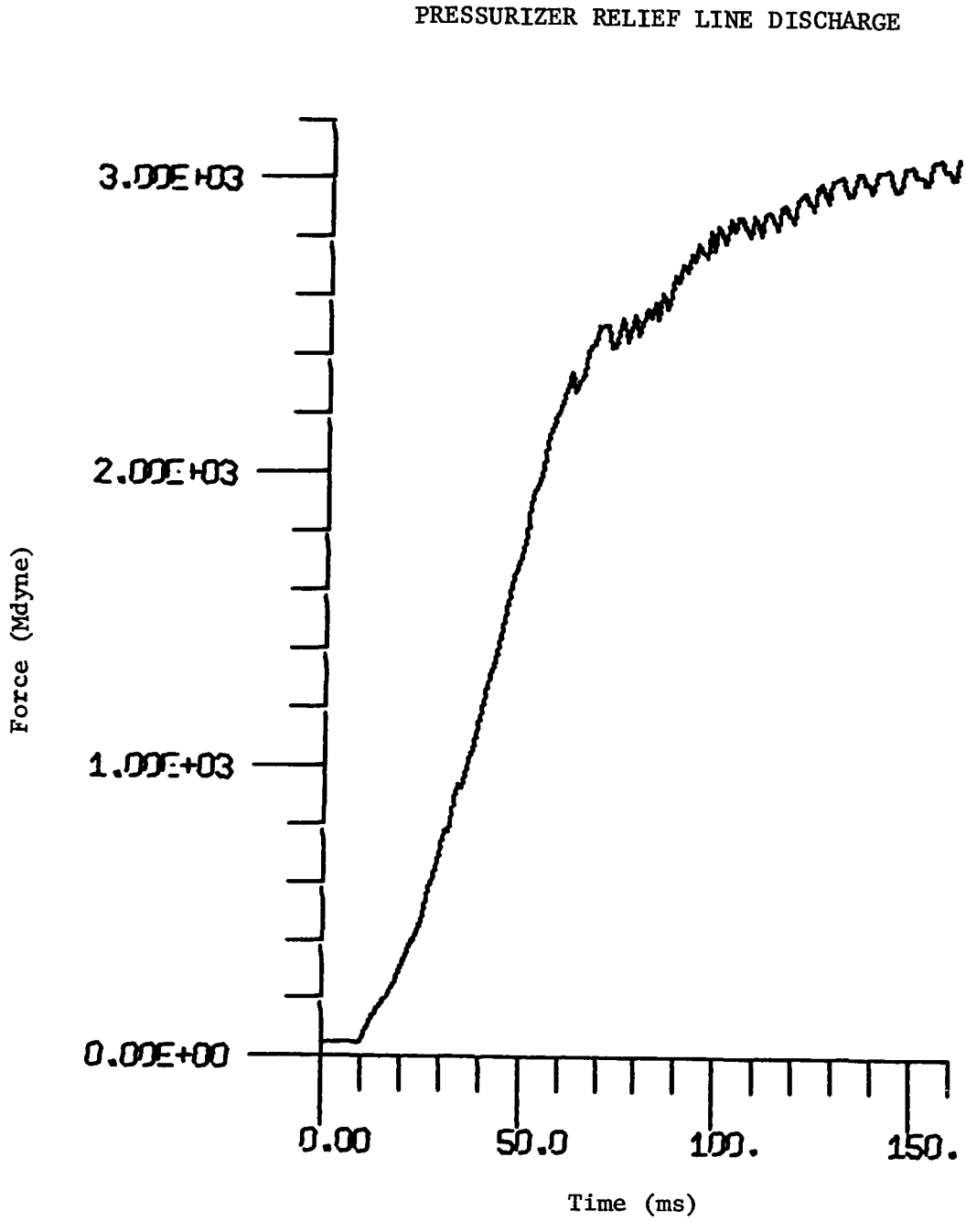

Figure C-29. Force history at the second 90° elbow.

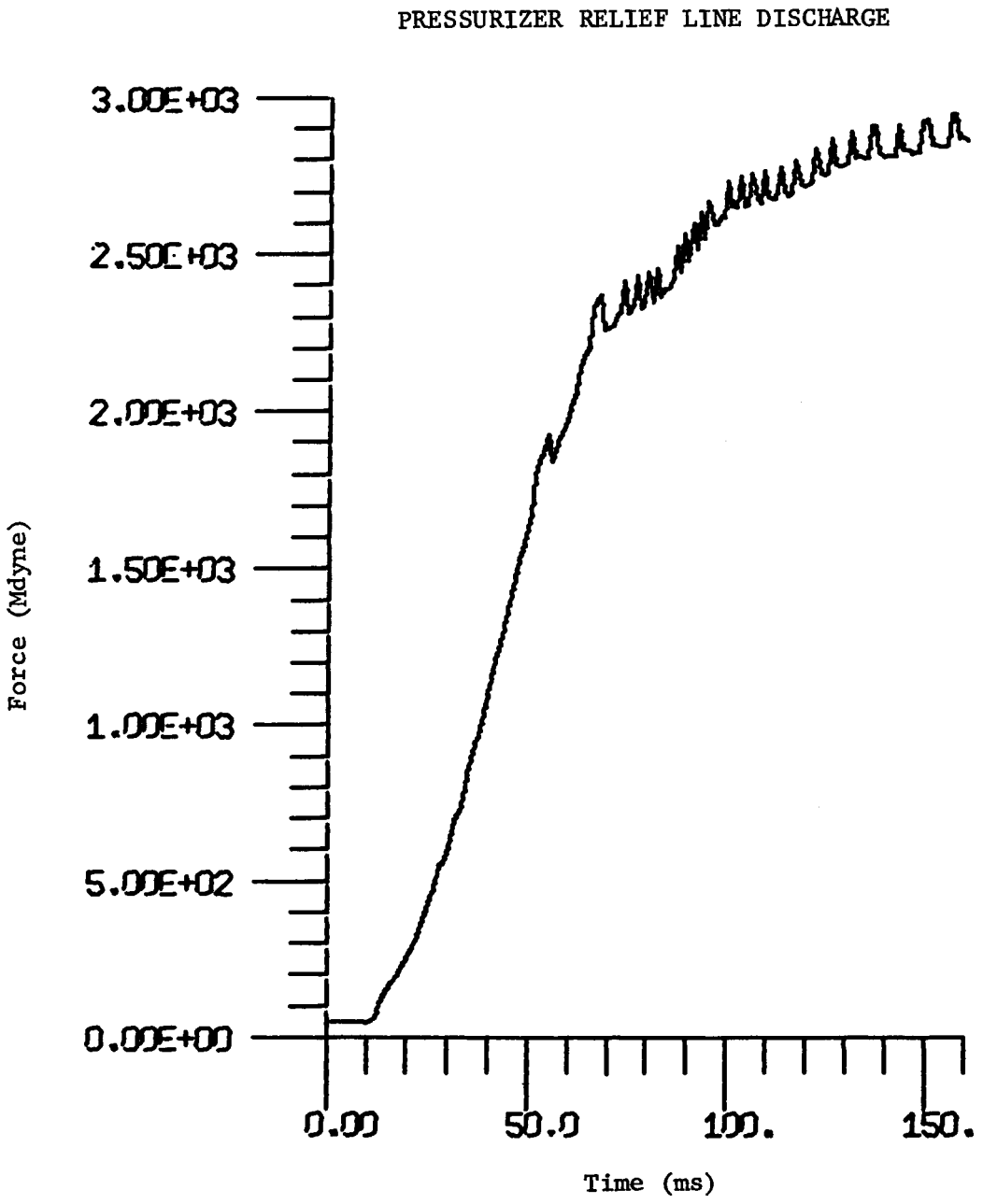

Figure C-30. Force history at the third 90° elbow.

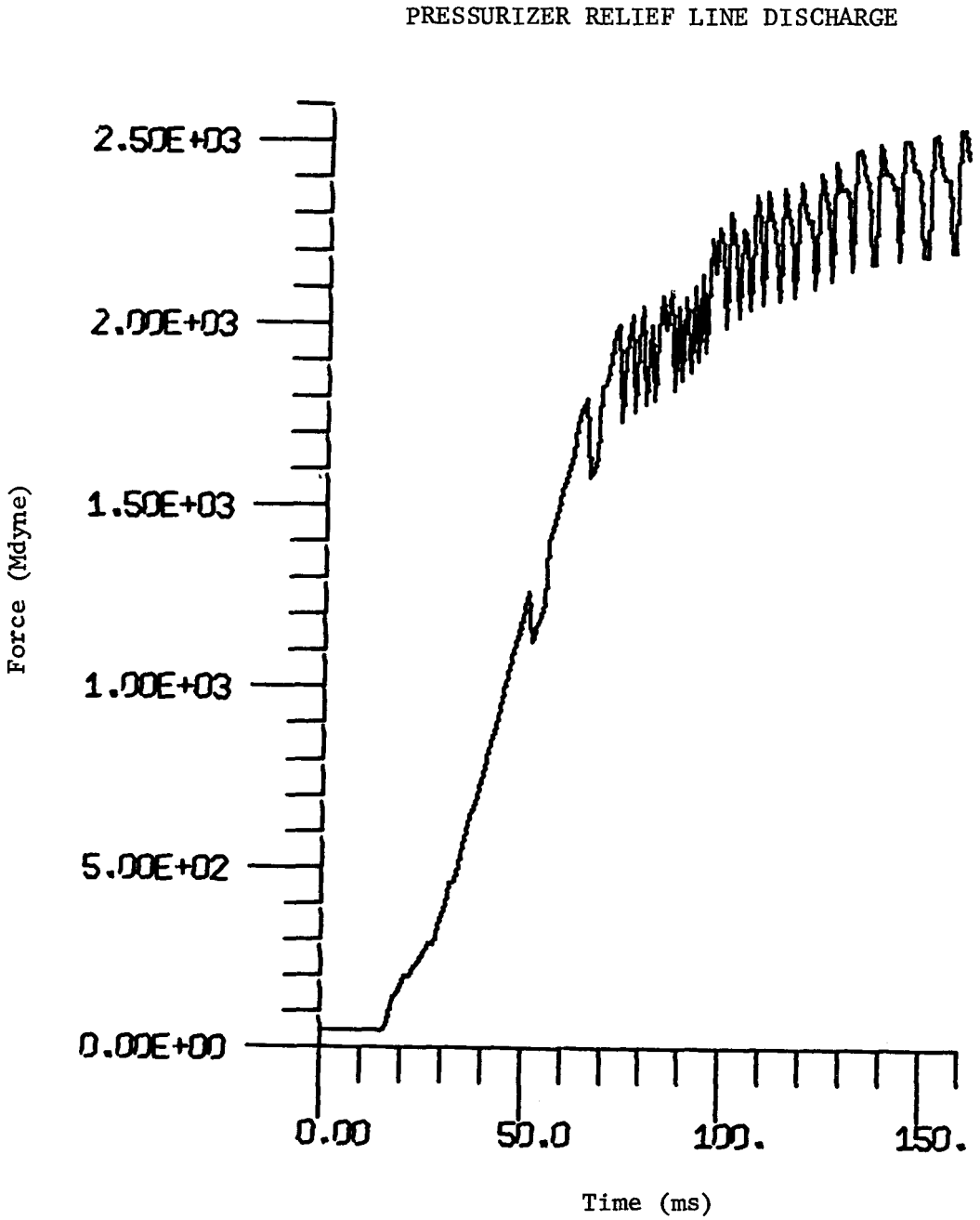

Figure C-31. Force history at the second expander.

C.4 CLOSURE

This simulation requires 5132 time cycles to span 160 ms of real time. With a field of 101 nodes, this involves 518,332 node-cycle calculations. On a CDC 7600 computer, the simulation is core-contained, and executes in 7 minutes, or 0.82 CP ms per node-cycle.*

*Note that this simulation was performed with an earlier version of the code than that used for the simulations in Appendix B, where the CP ms per node-cycle was improved to 0.34.

REFERENCES

C-1. Bence I. Gerber, "STEALTH, A Lagrange Explicit Finite-Difference Code for Solids, Structural, and Thermohydraulic Analysis, Volume 4, GRADIS Manual," EPRI NP-260, Vol. 4, Electric Power Research Institute, Palo Alto, California, August 1976. Prepared by Science Applications, Inc., San Leandro, California, under Contract RP307.

C-2. C. A. Meyer, R. S. McClintock, G. J. Silvestri, and R. C. Spencer, Jr., ASME Steam Tables (Thermodynamic and Transport Properties of Steam Comprising Tables and Charts for Steam and Water), The American Society of Mechanical Engineers, New York, 1977.

APPENDIX D
SIMULATION OF A PUMP TRIP WITH BYPASS

D.1 INTRODUCTION

In order to mitigate the effects of the pressure waves that are caused by pump trips, pump installations may possess bypass lines. Figure D-1 illustrates one such installation; the bypass, with check valve, is in parallel with the pump and discharge valve. Normally, the discharge valve is fully open, and the check valve is closed, isolating the bypass from the pipe flow.

When the pump trips, sending a compression hammer upstream and a rarefaction hammer downstream, the check valve snaps open instantaneously.* This establishes a bypass flow which acts to reduce the magnitudes of the hammer transients. At the same time, the discharge valve closes in 7.2 seconds, to protect the pump from the wave reflections of the initial pulses.

This Appendix documents a numerical simulation of the pump trip event described above. In all particulars, it is the same event that was simulated by Wylie and Streeter.** Moreover, the construction of the simulation reported herein adopts their modeling procedure of combining all components in one control volume. (This is different from the usual STEALTH-based modeling, where the simulation is a combination of basic control volumes, one for each piping component, in conjunction with computational grids for each section of pipe.) By adopting the procedure of Wylie and Streeter here, it is possible to validate this simulation by direct comparison with their results. This is consistent with the purpose of this Appendix, which is not to provide, necessarily, the most realistic simulation of a pump trip, but to demonstrate

---

*On the time scale of the trip; thus, in this event, the check valve is only a source of flow loss.

**See Appendix E of E. B. Wylie and V. L. Streeter, Fluid Transients, McGraw-Hill, Inc., New York, 1978.

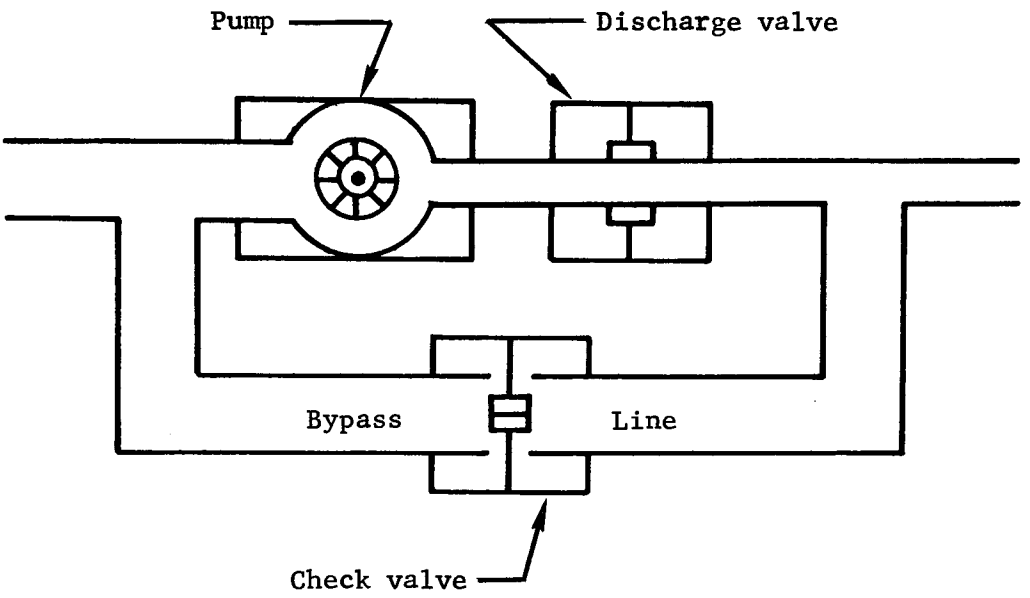

Figure D-1. Pump installation with bypass line.

that a control volume model for turbopumps is operational for STEALTH 1D simulations of time-dependent pipe flows.

D.2 CONSTRUCTION OF SIMULATION

The pump trip simulation incorporates the one-dimensional hydro version of STEALTH with one control volume model that accounts for the pump, discharge valve, bypass line, and check valve. (As mentioned above, this control volume model is the same as that developed by Wylie and Streeter.) In addition, the simulation accounts for the flow losses associated with pipe friction and the piping components. By including all the piping components in one control volume, the simulation does not account for spatial effects that act in the bypass line, or that act between piping components. In this representation, the effect of the bypass line enters as a mass sink upstream of the pump and a mass source downstream of the discharge line.

Figure D-2 illustrates, schematically, the computational grids, control volume, and boundary conditions that model the pump and bypass installation. The grids include the loss effects of pipe friction; the control volume accounts for the pump trip, closing discharge valve (see Figure D-3), the mass flow of the bypass line, and the flow losses associated with these components.

The two computational grids have the following characteristics:

- Grid #1
  - * upstream of control volume
  - * 20 zones
  - * nodes 1 through 21
  - * 1.75-ft flow diameter
  - * coordinates from 0 ft to 1800 ft
  - * length of 1800 ft
  - * constant pressure boundary at node 1
  - * control volume at node 21
  - * pipe friction losses, $f = 0.02$

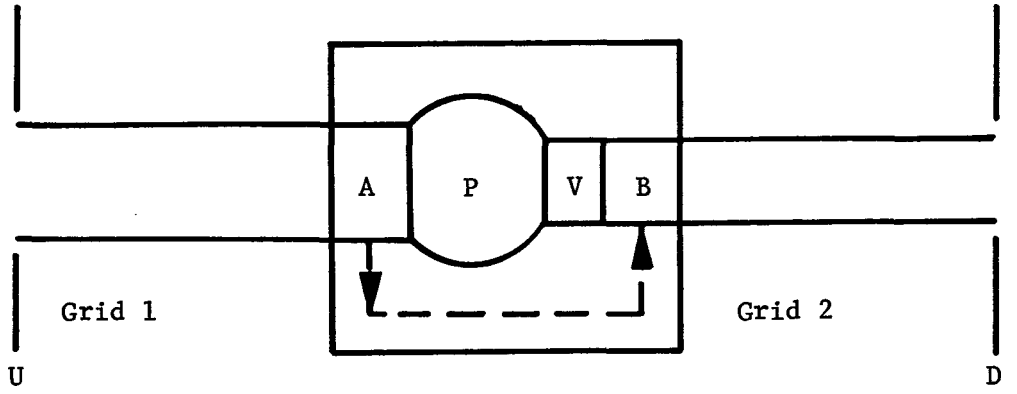

Boundaries

U upstream pressure boundary

D downstream pressure boundary

Control Volume Internals

A mass sink

P turbopump

V discharge valve

B mass source

Figure D-2. Simulation schematic of pump trip with bypass line.

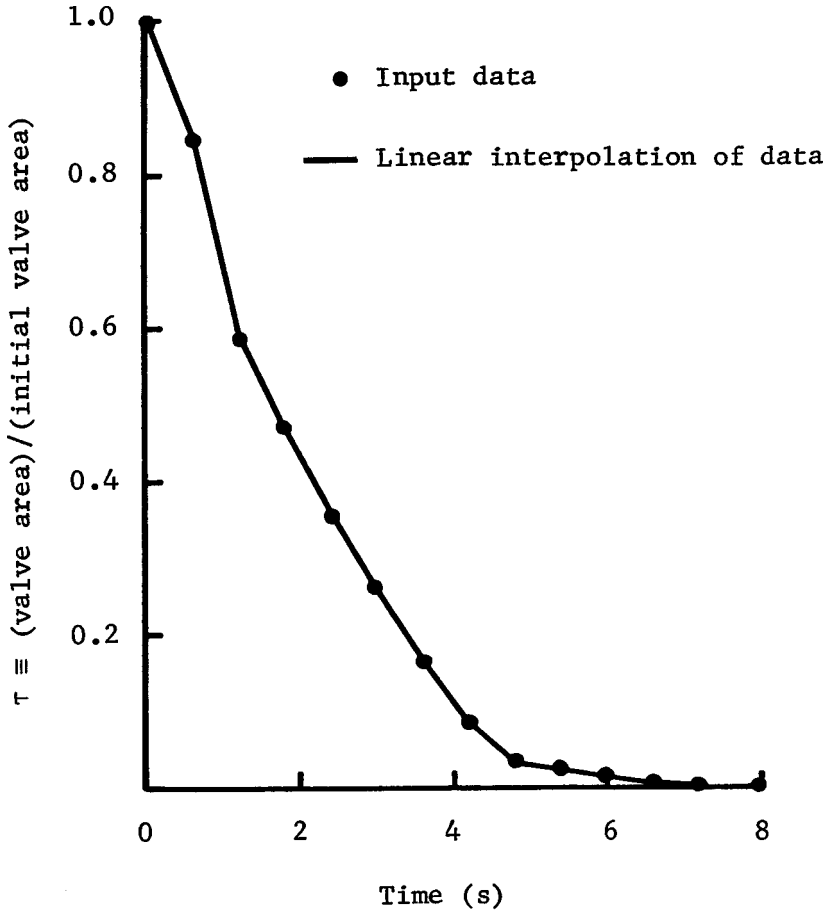

Figure D-3. Discharge valve kinematics.

- Grid #2

  * downstream of control volume
  * 20 zones
  * nodes 22 through 42
  * 1.5-ft flow diameter
  * coordinates from 1800 ft to 3800 ft
  * length of 2000 ft
  * control volume at node 22
  * constant pressure boundary at node 42
  * pipe friction losses, f = 0.02

Mathematically, the control volume accounting occurs in the equivalent Euler equation for turbopump models (see Page 32), as follows:

$$0 = \tau^2 \{ p_1 - p_4 + c(\rho_4 u_4 - \rho_1 u_1) + c \bar{\rho} Q_r Q_T' [1 + (A_2/A_3)] / A_2 + \bar{\rho} \Phi' [\Phi - \frac{1}{2}(u_3^2 - u_2^2)]_r \} - FL$$

where τ is defined on Figure D-3, the total flow rate (Q_T') is the sum of the pump flow rate (Q_{pump}'), and the bypass flow rate (Q_{bypass}'); the flow loss through the discharge valve (FL) is, in terms of the loss coefficient (K_{pcdv}):

$$FL \equiv 0.5 K_{pcdv} \bar{\rho} (Q_r Q_{pump}' / A_4)^2 .$$

The equivalence of the pressure drop through each of the parallel flow paths determines Q_{bypass}':

$$0.5 K_{pccv} \bar{\rho} (Q_r Q_{bypass}' / A_4)^2 = p_1 - p_4 + c(\rho_4 u_4 - \rho_1 u_1) + c \bar{\rho} Q_r Q_T' [1 + (A_2/A_3)] / A_2$$

where the loss coefficient of the check valve is K_{pccv}.

The fluid medium is subcooled water. It is characterized as follows:

- 2.5142×10^7 psf bulk modulus, upstream
- 3.1040×10^7 psf bulk modulus, downstream
- 4685.1 psfa reference pressure
- 1.94 slug/ft^3 reference density
- linear elastic material, with hydrodynamic spall property ($p_{spall} = 0.0$ psfa) .

There are two types of initial/boundary conditions. The first are independent, and are assigned through input data. These are the:

- upstream pressure boundary, assigned a value of 3123.4 psfa (50 in. H_2O, piezometric pressure head)
- downstream pressure boundary, assigned a value of 6246.8 psfa (100 in. H_2O, piezometric pressure head)
- relief line geometry
- discharge valve kinematics, Figure D-3
- pipe friction and piping component losses
- rated pump volumetric rate, 10 ft^3/s
- rated pump piezometric pressure head, 72 in. H_2O (4499.14 psf)
- rated pump angular speed, 75.4 rad/s
- rated pump torque, 800 ft-lb
- moment of inertia of the pump, 31.6 slug-ft^2
- four-quadrant curve for the pumping effect
- four-quadrant curve for the torque effect .

The second type of initial/boundary conditions are dependent, and must satisfy mass and energy conservation, in conjunction with the material model,

the control volume, flow losses, and the independent conditions. This second type includes the:

- initial pressure profiles in the grids
- initial density profiles in the grids
- initial flow rate of 10.33 ft^3/s, assuming that in the steady state, the pump is operating at rated speed.

In particular, with flow losses in effect, the initial pressure and density profiles must vary along the pipe length to maintain a constant flow rate. The simulation code determines the dependent initial/boundary conditions from assigned input data.

During the simulation, rezoning maintains the position consistency between the material frame grid zones and the fixed control volume model. The algorithm periodically returns each grid node* to its original (Eulerian) position. The nodes that are interior to the installation return under the constraints of mass conservation and energy conservation, while the two exterior boundary nodes return according to a constant pressure constraint. Also, the algorithm adjusts the velocities of the rezoned nodes to be consistent with the velocity profiles defined by their neighboring nodes.

Figure D-4 displays the input data which define the pump trip event. This involves the standard input package for the STEALTH code. The loss data and four-quadrant pump curve data are not part of the input data package; they are loaded directly into DATA statements. Also loaded in this fashion are the pipe diameters assigned to each node, and two integer scaling factors which control the magnitude of the effect of the loss coefficients. Figure D-5 illustrates these DATA statements.

*But no two adjacent nodes are rezoned simultaneously.

```
TTL       TURBO MACHINE TEST PROBLEM, SLUGS-FT-SEC
PRB
GRD       1.0                21.0
GRD       2.0                21.0
END
MAT
111       1.0
121       1.0       1.94
122       1.0       1.0       4685.1     2.5142E+07
123       1.0       -1.0      10.0
111       2.0
121       2.0       1.94
122       2.0       1.0       4685.1     3.1040E+07
123       2.0       -1.0      10.0
END
GPT
211       1.0       1.0                  0.0
211       2.0       22.0                 1800.0
221       1.0       1.0       21.0
221       2.0       22.0      42.0
242       1.0       20.0      0.0        1800.0
242       2.0       20.0      1800.0     2000.0
END
ZON
311       1.0       1.0       21.0
311       2.0       22.0      42.0
321       1.0       1.0
321       2.0       2.0
322       1.0       1.0
322       2.0       1.0
331       1.0       4.15751688
331       2.0       5.65884242
381       1.0       1.0       1.0
381       2.0       2.0       41.0
381       3.0       42.0      42.0
382       1.0       1.0       2.0        2.0        1.0
382       2.0       1.0       2.0        1.0        1.0
382       3.0       1.0       2.0        2.0        1.0
END
```

(continued on next page)

Figure D-4. Input data for pump trip simulation.

```
BDY
421       1.0       2.0       5.0       1.0
421       21.0      7.0       5.0       5011.0
421       22.0      7.0       5.0       5012.0
421       42.0      2.0       5.0       2.0
422       1.0       1.0
422       2.0       2.0
431       1.0       1.0       0.0       3600.0
431       2.0       1.0       0.0       3600.0
432       1.0       3123.4
432       2.0       6246.8
471       1.0       1.75      1.5       10.0      72.0      32.2      75.4
471       1.0       800.0     31.6      89.0      0.000001
END
TIM
511       0.00625
512       0.000001  1.0
513                 0.85
521       8.0       1000.0
END
EDT                                               1.0
621       1.0       0.0       8.0       1.0
622       1.0       42.0
623       1.0       11.0
623       2.0       12.0
623       3.0       64.0
623       4.0       46.0
623       5.0       21.0
623       6.0       51.0
623       7.0       5.0
623       8.0       6.0
623       9.0       47.0
623       10.0      45.0
623       11.0      41.0
623       12.0      42.0
623       13.0      66.0
623       14.0      13.0
623       15.0      48.0
623       16.0      65.0
624       1.0
END
END
```

Figure D-4. (concluded)

```
 DATA DIA /21*1.75,21*1.5/
 DATA FRK /42*0.02/
 DATA XKL /242*0.0/
 DATA LOSSF,LOSSK/1,1/
 DATA WH/-.69,-.599,-.512,-.418,-.304,-.181,-.078,-.011,.032,.074,
..13,.19,.265,.363,.46,.553,.674,.848,1.075,1.337,1.629,1.929,2.18,
.2.334,2.518,2.725,2.863,2.948,3.026,3.015,2.927,2.873,2.771,2.64,
.2.497,2.441,2.378,2.336,2.288,2.209,2.162,2.14,2.109,2.054,1.97,
.1.86,1.735,1.571,1.357,1.157,1.016,.927,.846,.744,.64,.5,.374,
..191,.001,-.19,-.384,-.585,-.786,-.972,-1.185,-1.372,-1.5,-1.94,
.-2.16,-2.29,-2.35,-2.35,-2.23,-2.2,-2.13,-2.05,-1.97,-1.895,-1.81,
.-1.73,-1.6,-1.42,-1.13,-.95,-.93,-.95,-1.,-.92,-.69/
 DATA WB/-1.42,-1.328,-1.211,-1.056,-.87,-.677,-.573,-.518,-.38,
.-.232,-.16,.0,.118,.308,.442,.574,.739,.929,1.147,1.37,1.599,
.1.839,2.08,2.3,2.48,2.63,2.724,2.687,2.715,2.688,2.555,2.434,
.2.288,2.11,1.948,1.825,1.732,1.644,1.576,1.533,1.522,1.519,1.523,
.1.523,1.49,1.386,1.223,1.048,.909,.814,.766,.734,.678,.624,.57,
..5,.407,.278,.146,.023,-.175,-.379,-.585,-.778,-1.008,-1.277,
.-1.56,-2.07,-2.48,-2.7,-2.77,-2.8,-2.8,-2.76,-2.71,-2.64,-2.54,
.-2.44,-2.34,-2.24,-2.12,-2.,-1.94,-1.9,-1.9,-1.85,-1.75,-1.63,
.-1.42/
 DATA VTAU /1.,.85,.58,.46,.35,.25,.16,.08,.03,.02,.01,.001,8*0./
```

DIA: pipe diameters

FRK: pipe friction loss coefficients

XKL: piping component loss coefficients (deactivated; this simulation incorporates component losses directly in the Euler energy equation)

LOSSF: scaling factor for friction coefficients

LOSSK: scaling factor for component coefficients

WH: four-quadrant curve data for the coefficient of pressure differential across pump; $\Delta\bar{\theta}$ is 0.0174 radians

WB: four-quadrant curve data for the coefficient of pump torque; $\Delta\bar{\theta}$ is 0.0714 radians

VTAU: discharge valve kinematic data (see Figure D-3)

Figure D-5. Data statements for pump trip simulation.

D.3 DISCUSSION OF SIMULATION

The simulation begins when the pump trip and the start of discharge valve closure interrupt the steady-state initial conditions. These initial conditions are represented in Figure D-6, by the initial piezometric pressure head profile through the pump branch. The profile demonstrates the head losses due to pipe friction upstream (A) and downstream (C) of the pump, as well as the head rise across the pump (B). The simulation ends at 8 seconds, soon after the discharge valve has closed (7.2 seconds).

Since the control volume model lumps a number of separate effects into one, and since the non-varying pressure boundaries are not realistic, there will be no attempt to interpret this simulation on the basis of physical events. (Figure D-7 illustrates the effect of the non-realistic boundary conditions: at 6 seconds into the trip, the boundaries are driving the pump.) This discussion will concentrate on the evidence that suggests the validty of the pump model: comparison with the benchmark simulation of Wylie and Streeter.

Pump performance during the trip event is the primary basis for comparing the two simulations -- in particular, the histories of pump rotational speed and pump flow rates. Table D-1 displays non-dimensionalized rotational speeds (see Page 31*), and a percentage difference between the two, at selected times for each simulation. The percentage difference is based on the initial speed, which is identical for each simulation. The average difference over 8 seconds is 0.3%, and the maximum is 0.4%. In a similar manner, Table D-2 displays non-dimensionalized pump flow rates, with a similar percentage difference. Here, the average difference is 0.21%, and the maximum is 0.58%. These extremely small differences imply that the two simulations are predicting virtually the same pump behavior.

Bypass performance during the pump trip is another basis of comparison between the two simulations. Table D-3 displays non-dimensionalized bypass flow rates, and a local percentage difference between the two

*For definition of non-dimensionalized rotational speeds.

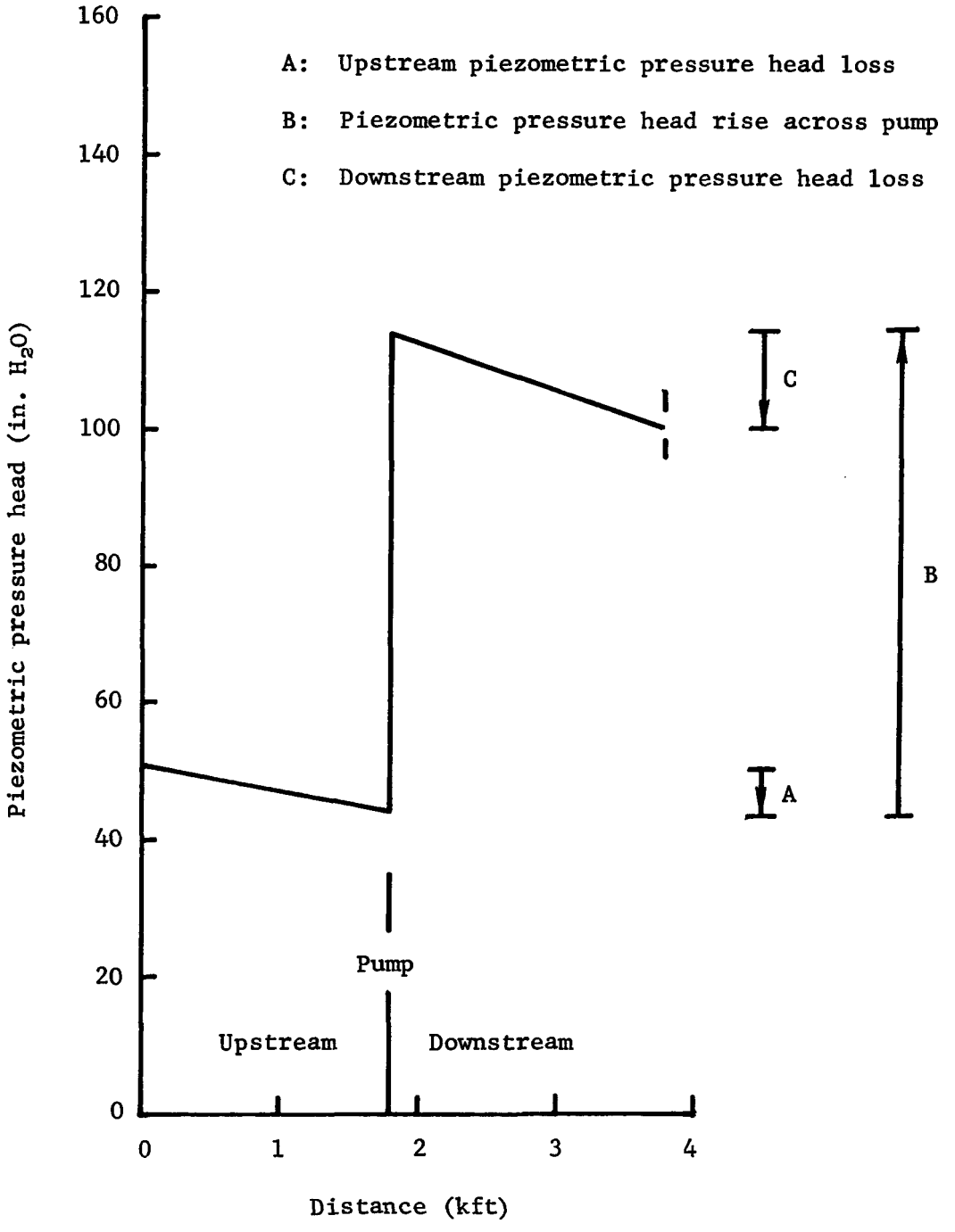

Figure D-6. Initial piezometric pressure head profile.

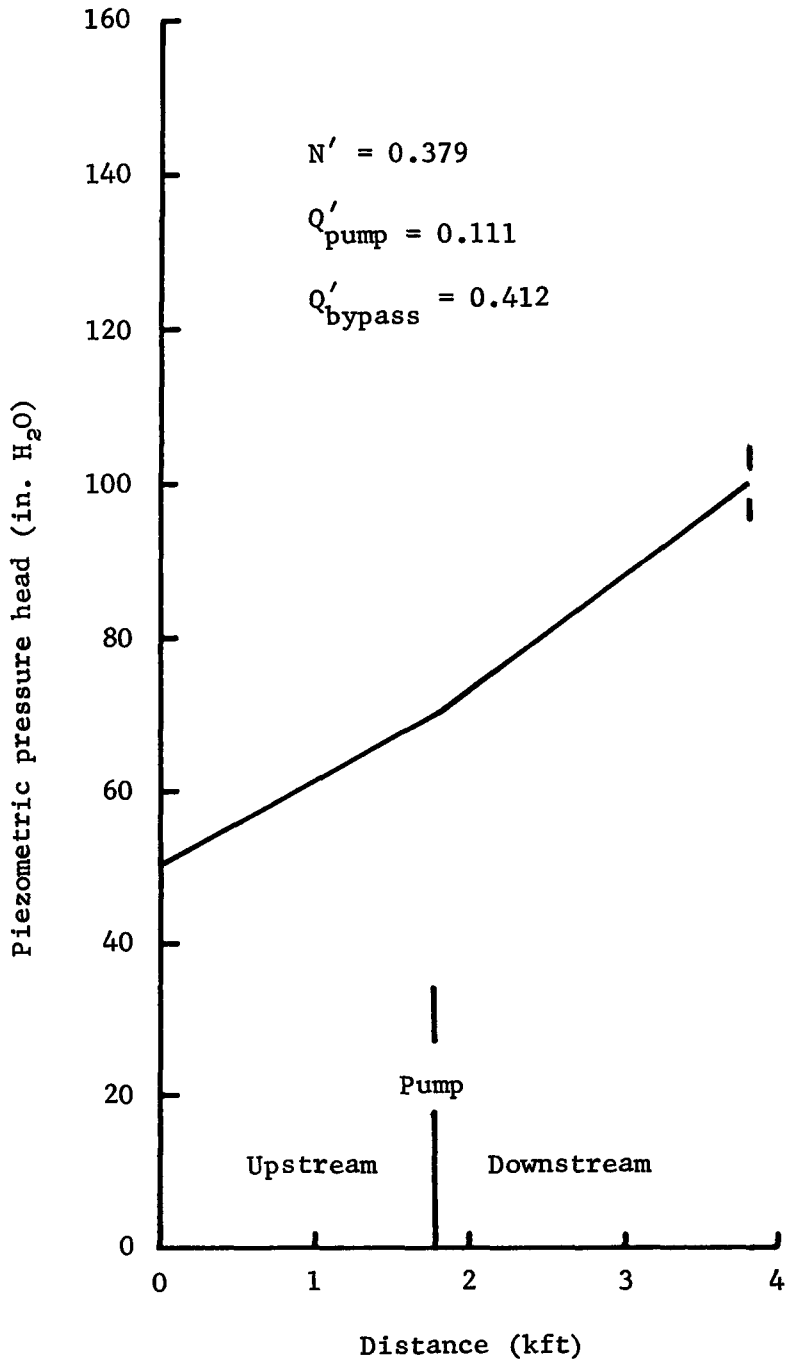

Figure D-7. Piezometric pressure head profile at 6 seconds.

TABLE D-1. NON-DIMENSIONALIZED PUMP ROTATIONAL SPEEDS

Time (s)	N'_s	N'_{ws}	% Δ
0	1.0	1.0	0.00
1	0.762	0.762	0.00
2	0.641	0.638	0.30
3	0.562	0.558	0.40
4	0.500	0.496	0.40
5	0.436	0.432	0.40
6	0.382	0.379	0.30
7	0.327	0.324	0.30
8	0.322	0.319	0.30

N'_s: From STEALTH simulation

N'_{ws}: From Wylie and Streeter simulation

$\% \Delta \equiv (100)\left| N'_{ws} - N'_s \right| / N'_{ws}$ at initial time

TABLE D-2. NON-DIMENSIONALIZED PUMP FLOW RATES

Time (s)	Q'_s	Q'_{ws}	% Δ
0	1.033	1.033	0.00
1	0.995	0.994	0.10
2	0.910	0.908	0.19
3	0.814	0.811	0.29
4	0.716	0.710	0.58
5	0.304	0.302	0.19
6	0.109	0.111	0.19
7	0.003	0.004	0.10
8	0.000	0.000	0.00

Q'_s: From STEALTH simulation

Q'_{ws}: From Wylie and Streeter simulation

$\%\Delta \equiv (100)\left|Q'_{ws} - Q'_s\right| / Q'_{ws}$ at initial time

TABLE D-3. NON-DIMENSIONALIZED BYPASS FLOW RATES

Time (s)	Q'_s	Q'_{ws}	$\%\bar{\Delta}$
0	0.000	0.000	--
1	0.000	0.000	--
2	0.000	0.000	--
3	0.000	0.000	--
4	0.000	0.000	--
5	0.314	0.309	1.61
6	0.412	0.403	2.21
7	0.426	0.417	2.14
8	0.341	0.331	2.98

Q'_s: From STEALTH simulation

Q'_{ws}: From Wylie and Streeter simulation

$\%\bar{\Delta} \equiv (100)\left|Q'_{ws} - Q'_s\right| / \text{average}\ (Q'_{ws}, Q'_s)$

simulations. (Here, the initial bypass flow rate is zero, which is not a meaningful basis for percentage difference.) The local average difference over the final 4 seconds is 2.24%, and the maximum is 2.98%. Owing to the different basis, these percentages are an order of magnitude greater than the primary comparisons. Even so, these differences are small, and they support the conclusion that the two simulations are virtually the same.

Thus, STEALTH 1D has an operational control volume model for turbopumps.

D.4 CLOSURE

This simulation requires 381 time cycles to span 8 seconds of real time. It performs 16,002 node-cycle calculations in 9 seconds of CDC 7600 CP time, and is core-contained in memory. This execution requires 0.56 CP ms per node-cycle. If the calculations were extended over thousands of time cycles, the CP ms per node-cycle would improve, approaching the 0.34 value reported in Appendix B.

APPENDIX E
SIMULATION OF THE SEMI-SCALE 711 EXPERIMENT

E.1 INTRODUCTION

The hypothetical sudden rupture of a cold leg in the primary loop of a pressurized water reactor (PWR), which operates at $\sim$ 150 bars, could induce an asymmetric blowdown flow field to develop within the reactor vessel containment region. This field would begin at the point of rupture with a rarefaction hammer that would travel through the water in the cold leg, toward the primary containment region of the PWR. As the pulse entered the water in the containment region, the field would become highly three-dimensional, expanding along the length and circumference of the outer surface of the core barrel. Finally, a portion of the hammer would carry the flow field into the internal volume of the barrel. In turn, these events would produce secondary pulses, which could sustain the flow field for hundreds of milliseconds. Flow fields with these characteristics can provide a useful data base for evaluating the validity of thermohydraulic numerical simulations.

In the first phase of a program to accomplish this evaluation, Idaho Nuclear Engineering Laboratory designed and performed the Semi-Scale 711 Experiment. The experiment produces an asymmetric blowdown flow field that is qualitatively similar to the event that might occur in the primary containment region of a PWR. Specifically, the apparatus contains flow passages, illustrated in Figure E-1, similar to a portion of a cold leg, the annular volume between the core barrel and the containment boundary, and the internal volume of the barrel. Prior to the start of the experiment, the passages were filled with water and pressurized to 158 bars. The experiment initiated when the blowdown nozzle, attached to the end of the cold leg, opened. Four transducers, located as shown on Figure E-1, recorded pressure histories during the blowdown.

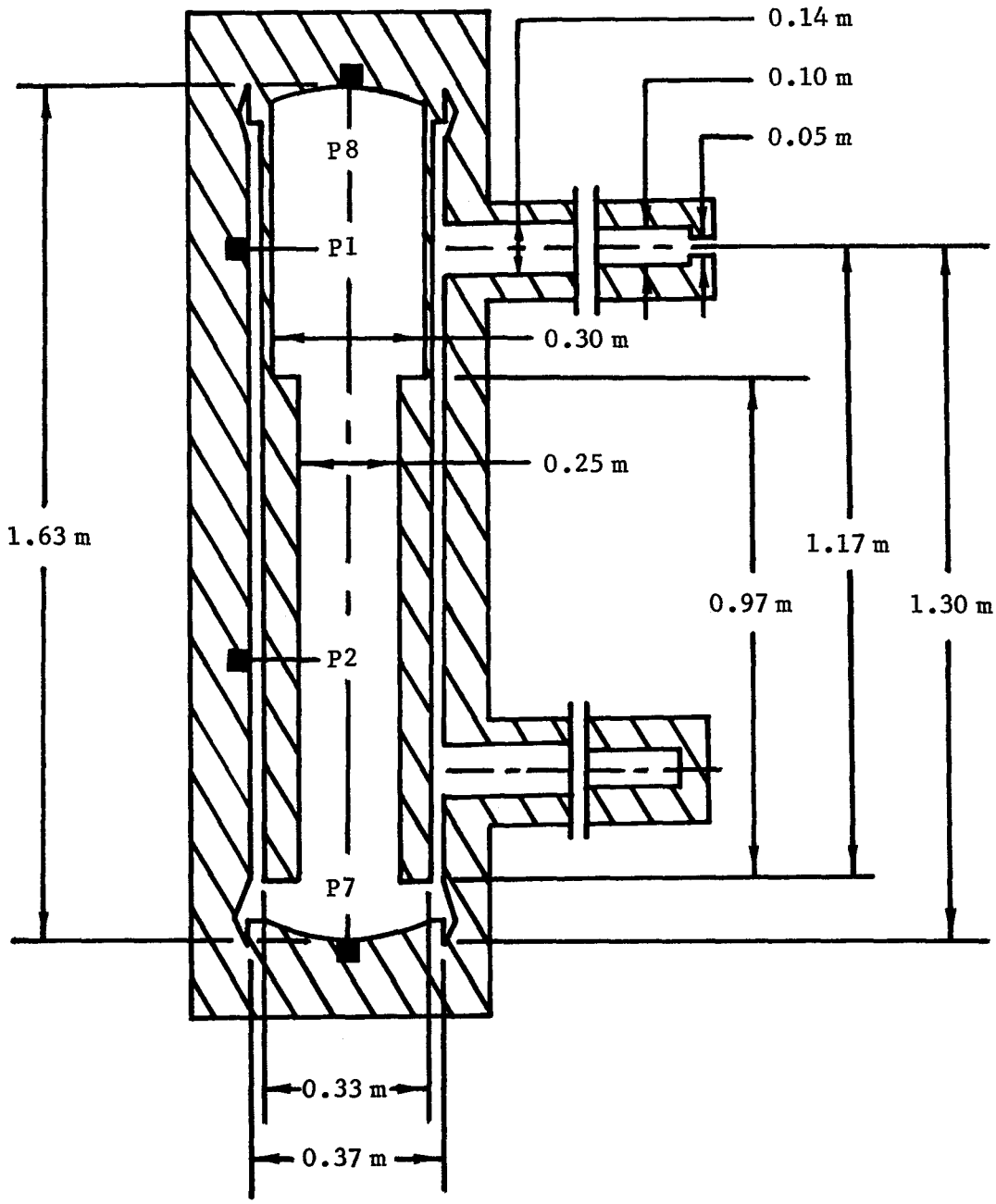

Figure E-1. Flow passages of the Semi-Scale 711 Experiment apparatus.

In the second phase of the program, Intermountain Technologies, Inc. (ITI) used the STEALTH hydrocode in conjunction with control volume models of piping components to perform a numerical simulation of the Semi-Scale 711 Experiment. Their application is unusual in that it is a one-dimensional piping simulation of a three-dimensional flow field.

This Appendix briefly describes ITI's numerical simulation of the Semi-Scale 711 Experiment. (It is not a comprehensive documentation of the simulation; that will appear in a forthcoming ITI report.) The simulation is reported here to demonstrate the versatility of the STEALTH piping component models.

E.2 ITI CONSTRUCTION OF SIMULATION

The numerical simulation of the Semi-Scale 711 Experiment incorporates the one-dimensional hydro version of STEALTH with the control volume models of the orifice, the tee junction, and the area change. Figure E-2 depicts, schematically, the computational grids, control volumes, and boundary conditions that model the experiment apparatus. The figure also indicates the equivalent locations of the experiment pressure transducers. (In this simulation, there was no model for flow losses.) Grids 1 and 2, an area change control volume, and a rigid boundary represent the volume that simulates the region inside a PWR core barrel. Another area change model links Grid 2 with Grid 3, which models the lower plenum region. Grid 4, which simulates the lower annular region, connects with Grid 3 through the third area change, and with Grids 5 (the middle annular simulation) and 9 (a section of pipe) through a tee junction model. Grid 8 models a blind nozzle that connects through an area change model to Grid 9, and terminates at a rigid boundary. The second tee junction links Grid 5 with Grid 10 (the simulation of the upper annular region that terminates at a rigid boundary) and Grid 6 (the model of the cold leg). Grid 7 models the blowdown nozzle that connects with Grid 6, and opens to the atmosphere through a blowdown orifice. Figure E-3 depicts the geometry of the control volumes. The ten computational

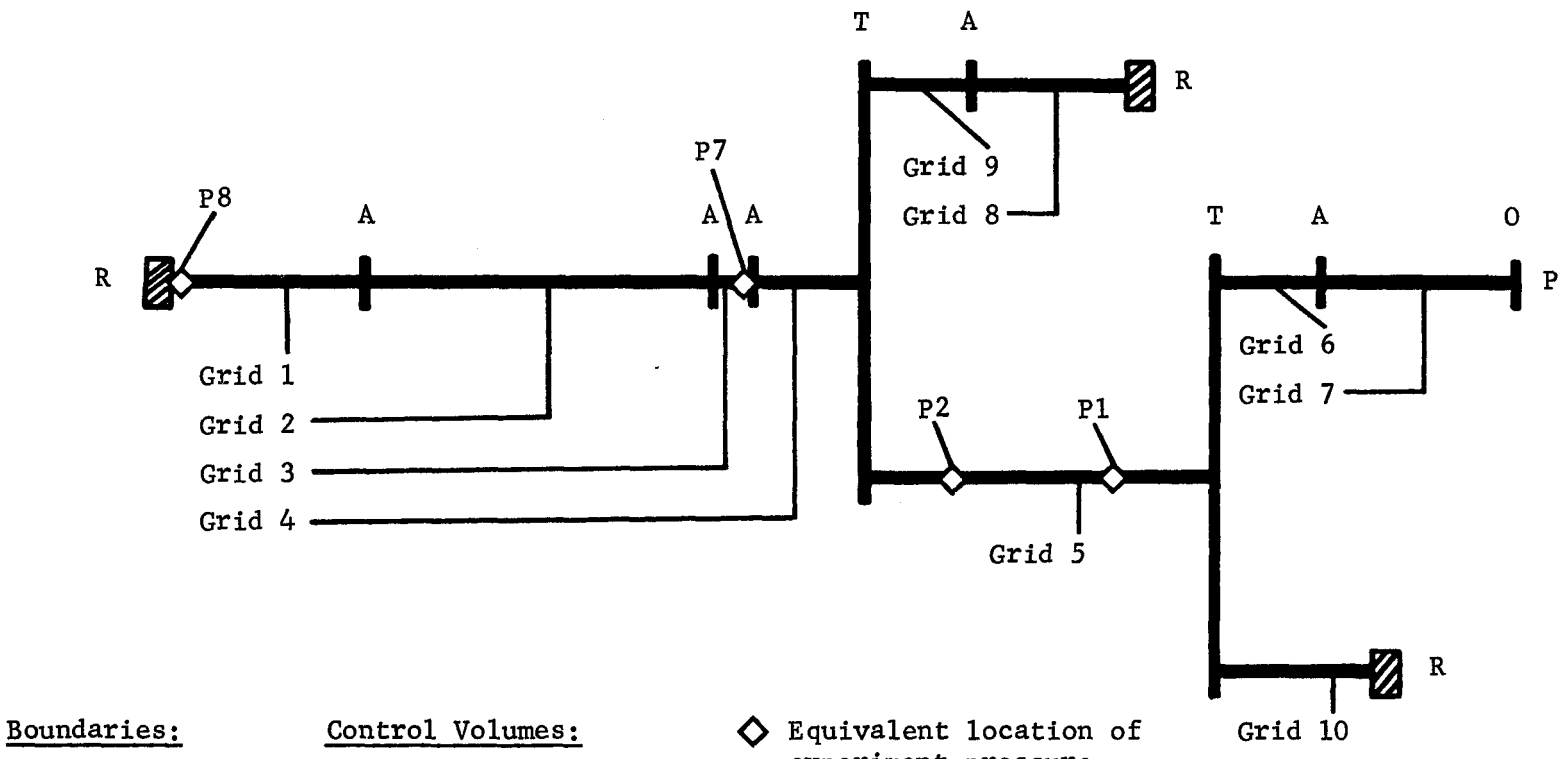

Figure E-2. Simulation schematic of blowdown event.

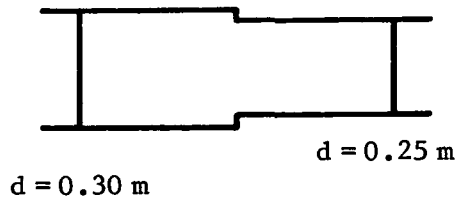

Area change between Grids 1 and 2

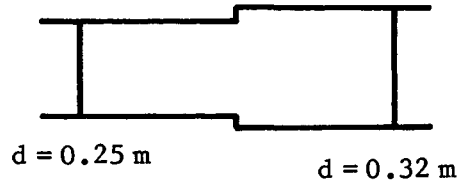

Area change between Grids 2 and 3

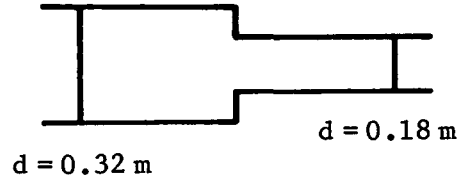

Area change between Grids 3 and 4

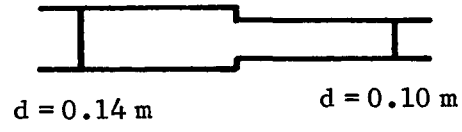

Area change between Grids 6 and 7, and between Grids 8 and 9

Figure E-3. Control volumes for blowdown simulation.

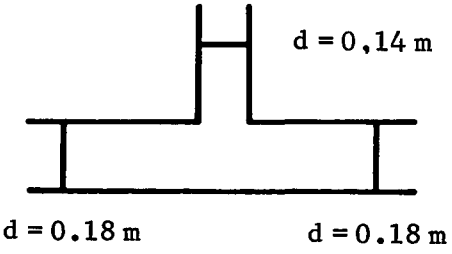

Tee linking Grids 4, 5, and 9, and linking Grids 5, 6, and 10

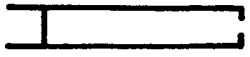

Orifice at the end of Grid 7

Figure E-3 (concluded).

grids possess the following characteristics:

- Grid #1
  - * interior core barrel region that is adjacent to the rigid boundary
  - * 22 zones
  - * nodes 1 through 23
  - * 0.303225-m flow diameter
  - * length of 0.5080 m
  - * rigid boundary at node 1
  - * area change at node 23

- Grid #2
  - * interior core barrel region (that is partially blocked with fuel assemblies)
  - * 39 zones
  - * nodes 24 through 63
  - * 0.254485-m flow diameter
  - * length of 0.9652 m
  - * area changes at nodes 24 and 63

- Grid #3
  - * lower plenum
  - * 4 zones
  - * nodes 64 through 68
  - * 0.323824-m flow diameter
  - * length of 0.1016 m
  - * area changes at nodes 64 and 68

- Grid #4
  - * lower annular region
  - * 12 zones
  - * nodes 69 through 81

* 0.175371-m flow diameter
* length of 0.3048 m
* area change at node 69
* tee junction at node 81

- Grid #5
  * middle annular region
  * 38 zones
  * nodes 82 through 120
  * 0.175371-m flow diameter
  * length of 0.9652 m
  * tee junctions at nodes 82 and 120

- Grid #6
  * cold leg section
  * 11 zones
  * nodes 121 through 132
  * 0.143876-m flow diameter
  * length of 0.2794 m
  * tee junction at node 121
  * area change at node 132

- Grid #7
  * blowdown nozzle
  * 23 zones
  * nodes 133 through 156
  * 0.103179-m flow diameter
  * length of 0.5842 m
  * area change at node 133
  * orifice at node 156

- Grid #8
  - * blind nozzle
  - * 17 zones
  - * nodes 157 through 174
  - * 0.103179-m flow diameter
  - * length of 0.4826 m
  - * area change at node 157
  - * rigid boundary at node 174

- Grid #9
  - * section of pipe
  - * 11 zones
  - * nodes 175 through 186
  - * 0.143876-m flow diameter
  - * length of 0.2794 m
  - * tee junction at node 175
  - * area change at node 186

- Grid #10
  - * upper annular region
  - * 12 zones
  - * nodes 187 through 199
  - * 0.175371-m flow diameter
  - * length of 0.3048 m
  - * tee junction at node 187
  - * rigid boundary at node 199

The fluid medium is subcooled water, with linear elastic behavior. Its acoustic speeds are assigned:

- 96.62 cm/ms in Grid 1
- 100.74 cm/ms in Grid 2
- 104.85 cm/ms in Grids 3 through 10

The initial conditions for the blowdown are:

- initial pressure of 158 bars
- initial density
  - * 0.761 g/cc in Grid 1
  - * 0.778 g/cc in Grid 2
  - * 0.793 g/cc in Grids 3 through 10

The boundary conditions that constrain the flow field are:

- an atmospheric pressure boundary at the orifice on the end of Grid 7
- rigid boundaries at the appropriate ends of Grids 1, 8, and 10

During the simulation, rezoning maintains the position consistency between the material frame grid zones and the fixed control volume models. The algorithm periodically returns each grid node* to its original (Eulerian) position. The nodes return under the constraints of mass conservation and energy conservation. Also, the algorithm adjusts the velocities of the rezoned nodes to be consistent with the velocity profiles defined by their neighboring nodes.

E.3 DISCUSSION OF SIMULATION

The pressure histories at the transducer locations (Figure E-1), or the equivalent locations (Figure E-2), verify that both the simulation and the experiment produced the same sequence of events. Figure E-4 shows that the P1 location experiences the pulse $\sim$ 1 ms into the event. One-half ms later, the wave reaches the P2 location (see Figure E-5). In the next half ms, the lower plenum begins to depressurize, as indicated on Figure E-6. Finally, traveling up the internal volume, the hammer reaches the top surface

*But no two adjacent nodes are rezoned simultaneously.

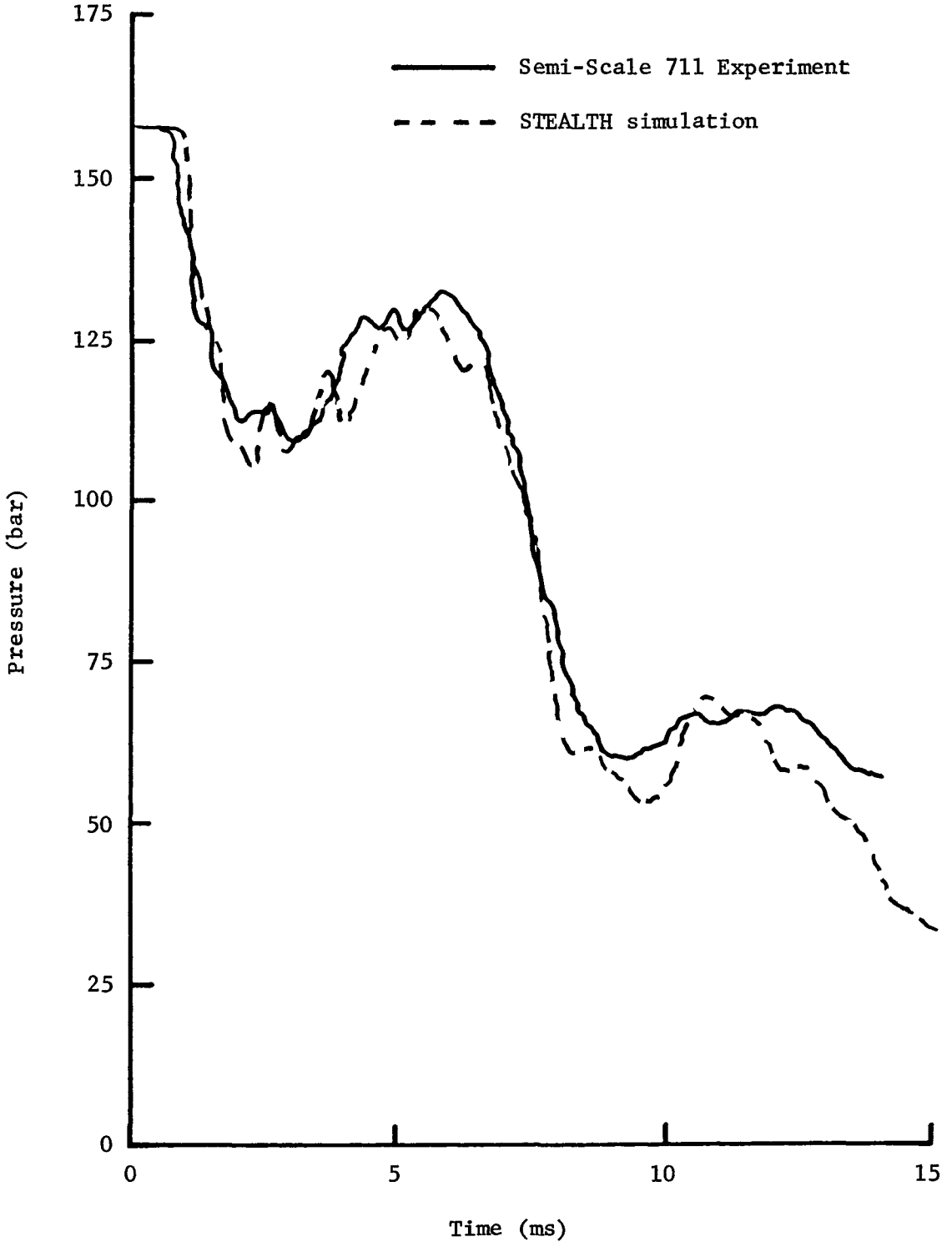

Figure E-4. Comparison of pressure histories at P1 location.

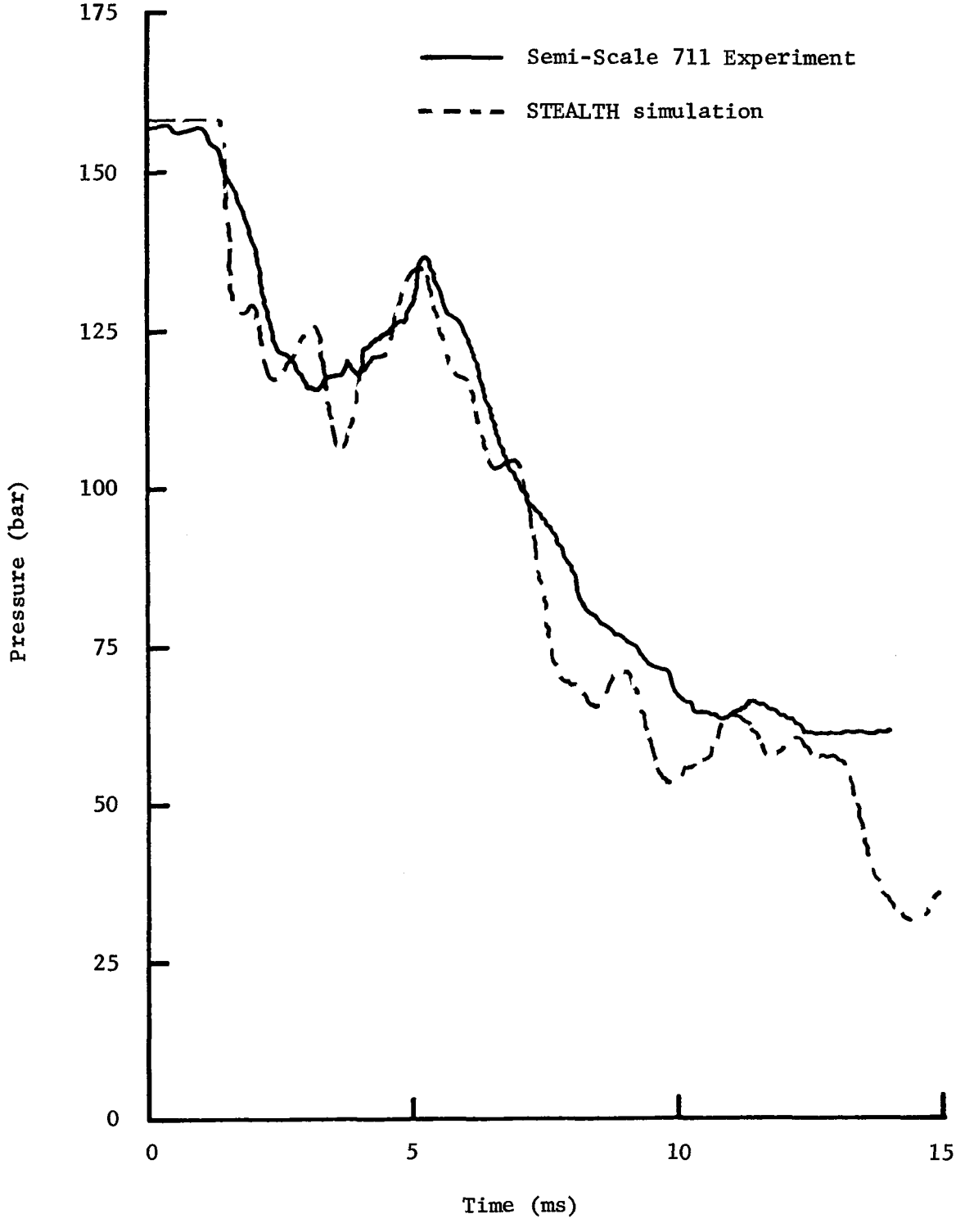

Figure E-5. Comparison of pressure histories at P2 location.

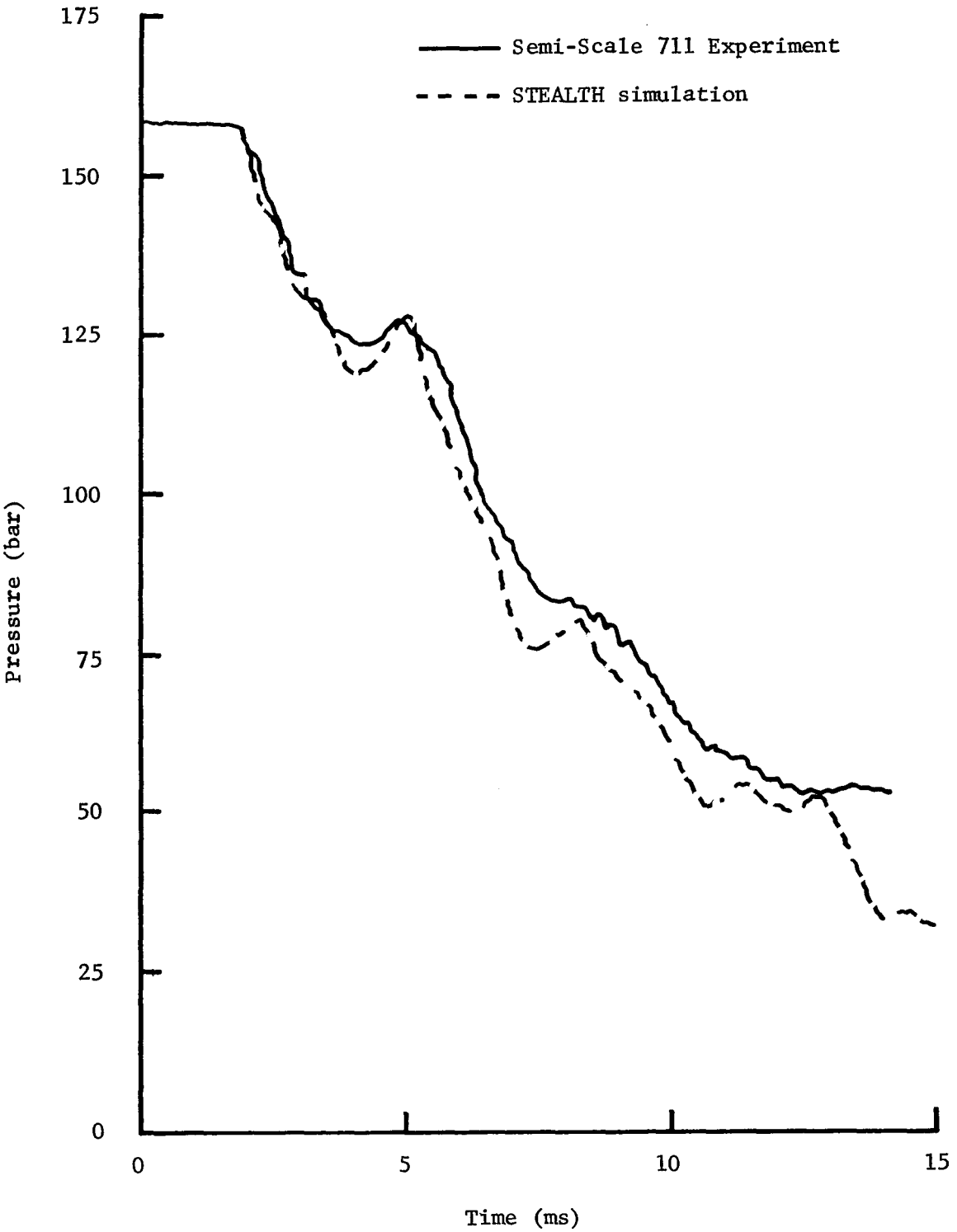

Figure E-6. Comparison of pressure histories at P7 location.

$\sim$ 3.5 ms into the event; see Figure E-7. The wave arrival times are consistent with a Mach 1 rarefaction.

The pressure history comparisons for the P1, P2, and P7 locations show that the simulation agrees very well with the experiment. These locations first depressurize, then experience some repressurization from secondary waves before continuing to depressurize. The P1 location undergoes another significant repressurization before the final depressurization.

The pressure histories for the P8 location do not match as well as those for the other locations. The pressure from the STEALTH simulation is consistently lower than that recorded for the experiment. (At this time, there is no definite explanation for the discrepancy.) Nevertheless, the comparison shows that both histories exhibit similar behavior, and that their differences are less than 8% of the initial level.

These histories indicate that the STEALTH 1D piping simulation sucessfully modeled the Semi-Scale 711 Experiment.

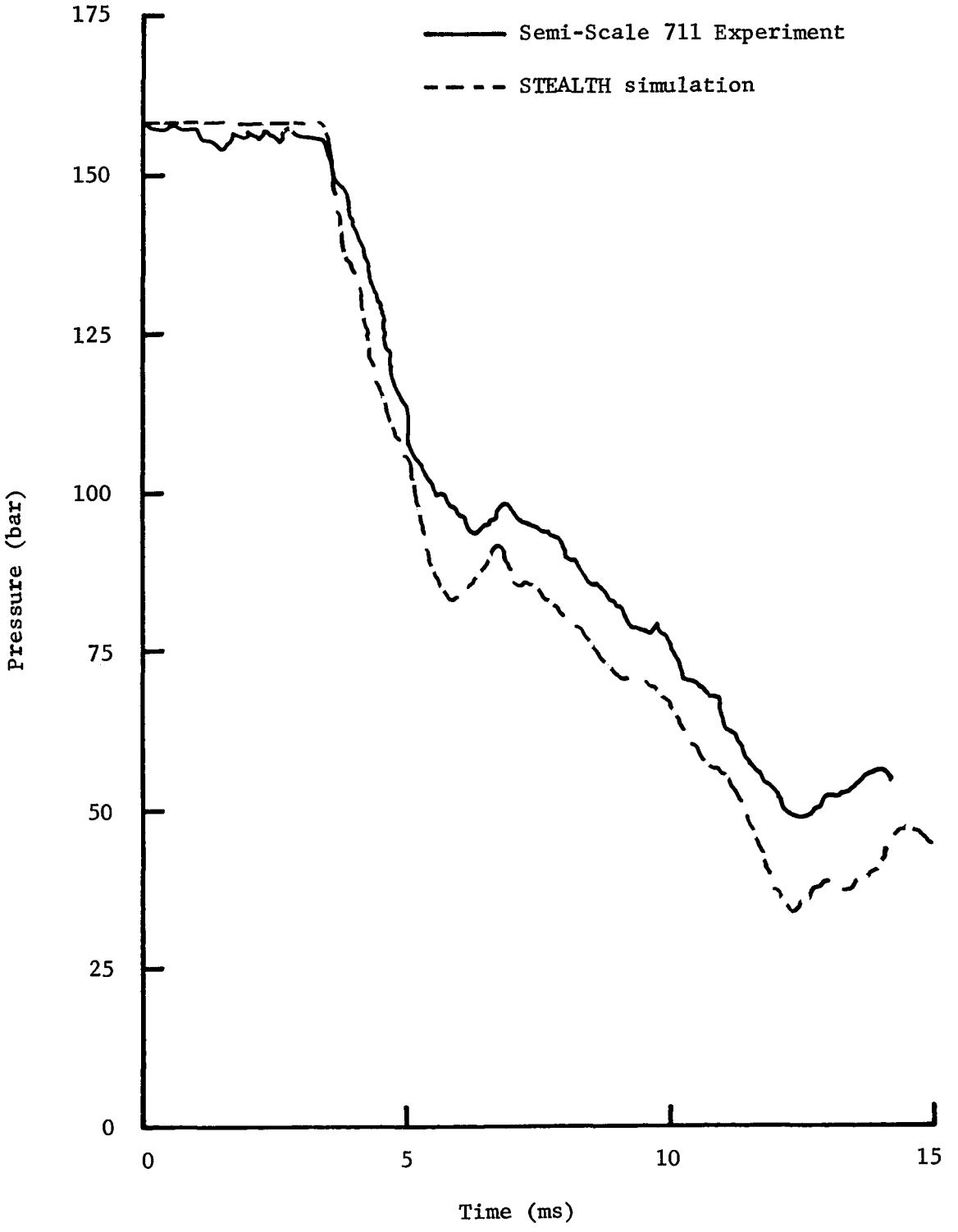

Figure E-7. Comparison of pressure histories at P8 location.

APPENDIX F

SIMULATION OF THE RESPONSE OF A WATER-FILLED, STRAIGHT PIPE TO A PRESSURE PULSE

F.1 INTRODUCTION

Consider a compression hammer that is traveling within a water-filled, straight pipe. Behind the wave front, the overpressure produces an increase in the fluid forces that tend to expand the internal cross section of the pipe. If the pipe is sufficiently rigid (strong), it expands elastically, with minimal strain; this causes only minor attenuation of the overpressure, over a distance of wave travel that is equivalent to several pipe diameters. If, however, the pipe is flexible (e.g., a thin-walled pipe, with a small ratio of wall thickness to nominal diameter), it can expand plastically, with an appreciable strain, and experience an associated internal volumetric increase. This increase, in conjunction with the relatively large bulk modulus of the water, will reduce the overpressure behind the front, considerably, within a short distance of wave travel. Downstream, the lowered overpressure will cause the pipe to undergo less strain.

These water-filled pipe responses, that are characterized by the interaction of compression hammers and plastic strains, are dynamic thermohydraulic piping events. As such, they provide opportunities for evaluating the ability of thermohydraulic codes to perform numerical simulations of piping phenomena.

In a program to provide a data base for these evaluations, SRI International designed and performed experiments where flexible piping systems were subjected to internal pressure pulses (Reference F-1). One series of these experiments investigated straight pipes, and used the apparatus shown on Figure F-1. Prior to an experiment, the entire pipe (15 feet) was filled with water at ambient puressure and temperature conditions. The experiment initiated when the pulse gun, shown in detail on Figure F-2, generated a compression hammer in the

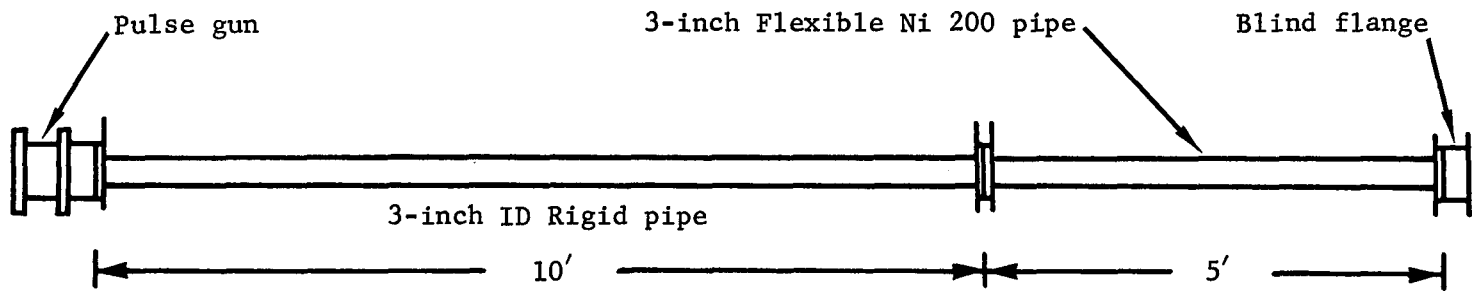

Figure F-1. Experiment apparatus for the water-filled, straight pipe experiments.

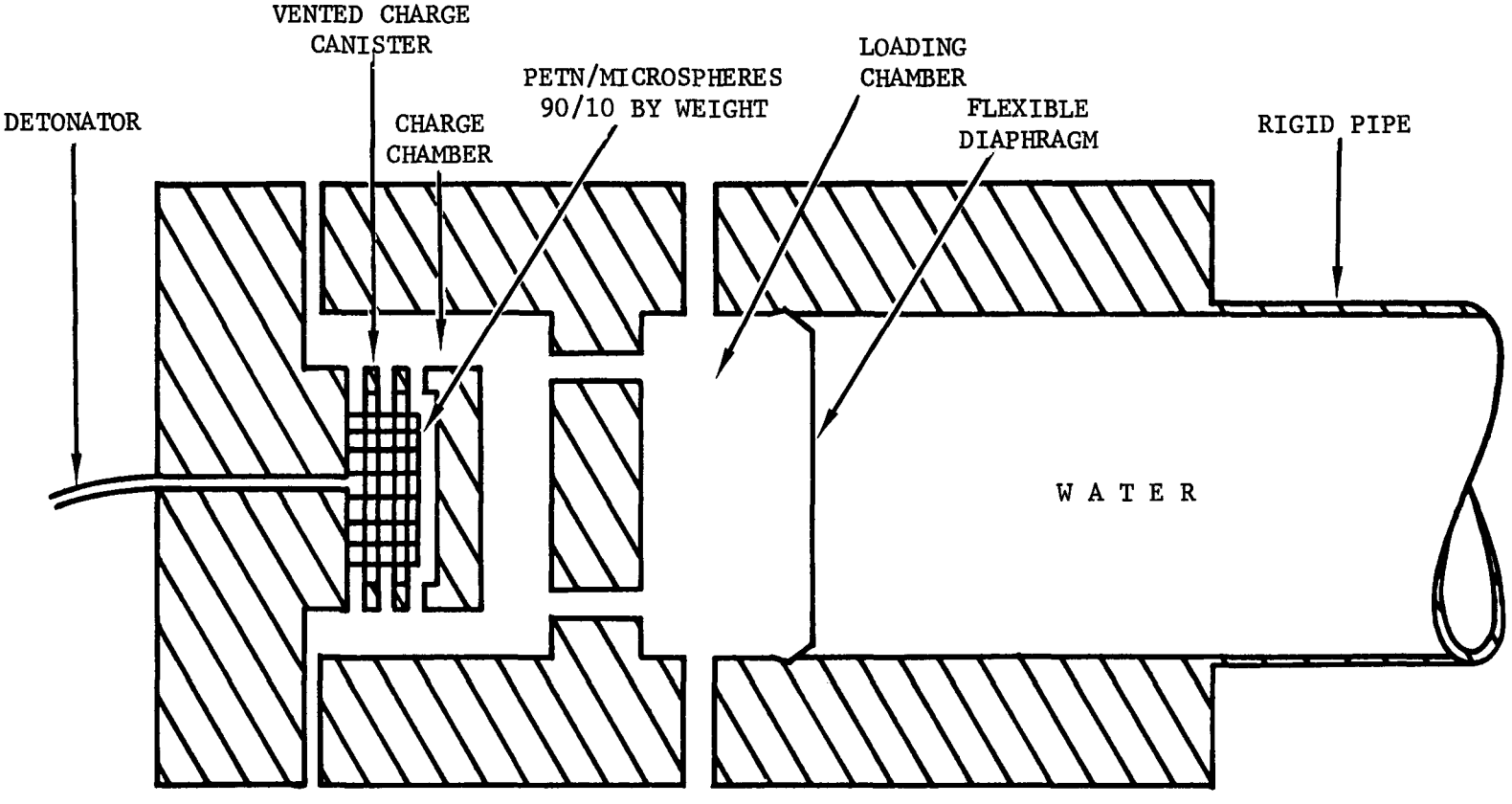

Figure F-2. Pulse gun for the water-filled, straight pipe experiments.

water, at the site of the flexible diaphragm. The ensuing flow field interacted with the pipe walls and boundaries, providing a data base that was obtained by the transducers shown on Figure F-3.

This Appendix describes a numerical simulation of the SRI Water-Filled Straight Pipe Experiments; in particular, it describes a STEALTH simulation of experiment FP-SP-102 (which is further documented in Reference F-2). The simulation combines the versatility of the STEALTH 1D flume option* with a rudimentary 1D thin shell model that simulates the elastic-plastic response of the pipe wall. The simulation demonstrates that for flexible straight pipe geometries, a simple application of the STEALTH code can predict the associated attenuation of a compression hammer.

F.2 CONSTRUCTION OF SIMULATION

The numerical simulation of SRI Experiment FP-SP-102 incorporates the one-dimensional version of the STEALTH code (variable area flume option) with a rudimentary thin shell model for elastic/plastic strain. Figure F-4 depicts the computational grid that models the experiment apparatus. The radius of the 10-foot upstream sections of the grid is fixed, while the radius of the 5-foot downstream section can vary, locally, according to the thin shell model. A varying pressure boundary drives the upstream end of the grid, while a rigid boundary constrains the downstream end.

The two sections of the grid are characterized as follows:

- Section 1
  - * rigid section
  - * 132 zones
  - * nodes 1 through 133
  - * 0.2395-ft flow diameter

*A standard variable flow area option of the STEALTH code.

P: pressure transducers

SG: strain gages

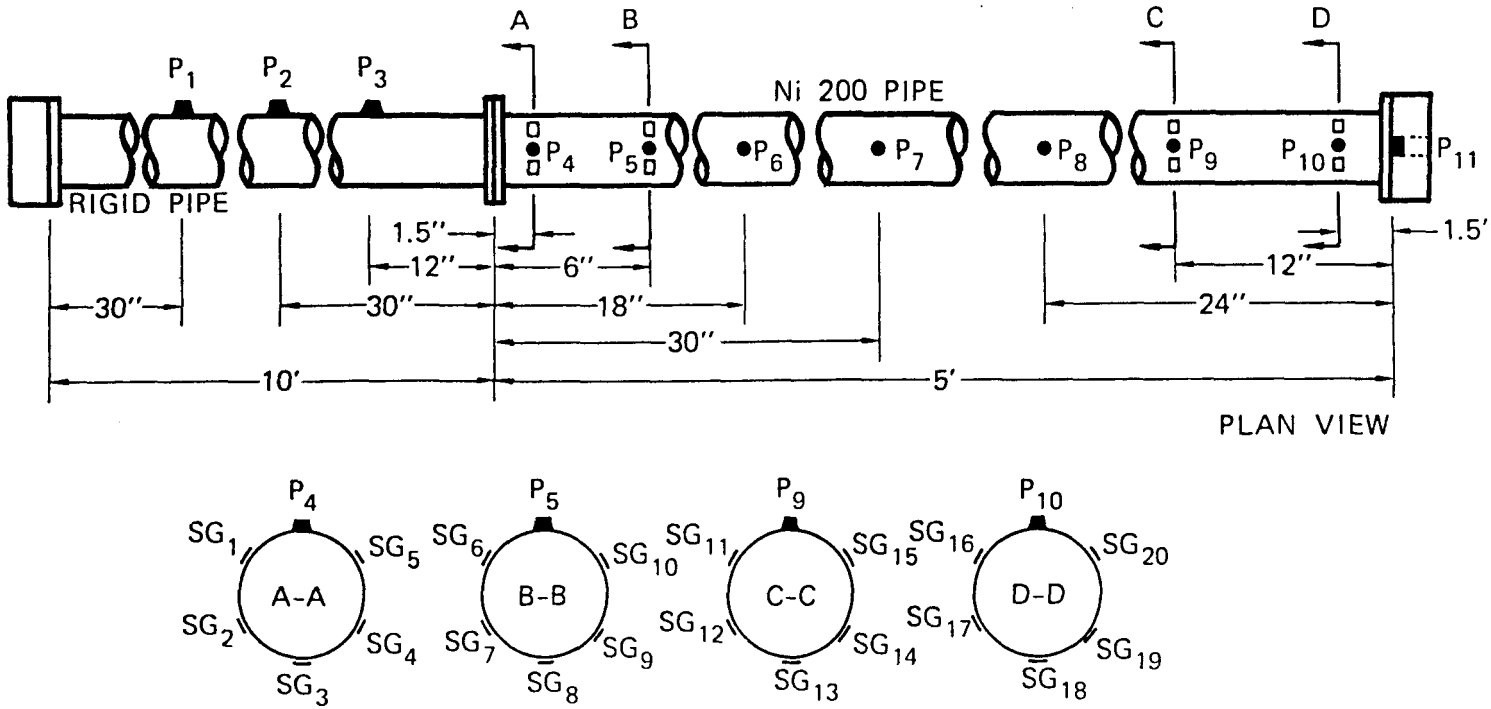

Figure F-3. Pressure and strain gage transducers for the water-filled straight pipe experiments.

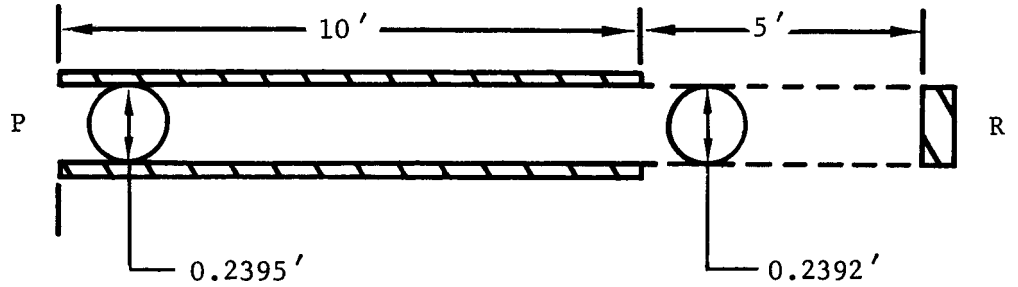

Boundaries

P: pressure boundary, p = p (time)

R: rigid boundary

Walls

: rigid

: flexible

Figure F-4. Simulation schematic for the water-filled, straight pipe experiments.

* coordinates from 0.0 ft to 10.0 ft
* length of 10 ft
* varying pressure boundary at node 1
* 3 flume wall points, rigid

- Section 2
  * flexible section
  * 66 zones
  * nodes 133 through 199
  * 0.2392-ft flow diameter
  * coordinates from 10.0 ft to 15.0 ft
  * length of 5 ft
  * rigid boundary at node 199
  * 81 flume wall points, thin shell model

The thin shell model that simulates pipe wall motion is comprised of a sequence of one-dimensional hoops with cylindrical symmetry and the properties of Nickel 200. Each flume wall point in the flexible section of pipe moves according to the response of a hoop to the local pressure difference between the internal fluid pressure and the external ambient pressure. Since the local internal pressure varies from wall point to wall point, the hoop response also varies from wall point to wall point.

Figure F-5 illustrates the flume orientation for the hoops of the thin shell model. The figure depicts three adjacent wall points (hoops) that comprise a portion of the flexible pipe section. P_{ext} is the constant ambient pressure that acts on all of the wall points, and $P_{int,i}$ is the internal fluid pressure that acts on wall point (i). The latter pressure is defined to be:

$$P_{int,i} \equiv [1/(b-a)] \int_a^b p(z)dz$$

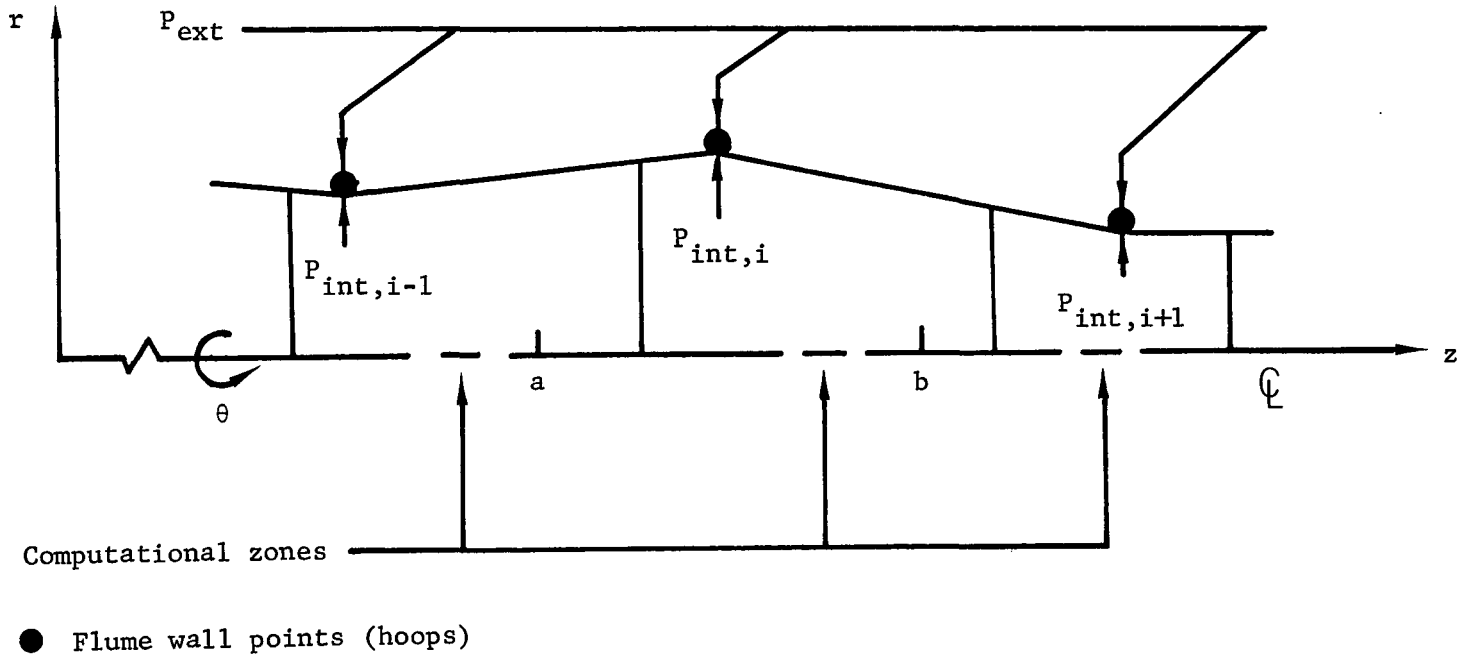

Figure F-5. Flume geometry for the thin shell model.

where

$a \equiv$ axial midpoint between wall points (i) and (i - 1)

$b \equiv$ axial midpoint between wall points (i) and (i + 1)

$p(z) \equiv$ fluid pressure at z, obtained from the appropriate STEALTH computational zone.

Each wall point responds to a radial driving stress (σ_r), where:

$$\sigma_r \equiv - \text{average}(P_{ext}, P_{int})$$

with plane strain, i.e.:

$$\epsilon_z \text{ (the axial strain)} \equiv 0 .$$

The equation of motion for each wall point is:

$$\ddot{r} = [\partial\sigma_r/\partial r + (\sigma_r - \sigma_\theta)/r] / \rho_{equiv}$$

where

$$\ddot{r} \equiv \partial^2 r/\partial t^2 .$$

In effect, this dynamic model defines the pipe wall to be a sequence of hoop rings, which "float" on the fluid medium within. The model does not account for shear stresses that can act between hoops (bending mode). The reason for the neglect of the bending mode is the assumption that for this event, shear stresses are not an important effect. The justification of this assumption occurs (in the next subsection) with the comparison of the simulation prediction and the experiment data.

The equivalent density (ρ_{equiv}) is based on an equivalent mass that accounts for the radial inertia effects of the water mass (m_w) as well as the mass of the Nickel 200 pipe wall (m_{Ni}). From a kinetic energy analysis (see, e.g., Reference F-3), and the assumption that the radial velocity of the water varies linearly with radial position, the equivalent density becomes:

$$\rho_{equiv} = \rho_{Ni}[m_{Ni} + 0.5\, m_w] / m_{Ni}$$

where

$$\rho_{Ni} = 17.28 \text{ slug/ft}^3 .$$

The material behavior for the pipe wall is defined by the stress (f) versus strain (ϵ) data shown on Figure F-6 (interpreted here as hoop stress versus hoop strain), an elastic constitutive equation, a yield criterion, and a plastic flow rule. The elastic constitutive equation is (see Reference F-4):

$$\dot{\sigma}_\alpha = (\lambda + 2G)\dot{\epsilon}_\alpha + \lambda(\dot{\epsilon}_\beta + \dot{\epsilon}_\gamma)$$

where

$$\left.\begin{array}{l} \alpha = r, \theta, z \\ \beta = z, r, \theta \\ \gamma = \theta, z, r \end{array}\right\} \quad \text{i.e., } \alpha \neq \beta \neq \gamma \neq \alpha$$

and the Lamé constants (λ and G) are

$$G = 0.5\, E/(1+\mu)$$

$$\lambda = \mu\, E/(1+\mu) / (1 - 2\mu)$$

with E (Young's modulus) determined from the stress-strain data (as shown on Figure F-6), and μ (Poisson's ratio for Nickel 200) set equal to 0.31.

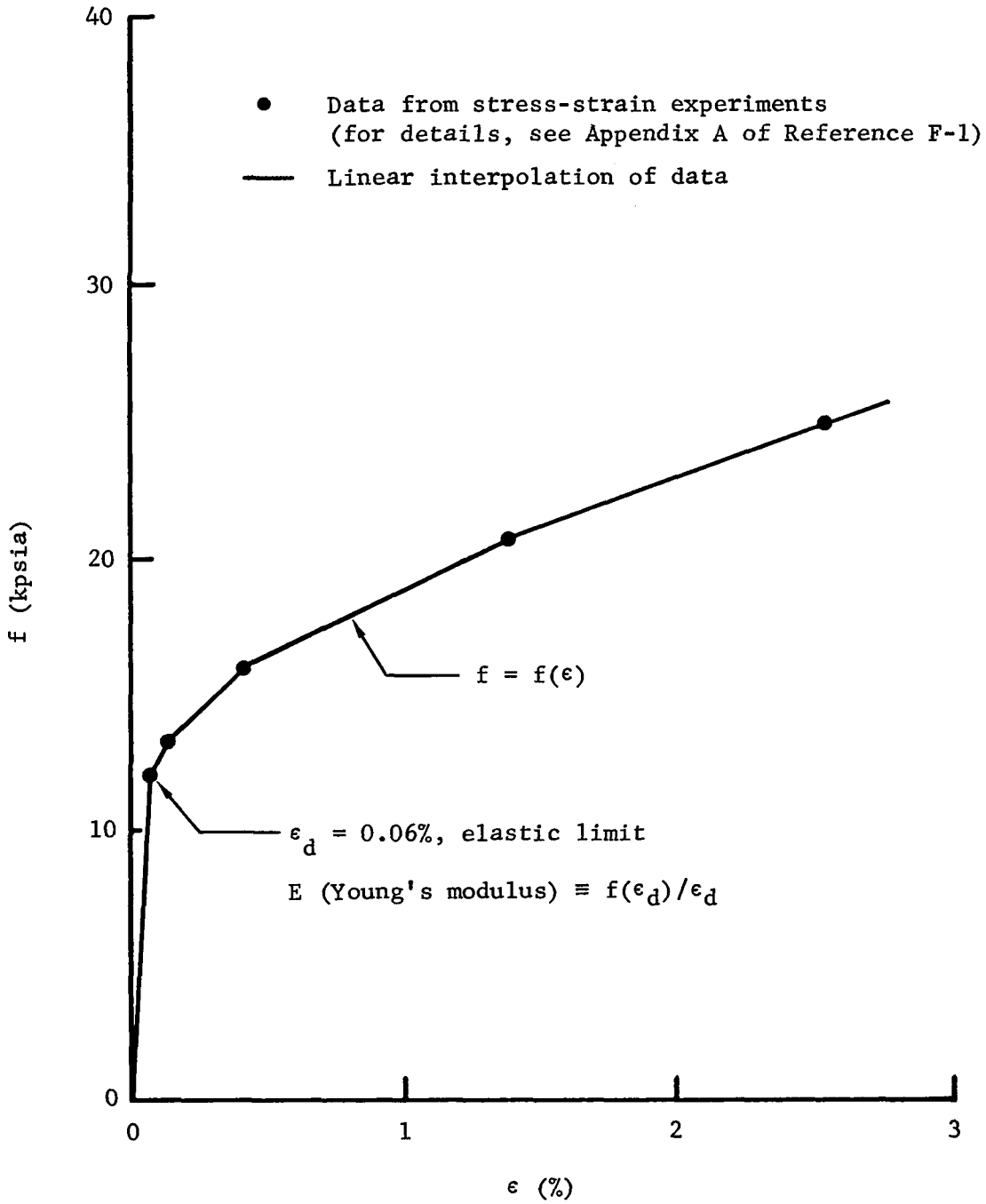

Figure F-6. Stress (f) versus strain (ε) for the Nickel 200 pipe wall.

The yield criterion for plastic flow is

$$\epsilon_\theta > \epsilon_d \rightarrow \text{plastic range}$$

where ϵ_d (the value of maximum elastic strain) is indicated on Figure F-6. In the plastic range, the stress deviators (S_r, S_θ, S_z) are adjusted by a flow rule which assures that the hoop stress follows the stress versus strain data:

$$S_\eta \equiv \varphi S_\eta, \quad \eta = r, \theta, z$$

where

$$\varphi \equiv (f + p_{Ni})/S_\theta$$

and

$f = f(\epsilon)$, the stress versus strain data

$p_{Ni} \equiv$ hydrostatic pressure within the pipe wall material .

The fluid medium is subcooled water. It is characterized as follows:

- 2116.8 psf reference pressure
- zero pressure spall limit
- 1.94 slug/ft^3 reference density
- linear elastic material .

The value for bulk modulus (k) must be consistent with the acoustic speed of the water in the rigid section of the experiment apparatus. From wave arrival times at transducers P_1, P_2, and P_3 (see Figure F-3), the average acoustic speed ($\bar{c}$) was determined to be 4381.90 ft/s. Thus, for the linear elastic water, k [$\equiv$ (reference density) $\times \bar{c}^2$] is 3.725×10^7 psf.

The initial and boundary conditions tailor the flow field that occurs in the water. Initially, the water is quiescent, and is at its reference state. The flow field is subject to the following boundary conditions:

- pressure boundary, upstream
- rigid wall boundary in the 10-foot, upstream section
- flexible wall boundary in the 5-foot, downstream section
- rigid boundary, downstream.

These boundary conditions limit the water motion to extremely small velocities. Thus, there is no practical reason to account for losses from fluid motion. Moreover, there is no need to apply rezoning. (Although rezoning was activated to determine if it affected the simulation.)

Figure F-7 displays the input data package for the simulation of the water-filled, straight pipe experiment. In addition, Figure F-8 illustrates the DATA statements which define the time history of the upstream pressure boundary. For this simulation, the upstream pressure boundary was defined to be the experiment pressure history that developed at the P_1 location (see Figure F-3). It is characterized by:

- $\sim$ 130 μs rise time
- $\sim$ 2060 psia peak amplitude
- $\sim$ 3.3 ms duration.

F.3 DISCUSSION OF SIMULATION

The simulation initiates with the application of the upstream pressure boundary, depicted on Figure F-9, to the computational grid. A compression hammer moves through the water within the rigid section at $\sim$ 4381.90 ft/s (acoustic speed), reaching the rigid/flexible interface at $\sim$ 2.28 ms. During this transit, the pulse maintains its initial character, as is illustrated on Figures F-10 through F-12. The figures also demonstrate the close agreement between the simulation and the experiment data.

```
TTL       SRI EXPERIMENT FP-SP-102
PRB
PRO       1.0
GRD       1.0       1.0       199.0
SYM       4.0
END
MAT
111       1.0       1.0
115       1.0       2.0
121       1.0       1.94
122       1.0       1.0       2116.8    3.725000E7
123       1.0       -1.0      100.0
END
GPT
211       1.0       1.0
212 MYGEN 1.0
221       1.0       1.0       199.0
241       1.0       198.0     0.0       15.0
END
ZON
311       1.0       1.0       199.0
321       1.0       1.0
322       1.0       1.0
341       1.0       -2116.8   -2116.8   -2116.8
381       1.0       1.0       1.0
381       2.0       2.0       198.0
381       3.0       199.0     199.0
382       1.0       1.0       2.0       2.0
382       2.0       1.0       2.0       1.0
382       3.0       1.0       2.0       2.0
END
BDY
421       1.0       2.0       5.0       1.0
421       199.0     5.0       5.0
422       1.0       1.0
431       1.0       9.0       0.0       5.00000E-3
END
TIM
511       0.63000E-6
512       0.62000E-60.57800E-5
521       .00600    9999.0
513       1.2       .33
END
```

(continued on next page)

Figure F-7. Input data for the simulation of the water-filled, straight pipe experiment.

```
EDT                                                          1.0
611       1.0
616       2.0
621       1.0       0.0       .0060     .0015
622       1.0       199.0
623       1.0       11.0
623       2.0       12.0
623       3.0       13.0
623       4.0       64.0
623       5.0       46.0
623       6.0       65.0
623       7.0       21.0
623       8.0       51.0
671       1.0       0.0       9999.0    1.0
672       1.00      1.0       64.0      1.0                    2.5
672       2.00      1.0       64.0      1.0                    7.5
672       3.00      1.0       2.0       1.0
672       4.00      1.0       5.0       1.0
672       5.00      1.0       6.0       1.0
672       6.00      1.0       91.0      1.0       2.0
672       7.00      1.0       64.0      1.0                    9.0
672       8.00      1.0       64.0      1.0                    10.125
672       9.00      1.0       64.0      1.0                    10.5
672       10.0      1.0       64.0      1.0                    11.5
672       11.0      1.0       64.0      1.0                    12.5
672       12.0      1.0       64.0      1.0                    13.0
672       13.0      1.0       64.0      1.0                    14.0
672       14.0      1.0       64.0      1.0                    14.875
672       15.0      1.0       64.0      1.0       199.0
672       16.0      1.0       92.0      1.0       5.0
672       17.0      1.0       92.0      1.0       11.0
672       18.0      1.0       92.0      1.0       67.0
672       19.0      1.0       92.0      1.0       81.0
672       20.0      1.0       91.0      1.0       3.0
672       21.0      1.0       93.0      1.0                    2.5
672       22.0      1.0       93.0      1.0                    7.5
672       23.0      1.0       93.0      1.0                    9.0
672       24.0      1.0       93.0      1.0                    10.125
672       25.0      1.0       93.0      1.0                    10.5
672       26.0      1.0       93.0      1.0                    11.5
672       27.0      1.0       93.0      1.0                    12.5
672       28.0      1.0       93.0      1.0                    13.0
672       29.0      1.0       93.0      1.0                    14.0
672       30.0      1.0       93.0      1.0                    14.875
672       31.0      1.0       93.0      1.0       199.9
END
END
```

Figure F-7. (concluded)

```
 DATA TIME /  .620,  .639,  .655,  .671,  .687,  .699,  .707,
*             .713,  .715,  .721,  .726,  .732,  .735,  .743,
*             .750,  .778,  .788,  .812,  .829,  .865,  .875,
*             .885,  .890,  .898,  .906,  .920,  .932,  .950,
*             .975,  .990,  .999, 1.011, 1.017, 1.027, 1.035,
*            1.044, 1.050, 1.068, 1.080, 1.085, 1.107, 1.119,
*            1.134, 1.151, 1.159, 1.165, 1.176, 1.187, 1.198,
*            1.208, 1.220, 1.232, 1.242, 1.250, 1.259, 1.268,
*            1.277, 1.287, 1.299, 1.307, 1.318, 1.326, 1.340,
*            1.350, 1.357, 1.367, 1.374, 1.384, 1.396, 1.414,
*            1.434, 1.444, 1.461, 1.486, 1.505, 1.526, 1.555,
*            1.585, 1.618, 1.678, 1.722, 1.765, 1.834, 1.878,
*            1.917, 1.965, 2.007, 2.032, 2.089, 2.142, 2.185,
*            2.287, 2.340, 2.426, 2.487, 2.563, 2.669, 2.748,
*            2.878, 2.952, 3.107, 3.215, 3.301, 3.496, 3.630,
*            3.712, 3.824, 3.898, 3.934/
 DATA PRES /   0.0, 222.7, 402.8, 739.3, 1175., 1555., 1853.,
*            2019., 2038., 1934., 2009., 1938., 2009., 1953.,
*            2047., 1588., 1678., 1412., 1573., 1104., 1218.,
*            1199., 1175., 1081., 1142., 952.6, 1052., 748.8,
*            995.3, 886.3, 1009., 928.9, 1019., 1085., 1033.,
*            1118., 1076., 891.0, 1043., 1085., 810.4, 862.6,
*            796.2, 947.9, 900.5, 848.3, 739.3, 782.0, 739.3,
*            805.7, 729.9, 691.9, 658.8, 649.3, 677.7, 706.2,
*            715.6, 701.4, 673.0, 668.2, 701.4, 772.5, 824.6,
*            644.5, 625.6, 611.4, 663.5, 673.0, 658.8, 635.1,
*            582.9, 573.5, 582.9, 559.2, 549.8, 545.0, 511.8,
*            507.1, 497.6, 469.2, 450.2, 440.8, 412.3, 398.1,
*            379.1, 364.9, 346.0, 336.5, 308.1, 279.6, 260.7,
*            251.2, 213.3, 184.8, 165.9, 151.7, 123.2, 142.2,
*            113.7,  90.1,  90.1,  52.1,  66.3,  33.2,  37.9,
*             33.2,  47.4,  28.4,   0.0/
```

TIME: time (ms)

PRES: pressure (psig)

Figure F-8. Data statements for the simulation of the water-filled, straight pipe experiment.

WATER-FILLED, STRAIGHT PIPE RESPONSE TO A PRESSURE PULSE

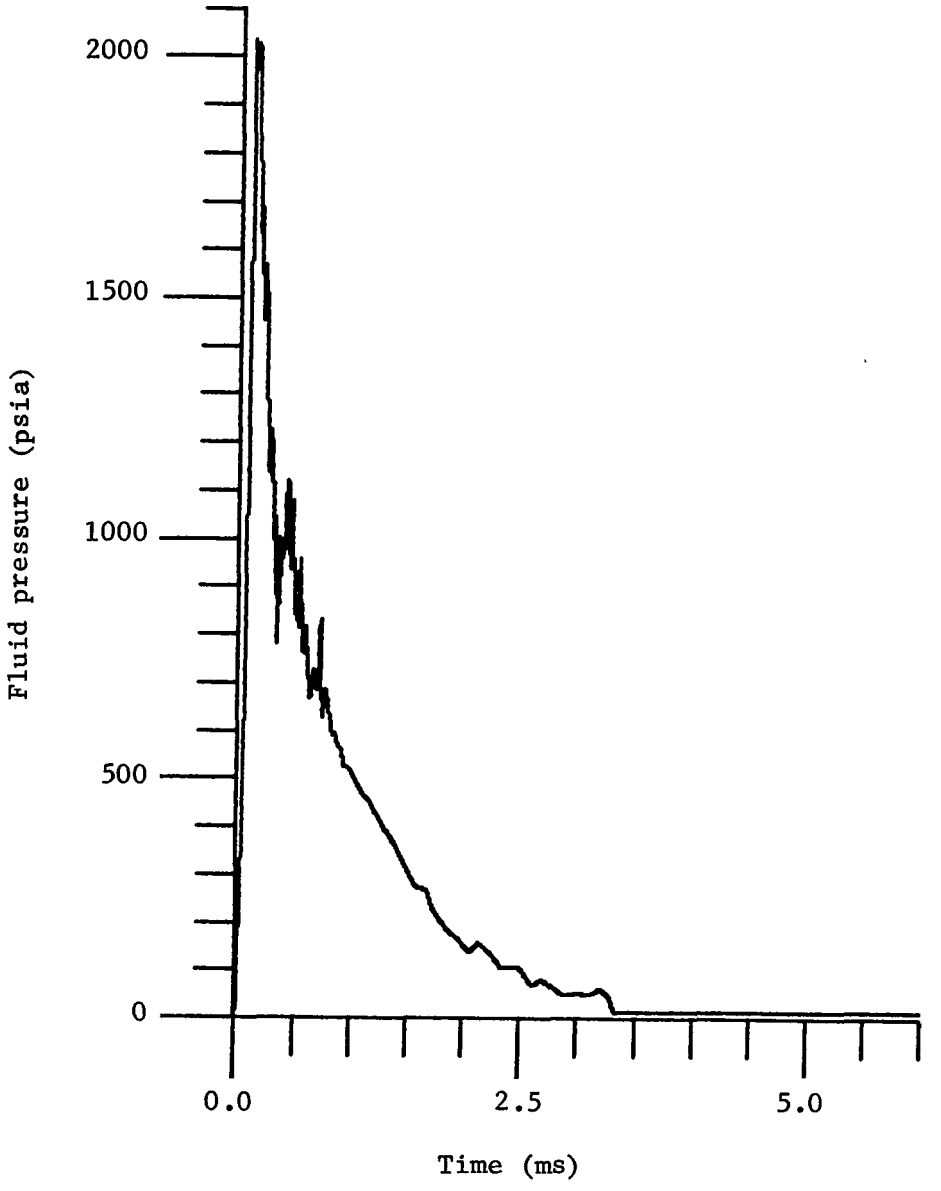

Figure F-9. Pressure history in the thick-walled (rigid) section of pipe, at site of pressure pulse initiation.

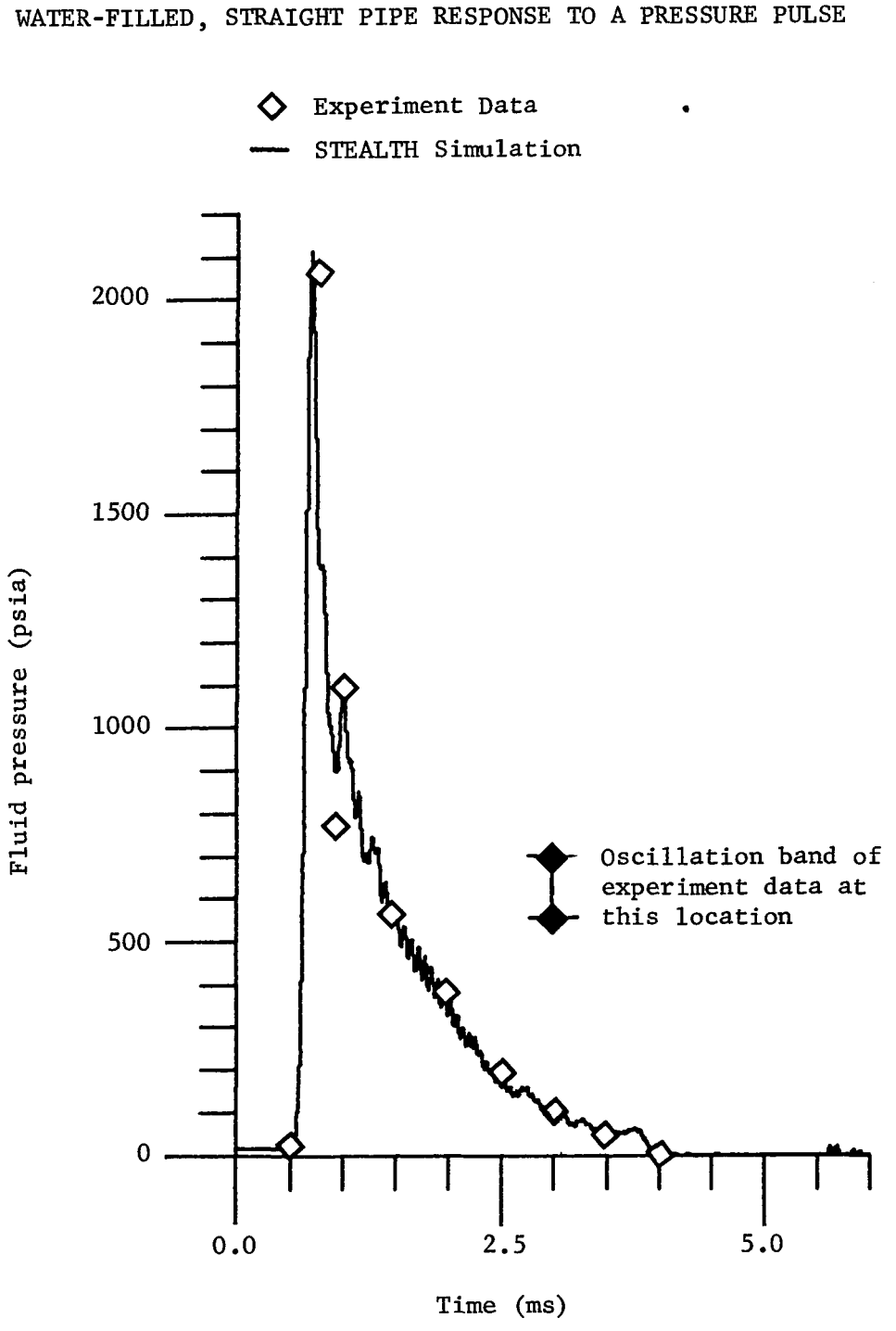

Figure F-10. Pressure history in the thick-walled (rigid) section of pipe, 2.5 ft from site of pressure pulse initiation.

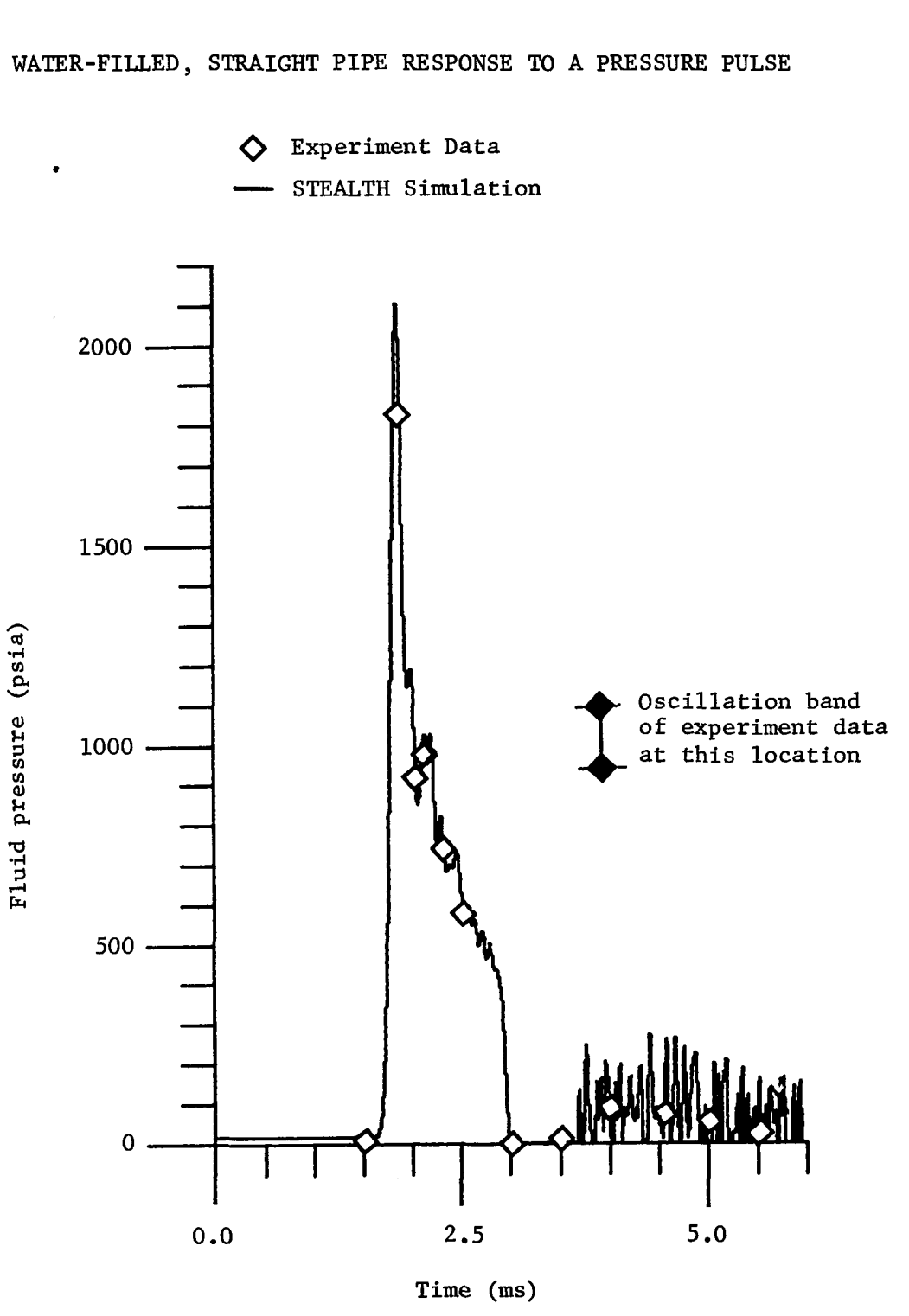

Figure F-11. Pressure history in the thick-walled (rigid) section of pipe, 7.5 ft from site of pressure pulse initiation.

WATER-FILLED, STRAIGHT PIPE RESPONSE TO A PRESSURE PULSE

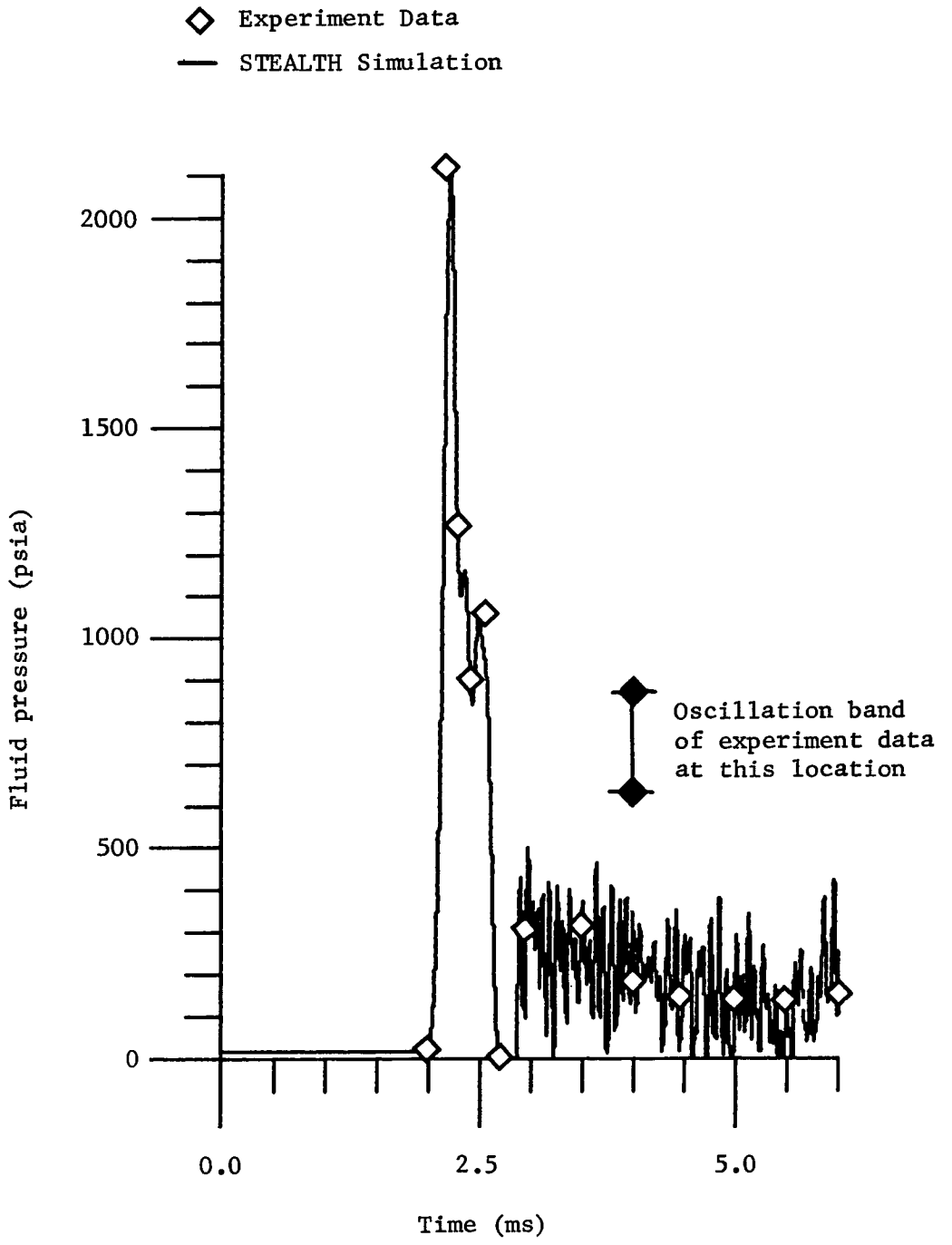

Figure F-12. Pressure history in the thick-walled (rigid) section of pipe, 9.0 ft from site of pressure pulse initiation.

At later times, the simulation displays considerable oscillations. In fact, so do the experiment data; the figures display oscillation bands which describe the extent of the data oscillations. These oscillations are associated with the cavitation (hydrodynamic spall) of the water, that is induced by the flexible section. In that section, the plastic strain and associated volumetric expansion are large enough to eliminate positive hydrostatic pressure in the water. While the simple spall model in the simulation certainly does not model the correct physics of water cavitation, nevertheless the macroscopic pressure oscillations show a reasonable comparison with data.

Upon reaching the rigid/flexible interface, the pulse refracts into the flexible section as a weaker compression, and simultaneously reflects back into the rigid section as a rarefaction. Both of these waves develop as a consequence of the volumetric expansion, due to the plastic strain of the nickel pipe walls. Figure F-13 illustrates the extent of compression attenuation at 1.5 in. downstream of the interface. The original >2000 psi pulse is now only ~ 775 psi. Here, also, the cavitation phenomena create high frequency oscillations. Again, the comparison between the simulation and the data is very good, including the extent of oscillations. The pressure rise at late times is the effect of a returning compression hammer, created when the refracted pulse reflects off of the rigid end plate.

Figure F-14 shows the associated strain history which develops 1.5 in. downstream of the interface. The strain is highly plastic (0.06% elastic limit), and permanent. The comparison between data at one strain gage and the simulation is very good. The figure also indicates the range of data readings that were obtained by the five separate strain gages located at Section A-A (see Figure F-3). The probable causes for the different readings are asymmetries in the pipe wall cross section and the configuration asymmetry induced by the location of the pressure transducer.

Figures F-15 through F-18 demonstrate the close agreement between the pressure data and simulation pressures for various locations within the flexible section. Figure F-19 illustrates a location where the comparison between

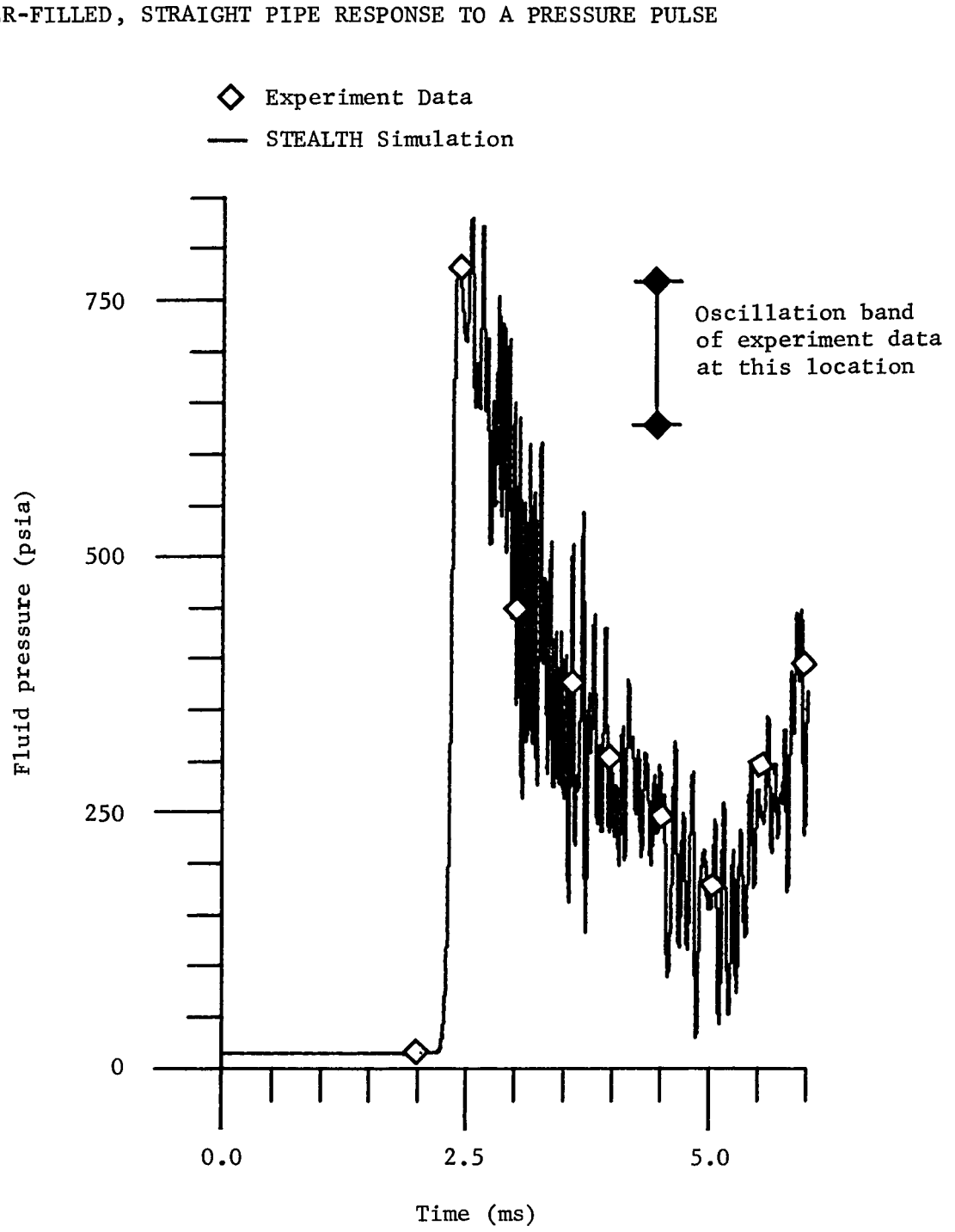

Figure F-13. Pressure history in the thin-walled (flexible) section of pipe, 10.125 ft from site of pressure pulse initiation.

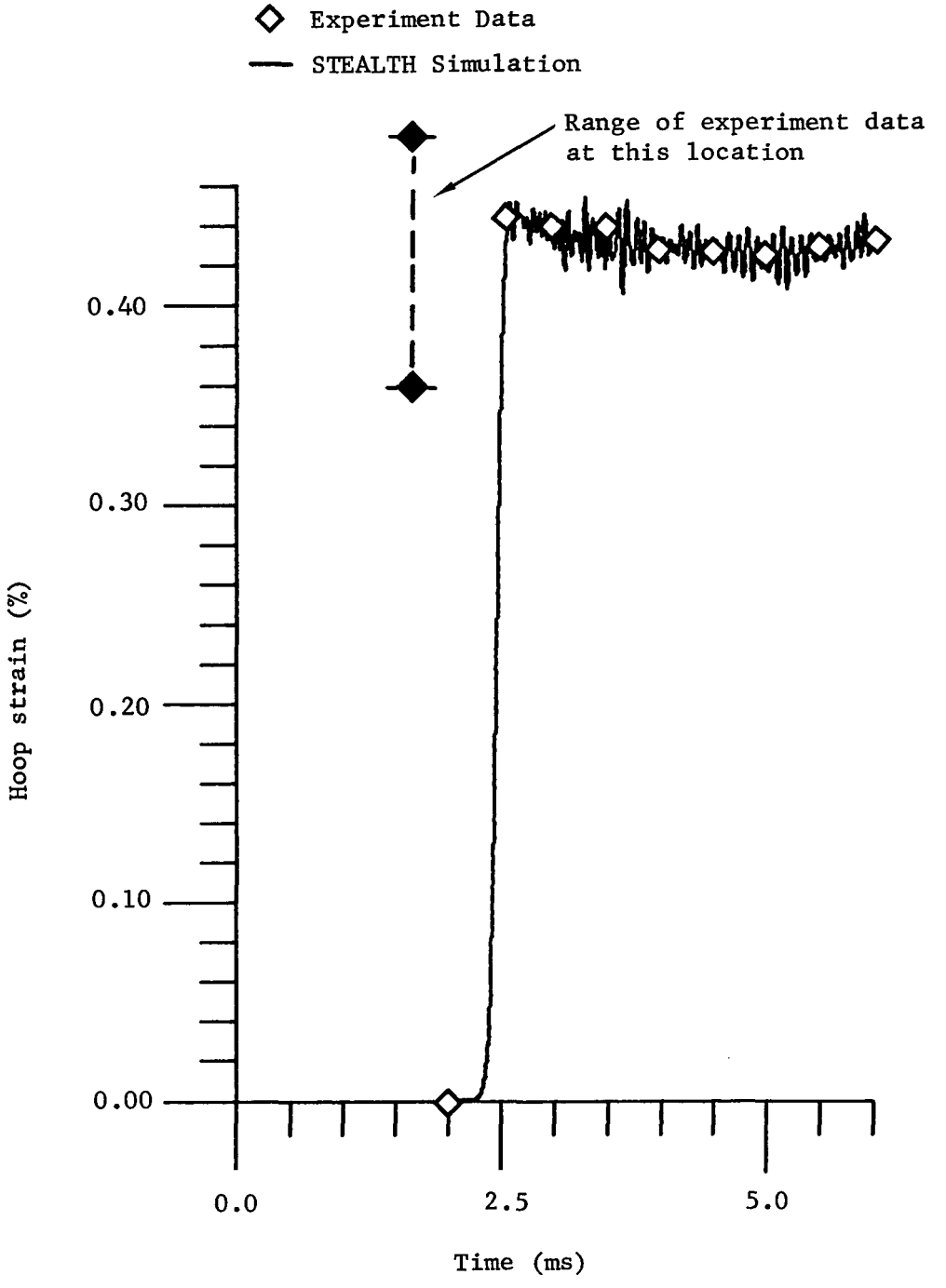

Figure F-14. Strain history in the thin-walled (flexible) section of pipe, 10.125 ft from site of pressure pulse initiation.

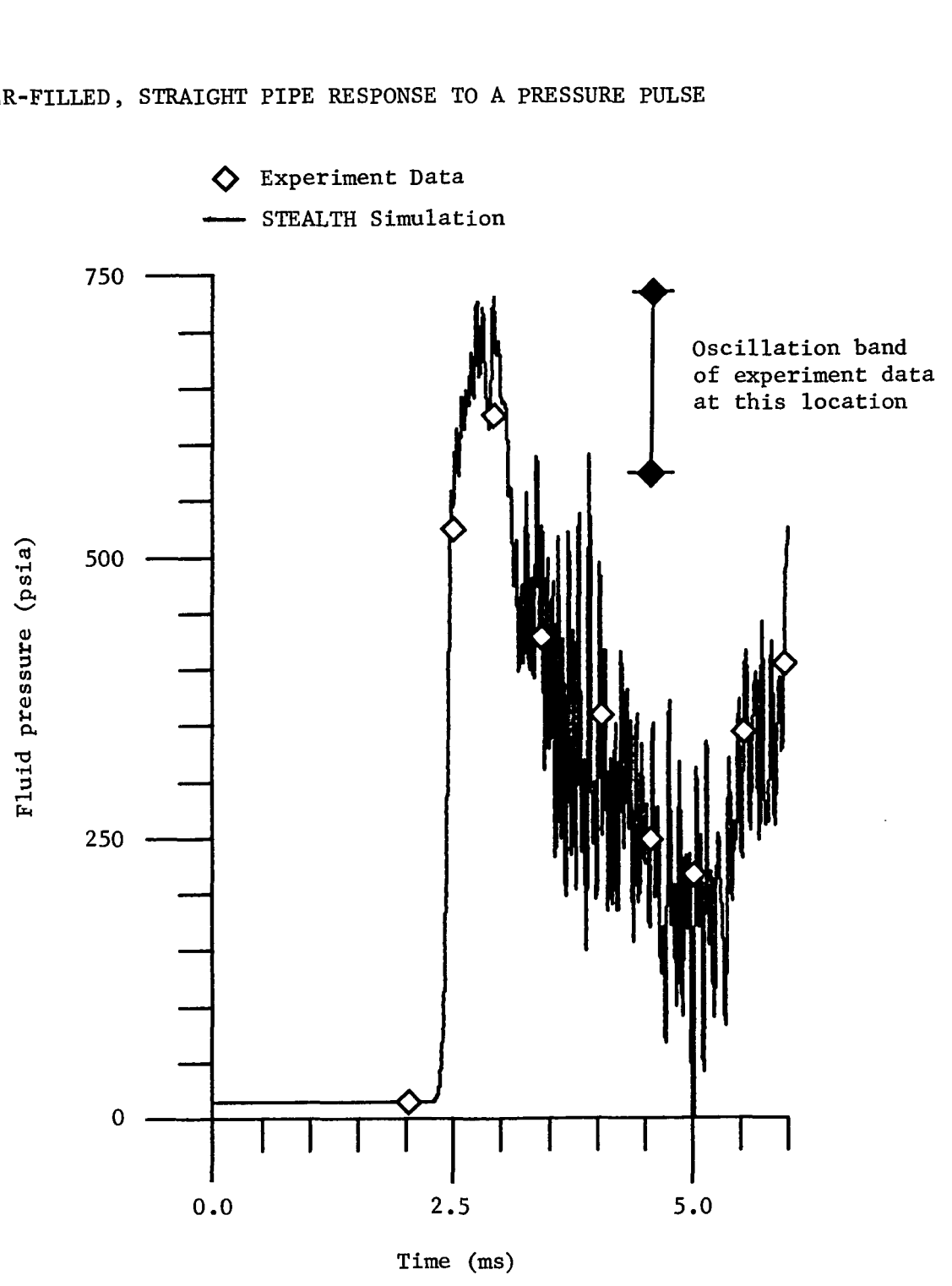

Figure F-15. Pressure history in the thin-walled (flexible) section of pipe, 10.5 ft from site of pressure pulse initiation.

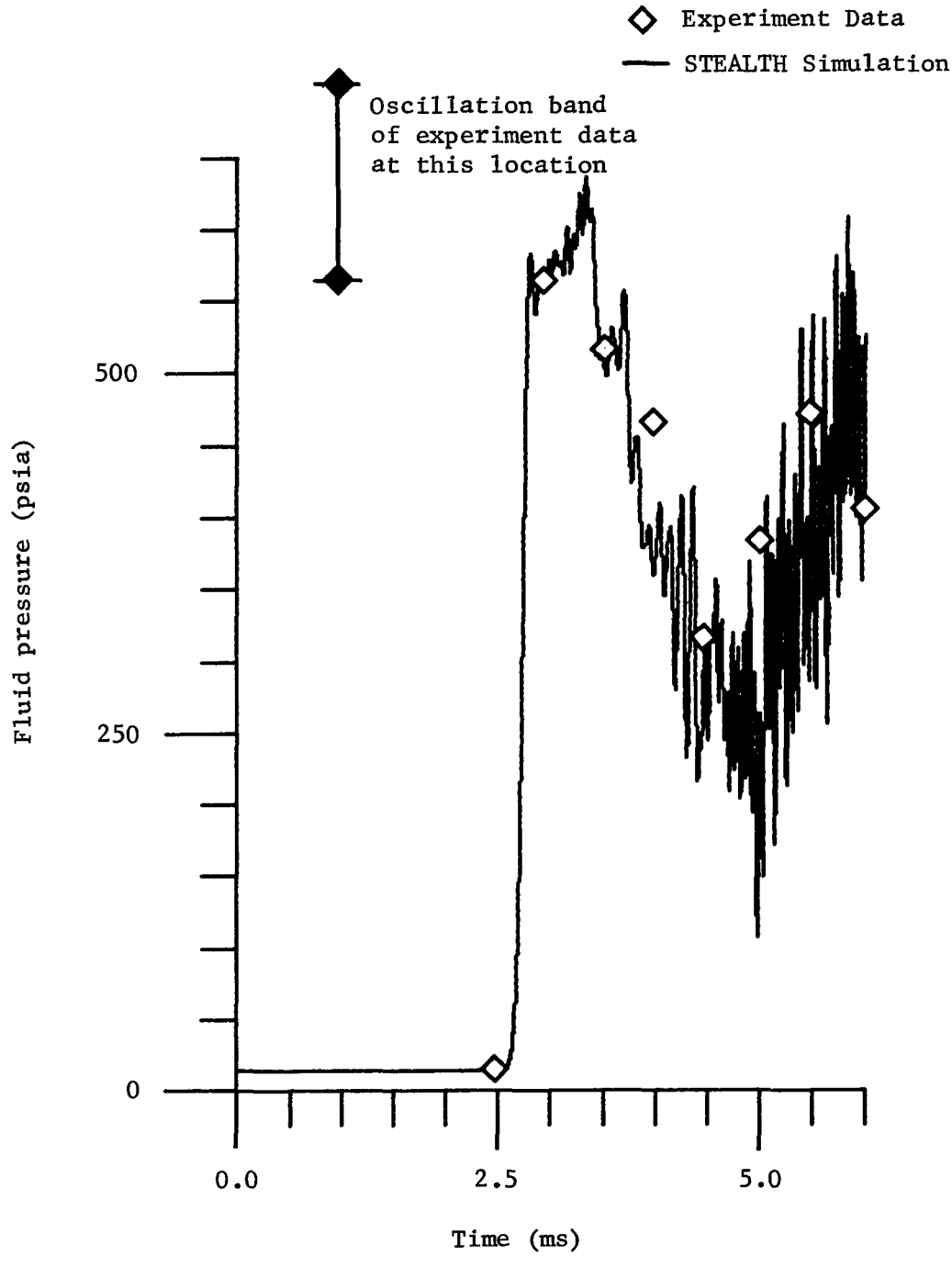

Figure F-16. Pressure history in the thin-walled (flexible) section of pipe, 11.5 ft from site of pressure pulse initiation.

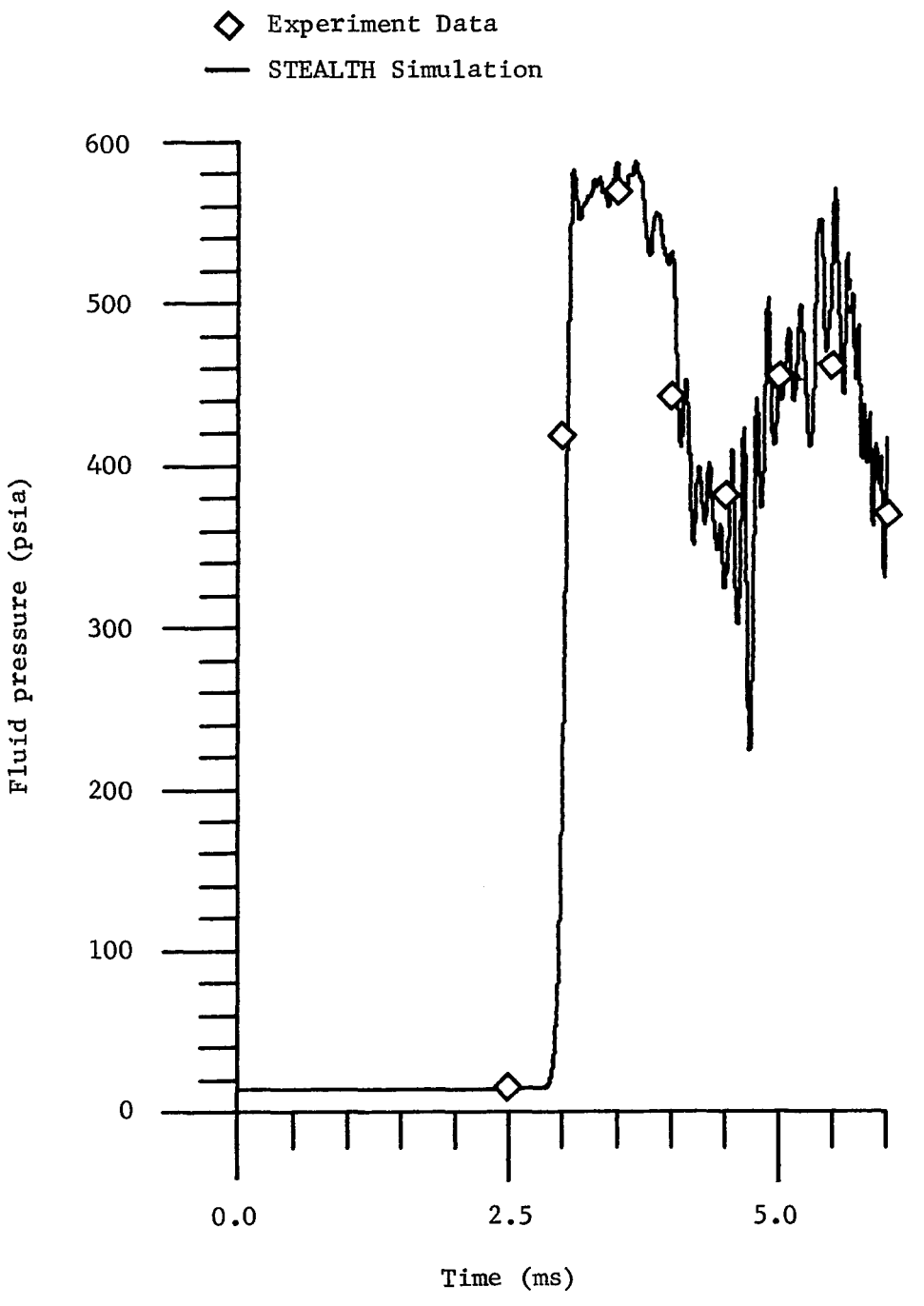

Figure F-17. Pressure history in the thin-walled (flexible) section of pipe, 12.5 ft from site of pressure pulse initiation.

WATER-FILLED, STRAIGHT PIPE RESPONSE TO A PRESSURE PULSE

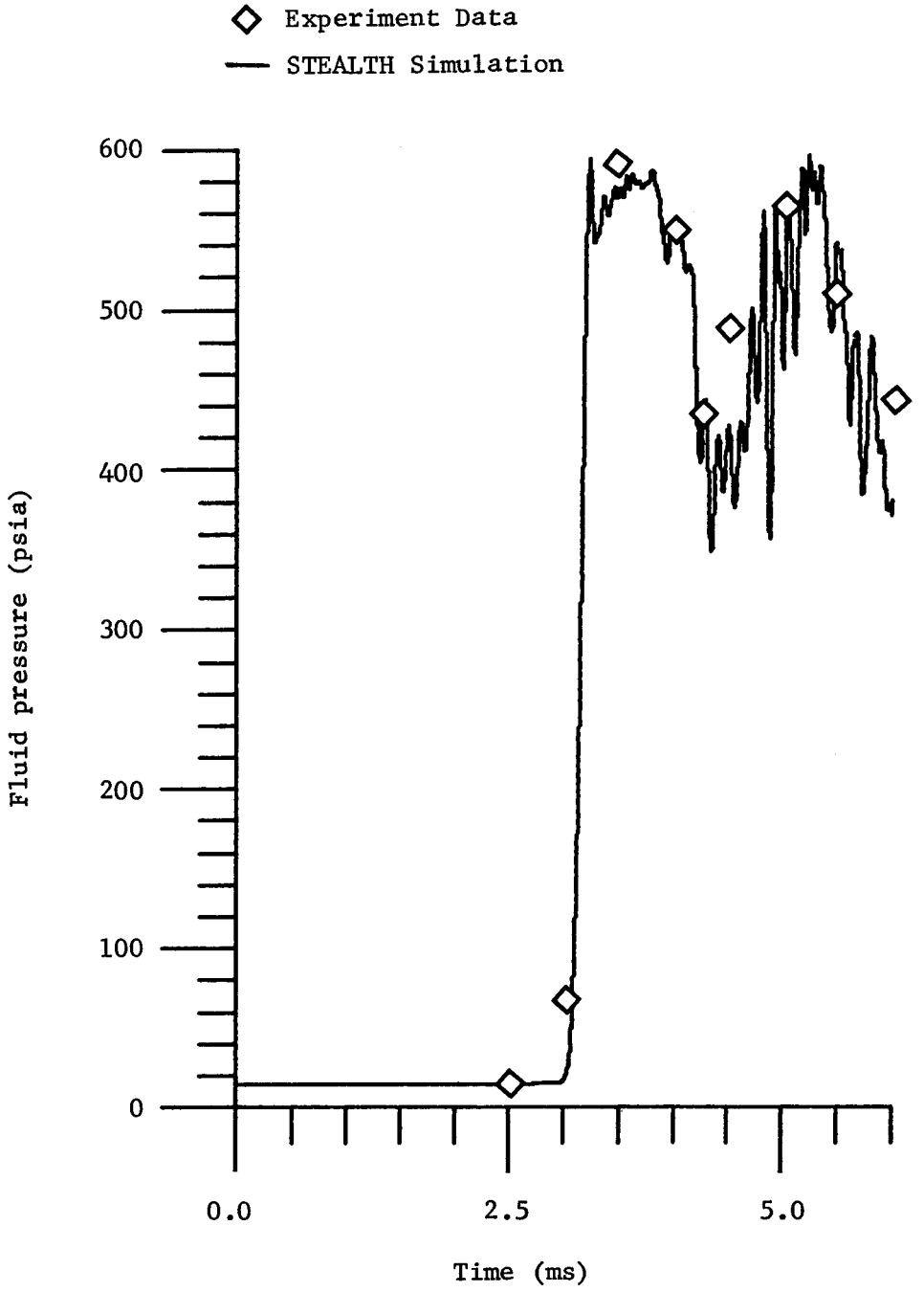

Figure F-18. Pressure history in the thin-walled (flexible) section of pipe, 13.0 ft from site of pressure pulse initiation.

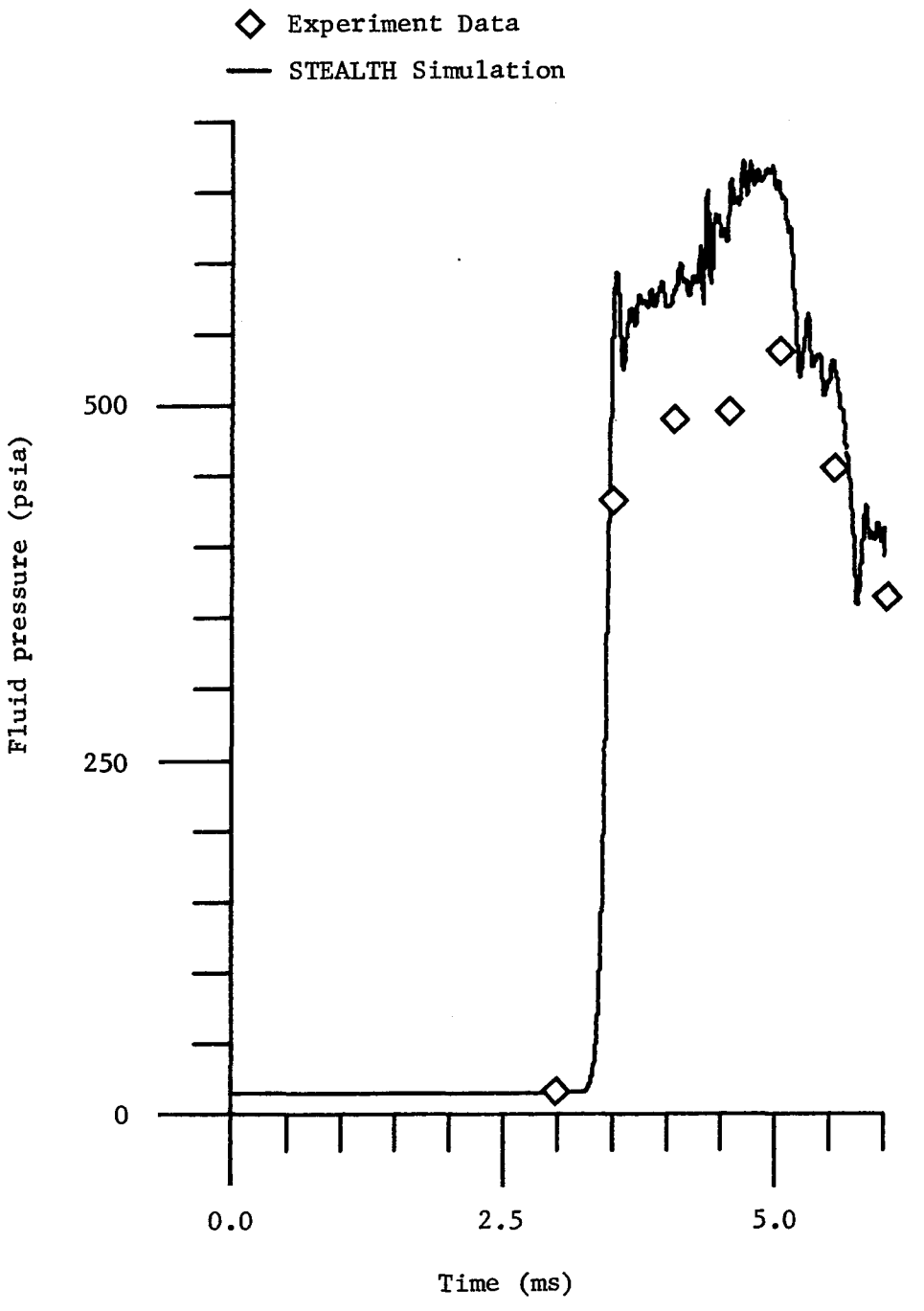

Figure F-19. Pressure history in the thin-walled (flexible) section of pipe, 14.0 ft from site of pressure pulse initiation.

the data and the simulation is not good. In view of the excellent comparisons upstream of this location, the discrepancy is a mystery. Figures F-20 and F-21 show the strain histories associated with Figures F-15 and F-19, respectively. The agreement between strain data and the simulation is very good. Figure F-21 shows that the simulation was able to predict the elastic strain precursor that occurred prior to 4.5 ms. The good agreement shown on Figure F-21 serves to underscore the puzzling discrepancy shown on Figure F-19.

Figures F-22 and F-23 illustrate discrepancies in the comparisons of pressure and strain, respectively, at the location that is 1.5 in. from the downstream boundary. Here, the discrepancies are understandable. The simulation had an absolutely rigid boundary, while the experiment had a finite end plate which yielded enough to affect the data. This is consistent with the simulation predictions being higher than the data. In effect, the simulation did not represent the experiment near the end plate.

The high degree of correlation between the experiment data and the predictions of the simulation suggests that the STEALTH code can predict compression hammer attenuation within a water-filled, straight pipe with flexible walls. Moreover, the rudimentary thin shell model responds accurately to the pressure differences across the pipe wall, verifying the assumption of negligible shear stresses within the pipe wall material. Finally, the comparison (not shown) of this simulation with an abbreviated one, where the rezoner was not activated, indicates that rezoning does not affect the simulation.

F.4 CLOSURE

The simulation required 1063 time cycles to span 6 ms of real time. Since there were 280 computational nodes (199 fluid nodes and 81 wall points), the simulation required $\sim$ 300,000 node-cycle calculations. On a CDC 7600 computer, the simulation executed in $\sim$ 140 CP seconds. Thus, the simulation performance was 0.47 CP ms per node-cycle.

WATER-FILLED, STRAIGHT PIPE RESPONSE TO A PRESSURE PULSE

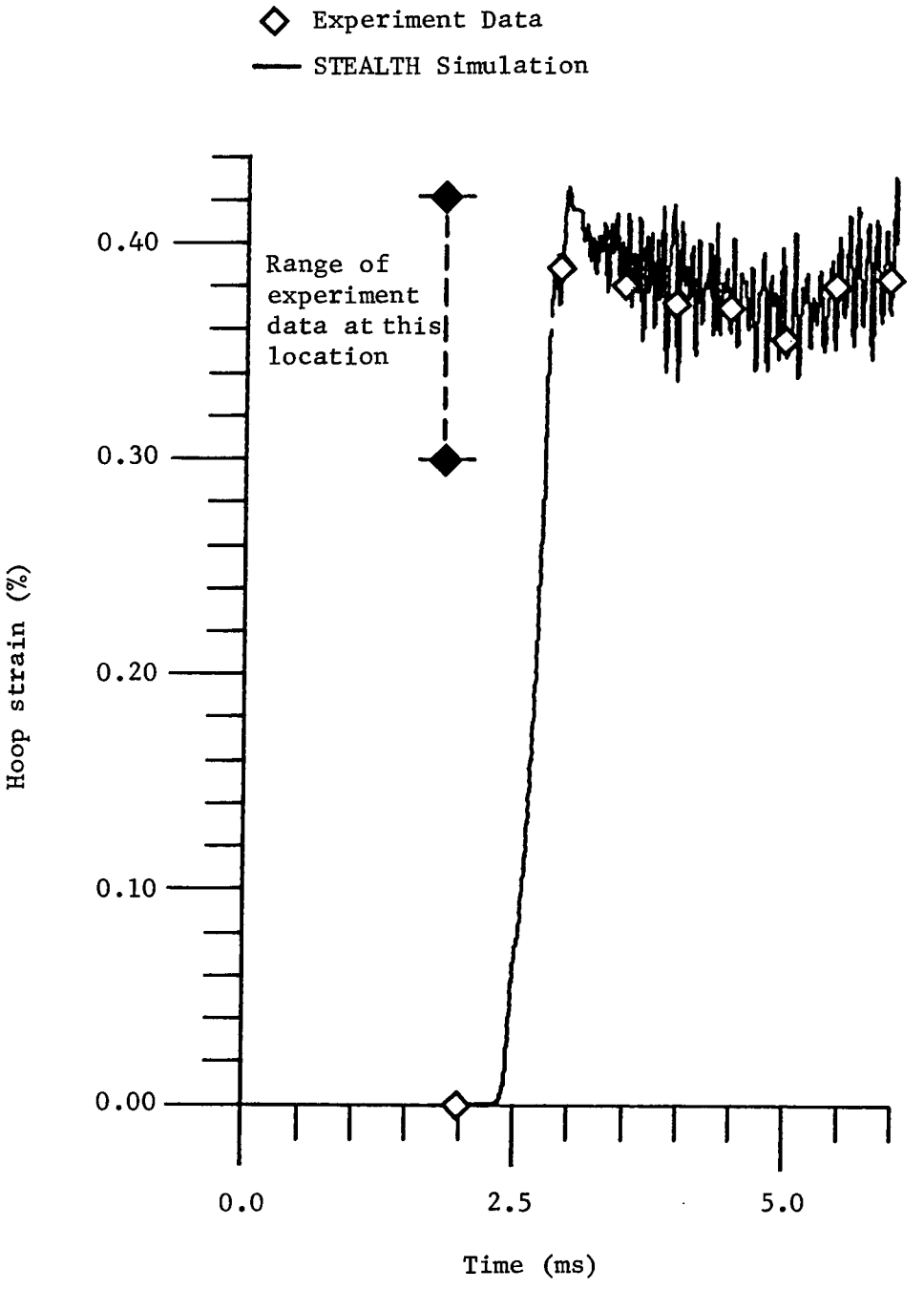

Figure F-20. Strain history in the thin-walled (flexible) section of pipe, 10.5 ft from site of pressure pulse initiation.

WATER-FILLED, STRAIGHT PIPE RESPONSE TO A PRESSURE PULSE

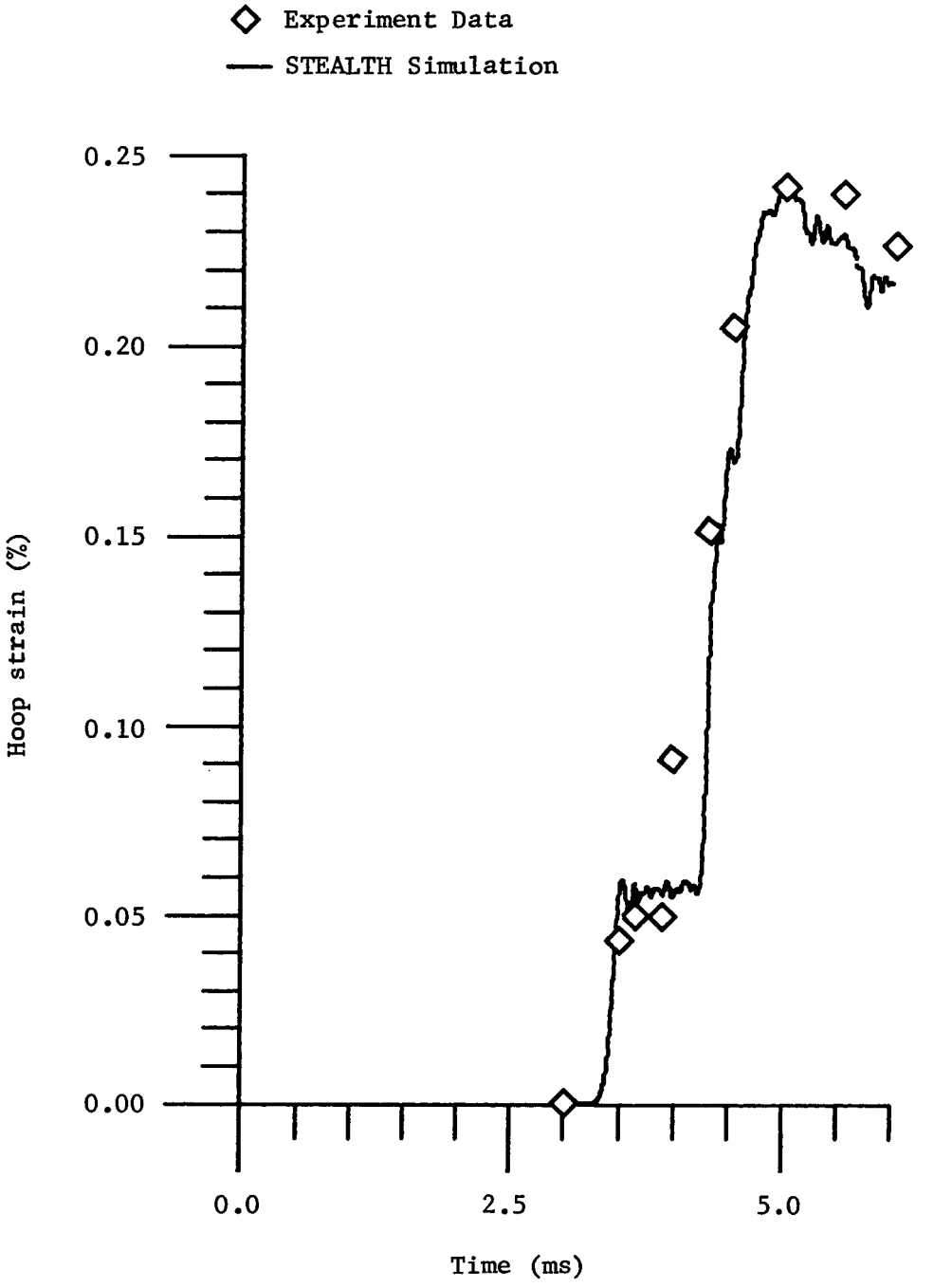

Figure F-21. Strain history in the thin-walled (flexible) section of pipe, 14.0 ft from site of pressure pulse initiation.

WATER-FILLED, STRAIGHT PIPE RESPONSE TO A PRESSURE PULSE

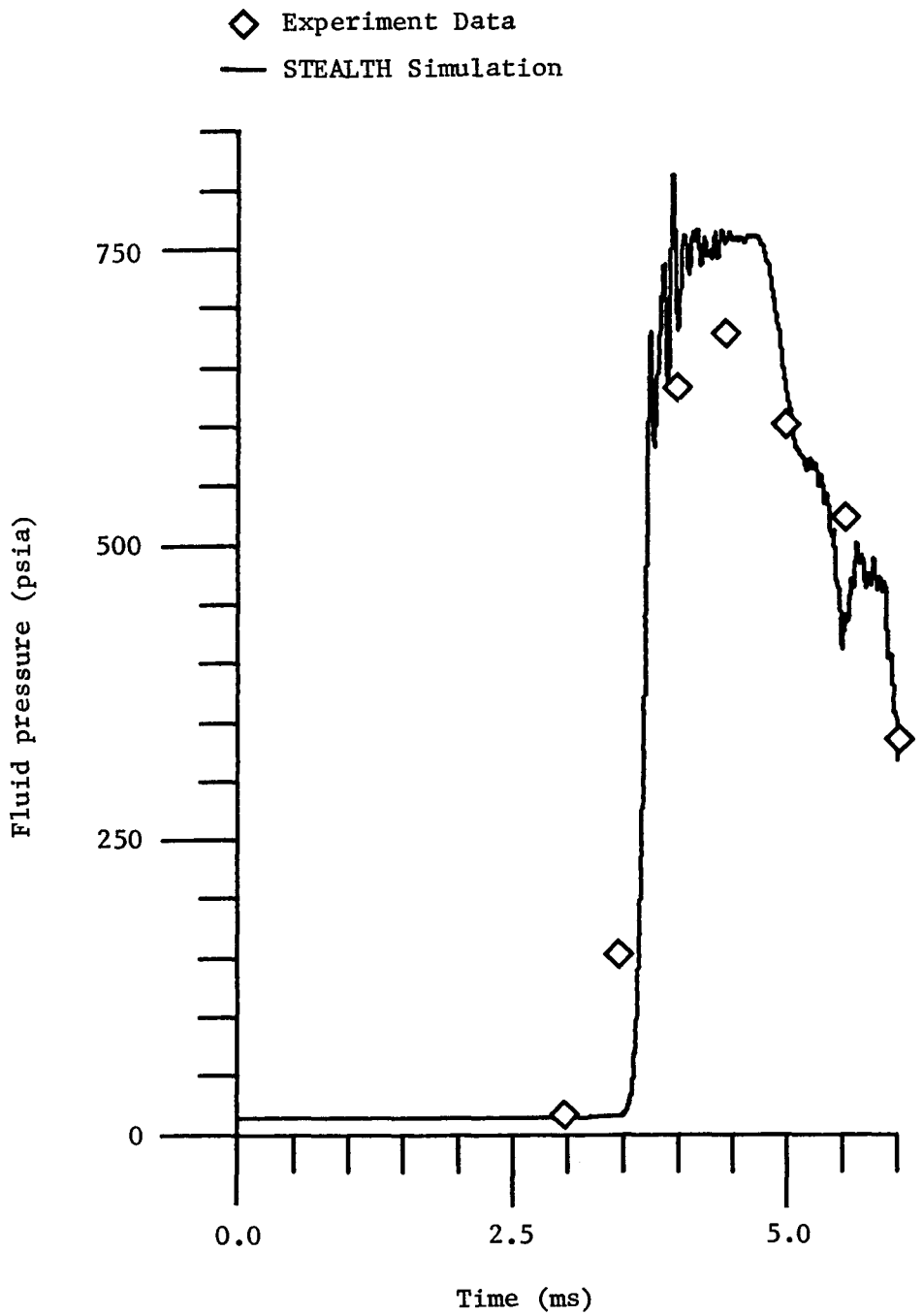

Figure F-22. Pressure history in the thin-walled (flexible) section of pipe, 14.875 ft from site of pressure pulse initiation.

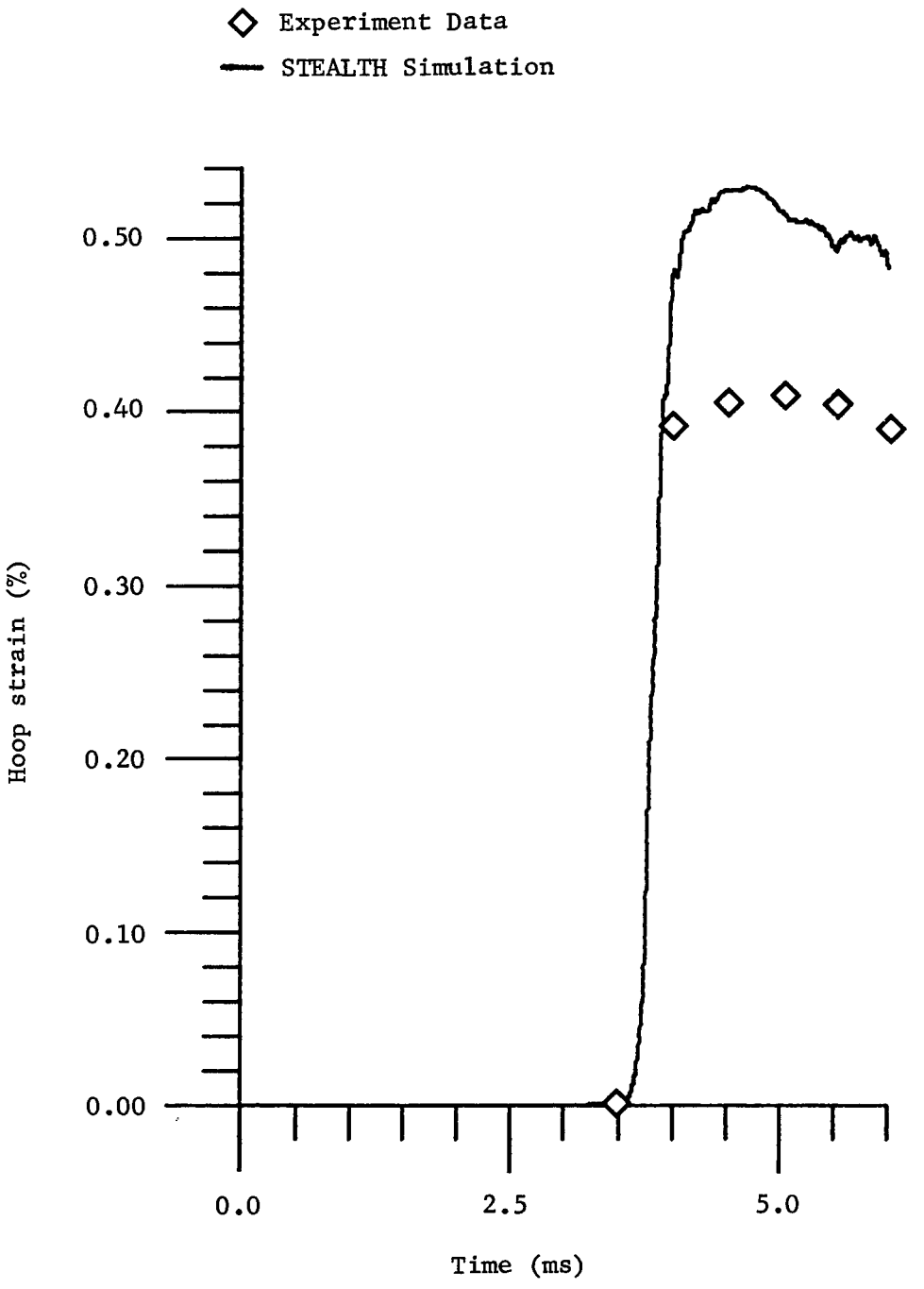

Figure F-23. Strain history in the thin-walled (flexible) section of pipe, 14.875 ft from site of pressure pulse initiation.

REFERENCES

F-1. C. M. Romander and D. J. Cagliostro, "Experiments on the Response of Flexible Piping Systems to Internal Pressure Pulses," PYD-1960, Stanford Research Institute, Menlo Park, California, April 1976. Prepared for Argonne National Laboratory, Argonne, Illinois.

F-2. C. M. Romander, L. E. Schwer, and D. J. Cagliostro, "Response of Water-Filled Thin-Walled Pipes to Pressure Pulses: Experiments and Analysis," ASME Paper 78-PVP-53, presented at Joint ASME/CSME Pressure Vessels & Piping Conference, Montreal, Canada, June 25-30, 1978.

F-3. W. T. Thomson, Theory of Vibrations with Applications, Prentice Hall, Inc., Englewood Cliffs, New Jersey, 1972.

F-4. Y. C. Fung, Foundations of Solid Mechanics, Prentice Hall, Inc., Englewood Cliffs, New Jersey, 1965.